University of Nevada, Reno

Mass and heat transfer processes in magmatic orogens driven by magmatism, tectonic deformation, and surface erosion

A dissertation submitted in partial fulfillment of the requirements for the degree of

Doctor of Philosophy in Geology

by

Jiaming Yang

Wenrong Cao/Dissertation Advisor:

August 2022

THE GRADUATE SCHOOL

We recommend that the dissertation
prepared under our supervision by

JIAMING YANG

entitled

Mass and heat transfer processes in magmatic orogens driven by magmatism, tectonic deformation, and surface erosion

be accepted in partial fulfillment of the
requirements for the degree of

DOCTOR OF PHILOSOPHY

Wenrong Cao, Ph.D.
Advisor

Stacia M. Gordon, Ph.D.
Committee Member

Philipp Ruprecht, Ph.D.
Committee Member

Andrew V. Zuza, Ph.D.
Committee Member

Xiaoliang Wang, Ph.D.
Graduate School Representative

David W. Zeh, Ph.D., Dean
Graduate School

August, 2022

ABSTRACT

Magmatic orogens are continental arcs and collisional belts that are associated with syn-tectonic magmatism. They record heat and mass transfer processes acting from the mantle to the surface. While magmatism, deformation, and surface erosion each take place at various depth levels, they are dynamically linked processes through interaction in the lithosphere. This dissertation presents an investigation of how heat and mass transfer processes in the lithosphere affect the evolution of magmatic orogens. I first present an evaluation of magma genesis resulting from partial melting of underthrusted lower crust. The causes of episodic magmatism in the Mesozoic Sierra Nevada continental magmatic arc and the sources of high-magma flux (flare-ups) are under debate. Here, I use the results of numerical modeling and scaling analysis to assess the mass balance and thermodynamic feasibility of generating arc magma as a result of partial melting of underthrusted lower crust. I show with a constant underthrusting rate of 5 km/Myr, the magmatic thickening rate is 0.1-0.3 km/Myr, accounting for 10-30% of the magmatic thickening rate during a flare-up. The cumulative volume of magma generated from the partial melting of a 20-km-thick underthrusted lower crust is on the order of 10^5 km^3, ~10-40% of the estimated magma volume generated during a flare-up. Therefore, the results show that partial melting of underthrusted lower crust plays a subsidiary role in driving a magmatic flare-up event. Additional magma derived from the mantle and/or other crustal sources are needed to achieve the observed magmatic output during flare-ups. However, the arc root developed by partial melting of the underthrusted crust

reduces the time needed to obtain the critical thickness for root foundering, thus influencing the tempo of arc magmatism.

As magma ascends into the crust, its interactions with the deforming crust are recorded in the exhumation history of a tilted crustal section and fabrics in plutons. The Gangdese Batholith is well exposed in southern Tibet and presents a unique opportunity to investigate the evolution of a continental arc from subduction to collision. I applied Al-in-hornblende barometry across the eastern Gangdese Batholith to obtain pluton emplacement pressures to identify potential spatial trends in bedrock pressure. The results reveal a regional paleo-depth pattern with plutons emplaced at 1-2 kbar in the west near Lhasa that deepens to 6-12 kbars in the east, near Nyingchi. By coupling the pressure data with U-Pb zircon ages, I estimate the exhumation history of the Gangdese Batholith since 100 Ma and show a sequence of exhumation and burial phases as well as the expected changes in crustal thickness, reflecting major tectonic events including the development of a continental arc and the India-Asia continent-continent collision. I hypothesize that the Gangdese Batholith was tilted due to differential exhumation along the E-W direction since ~10 Ma, associated with the formation of the eastern Himalayan syntaxis. Along with the exhumation history, I also studied fabrics recorded by the Gangdese plutons and report magmatic fabric measurements from the eastern Gangdese Batholith, aimed to decipher the crustal response to changes in India-Asia convergence style from subduction to collision. Results show magmatic fabric orientations are variable through time and represent: (1) a pre-collision Late Cretaceous subduction phase of orogen-perpendicular contraction and crustal thickening. (2) Transitional Paleocene-

Eocene crustal thinning and a change in crustal contraction stress from ~N-S to ~E-W. (3) Post-Eocene crustal thickening without a clear, dominant principal stress direction. The pre-collision Late Cretaceous fabrics are interpreted to record approximate head-on subduction of the Neo-Tethyan oceanic plate beneath the Asian continent, while the post-collision fabrics reflect the enigmatic nature of the India-Asia collision, as well as the complexity of the post-collisional processes.

Motivated by the recognition of the tilted Gangdese crust, I explored the role of surface erosion in driving solid earth processes. Particularly, whether erosion-driven rock uplift is responsible for the rapid exhumation of the eastern Himalayan syntaxis (EHS). Results of numerical simulations show that localized surface erosion (5 km/Myr) is able to exhume lower crust from depths of >40 km on timescale of ~10 Myr, produce high topography, and generate partial melt in the lower crust. Erosion-driven advection elevates the local geothermal gradient and reduces crustal viscosity, promoting deformation. Exhumation is sustained by isostatic flow resulting from lithostatic pressure difference and amplified by crustal diapirism, associated with the presence of hot and buoyant molten rocks in the weakened advection channel. Such diapiric upwellings trigger a rapid acceleration in rock uplift rates to values greater than the driving erosional forcing and cause localized surface uplift, resulting in topography higher than surrounding regions. The erosion-driven exhumation model demonstrates the intricate coupling between surface erosion and rock uplift, as well as the active role of surface erosion in driving orogenic evolution.

ACKNOWLEDGMENTS

This dissertation and the associated research were supported by the University of Nevada, Reno, Graduate Teaching Assistantship; the National Science Foundation grants (EAR-1830139; EAR-1914501; EAR-1649254); the National Science Foundation of China (41888101); the Second Tibetan Plateau Scientific Expedition and Research program grant (2019QZKK0802); Chinese Academy of Sciences State Key Laboratory of Lithospheric Evolution grant (SKL-Z201706); Wenrong Cao's startup funds at the University of Nevada, Reno; the University of Nevada, Reno, mICRo grant awarded to Wenrong Cao and Stacia Gordon; and the Liang-Chi Hsu Graduate Research Endowment.

TABLE OF CONTENTS

LIST OF TABLES

LIST OF FIGURES

CHAPTER 1: Introduction to the dissertation

MASS AND HEAT TRANSFER PROCESSES IN MAGMATIC OROGENS

Orogens are the result of multiple processes such as magmatism, metamorphism, tectonic deformation, sedimentation, and surface erosion operating in the mantle up to the surface. In particular, the formation of orogenic belts involves prolonged mass and heat transfer processes across different depths in the lithosphere and Earth's surface (e.g., Jamieson & Beaumont, 2013). Both continental magmatic arcs and collisional belts are typically associated with syn-tectonic magmatism (e.g., Dewey & Bird, 1970; Pfiffner, 1992; Clift et al., 2003; Simoes et al., 2007; Roeder et al., 2013). Therefore, both orogenic systems can be referred to as 'magmatic orogens' or 'hot orogens' because of the intense deformation and magmatism that affects them (Collins 2002). Magmatic orogens play an important role in volcanic hazards (e.g., Crisp 1984), global carbon budget (e.g., McKenzie et al., 2016), in the formation of new continental crust (e.g., Rudnick 1995, Stern, 2002) as well as the formation of most ore deposits (e.g., Richards, 2013). In a typical magmatic orogen, there are several processes occurring in the mantle to the surface that are linked, including: (1) melt generation in the mantle wedge and lower crust (e.g., Davies & Stevenson, 1992; Stern & Kilian, 1996); (2) magma ascent and emplacement into the deforming crust (e.g., Brown, 1994; Petford et al., 2000); (3) orogeny as a result of magmatism and tectonic deformation (e.g., Dickinson et al., 1978; Agard et al., 2011; Mouthereau et al., 2012); and (4) surface erosion modifying crustal thickness and topography (e.g., Molnar & England, 1990; Avouac & Burov, 1996; Willett 1999; Zeitler et al., 2001). However, our understanding of various processes operating in magmatic orogens such as subduction zone dynamics, magma production, crustal growth, and surface processes and their interactions is still limited.

In my dissertation, I focused on the Sierra Nevada Batholith in California and the Gangdese Batholith in southern Tibet, China. The Sierra Nevada Batholith represents a long-lived Mesozoic continental arc formed by subduction of the Farallon plate beneath the North American plate. The plutonic part of the arc is referred to as the Sierra Nevada Batholith, which has been exhumed to the surface (e.g., Chen & Moore, 1982; Bateman, 1992; Ducea, & Saleeby, 1998; Ducea, 2001; Saleeby et al., 2008). The Sierra Nevada Batholith is recognized as an example of episodic magmatic behaviors in continental arc systems (Ducea, 2001, DeCelles et al., 2009, Paterson & Ducea, 2015) and presents an opportunity to investigate how mass and heat transfer processes in the crust and upper mantle affect the evolution of the orogen. One of the critical questions related to the Sierra Nevada Batholith is the cause of the episodic magmatism (i.e., arc tempos) (e.g., Paterson & Ducea, 2015; Kirsch et al., 2016). While some models provide an integrated framework to explain episodic magmatism (e.g., Ducea, 2001, DeCelles et al., 2009), the mantle versus crustal contributions to the genesis of arc magma are not well constrained.

The Gangdese Batholith developed as the result of the northward subduction of the Neo-Tethys paleoocean beneath the Eurasian plate, and the subsequent India-Eurasia collision (e.g., Yin & Harrison, 2000; Kapp et al., 2007; Ji et al., 2009, 2014; Zhu et al., 2015). The Gangdese plutons are well exposed in southern Tibet with numerous crystallization ages spanning from Cretaceous to Neogene (see summary in Chapman & Kapp, 2017). Thus, the Gangdese Batholith presents a unique opportunity to investigate the evolution of a continental arc from subduction to collision. Although significant research has focused on the composition and geochronology of the igneous rocks in the Gangdese Batholith (e.g., Ji et al., 2014; Zhu et al., 2015), many key questions remain:

(1) What is the regional bedrock pressure pattern in the Gangdese orogen? Does the Gangdese represent a tilted crustal section? (2) How does the upper plate accommodate deformation during subduction and collision? (3) What is the role of surface erosion in exhuming the deeper crust?

My dissertation addresses the above questions related to the Sierra Nevada and the Gangdese Batholiths. The chapters of this dissertation are presented as independent journal-style papers. The second chapter, *Does underthrusting crust feed magmatic flare-ups in continental arcs?* was published in *Geochemistry, Geophysics, Geosystems* in 2020 (Yang et al., 2020). In this study, I use numerical models and scaling analysis to assess the mass balance and thermodynamic feasibility of generating arc magma as a result of partial melting of underthrusted lower crust. By applying the model to the Mesozoic Sierra Nevada arc, I show both the magmatic thickening rate and cumulative magma volume are not sufficient to drive arc flare-up events. Instead, additional melts from the mantle and/or other crustal sources are needed to achieve the observed magmatic output during flare-ups. Therefore, partial melting of underthrust lower crust plays a subsidiary role in driving a magmatic flare-up event. However, the arc root developed by partial melting of the underthrusted crust reduces the time needed to obtain the critical thickness for root foundering, thus influencing the tempo of arc magmatism.

The third chapter, *Crustal tilting and differential exhumation of Gangdese Batholith in southern Tibet revealed by bedrock pressures*, was published in *Earth and Planetary Science Letters* in 2020 (Cao and Yang et al., 2020). In this study, we applied Al-in-hornblende barometry across the eastern Gangdese Batholith to obtain pluton

emplacement pressures. The results reveal a regional paleo-depth pattern with plutons emplaced at 1-2 kbar in the west near Lhasa that deepens to 6-12 kbars in the east, near Nyingchi. Therefore, the Lhasa-Nyingchi region (the eastern Gangdese orogen) likely represents a tilted crustal section. We coupled this pressure data with U-Pb zircon ages to further constrain the exhumation history of the Gangdese Batholith since 100 Ma. The results showed that the upper crust experienced limited exhumation, while the middle-lower crust underwent a complex exhumation and burial history, reflecting major tectonic events including the development of the continental arc and India-Asia continent-continent collision. We conclude that the Gangdese Batholith was probably tilted due to differential exhumation along the E-W direction since ~10 Ma, associated with the formation of the eastern Himalayan syntax. Our findings show the upper and middle-lower crust can behave differently, and the exhumation history reflects integrated tectonic, magmatic, and surface processes. I was the second author of this paper and my contributions included: (1) four weeks of fieldwork in Tibet in July 2018 to collect samples; (2) two trips to Rice University to conduct Electron Probe MicroAnalysis (EPMA) for Al-in-hornblende barometry for ~20 samples (one visit with dissertation advisor and one independent visit); (3) wrote MATLAB scripts for a kinematic model of rock exhumation during crustal thickening and surface erosion; (4) data compilation, post-processing, and visualization using QGIS and MATLAB; (5) and assisted in drafting and editing of the manuscript.

The fourth chapter, *Magmatic fabrics of the Gangdese Batholith as an indicator of upper plate deformation and implications for plate convergence between India and Asia since Late Cretaceous*, is a manuscript based on the field data collected during the

2018 trip to Tibet. I intended to revisit Tibet to finish field data collection, but the plan was disrupted by travel restrictions to China due to the COVID-19 pandemic. In this paper, I report magmatic fabric measurements from the eastern Gangdese Batholith and attempt to decipher the crustal response to changes in India-Asia convergence style from subduction to collision. I explore how magmatic fabric orientations vary with pluton emplacement U/Pb zircon ages to constrain upper plate deformation during plate convergence (subduction and collision). Results show magmatic fabric orientations are variable through time and represent: (1) the pre-collision subduction phase of orogen-perpendicular contraction and crustal thickening; (2) transitional crustal thinning and a change in crustal contraction stress from ~N-S to ~E-W; and (3) post-Eocene crustal thickening without a clear, dominant principal stress direction. Tectonic foliation in (meta-)volcanic-sedimentary country rocks in the region show consistent orogen-parallel orientations indicative of finite strain dominated by orogen-perpendicular shortening. I interpret pre-collision Late Cretaceous magmatic fabrics to record approximate head-on subduction of the Neo-Tethyan oceanic plate beneath the Asian continent. The post-collision fabrics reflect the enigmatic nature of the India-Asia collision, as well as the complexity of the post-collisional processes.

The fifth chapter, *Numerical and scaling models of erosion-driven isostatic flow and diapirism in continental crust: Implications for the evolution of the Eastern Himalayan Syntaxis*, will soon be submitted to *Geochemistry, Geophysics, Geosystems*. This work builds on the outstanding questions of Chapter 3 and investigates the likelihood of surface erosion-driven exhumation of the eastern Himalayan syntaxis (EHS). In this study, I used numerical simulations to quantify the effects of erosion-

driven exhumation on the lithosphere using a 2-D thermo-mechanical finite element code implemented with visco-elasto-plastic rheology and particle-in-cell approach. Results show that constant, focused surface erosion can exhume lower crust from >40 km depth on the timescale of ~10 Myr, produce high topography, and generate partial melt. Erosion-driven advection elevates the local geothermal gradient and drastically reduces crustal viscosity. Rock exhumation is sustained by isostatic flow and amplified by the occurrence of crustal diapirism in a warm, felsic crust. The combined effect of exhumation mechanisms (isostatic flow and diapir) triggers a rapid acceleration in rock uplift rates that could further enhance surface erosion and establish positive feedback. Our erosion-driven exhumation model demonstrates the active role of surface erosion in driving tectonic evolution of the EHS.

The final chapter of the dissertation summarizes the key findings of this dissertation and expands on their implications for the evolution of the Sierra Nevada and Gangdese Batholith. A conceptual model is presented to illustrate mass and heat transfer processes in magmatic orogens along the vertical dimension, starting with magma genesis at the upper mantle, transitioning into magma ascent and interactions with a tectonically deforming crust, and ending with the coupling between surface and solid Earth processes.

REFERENCES

Agard, P., Omrani, J., Jolivet, L., Whitechurch, H., Vrielynck, B., Spakman, W., Monié, P., Meyer, B. and Wortel, R., 2011. Zagros orogeny: a subduction-dominated process. Geological Magazine, 148(5-6), pp.692-725.

Avouac, J.P. and Burov, E.B., 1996. Erosion as a driving mechanism of intracontinental mountain growth. Journal of Geophysical Research: Solid Earth, 101(B8), pp.17747-17769.

Bateman, P.C., 1992. Plutonism in the central part of the Sierra Nevada batholith, California (No. 1483). US Government Printing Office.

Beaumont, C., Jamieson, R.A., Nguyen, M.H. and Lee, B., 2001. Himalayan tectonics explained by extrusion of a low-viscosity crustal channel coupled to focused surface denudation. Nature, 414(6865), pp.738-742.

Braun, J., Simon-Labric, T., Murray, K.E. and Reiners, P.W., 2014. Topographic relief driven by variations in surface rock density. Nature Geoscience, 7(7), pp.534-540.

Brown, M., 1994. The generation, segregation, ascent and emplacement of granite magma: the migmatite-to-crustally-derived granite connection in thickened orogens. Earth-Science Reviews, 36(1-2), pp.83-130.

Cao, W., Yang, J., Zuza, A.V., Ji, W.Q., Ma, X.X., Chu, X. and Burgess, Q.P., 2020. Crustal tilting and differential exhumation of Gangdese Batholith in southern Tibet revealed by bedrock pressures. Earth and Planetary Science Letters, 543, p.116347.

Chapman, J.B. and Kapp, P., 2017. Tibetan magmatism database. Geochemistry, Geophysics, Geosystems, 18(11), pp.4229-4234.

Clift, P.D., Schouten, H. and Draut, A.E., 2003. A general model of arc-continent collision and subduction polarity reversal from Taiwan and the Irish Caledonides. Geological Society, London, Special Publications, 219(1), pp.81-98.

Collins, W.J., 2002. Nature of extensional accretionary orogens. Tectonics, 21(4), pp.6-1.

Crisp, J.A., 1984. Rates of magma emplacement and volcanic output. Journal of Volcanology and Geothermal Research, 20(3-4), pp.177-211.

Davis, D., Suppe, J. and Dahlen, F.A., 1983. Mechanics of fold-and-thrust belts and accretionary wedges. Journal of Geophysical Research: Solid Earth, 88(B2), pp.1153-1172.

Davies, J.H. and Stevenson, D.J., 1992. Physical model of source region of subduction zone volcanics. Journal of Geophysical Research: Solid Earth, 97(B2), pp.2037-2070.

DeCelles, P.G., Ducea, M.N., Kapp, P. and Zandt, G., 2009. Cyclicity in Cordilleran orogenic systems. Nature Geoscience, 2(4), pp.251-257.

Dewey, J.F. and Bird, J.M., 1970. Mountain belts and the new global tectonics. Journal of geophysical Research, 75(14), pp.2625-2647.

Dickinson, W.R., Snyder, W.S. and Matthews, V., 1978. Plate tectonics of the Laramide orogeny (Vol. 3, pp. 355-366). Matthews.

Ducea, M., 2001. The California arc: Thick granitic batholiths, eclogitic residues, lithospheric-scale thrusting, and magmatic flare-ups. GSA today, 11(11), pp.4-10.

Jamieson, R.A. and Beaumont, C., 2013. On the origin of orogens. Bulletin, 125(11-12), pp.1671-1702.

Ji, W.Q., Wu, F.Y., Chung, S.L., Li, J.X. and Liu, C.Z., 2009. Zircon U–Pb geochronology and Hf isotopic constraints on petrogenesis of the Gangdese batholith, southern Tibet. Chemical Geology, 262(3-4), pp.229-245.

Ji, W.Q., Wu, F.Y., Chung, S.L. and Liu, C.Z., 2014. The Gangdese magmatic constraints on a latest Cretaceous lithospheric delamination of the Lhasa terrane, southern Tibet. Lithos, 210, pp.168-180.

Kapp, P., DeCelles, P.G., Gehrels, G.E., Heizler, M. and Ding, L., 2007. Geological records of the Lhasa-Qiangtang and Indo-Asian collisions in the Nima area of central Tibet. Geological Society of America Bulletin, 119(7-8), pp.917-933.

Kirsch, M., Paterson, S.R., Wobbe, F., Ardila, A.M.M., Clausen, B.L. and Alasino, P.H., 2016. Temporal histories of Cordilleran continental arcs: Testing models for magmatic episodicity. American Mineralogist, 101(10), pp.2133-2154.

Lee, Y.H., Chen, C.C., Liu, T.K., Ho, H.C., Lu, H.Y. and Lo, W., 2006. Mountain building mechanisms in the Southern Central Range of the Taiwan Orogenic Belt—From accretionary wedge deformation to arc–continental collision. Earth and Planetary Science Letters, 252(3-4), pp.413-422.

McKenzie, N.R., Horton, B.K., Loomis, S.E., Stockli, D.F., Planavsky, N.J. and Lee, C.T.A., 2016. Continental arc volcanism as the principal driver of icehouse-greenhouse variability. Science, 352(6284), pp.444-447.

Molnar, P. and England, P., 1990. Late Cenozoic uplift of mountain ranges and global climate change: chicken or egg?. nature, 346(6279), pp.29-34.

Mouthereau, F., Lacombe, O. and Vergés, J., 2012. Building the Zagros collisional orogen: timing, strain distribution and the dynamics of Arabia/Eurasia plate convergence. Tectonophysics, 532, pp.27-60.

Olive, J.A., Behn, M.D. and Malatesta, L.C., 2014. Modes of extensional faulting controlled by surface processes. Geophysical Research Letters, 41(19), pp.6725-6733.

Paterson, S.R. and Ducea, M.N., 2015. Arc magmatic tempos: Gathering the evidence. Elements, 11(2), pp.91-98.

Petford, N., Cruden, A.R., McCaffrey, K.J.W. and Vigneresse, J.L., 2000. Granite magma formation, transport and emplacement in the Earth's crust. Nature, 408(6813), pp.669-673.

Pfiffner, A., 1992. Alpine orogeny. A Continent Revealed: The European Geotraverse, pp.180-190.

Richards, J.P., 2013. Giant ore deposits formed by optimal alignments and combinations of geological processes. Nature geoscience, 6(11), pp.911-916.

Roeder, D., Roberts, D.G. and Bally, A.W., 2013. Convergent margins and orogenic belts. Regional Geology and Tectonics: Principles of Geologic Analysis A, 1, pp.114-177.

Rudnick, R.L., 1995. Making continental crust. Nature, 378(6557), pp.571-578.

Simoes, M., Avouac, J.P., Beyssac, O., Goffé, B., Farley, K.A. and Chen, Y.G., 2007. Mountain building in Taiwan: A thermokinematic model. Journal of Geophysical Research: Solid Earth, 112(B11).

Stern, R.J., 2002. Subduction zones. Reviews of geophysics, 40(4), pp.3-1.

Stern, C.R. and Kilian, R., 1996. Role of the subducted slab, mantle wedge and continental crust in the generation of adakites from the Andean Austral Volcanic Zone. Contributions to mineralogy and petrology, 123(3), pp.263-281.

Willett, S.D., 1999. Orogeny and orography: The effects of erosion on the structure of mountain belts. Journal of Geophysical Research: Solid Earth, 104(B12), pp.28957-28981.

Yang, J., Cao, W., Gordon, S.M. and Chu, X., 2020. Does Underthrusting Crust Feed Magmatic Flare-Ups in Continental Arcs?. Geochemistry, Geophysics, Geosystems, 21(11), p.e2020GC009152.

Yin, A. and Harrison, T.M., 2000. Geologic evolution of the Himalayan-Tibetan orogen. Annual review of earth and planetary sciences, 28(1), pp.211-280.

Zeitler, P.K., Meltzer, A.S., Koons, P.O., Craw, D., Hallet, B., Chamberlain, C.P., Kidd, W.S., Park, S.K., Seeber, L., Bishop, M. and Shroder, J., 2001. Erosion, Himalayan geodynamics, and the geomorphology of metamorphism. Gsa Today, 11(1), pp.4-9.

Zhu, D.-C., Wang, Q., Zhao, Z.-D., Chung, S.-L., Cawood, P.A., Niu, Y., Liu, S.A., Wu, F.-Y. and Mo, X.-X., 2015. Magmatic record of India-Asia collision. Scientific Reports, 5, p.14289

CHAPTER 2: Does underthrusting crust feed magmatic flare-ups in continental arcs?

Jiaming Yang[1*], Wenrong Cao[1], Stacia M. Gordon[1], and Xu Chu[2]

[1] Department of Geological Sciences and Engineering, University of Nevada, Reno, MS-172, 1664 N. Virginia St., Reno, NV 89557, United States of America.

[2] Department of Earth Sciences, University of Toronto, 22 Ursula Franklin Street, Toronto, Ontario, M5S3B1, Canada.

This chapter has already been published and is included as part of this dissertation with permission from ***Geochemistry, Geophysics, Geosystems*, 21 e2020GC009152, doi.org/10.1029/2020GC009152,**

ABSTRACT

Episodic magmatic flare-ups are documented in many continental arcs worldwide. Yet, the causes of such episodicity and the sources feeding the flare-ups are not well-understood. In this study, we use a 1D numerical model and scaling analysis to assess the mass balance and thermodynamic feasibility of generating arc magma as a result of partial melting of underthrusted retro-arc lower crust. Results show the magma volumetric flux or magmatic thickening rate, is directly correlated with the crustal underthrusting rate and the relative timescales of heat transfer and underthrusting. For a continental arc with dimensions similar to the Sierra Nevada arc in California, we show with a constant underthrusting rate of 5 km/Myr, the magmatic thickening rate is 0.1-0.3 km/Myr. This is slightly below the baseline of arc magma thickening rate (~0.3 km/Myr) from the mantle wedge and accounts for 10-30% of the magmatic thickening rate during a flare-up. The cumulative volume of magma generated from the partial melting of a 20-km-thick underthrusted lower crust is on the order of 10^5 km^3, about 10-40% of the estimated magma volume generated during a flare-up. Therefore, we argue partial melting of underthrusted lower crust plays a subsidiary role in driving a magmatic flare-up event. Additional melts from the mantle and/or other crustal sources are needed to achieve the observed magmatic output during flare-ups. The arc root developed by partial melting of the underthrusted crust reduces the time needed to obtain the critical thickness for root foundering, thus influencing the tempo of arc magmatism.

INTRODUCTION

Continental arc magmatism is an important process for the formation of continental crust and most ore deposits (e.g., Rudnick, 1995; Stern 2002; Condie, 2013). Continental arcs also play a critical role in Earth's long-term carbon cycle through volcanic and metamorphic degassing and chemical weathering (e.g., Lee et al., 2012; McKenzie, 2017; Cao et al., 2017; Chu et al., 2019). There is growing field and geochemical evidence suggesting that magmatism is episodic and non-steady state in continental arcs worldwide (**Figure 2.1**; e.g., Armstrong & Clark, 1988; Ducea 2001; Haschke et al., 2006; Ducea & Barton, 2007; Gehrels et al., 2009; DeCelles et al., 2009, 2014; Paterson & Ducea, 2015; Kirsch et al., 2016; Zhu et al., 2016; Zhang et al., 2019; Ardill et al., 2018).

Compilations of U/Pb zircon geochronology from igneous rocks and arc-derived sediments show age peaks and troughs defining magmatic 'flare-ups' and 'lulls', respectively, on the timescales of tens of millions of years (e.g., Paterson and Ducea, 2015). Typically, these flare-ups or high magma flux events last ~30 Myr and are separated by magmatic lulls spanning 20–50 Myr (e.g., Kirsch et al., 2016). Magma generation rates during the lulls in a continental arc are comparable to the rate of mantle-derived primitive magma generation in island arcs (DeCelles et al., 2009), representing a baseline for the magma contribution from the mantle wedge. The Armstrong Unit (AU) is used to quantify the baseline magma generation rate, with 1 AU = 30 km^3/Myr per kilometer length of arc (Reymer & Schubert, 1984). During a flare-up, the magma generation rate reaches 3-4 AU in the upper-middle crust (DeCelles et al., 2009). The Armstrong unit can be converted to a volumetric flux (km^3/km^2/Myr or km/Myr) if the

arc width is known. Given a characteristic arc width of 100 km, the baseline 1 AU is ~0.3 $km^3/km^2/Myr$. For flare-ups in continental magmatic arcs, an estimated volumetric flux of ~1 $km^3/km^2/Myr$ (~3-4 AU equivalent) is proposed for the main arc and > 0.6 $km^3/km^2/Myr$ (>2 AU equivalent) for a broader region from the forearc to the retro-arc (Ratschbacher et al., 2019). This volumetric flux is also referred to as the magmatic thickening rate (km/Myr), representing the magmatic contribution to the vertical growth of arc crust (Jicha & Jagoutz, 2015; Lee et al., 2015a; Cao & Paterson, 2016; Jiang & Lee, 2017).

Previous models explaining non-steady-state magmatism focus on: (1) the convergence rate between the subducting and overriding plates regulating magma production (e.g., Pilger 1984); (2) slab dynamics, including the opening of slab windows and changes in the subduction angle (Zhang et al., 2010); (3) delamination of an eclogitic arc root (e.g., Kay & Kay, 1993; Lee and Anderson, 2015); (4) temporal filtering of mantle-lithosphere interactions where the crust modulates mantle input (de Silva et al., 2015); (5) relamination of material off of the subducting plate and emplacement at the base of the arc crust (e.g., Hacker et al., 2011; Chapman et al., 2013; Ducea & Chapman, 2018); (6) incorporation of forearc sediments into the active arc (Pearson et al., 2017; Sauer et al., 2017; Sauer et al., 2018); (7) arc migration into the fertile retro-arc region (Chapman & Ducea, 2019); and (8) feedback among linked tectonic processes (e.g., Ducea, 2001; Ducea & Barton 2007; DeCelles et al., 2009).

For North and South America Cordilleran arcs, the temporal correlation between magmatism and plate convergence rate is weak (e.g., Ducea, 2001; Kirsch et al., 2016). Whole rock Nd isotope data show a correlation with magmatism. There is a decrease in

ε_{Nd} towards more evolved compositions during flare-ups in comparison to increases in ε_{Nd} during magmatic lulls (e.g., Ducea, 2001). The negative ε_{Nd} excursion is interpreted to signify ~50% contribution from crustal materials to a magmatic flare-up (Ducea, 2001; Ducea & Barton, 2007). Many studies thus hypothesize that magmatism is driven by the repeated incorporation of underthrusted retro-arc crustal materials beneath the arc, boosting melt generation (e.g., Ducea, 2001; DeCelles et al., 2009; DeCelles & Graham, 2015).

However, the thermodynamic feasibility of arc magma generation through partial melting of continental lower crust has not been tested. Quantitative evaluation of such a process requires the inclusion of latent heat associated with melting, the temperature dependency of thermal diffusivity and heat capacity, as well as kinematic conditions such as the underthrusting rate of the retro-arc crust. In this study, we use numerical modeling and scaling analysis to address the following questions: (1) What controls the total volume and rate of magma generation during partial melting of underthrusted crust? (2) Is partial melting of underthrusted crust capable of generating enough arc magma in a relatively short period (~30 Myr) to form a magmatic flare-up? (3) How do the arc root and melts from the mantle interact with the underthrusting crust and contribute to the magmatic flare-up?

METHODS

Initial, boundary conditions and governing equation

To investigate arc magma generation during underthrusting, we simulate the 1D thermal evolution of the underthrusting crust in a numerical model. The vertical temperature profile of the crustal column is coupled with lateral motion, approximating a 2D cross section of the underthrusting crust. To focus on underthrusting, the model does not include arc root foundering or melting of the mantle. We recognize the importance of these processes and address them in the discussion.

The model consists of a 20-km-thick retro-arc lower crustal slab that is underthrusting into the sub-arc mantle (**Figure 2.2**). We use a half-space heating model in which the initial temperature of the underthrusting crustal slab is 600°C everywhere, except for the basal boundary where a constant mantle temperature of 1100°C is enforced. The mantle temperature used in our model is based on the thermal profile of the modern Chilean Andes where the average thermal gradient of the shallow sub-arc mantle below the Moho is ~25°C/km, and the Moho temperature is ~600°C (Syracuse et al., 2010). Implementing this thermal profile into our model, we get 1100°C for the temperature at the base of the underthrusted crust which is 20 km below the 600°C Moho (600°C + 25°C/km × 20 km = 1100°C). For the purpose of investigating first-order thermal effects, we take a simple approach that does not include the geothermal gradient in the underthrusting crust nor cooling of the mantle due to the thickening of the arc crust (Chin et al., 2015). The simulated results thus represent the upper bound of melt generation and the maximum productivity of arc magma. The governing heat equation is:

$$\frac{\partial T}{\partial t} = \frac{\partial}{\partial z}\left[\kappa(T)\frac{\partial T}{\partial z}\right] - \frac{L}{C_p(T)}\frac{\partial F}{\partial T}\frac{\partial T}{\partial t} \quad (1)$$

$\kappa(T)$ is the temperature-dependent diffusivity, and $\frac{L}{C_p}\frac{\partial F}{\partial T}\frac{\partial T}{\partial t}$ is for latent heat (e.g., Bergantz, 1989; Lee et al., 2015b), where *L* is the total latent heat of fusion absorbed between the solidus and the liquidus of the lower crust, $C_p(T)$ is temperature-dependent heat capacity, and *F* is melt fraction. The temperature-melt fraction relationship ($\partial F/\partial T$) is constrained using a MELTS-modeled phase change for a lower crust composition (see Section 2.3). Parameters used in the model are listed in Table 1. Equation (1) can be rearranged to:

$$\frac{\partial T}{\partial t} = \frac{\partial}{\partial z}\left[\kappa'(T)\frac{\partial T}{\partial z}\right] \quad (2)$$

where $\kappa'(T)$ is the equivalent diffusivity taking latent heat into account (e.g., Lee et al., 2015b):

$$\kappa'(T) = \frac{\kappa(T)}{1 + \frac{L}{C_p(T)}\frac{\partial F}{\partial T}} \quad (3)$$

It is noted that $\kappa'(T) < \kappa(T)$ since the denominator in Eq. (3) is larger than 1. Implicit Finite Difference Method and Picard iteration are used to solve the non-linear heat equation (Eq. 2). The MATLAB script used for the numerical model is included in the supporting information.

Effects of temperature-dependent diffusivity and latent heat

Studies have shown that rock thermal diffusivity decreases rapidly with increasing temperature (Vosteen & Schellschmidt, 2003; Mottaghy et al., 2008). Whittington et al. (2009) shows that the thermal diffusivity of crustal rocks near and above Moho temperatures is about 0.5×10^{-6} $m^2 s^{-1}$, which is approximately half its value at temperatures on Earth's surface. The temperature dependence of diffusivity effectively slows conductive heat transfer within the underthrusting crust, thus reducing the rate of partial melting.

The effects of the temperature dependence of thermal diffusivity and latent heat are illustrated in **Figure 2.3**. In the half-space heating model, a column of initially isothermal 600°C crust is exposed at one end to mantle temperatures of 1100°C. By tracking the propagation of the 900°C isotherm, heating of the rock column is inhibited when the temperature dependency of thermal diffusivity or the effect of latent heat is applied. The combined effects of temperature dependent thermal diffusivity and latent heat drastically slows down the rate of thermal conduction by a factor of ~3 for the given scenario.

Partial melting of lower crust and formation of arc root

To obtain the temperature-melt fraction relationship needed for the calculation of latent heat, we use the MELTS thermodynamic algorithm (Ghiorso & Sack, 1995) to constrain the temperature-melt fraction relationship ($\partial F/\partial T$) during partial melting. For our generalized model of continental arc systems, we adopt the temperature-melt fraction relationship using the global average lower crust composition (Rudnick & Gao, 2003).

The MELTS calculations were performed at 1.5 GPa (lithostatic pressure at ~55 km depth using crustal density of 2800 kg/m^3) and a temperature range of 600°C to 1300°C to mimic the conditions at which the underthrusting crust undergoes partial melting. Detailed MELTS setup and parameters are presented in the supporting information.

The global average lower crust used in the model is of mafic composition with a silica content of 52 wt. %. To investigate the effects of water during partial melting of the underthrusting lower crust, our experiments were performed assuming a range (1, 1.5 and 2 wt. %) of H_2O. The bulk source rock composition is listed in the MELTS setup file in the supporting information. Residual phase diagram and melt silica content for 1, 1.5 and 2 wt. % of H_2O is presented in **Figure 2.4**.

Ducea (2002) argues that the Sierra Nevada granitoids (arc magma) and the pyroxenite xenoliths (arc root) are complementary melts and residues, respectively, resulting from partial melting of mafic, amphibolitic lower continental crust, with 0.1-0.5 melt fractions. Segregation of partial melt in the lower crust begins at the melt connectivity transition (MCT), where isolated melt pockets coalesce to form an interconnected melt network along the grain boundaries, enabling melt permeability at the source region and allowing melt to migration (e.g., Sawyer 1994, Rosenberg & Handy, 2005). We assume partial melting of the lower crust continues until melt of intermediate composition is extracted, and dense restitic minerals (mostly garnet and pyroxenite) are left over. We define a critical melt fraction (F_{crit}) as the degree of partial melting of underthrusted lower crust required to generate melt of intermediate composition.

The value of critical melt fraction is set to F_{crit} = 0.25 because of the following reasons. First, at F_{crit} = 0.25, for all three choices of different water contents, the restite consists of mostly garnet and pyroxene, an eclogitic assemblage (**Figure 2.4**). This is similar to the characteristic mineralogy of the Sierra Nevada arc root (Ducea & Saleeby, 1996; Ducea et al., 2002). The melt produced at F_{crit} = 0.25 is also granitic with a silica content of 65-70 wt. %. Second, after testing different F_{crit} values ranging from 0.1 to 0.5, we found F_{crit} of 0.25 provides the maximum amount of melt produced in 50 Myr timescales because a higher F_{crit} corresponds to a higher temperature (T_{crit}, defined in the following paragraph) that makes melting more difficult (see Supporting Information, **Figure 2.S1**). Third, the 0.25 melt fraction is also similar to that estimated in Betic Cordilleran orogen in southern Spain, based on Mn growth zoning in peritectic garnets (0.3 melt fraction; Yu & Lee, 2016). In our 1D model, F_{crit} also equals the thickness ratio of total partial melt generated to the underthrusted lower crust. An eclogitic arc root forms after extraction of intermediate melt (Ducea, 2002). With F_{crit} = 0.25, the thickness of the arc root resulting from partial melting is three times the thickness of the extracted melt. This arc root could exist throughout an arc's evolution, but it may also founder into the mantle due to gravitational instability (e.g., Arndt & Goldstein, 1989; Lee, 2014). The eclogitic root undergoes no further melting because of the high solidus (>1300°C) for eclogitic compositions (Mallik & Dasgupta, 2012).

Finally, we define a critical temperature (T_{crit}) corresponding to F_{crit} = 0.25 (**Figure 2.5**). Increased water content lowers the solidus as well as T_{crit}, making partial melting more rapid. When the lower crust contains 1.5 and 2 wt. % H_2O, the T_{crit} is lowered by 72 and 108 °C, respectively, compared to the 1 wt. % H_2O case (**Figure 2.5**).

Models of the underthrusting rate

Underthrusting of the retro-arc lower crust is initiated at the start of the simulation and terminated when the lower crust intercepts the cold mantle lithospheric wedge beneath the forearc region (**Figure 2.2**). Based on geological estimates of total retro-arc crustal shortening (e.g., Sevier thrust belts and hinterland shortening) associated with the Cretaceous Sierra Nevada arc, the average upper crust shortening rate is ~5 km/Myr and is more or less constant from ~120-80 Ma (DeCelles, 2004; Yonkee & Weil, 2015). If the lower crust experienced the same amount of shortening, the average underthrusting rate of the lower crust would also be ~5 km/Myr.

Magmatic thickening rate and volume of arc magma

Melt volume is calculated via the product of underthrusting distance $x(t)$, the thickness of the 1D crustal column undergoing partial melting and melt extraction $z(t)$, the along strike arc length (l), and the critical melt fraction (F_{crit}) (Eq. 4). $z(t)$ is determined based on the result of the 1D half-space heating model where the temperature exceeds a critical temperature (T_{crit}) (**Figure 2.5**). We then apply $z(t)$ laterally across the entire underthrusted crust to obtain the estimated magma volume (Eq. 4):

$$V(t) = A \cdot l \cdot F_{crit} = x(t) \cdot z(t) \cdot l \cdot F_{crit} \quad (4)$$

Where A is the melt area in the 2D profile. Since $v(t)$ is underthrusting rate (Eq. 5), we have

$$x(t) = \int_0^t v(t)dt \quad (5)$$

We assume the arc magma generated through partial melting is uniformly distributed along the width of the arc. To calculate the magmatic thickening rate *M(t)*, we take the time derivative of Eq. 4 and divide it by the 2D surface area of the arc ($w \cdot l$) (Eq. 6):

$$M(t) = \frac{dV}{dt} \cdot \frac{1}{wl} \tag{6}$$

Since we do not solve thermal diffusion in 2D, the melt area is slightly overestimated. The actual area of melt can be constrained between the upper limit of $x \cdot z$ (the value we used in the model) and the lower limit of $\frac{2}{3}\, x \cdot z$. The lower limit is calculated via integrating the area of melt assuming only 1D vertical thermal diffusion (see Supporting Information, **Figure 2.S2**). In this sense, our simplified method overestimates the melt volume by no more than ~30%. This approach works together with other assumptions in our model (e.g. constant mantle temperature) yielding the upper limit of magma generation during the underthrusting process.

Model limitations

Our numerical model provides first-order estimates on the total magma volume and magmatic thickening rate associated with the underthrusting process. While we focused on the process of retro-arc underthrusting, the results from our generic model is applicable to fore-arc underthrusting as well. However, this model is simplified, and there are several limitations. (1) Our approach does not account for the refrigerating effect on the mantle (Chin et al., 2015) due to the magmatic and tectonic thickening of arc crust (Karlstrom et al., 2014: Lee et al., 2015a; Cao et al., 2016b) and underthrusting of a

relatively colder crust. The refrigerating effect could gradually lower the temperature of the mantle, hamper heating of the underthrusting crust. (2) We assume all melts are added to the arc crust as soon as they are generated. There is no lag time associated with melt transport, and the physical processes of magma ascent and emplacement (e.g., Cao et al., 2016a; Rummel et al., 2020) are not considered. (3) Magma advection as dikes or diapirs are not included. Advection could promote heat transfer by increasing the equivalent thermal diffusivity (e.g., England et al., 2007; Jaupart & Mareschal, 2010); therefore, it may boost the rate of heat transfer within the underthrusted crust. In section 4.2 of the discussion, we parameterized thermal advection in a simple, semi-quantitative manner. More advanced modeling on the actual physical processes of magma advection is needed in future studies. (4) We do not include any spatial or temporal focusing processes which could boost the local magmatic thickening rate. For example, the center of the arc front may receive a higher melt flux via arc axial focusing relative to the peripheral arc region (Ardill et al., 2018). (5) Our model does not include the dynamics of arc root foundering, mantle flow upwellings, and subsequent partial melting of the lower crust. Some of the above aspects may have competing effects on melt generation and would require more comprehensive 2D/3D modeling.

RESULTS

We present two results of numerical simulations with different water contents. In **Figure 2.6** the water content of the underthrusted crust is set to 1 wt. %, while **Figure 2.7** corresponds to a water content of 2 wt. % to demonstrate the effect of water on the melt generation rate. For each simulation, we tested three models of underthrusting rate. The

reference model (Model A) has a constant rate of 5 km/Myr representing the most likely case for a typical continental arc such as the Cretaceous Sierra Nevada arc (e.g., Yonkee & Weil, 2015). Model B has a linearly increasing and decreasing rate which steadily increases to 10 km/Myr during the first half of underthrusting, then decreases to 0 during the second half. Model C has a linear decreasing rate where v = 10 km/Myr at the start and decreases to 0 at the end. The purpose of the time-dependent rates in Model B and C is to investigate how underthrusting rate influences the magmatic thickening rate. These models (Model B and C) do not reflect the geological constraints on the underthrusting rate. For each case, the average underthrusting rate is 5 km/Myr. To facilitate discussion, we defined two characteristic times. The characteristic time of underthrusting ($\tau_{underthrust}$) is the timescale of active underthrusting (the ratio between the given arc width, 125km, and average underthrusting rate). $\tau_{underthrust}$ is 25 Myr in all models. We also defined the characteristic time of heat transfer ($\tau_{thermal}$) as the time needed to complete the partial melting of the underthrusted crust along its vertical dimension.

Case 1 with 1 wt. % water

The results of case 1 containing 1 wt. % water can be categorized into 3 stages. Below we summarize the results for each stage.

Stage I: Active underthrusting with vertical growth of the partial melt layer *(*$t < \tau_{underthrust}$). The lower crust begins underthrusting from the retro-arc direction, and partial melting occurs. During this stage melt generation is sustained by both lateral underthrusting of the lower crust and vertical growth of the partial melt layer. Stage I

ends when the entire sub-arc mantle is occupied by the crustal slab, and it intercepts the mantle wedge beneath the forearc (**Figure 2.2**).

Models of different underthrusting rates (**Figure 2.6B**) result in slightly different underthrusting distances during this stage, though the final underthrusting distance of 125km is the same for all cases (**Figure 2.6C**). The cumulative melt thickness increases as the isotherm T_{crit} vertically propagates upward through the crustal column (**Figure 2.6D**, pink curve). The thickness scales with $\sim t^{1/2}$ during this stage because the melt thickness is controlled by thermal diffusion and is independent of the underthrusting rate. Cumulative melt thickness and melt volume also increases with time (**Figure 2.6E**). At the end of Stage I, melt volume reaches 2×10^5 km^3.

The magmatic thickening rate is sensitive to the underthrusting rate (**Figure 2.6F**). For the reference Model A with the constant 5 km/Myr underthrusting rate, the magmatic thickening rate slowly climbs to a maximum of ~0.15 km/Myr when underthrusting ends. For Model B with linearly increasing and decreasing rates, the magmatic thickening rate mimics the temporal pattern of the underthrusting rate. The maximum thickening rate of ~0.2 km/Myr is achieved in the middle of the stage when the underthrusting rate reaches a peak of 10 km/Myr. For Model C with a linear decreasing rate, the maximum thickening rate of ~0.1 km/Myr occurs within the first half of Stage I, before 10 Myr.

Stage II: Vertical growth of the partial melt layer after underthrusting terminates at 25 Myr ($\tau_{underthrust} < t < \tau_{thermal}$). Partial melting is sustained by the upward propagation of the isotherm T_{crit}. Even without additional underthrusting lower crust, the

cumulative melt area and volume still increase during stage II but at a slower rate than Stage I (**Figure 2.6E**). This behavior is also reflected in the magmatic thickening rate, which decreases to ~0.05 km/Myr (**Figure 2.6F**). Stage II ends when the entire vertical column of the underthrusted slab has undergone partial melting. In other words, the end of stage II is marked by the T_{crit} isotherm reaching the top of the 20 km-thick underthrusted slab ($t = \tau_{thermal}$). $\tau_{thermal}$ is 117 Myr in the Case 1 simulation and Stage II lasts 92 Myr (117 - 25 = 92 Myr). Once stage II is complete, no additional melt can be produced because the entire slab has undergone partial melting. At the end of Stage II, the maximum melt volume has reached 3.75×10^5 km^3, and the arc root is completely formed.

Stage III: Cessation of partial melting in the underthrusted crust ($t > \tau_{thermal}$). One complete underthrusting-partial melting process in Case 1 takes 117 Myr which equals $\tau_{thermal}$.

Case 2 with 2 wt. % water

Similar to Case 1, we defined the same 3 stages in Case 2, with the increased water content (2 wt. % H_2O). In this case, partial melting along the vertical dimension of the underthrusted crust is completed shortly after lateral underthrusting terminates. Therefore, the duration of Stage II (3 Myr) is much shorter in Case 2 (3 Myr compared to 92 Myr in Case 1).

Stage I: Active underthrusting with vertical growth of the partial melt layer ($t < \tau_{underthrust}$). Compared to Case 1, the magmatic thickening rate is higher in Case 2. The three models achieve different maximum rates at different times: 1) magmatic thickening

rate of ~0.3 km/Myr at the end of Stage I in Model A; 2) ~0.35 km/Myr at 12.5 Myr when the peak underthrusting rate of 10 km/Myr is reached in Model B; and 3) ~0.25 km/Myr around 10 Myr in Model C. Stage I ends when the entire sub-arc mantle is occupied by the crustal slab, and it intercepts the mantle wedge beneath the forearc (**Figure 2.2**).

Stage II: Vertical growth of the partial melt layer after underthrusting terminates at 25 Myr ($\tau_{underthrust} < t < \tau_{thermal}$). During this stage, partial melting is sustained by the upward propagation of the isotherm T_{crit}. Without the underthrusting of the lower crust, we observe a decrease in magmatic thickening rate to ~0.1 km/Myr (**Figure 2.7F**), roughly twice the value shown in Case 1. Since the characteristic time of heat transfer within the underthrusted crust ($\tau_{thermal}$) is 28 Myr, Stage II in this case only lasts for 3 Myr (28 – 25 = 3 Myr). No additional melt can be produced after the end of stage II because the entire underthrusted crust has undergone partial melting. At this point the maximum melt volume of 3.75×10^5 km^3 is reached for an assumed continental arc whose width w = 125 km and length l = 600 km (**Figure 2.7E**) and the formation of the arc root for the entire underthrusted crust is complete.

Stage III: Cessation of partial melting in the underthrusted crust ($t > \tau_{thermal}$). The complete underthrusting–partial melting process in Case 2 takes 28 Myr which equals $\tau_{thermal}$.

DISCUSSION

Scaling Analysis: steady-state model

A simple, idealized steady-state model is presented to illustrate the scaling relationships among the parameters controlling arc magma generation as a result of partial melting (**Figure 2.8**). This scaling model does not include the effects of latent heat nor water in the lower crust, and thermal diffusivity is treated as a constant (κ). At steady-state, the lower crust is underthrusted into the sub-arc mantle at a constant rate v, and arc root is readily removed. Using the characteristic thickness of the conductive thermal boundary ($\sqrt{\kappa t}$,) and a critical fraction (F_{crit}), we obtain a melt thickness of (Eq. 7):

$$z = F_{crit}\sqrt{\kappa t} \tag{7}$$

In this scaling analysis, the characteristic time of underthrusting, $\tau_{underthrust}$, is given by the quotient of arc width *w* and underthrusting rate v (Eq. 8):

$$\tau_{underthrust} = \frac{w}{v} \tag{8}$$

The magmatic thickening rate M of the lower crust during steady-state conditions can be obtained by taking the time derivative of *z* (Eq. 7) and replacing t with $\tau_{underthrust}$ (Eq. 9):

$$M = \frac{dz}{dt} = \frac{1}{2} \cdot F_{crit}\sqrt{\frac{\kappa v}{w}} \tag{9}$$

Finally, the total volume of arc magma generated within the characteristic time of underthrusting can be calculated by the product of the arc width *w*, the along strike arc length *l*, and the melt thickness (*z)* at time $\tau_{underthrust}$ (Eq. 10):

$$V = w \cdot l \cdot z = w \cdot l \cdot F_{crit}\sqrt{\frac{\kappa w}{v}} \quad (10)$$

Figure 2.8 illustrates the magmatic thickening rate and the total magma volume as a function of the underthrusting rate, the thermal diffusivity, and the arc width using F_{crit} = 0.25. At steady-state, the magmatic thickening rate is positively correlated with the underthrusting rate and thermal diffusivity (**Figure 2.8A**) and inversely correlated with arc width (**Figure 2.8B**). In comparison, cumulative melt volume is largely a function of arc width. A larger arc width enables more material to be underthrusted, resulting in greater cumulative melt volume.

The magmatic thickening rate only weakly depends on the arc width within a reasonable range of widths (100 -150 km) (**Figure 2.8B**).

The upper bound estimates of magmatic thickening rate and cumulative melt volume correspond to an unlikely scenario of F_{crit} = 1, in which the underthrusted lower crust is completely melted and all materials are added to the arc crust. Using values representative of the Sierra Nevada arc where l = 600 km, w = 125 km, and v = 5 km/Myr, the magmatic thickening rate is 0.6 km/Myr or ~2 AU equivalent. Also, for the F_{crit} = 1 case, one complete underthrusting event yields a cumulative melt volume of 1.5×10^6 km^3. This melt volume is 67% of the original arc crust (125 km width × 600 km length × 30 km depth). The 0.6 km/Myr thickening rate and magma volume of 1.5×10^6 km^3 are close to the lower end of the estimated values of the Cretaceous flare-up event in the entire Sierra Nevada (M = ~0.6–1 km/Myr and V = ~1-3×10^6 km^3) (e.g., Cao & Paterson, 2016; Ratschbacher et al., 2019). However, only a portion of the crust undergoes partial melting; the rest becomes residue. In the case of F_{crit} = 0.25 (**Figure**

2.8), the magmatic thickening rate and cumulative melt volume will be reduced by a factor of 4, resulting in M = 0.15 km/Myr or 0.5 AU equivalent and $V = 3.7 \times 10^5$ km^3. Volumetrically, it is less than 20% of the original arc crust. This simple scaling analysis shows that the volume of magma generated by partial melting of the crust and the magmatic thickening rate cannot suffice flare-up events. Magma from additional sources is required to reach the estimated magma thickening rate and volume.

Effects of water and heat advection

Higher water content in the underthrusted crust lowers the solidus as well as the T_{crit} of the crust, increasing the rate of partial melting (**Figure 2.5**). For the top row in **Figure 2.9 (A1**, **A2**, and **A3)** where the water content increases from left to right, these is an increase in peak magmatic thickening rate corresponding to higher water content. The higher water content also reduces the $\tau_{thermal}$, enabling faster partial melting along the vertical dimension of the underthrusted crust. However, the magmatic thickening rate in the highest water content case is still much lower than the estimated thickening rate during a flare-up. For the reference model A (blue curves in **A2** and **A3** of **Figure 2.9**), the addition of water only boosts the peak magmatic thickening rate to ~0.3 km/Myr. In terms of magma volume, the total amount of melt produced from partial melting of the underthrusted crust remains unchanged because it is capped by the size of the underthrusted crust and the given critical melt fraction. Since $\tau_{thermal}$ corresponding to the 1 wt. % water case is ~117 Myr, only a portion of the total magma volume is released in timescales of ~30 Myr, typical for an arc flare-up (**Figure 2.6**). Whereas for 1.5 and 2

wt. % water, $\tau_{thermal}$ is much shorter (30 and 28 Myr, respectively, **Figure 2.9**); thus, the maximum magma volume is reached much faster with increased water content.

Advective heat transfer (e.g., diking) from mantle basalts intruding into the lower crust could heat the crust in addition to thermal conduction. The intruding basalts will thus in turn play an important role in increasing the magma production rate. Magma advection via diking are difficult phenomena to implement even in advanced 2D or 3D models because the processes depends on many complex, dynamic processes and parameters such as rock rheology, melt transport, phase transition, and dike formation mechanisms (e.g., Liang & Parmentier, 2010; Cao et al., 2016; Rummel et al., 2020). While others have quantitively assessed the process of advective magma transport and the thermal impact of mantle melt on the lithosphere using sophisticated, two-phase flow dynamics (Keller et al., 2013; Rees Jones et al., 2018). We acknowledge that our simple thermal-kinematic model is incapable of simulating the actual processes of magma advection. Instead, we adopted an 'amplification factor of thermal diffusivity' to quantify the thermal effect of advection in addition to conduction.

In addition to the original temperature dependent thermal diffusivity with latent heat included, we tested 5x and 10x amplification factors of thermal diffusivity in our models (**Figure 2.9**). The 5x and 10x factors are based on the following argument. Karakas & Dufek (2015) used stochastic modeling of repetitive basaltic magma emplacement from the mantle into the lower crust as dikes and sills. Their simulation results show a temperature perturbation with a vertical length scale of ~20 km emerging

within 1-2 Myr. Using the characteristic timescale of thermal diffusion, we can infer an equivalent thermal diffusivity (κ_{eq}) using Eq. (11).

$$\kappa_{eq} = \frac{x^2}{t} \tag{11}$$

where *t* is time, and *x* is length of the crustal temperature perturbation in this case. The resulting $\kappa_{eq} = 10^{-5}$ m^2/s if *t* = 1 Myr and *x* = 20 km. If *t* = 2 Myr, $\kappa_{eq} = 5 \times 10^{-6}$ m^2/s. These values are 10 and 5 times the reference thermal diffusivity ($\kappa = 10^{-6}$ m^2/s), respectively.

The effect of such parameterized thermal advection is illustrated in **Figure 2.9**. As expected, the magmatic thickening rate is increased due to a faster vertical thermal propagation rate, reducing the time needed to heat the underthrusted crust for partial melting. Since $\tau_{thermal}$ is inversely correlated with thermal diffusivity, as the amplification factor of thermal diffusivity increases, $\tau_{thermal}$ becomes shorter. However, even with water added to the system (2 wt. %) and a 10x amplification factor (**C3** in **Figure 2.9**), the magmatic thickening rate is still below 0.3 km/Myr for the constant underthrusting case (blue curve, the mostly likely underthrusting velocity profile). This value is too low to qualify as an arc flare-up. In some cases (e.g., **B3**, **C2** in **Figure 2.9**), brief pulses of magmatic thickening rates exceeding 0.4 km/Myr appear in the early stage (~5 Myr) of the simulation. These pulses are due to the initial rapid melt generation of the underthrusted crust as it enters the sub-arc mantle in high κ_{eq} (or high amplification factor) and water-rich cases. The magmatic thickening rates then return to lower values sustained by the lateral underthrusting.

Controls on the magma volume and magmatic thickening rate

The total cumulative volume of arc magma generated through partial melting of underthrusted crust is limited by the thickness of the underthrusted crust for a given critical melt fraction (F_{crit}). Results of the numerical simulation suggest that for a continental arc analogous to the Sierra Nevada arc, in pure conduction and 1 wt.% water case, one underthrusting event produces a cumulative melt volume of 3.75×10^5 km^3, and 45% of this volume is generated by the end of Stage I (**Figure 2.6E**). This equates to roughly 2.3 km of magmatic thickening in the overriding crust within 25 Myr. The crust would thicken an additional 2.7 km during stage II, from 25 to 117 Myr. In simulations having higher water content or higher diffusivity amplification factor (or higher κ_{eq}), the maximum melt volume is generated within 30 Myr (**Figure 2.9**). The maximum melt volume estimate from numerical simulation (3.75×10^5 km^3) is similar to the scaling analysis result (3.7×10^5 km^3), both of which are much lower than the estimated magma volume (~1 - 3×10^6 km^3) during the Late Cretaceous Sierra Nevada flare-up (Cao & Paterson, 2016; Ratschbacher et al., 2019). The total volume of magma generated through partial melting is 13 - 40% the estimated volume for a flare-up event.

Whether partial melting of the underthrusted lower crust is completed before or after underthrusting stops depends on the ratio between $\tau_{thermal}$ and $\tau_{underthrust}$, in a similar form to the Péclet number (Pe):

$$Pe = \frac{\tau_{thermal}}{\tau_{underthrust}} \tag{12}$$

When $Pe > 1$, underthrusting is finished before the underthrusted crust undergoes complete partial melting for its entire thickness. The magmatic thickening rate is thus limited by the rate of vertical heat transfer, which is slower than the underthrusting rate (**A1**, **A2** in **Figure 2.9**). When $Pe = \sim 1$, underthrusting is finished almost at the same time when the underthrusted crust goes through partial melting (**A3**, **B1** in **Figure 2.9**). When $Pe < 1$, vertical heat transfer rate outpaces the underthrusting rate and the underthrusted crust experiences complete partial melting before underthrusting is finished. In this case, the magmatic thickening rate is limited by the lateral underthrusting process (e.g., **B2**, **C1** in **Figure 2.9**). This effect can be seen where the magmatic thickening rate simply mimics the underthrusting rate in the later stage of the evolution. When $Pe \ll 1$, the magmatic thickening rate is essentially controlled by the underthrusting rate (e.g., **B3**, **C2**, **C3** in **Figure 2.9**).

Results of both the scaling analysis and the numerical modeling demonstrate that the magmatic thickening rate strongly depends on the underthrusting rate (**Figure 2.6**, **2.7**, and **2.9**). This dependency is more apparent for the cases where $Pe \ll 1$. Such dependence of magmatic thickening rate on the underthrusting rate suggests that the observed bell-shaped magmatic flare-up signals defined by zircon age peaks (e.g. Paterson & Ducea, 2016) may necessitate a similar bell-shaped underthrusting rate through time (similar to the underthrusting rate in Model B). However, current estimates on how the underthrusting rate has changed with time does not support a bell-shaped profile of underthrusting rate with time. For example, the retro-arc shortening rate is fairly constant as we show in our reference model (Model A) (e.g., Yonkee & Weil, 2015). Thus, magma solely generated via underthrusting cannot produce the observed

temporal pattern of a flare-up. Furthermore, the magmatic thickening rate (0.1-0.3 km/Myr) predicted in both the numerical reference model (Model A, blue curves in **Figure 2.9**) and the scaling analysis is significantly lower than observed values (0.6-1 km/Myr) during flare-ups in many Cordilleran arcs (e.g., Cao & Paterson, 2016; Jiang & Lee, 2017; Ratschbacher et al., 2019). The model predicted values are slightly below or similar to the baseline of arc magma thickening rate (~0.3 km/Myr) from the mantle wedge (Reymer & Schubert, 1984; DeCelles et al., 2009).

Mantle-derived magma and arc root foundering

Our modeling results suggest that partial melting of the underthrusted crust alone does not generate the volume nor thickening rates needed to produce a magmatic flare-up. Thus, magmatic contributions from other sources are be needed. Crustal melt generated from processes other than partial melting of the underthrusted crust (e.g., burial of forearc sediments and relamination) could play a role but their magmatic contribution is not well-quantified. Melt from *in situ* crustal melting could intensify the magmatism, but such melt does not contribute to the net growth of the arc crust. The other important source of arc magma is from the mantle (e.g., Bouiol et al., 2015; Schwartz el al., 2017; Ardila et al., 2019; Attia et al., 2020). For example, a recent zircon Hf isotopes study of the central Sierra Nevada (Attia et al., 2020) and studies on geochemistry and/or Sr, Nd, and Pb isotopes in the North and South Cordilleran arc (Martínez Ardila et al., 2019) and Fiordland arc (Schwartz el al., 2017) all reveal primitive compositions, proposing a mantle source fueled magmatic flare-up events. In the “Cordilleran cycle” model (DeCelles et al., 2009), foundering of the arc root triggers asthenospheric upwelling,

resulting in rapid decompression melting (e.g., Kay & Kay, 1992) of the mantle and causing a magmatic pulse that is above the mantle flux baseline (Lee & Anderson, 2015).

In order to highlight the role of mantle melt and how foundering of the arc root regulates the magmatic tempo, we constructed a simple numerical model to illustrate the cycle of lower crustal underthrusting, arc root buildup, foundering, and renewed underthrusting (**Figure 2.10**). The model begins assuming that the arc root had just foundered, and the asthenospheric mantle begins to upwell. We use a mantle-derived arc magma generation rate of 1 km/Myr, a 300% increase compared to the baseline (~0.3 km/Myr, 1 AU), to represent the increase of arc magma generation associated with the upwelling; the 300% increase is an arbitrary choice to demonstrate the increased magma produced by adiabatic decompression of the asthenosphere. We let the mantle-derived magma decrease with time mainly due to (1) pinching out of the sub-arc mantle by renewed crustal underthrusting and arc root formation (Chin et al., 2015); and (2) dissipation of upwellings after foundering of the arc root. The arc root in the model is the sum of the root generated via partial melting of the underthrusted crust (e.g., Ducea, 2001; 2002) and the root due to the differentiation of mantle-derived magmas (Lee et al., 2006; Lee & Anderson, 2015; Ming et al., 2019). We refer to the former root as crustal arc root and the latter as the mantle arc root. The model presented here is based on the geometry shown in **Figure 2.2** and has the same initial and boundary conditions as Case 2 of the numerical model: constant 5km/Myr underthrusting rate, 2 wt. % water content, and pure conduction with no amplification of thermal diffusivity. The model setup is presented in the supporting information.

Figure 2.10 shows that with the combined crustal root generated from partial melting of the underthrusted crust and the formation of the mantle root, the critical thickness of root is reached every 36 Myr (green curve in Panel C). If there is no underthrusting of the lower crust and formation of the crustal root but only mantle root, the same critical thickness is reached every 69 Myr (dotted purple curve in Panel C), roughly twice longer than the former case. Such a difference affects the recurring time of root foundering and potential arc flare-up. It is noted for the simple model presented here, we do not include any additional crustal partial melt and the mechanical process associated with root foundering is ignored. Therefore, the model is incapable of resolving the ratio of crustal versus mantle melts nor the exact timing of root foundering. Chin et al. (2015) and Cao et al., (2016b) suggested that the increasing thickness of the arc upper plate due to magmatic and tectonic thickening also causes a self-limiting effect on arc magmatism and controls the arc magmatism tempo. Here, we use a simple model to highlight that crustal underthrusting plays an important role in limiting arc magma generation and regulating the magmatic tempo via contribution to the arc root formation and foundering.

CONCLUSION

Numerical modeling results show that the total volume of arc magma and the magmatic thickening rate associated with partial melting of underthrusting retro-arc lower crust are not sufficient to drive arc flare-up events of similar magnitude as those that occurred in the Cretaceous Sierra Nevada arc. While this study is focused on underthrusting of the retro-arc, the results from our generic model are potentially

applicable to the process of fore-arc underthrusting. We demonstrated the total volume of magma generated through partial melting of the underthrusted lower crust depends on the size of the underthrusted lower crustal slab, while the temporal pattern of the magmatic thickening rate is directly correlated with the underthrusting rate and is controlled by the ratio between the characteristic timescales of heat transfer and underthrusting. Crustal underthrusting contributes to the growth of the arc root whose subsequent foundering may regulate the tempo of arc magmatism. We suggest additional melts from the mantle and/or other crustal sources are needed during arc flare-ups.

ACKNOWLEDGEMENTS

This study is supported by the UNR microgrant awarded to Cao and Gordon and National Science Foundation (NSF) grant (EAR-1830139). Ming Tang is thanked for the help with the setup of the MELTS program. Nicolas Riel and an anonymous reviewer are thanked for their comments. Editor Claudio Faccenna and associate editor Boris Kaus are thanked for handling the manuscript. Data were not used, nor created for this research. Software for this research is not publicly available and software license should be purchased from the MathWorks company (www.mathworks.com).

APPENDIX 2.1: Effects of critical melt fraction

The choice of critical melt fraction for the extraction of melt will affect the amount and rate of melt generation. In **Figure 2.S1A** we show the evolution of thermal boundary thicknesses representing the temperature at which critical melt fraction of 0.1, 0.25, 0.35, and 0.5 is achieved. Because higher temperatures (T_{crit}) are required for higher melt fractions, the thickening rate of the melt region (area undergoing partial melting and melt extraction) is inversely correlated with critical melt fraction. In the F_{crit} = 0.1 case, the entire 20 km representing the thickness of the underthrusted crustal slab is melt mobile within ~12 Myr, while less than 4 km is melt mobile at 60 Myr if F_{crit} = 0.5 is used. While the rate of growth of isotherm thickness for lower degree of melting (F_{crit} = 0.1) is more rapid, but due to the small F_{crit} value, only a relatively small amount of melt can be extracted (**Figure 2.S1B**).

Figure 2.S1B shows the cumulative melt thickness, with the same 4 critical melt fractions. The 1-D melt thickness is calculated by multiplying the corresponding thermal boundary thickness by its melt fraction. We observe while the thickness of thermal boundary layer corresponding to a higher critical melt fraction (F_{crit} = 0.25) is less than that of a lower melt fraction (F_{crit} = 0.1) (**Figure 2.S1B**); the amount of melt however is greater (**Figure 2.S1B**). For the higher end of critical melt fraction (F_{crit} = 0.5), because growth of the melt mobile region is slow, relatively little melt can be extracted. If we limit the timescale to 30 Myr (typical timescale for a flare-up), a critical melt fraction of ~0.25 results in the most amount of melt produced (**Figure 2.S1B**, red curve). Thus in

our calculations the assumption of F_{crit} = 0.25 represents an upper limit to the production of arc magma via partial melting of underthrusted crust.

APPENDIX 2.2: Estimate 2D melt area

In our model, we use an area of $A = x \cdot z$ to represent the area of underthrusted slab undergoing partial melting and melt extraction. Since we do not solve heat diffusion in 2D, we argue that the area of $A = x \cdot z$ is slightly larger than the actual melt area (area having a temperature higher than T_{crit}) but by no more than ~30%.

Here we define three areas. $A_1 = x \cdot z$, this is simply the product of underthrust distance (x) and the thickness of melt area at the leading edge of the underthrusting crust (z). A_{actual} is the actual melt area if it is solved by 2D heat diffusion. A_{1D} is the melt area if only vertical heat diffusion is applied. It is obvious to note that $A_1 > A_{actual} > A_{1D}$.

We can calculate A_{1D} in the following way (**Figure 2.S2**). In the constant underthrusting rate case, $t = x/v$, v is the constant underthrusting rate. For z, using scaling law, we have

$$z = \sqrt{\kappa t} = \sqrt{\frac{\kappa}{v}} \cdot \sqrt{x}$$

A_{1D} can be obtained by integrating the area assuming only vertical diffusion is applied:

$$A_{1D} = \int_0^x z \cdot dx = \int_0^x \sqrt{\frac{\kappa}{v}} \cdot \sqrt{x} \cdot dx = \sqrt{\frac{\kappa}{v}} \cdot \int_0^x \sqrt{x} \cdot dx$$

After integration, we have

$$A_{1D} = \sqrt{\frac{\kappa}{v}} \cdot \frac{2}{3} x^{\frac{3}{2}} = \frac{2}{3} x \cdot \sqrt{\frac{\kappa x}{v}} = \frac{2}{3} x \cdot \sqrt{\kappa t} = \frac{2}{3} x \cdot z = \frac{2}{3} A_1$$

Thus, we have

$$A_1 > A_{actual} > \frac{2}{3} A_1$$

or

$$x \cdot z > A_{actual} > \frac{2}{3} x \cdot z$$

APPENDIX 2.3: Cyclic underthrusting and root foundering model setup

The model initiates with a constant underthrusting rate of 5 km/Myr after a foundering event. We set the background mantle melt generation rate to 0.3 km/Myr (1AU) and enforce a 300% increase at the initiation of the underthrusting, immediately after root foundering due to the associated asthenospheric upwellings. This pulse of increased mantle melt production decreases back to the normal value in 14 Myr based on the calculated delamination time by assuming gravitational instability induced wholesale delamination of a 35 km thick arc root with a viscosity of 10^{23} Pa·s (Lee, 2014).

This arc root is generated via both restite left over from partial melting of the underthrusted lower crust (crustal arc root, Ducea, 2002), and differentiation of the mantle (mantle arc root, Lee et al., 2006). Because we use F_{crit} = 0.25 the ratio of crustal

melt to root is 1:3. For the mantle arc root, the ratio of melt to restite is assumed to be 1:2 (Lee, 2014). Since both underthrusting of the lower crustal slab and formation of the restite arc root displaces the sub-arc asthenosphere, resulting in reduction in the volume of mantle material from which melt can be extracted. Accordingly, we scale melt generation by the 2-D area of the sub-arc mantle that's occupying the region between the slab and lithosphere. The arc root (crustal + mantle arc root) is allowed to grow until a critical thickness of 35 km. After this point the root is removed from the simulation with renewed underthrusting and the cycle starts over.

REFERENCES

Ardill, K., Paterson, S., & Memeti, V. (2018). Spatiotemporal magmatic focusing in upper-mid crustal plutons of the Sierra Nevada arc. *Earth and Planetary Science Letters*, *498*, 88-100.

Armstrong, R. L., & Clark, S. P. (1988). Mesozoic and early Cenozoic magmatic evolution of the Canadian Cordillera. *Geological Society of America Special Paper*, *218*, 55-91.

Arndt, N. T., & Goldstein, S. L. (1989). An open boundary between lower continental crust and mantle: its role in crust formation and crustal recycling. *Tectonophysics*, *161*(3-4), 201-212.

Attia, S., Cottle, J. M., & Paterson, S. R. (2020). Erupted zircon record of continental crust formation during mantle driven arc flare-ups. *Geology*, *48*(5), 446-451.

Bergantz, G. W. (1989). Underplating and partial melting: implications for melt generation and extraction. *Science*, *245*(4922), 1093-1095.

Cao, W., & Paterson, S. (2016). A mass balance and isostasy model: Exploring the interplay between magmatism, deformation and surface erosion in continental arcs using central Sierra Nevada as a case study. *Geochemistry, Geophysics, Geosystems*, *17*(6), 2194-2212.

Cao, W., Kaus, B. J., & Paterson, S. (2016a). Intrusion of granitic magma into the continental crust facilitated by magma pulsing and dike-diapir interactions: Numerical simulations. *Tectonics*, *35*(6), 1575-1594.

Cao, W., Paterson, S., Saleeby, J., & Zalunardo, S. (2016b). Bulk arc strain, crustal thickening, magma emplacement, and mass balances in the Mesozoic Sierra Nevada arc. *Journal of Structural Geology*, *84*, 14-30.

Cao, W., Lee, C. T. A., & Lackey, J. S. (2017). Episodic nature of continental arc activity since 750 Ma: A global compilation. *Earth and Planetary Science Letters*, *461*, 85-95.

Chu, X., Lee, C. T. A., Dasgupta, R., & Cao, W. (2019). The contribution to exogenic CO2 by contact metamorphism at continental arcs: A coupled model of fluid flux and metamorphic decarbonation. *American Journal of Science*, *319*(8), 631-657.

Cecil, M. R., Rusmore, M. E., Gehrels, G. E., Woodsworth, G. J., Stowell, H. H., Yokelson, I. N., Chisom, C., Trautman, M., & Homan, E. (2018). Along-strike variation in the magmatic tempo of the Coast Mountains batholith, British Columbia, and implications for processes controlling episodicity in arcs. *Geochemistry, Geophysics, Geosystems*, *19*(11), 4274-4289.

Chapman, A. D., Saleeby, J. B., & Eiler, J. (2013). Slab flattening trigger for isotopic disturbance and magmatic flare-up in the southernmost Sierra Nevada batholith, California. *Geology*, *41*(9), 1007-1010.

Chapman, J. B., & Ducea, M. N. (2019). The role of arc migration in Cordilleran orogenic cyclicity. *Geology*, *47*(7), 627-631.

Chapman, J. B., & Kapp, P. (2017). Tibetan magmatism database. *Geochemistry, Geophysics, Geosystems*, *18*(11), 4229-4234.

Chin, E. J., Lee, C. T. A., & Blichert-Toft, J. (2015). Growth of upper plate lithosphere controls tempo of arc magmatism: Constraints from Al-diffusion kinetics and coupled Lu-Hf and Sm-Nd chronology. *Geochemical Perspectives Letters*, *1*(1), 20-32.

Condie, K. C. (2013). *Plate tectonics & crustal evolution*. Elsevier.

Cope, T. (2017). Phanerozoic magmatic tempos of North China. *Earth and Planetary Science Letters*, *468*, 1-10.

De Silva, S. L., Riggs, N. R., & Barth, A. P. (2015). Quickening the pulse: fractal tempos in continental arc magmatism. *Elements*, *11*(2), 113-118.

DeCelles, P. G. (2004). Late Jurassic to Eocene evolution of the Cordilleran thrust belt and foreland basin system, western USA. *American Journal of Science*, *304*(2), 105-168.

DeCelles, P. G., Ducea, M. N., Kapp, P. and Zandt, G., (2009). Cyclicity in Cordilleran orogenic systems. *Nature Geoscience*, *2*(4), p.251.

DeCelles, P. G., & Graham, S. A. (2015). Cyclical processes in the North American Cordilleran orogenic system. *Geology*, *43*(6), 499-502.

Decelles, P. G., Zandt, G., Beck, S. L., Currie, C. A., Ducea, M. N., Kapp, P., Gehrels, G. E., Carrapa, B., Quade, J., & Schoenbohm, L. M. (2014). Cyclical orogenic processes in the Cenozoic central Andes. *Geological Society of America Memoirs*, *212*, MWR212-22.

Ducea, M. N. (2001). The California arc: Thick granitic batholiths, eclogitic residues, lithospheric-scale thrusting, and magmatic flare-ups. *GSA today*, *11*(11), 4-10.

Ducea, M. N. (2002). Constraints on the bulk composition and root foundering rates of continental arcs: A California arc perspective. *Journal of Geophysical Research: Solid Earth*, *107*(B11), ECV-15.

Ducea, M. N., & Barton, M. D. (2007). Igniting flare-up events in Cordilleran arcs. *Geology*, *35*(11), 1047-1050.

Ducea, M. N., & Chapman, A. D. (2018). Sub-magmatic arc underplating by trench and forearc materials in shallow subduction systems; A geologic perspective and implications. *Earth-Science Reviews*, *185*, 763-779.

Ducea, M. N., & Saleeby, J. B. (1996). Buoyancy sources for a large, unrooted mountain range, the Sierra Nevada, California: Evidence from xenolith thermobarometry. *Journal of Geophysical Research: Solid Earth*, *101*(B4), 8229-8244.

England, P., Molnar, P., & Richter, F. (2007). John Perry's neglected critique of Kelvin's age for the Earth: A missed opportunity in geodynamics. *GSA Today*, *17*(1).

Erdman, M. E., & Lee, C. T. A. (2014). Oceanic-and continental-type metamorphic terranes: Occurrence and exhumation mechanisms. Earth-Science Reviews, 139, 33-46.

Gehrels, G., Rusmore, M., Woodsworth, G., Crawford, M., Andronicos, C., Hollister, L., Patchett, J., Ducea, M., Butler, R., Klepeis, K., & Davidson, C. (2009). U-Th-Pb geochronology of the Coast Mountains batholith in north-coastal British Columbia: Constraints on age and tectonic evolution. *Geological Society of America Bulletin*, *121*(9-10), 1341-1361.

Ghiorso, M. S., & Sack, R. O. (1995). Chemical mass transfer in magmatic processes IV. A revised and internally consistent thermodynamic model for the interpolation and extrapolation of liquid-solid equilibria in magmatic systems at elevated temperatures and pressures. *Contributions to Mineralogy and Petrology*, *119*(2-3), 197-212.

Hacker, B. R., Kelemen, P. B., & Behn, M. D. (2011). Differentiation of the continental crust by relamination. *Earth and Planetary Science Letters*, *307*(3-4), 501-516.

Hajná, J., Žák, J., & Dörr, W. (2017). Time scales and mechanisms of growth of active margins of Gondwana: a model based on detrital zircon ages from the Neoproterozoic to Cambrian Blovice accretionary complex, Bohemian Massif. *Gondwana Research*, *42*, 63-83.

Haschke, M., Günther, A., Melnick, D., Echtler, H., Reutter, K. J., Scheuber, E., & Oncken, O. (2006). Central and southern Andean tectonic evolution inferred from arc magmatism. In *The Andes* (pp. 337-353). Springer, Berlin, Heidelberg.

Jaupart, C., & Mareschal, J. C. (2010). *Heat generation and transport in the Earth*. Cambridge university press.

Jiang, H., & Lee, C. T. A. (2017). Coupled magmatism–erosion in continental arcs: Reconstructing the history of the Cretaceous Peninsular Ranges batholith, southern California through detrital hornblende barometry in forearc sediments. *Earth and Planetary Science Letters*, *472*, 69-81.

Jicha, B. R., & Jagoutz, O. (2015). Magma production rates for intraoceanic arcs. Elements, 11(2), 105-111.

Karakas, O., & Dufek, J. (2015). Melt evolution and residence in extending crust: Thermal modeling of the crust and crustal magmas. Earth and Planetary Science Letters, 425, 131-144.

Karlstrom, L., Lee, C. T., & Manga, M. (2014). The role of magmatically driven lithospheric thickening on arc front migration. *Geochemistry, Geophysics, Geosystems*, *15*(6), 2655-2675.

Kay, R. W., & Kay, S. M. (1993). Delamination and delamination magmatism. *Tectonophysics*, *219*(1-3), 177-189.

Keller, T., May, D. A., & Kaus, B. J. (2013). Numerical modelling of magma dynamics coupled to tectonic deformation of lithosphere and crust. Geophysical Journal International, 195(3), 1406-1442.

Kirsch, M., Paterson, S. R., Wobbe, F., Ardila, A. M. M., Clausen, B. L., & Alasino, P. H. (2016). Temporal histories of Cordilleran continental arcs: Testing models for magmatic episodicity. *American Mineralogist*, *101*(10), 2133-2154.

Lange, R. A., Cashman, K. V., & Navrotsky, A. (1994). Direct measurements of latent heat during crystallization and melting of a ugandite and an olivine basalt. *Contributions to Mineralogy and Petrology*, *118*(2), 169-181.

Lee, C. T. A. (2014). The physics and chemistry of recycling lower continental crust. *Treatise of Geochemistry*, 423-456.

Lee, C. T. A., & Anderson, D. L. (2015). Continental crust formation at arcs, the arclogite "delamination" cycle, and one origin for fertile melting anomalies in the mantle. *Science Bulletin*, *60*(13), 1141-1156.

Lee, C. T. A., Cheng, X., & Horodyskyj, U. (2006). The development and refinement of continental arcs by primary basaltic magmatism, garnet pyroxenite accumulation, basaltic recharge and delamination: insights from the Sierra Nevada, California. *Contributions to Mineralogy and Petrology*, *151*(2), 222-242.

Lee, C. T. A., Jiang, H., Dasgupta, R., & Torres, M. (2019). A Framework for Understanding Whole-Earth Carbon Cycling. In *Deep Carbon: Past to Present* (pp. 313-357). Cambridge University Press.

Lee, C. T. A., Thurner, S., Paterson, S., & Cao, W. (2015a). The rise and fall of continental arcs: Interplays between magmatism, uplift, weathering, and climate. *Earth and Planetary Science Letters*, *425*, 105-119.

Lee, C. T. A., MorTon, D. M., FArner, M. J., & MoiTrA, P. (2015b). Field and model constraints on silicic melt segregation by compaction/hindered settling: The role of water and its effect on latent heat release. *American Mineralogist*, *100*(8-9), 1762-1777.

Li, X. H., Li, Z. X., Li, W. X., Liu, Y., Yuan, C., Wei, G., & Qi, C. (2007). U–Pb zircon, geochemical and Sr–Nd–Hf isotopic constraints on age and origin of Jurassic I-and A-type granites from central Guangdong, SE China: a major igneous event in response to foundering of a subducted flat-slab?. *Lithos*, *96*(1-2), 186-204.

Liang, Y., & Parmentier, E. M. (2010). A two-porosity double lithology model for partial melting, melt transport and melt–rock reaction in the mantle: Mass conservation equations and trace element transport. Journal of Petrology, 51(1-2), 125-152.

Mallik, A., & Dasgupta, R. (2012). Reaction between MORB-eclogite derived melts and fertile peridotite and generation of ocean island basalts. *Earth and Planetary Science Letters*, *329*, 97-108.

Martínez Ardila, A. M., Paterson, S. R., Memeti, V., Parada, M. A., & Molina, P. G. (2019). Mantle driven cretaceous flare-ups in Cordilleran arcs. *Lithos*, *326*, 19-27.

McKenzie, N. R. (2017). Zircons reveal ancient perturbations. *Nature Geoscience*, *10*(12), 884-886.

Moghadam, H. S., Li, X. H., Griffin, W. L., Stern, R. J., Thomsen, T. B., Meinhold, G., Aharipour, R., & O'Reilly, S. Y. (2017). Early Paleozoic tectonic reconstruction of Iran: tales from detrital zircon geochronology. *Lithos*, *268*, 87-101.

Mottaghy, D., Vosteen, H. D., & Schellschmidt, R. (2008). Temperature dependence of the relationship of thermal diffusivity versus thermal conductivity for crystalline rocks. *International Journal of Earth Sciences*, *97*(2), 435-442.

Paterson, S. R., & Ducea, M. N. (2015). Arc magmatic tempos: gathering the evidence. *Elements*, *11*(2), 91-98.

Paulsen, T., Deering, C., Sliwinski, J., Bachmann, O., & Guillong, M. (2016). A continental arc tempo discovered in the Pacific-Gondwana margin mudpile?. *Geology*, *44*(11), 915-918.

Pearson, D. M., MacLeod, D. R., Ducea, M. N., Gehrels, G. E., & Jonathan Patchett, P. (2017). Sediment underthrusting within a continental magmatic arc: Coast Mountains batholith, British Columbia. *Tectonics*, *36*(10), 2022-2043.

Pepper, M., Gehrels, G., Pullen, A., Ibanez-Mejia, M., Ward, K. M., & Kapp, P. (2016). Magmatic history and crustal genesis of western South America: Constraints from U-Pb ages and Hf isotopes of detrital zircons in modern rivers. *Geosphere*, *12*(5), 1532-1555.

Pilger, R. H. (1984). Cenozoic plate kinematics, subduction and magmatism: South American Andes. *Journal of the Geological Society*, *141*(5), 793-802.

Ratschbacher, B. C., Paterson, S. R., & Fischer, T. P. (2019). Spatial and depth-dependent variations in magma volume addition and addition rates to continental arcs: Application to global CO2 fluxes since 750 Ma. *Geochemistry, Geophysics, Geosystems*, *20*(6), 2997-3018.

Rees Jones, D. W., Katz, R. F., Tian, M., & Rudge, J. F. (2018). Thermal impact of magmatism in subduction zones. Earth and Planetary Science Letters, 481, 73–79. doi:10.1016/j.epsl.2017.10.015

Reymer, A., & Schubert, G. (1984). Phanerozoic addition rates to the continental crust and crustal growth. *Tectonics*, *3*(1), 63-77.

Rosenberg, C. L., & Handy, M. R. (2005). Experimental deformation of partially melted granite revisited: implications for the continental crust. Journal of metamorphic Geology, 23(1), 19-28.

Rudnick, R. L. (1995). Making continental crust. *Nature*, *378*(6557), 571-578.

Rudnick, R. L., & Gao, S. (2003). Composition of the continental crust. *The crust*, *3*, 1-64.

Rummel, L., Kaus, B. J., Baumann, T. S., White, R. W., & Riel, N. (2020). Insights into the compositional evolution of crustal magmatic systems from coupled petrological-geodynamical models. Journal of Petrology.

Saleeby, J. B. (1990). Progress in tectonic and petrogenetic studies in an exposed cross-section of young (~ 100 Ma) continental crust, southern Sierra Nevada, California. In Exposed cross-sections of the continental crust (pp. 137-158). Springer, Dordrecht.

Sauer, K. B., Gordon, S. M., Miller, R. B., Vervoort, J. D., & Fisher, C. M. (2017). Transfer of metasupracrustal rocks to midcrustal depths in the North Cascades continental magmatic arc, Skagit Gneiss Complex, Washington. *Tectonics*, *36*(12), 3254-3276.

Sauer, K. B., Gordon, S. M., Miller, R. B., Vervoort, J. D., & Fisher, C. M. (2018). Provenance and metamorphism of the Swakane Gneiss: Implications for incorporation of sediment into the deep levels of the North Cascades continental magmatic arc, Washington. *Lithosphere*, *10*(3), 460-477.

Sawyer, E. W. (1994). Melt segregation in the continental crust. Geology, 22(11), 1019-1022.

Schwartz, J. J., Klepeis, K. A., Sadorski, J. F., Stowell, H. H., Tulloch, A. J., & Coble, M. A. (2017). The tempo of continental arc construction in the Mesozoic Median Batholith, Fiordland, New Zealand. *Lithosphere*, *9*(3), 343-365.

Sen, C., & Dunn, T. (1994). Dehydration melting of a basaltic composition amphibolite at 1.5 and 2.0 GPa: implications for the origin of adakites. *Contributions to Mineralogy and Petrology*, *117*(4), 394-409.

Stern, R. J. (2002). Subduction zones. *Reviews of geophysics*, *40*(4), 3-1.

Syracuse, E. M., van Keken, P. E., & Abers, G. A. (2010). The global range of subduction zone thermal models. Physics of the Earth and Planetary Interiors, 183(1-2), 73-90.

Tsujimori, T., Sisson, V. B., Liou, J. G., Harlow, G. E., & Sorensen, S. S. (2006). Very-low-temperature record of the subduction process: A review of worldwide lawsonite eclogites. Lithos, 92(3-4), 609-624.

Turner, A.J., Katz, R.F., Behn, M.D. and Keller, T., 2017. Magmatic focusing to mid-ocean ridges: the role of grain-size variability and non-Newtonian viscosity. Geochemistry, Geophysics, Geosystems, 18(12), pp.4342-4355.

Vosteen, H. D., & Schellschmidt, R. (2003). Influence of temperature on thermal conductivity, thermal capacity and thermal diffusivity for different types of rock. *Physics and Chemistry of the Earth, Parts A/B/C*, *28*(9-11), 499-509.

Whittington, A. G., Hofmeister, A. M., & Nabelek, P. I. (2009). Temperature-dependent thermal diffusivity of the Earth's crust and implications for magmatism. *Nature*, *458*(7236), 319-321.

Yonkee, W. A., & Weil, A. B. (2015). Tectonic evolution of the Sevier and Laramide belts within the North American Cordillera orogenic system. *Earth-Science Reviews*, *150*, 531-593.

Yu, X., & Lee, C. T. A. (2016). Critical porosity of melt segregation during crustal melting: Constraints from zonation of peritectic garnets in a dacite volcano. *Earth and Planetary Science Letters*, *449*, 127-134.

Zhang, X., Chung, S. L., Lai, Y. M., Ghani, A. A., Murtadha, S., Lee, H. Y., & Hsu, C. C. (2019). A 6000-km-long Neo-Tethyan arc system with coherent magmatic flare-ups and lulls in South Asia. *Geology*, *47*(6), 573-576.

Zhang, Z., Zhao, G., Santosh, M., Wang, J., Dong, X., & Shen, K. (2010). Late Cretaceous charnockite with adakitic affinities from the Gangdese batholith, southeastern Tibet: evidence for Neo-Tethyan mid-ocean ridge subduction?. *Gondwana Research*, *17*(4), 615-631.

TABLES

Table 2.1. Parameter definitions and values used in this study.

Parameter	Symbol	Value	Unit
Thickness of underthrusting crust	z	20	km
Width of the arc	w	125	km
Along strike arc length	l		km
Temperature of crustal slab	T_{crust}	600	°C
Mantle temperature	T_{mantle}	1100	°C
Total latent heat of fusion[a]	L	400	kJ kg^{-1}
Temperature dependent heat capacity	$C_p(T)$		J kg^{-1} K^{-1}
Reference thermal diffusivity	κ	10^{-6}	m^2 s^{-1}
Temperature dependent thermal diffusivity	$\kappa(T)$		m^2 s^{-1}
Thermal diffusivity (latent heat effect included)	$\kappa'(T)$		m^2 s^{-1}
Equivalent thermal diffusivity (advection included)	κ_{eq}		m^2 s^{-1}
Characteristic time of heat transfer	$\tau_{thermal}$		Myr
Melt fraction	F		
Critical melt fraction	F_{crit}	0.25	
Critical temperature	T_{crit}		°C
Volume of melt	V		km^3
Underthrusting rate	v		km Myr^{-1}
Underthrusting distance	x		km
Melt area	A		km^2
Characteristic time of underthrusting	$\tau_{underthrust}$		Myr
Underthrust distance arc width ratio	β		
Péclet number	Pe		
Magmatic thickening rate	M		km Myr^{-1}

[a] Lange et al. (1994)

FIGURES

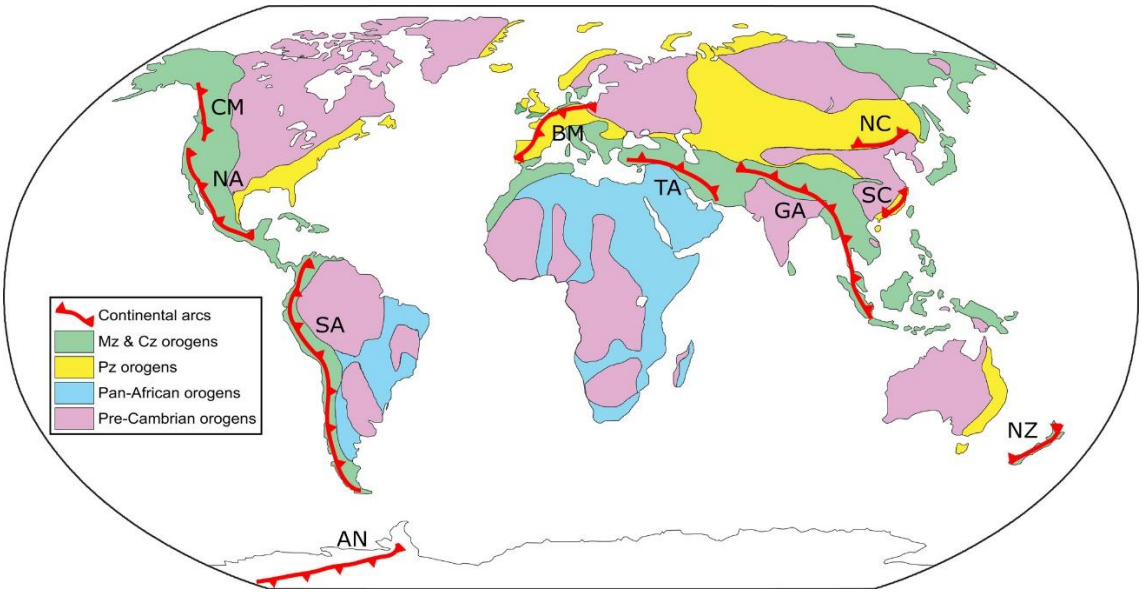

Figure 2.1. World map in Robinson projection showing the locations of continental arcs where non-steady state magmatism has been observed. Arc locations are shown as abbreviations: AN = Antarctica (Paulsen et al., 2016), BM = Bohemian Massif (Hajná & Dörr, 2017), CM = Coast Mountains batholith (Cecil et al., 2018), GA = Gangdese-Burma-Sumatra arc (Zhang et al., 2019), NC = North China (Cope, 2017), NZ = New Zealand (Schwartz et al., 2017), SA = South American Cordilleran arcs (Kirsch et al., 2016; Pepper et al., 2016), SC = South China (Li et al., 2007), NA = North American Cordilleran arcs (Paterson & Ducea, 2015; Kirsch et al., 2016), TA = Taknar complex (Moghadam et al., 2017). Base map modified from Tsujimori et al., (2006) and Erdman and Lee (2014).

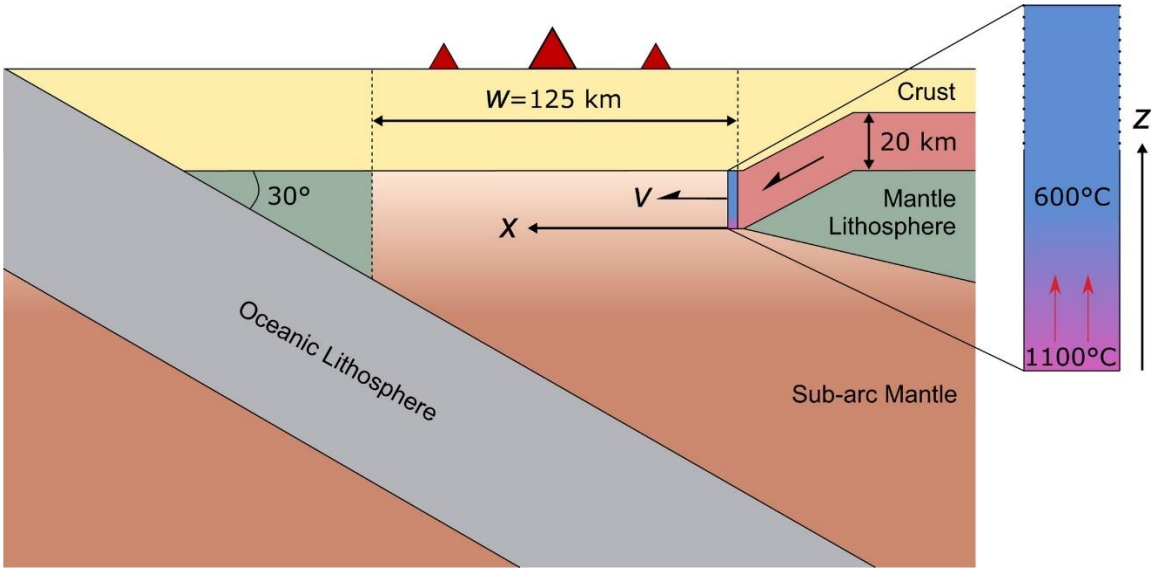

Figure 2.2. Schematic illustration of the numerical model setup showing model geometry and initial thermal state of the half-space heating model where the underthrusted slab is 600°C everywhere except for the fixed 1100°C bottom boundary.

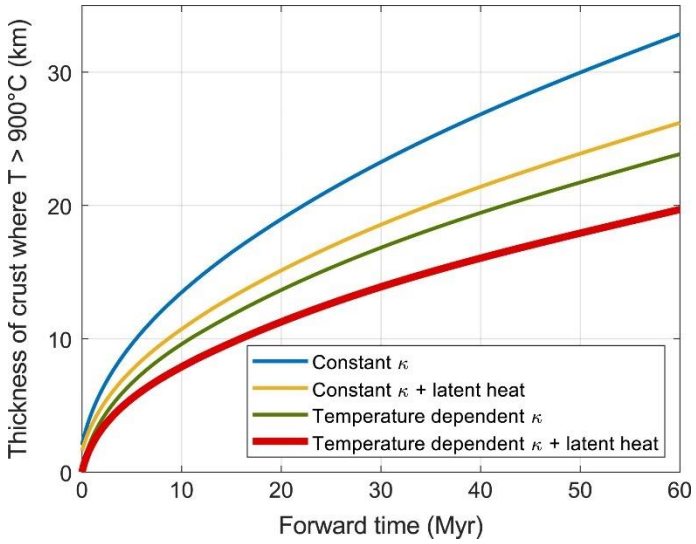

Figure 2.3. Temporal evolution of the underthrusted lower crustal slab showing the propagation of the 900°C isotherm. Inclusion of temperature dependent diffusivity and latent heat significantly reduces the rate of heat transfer.

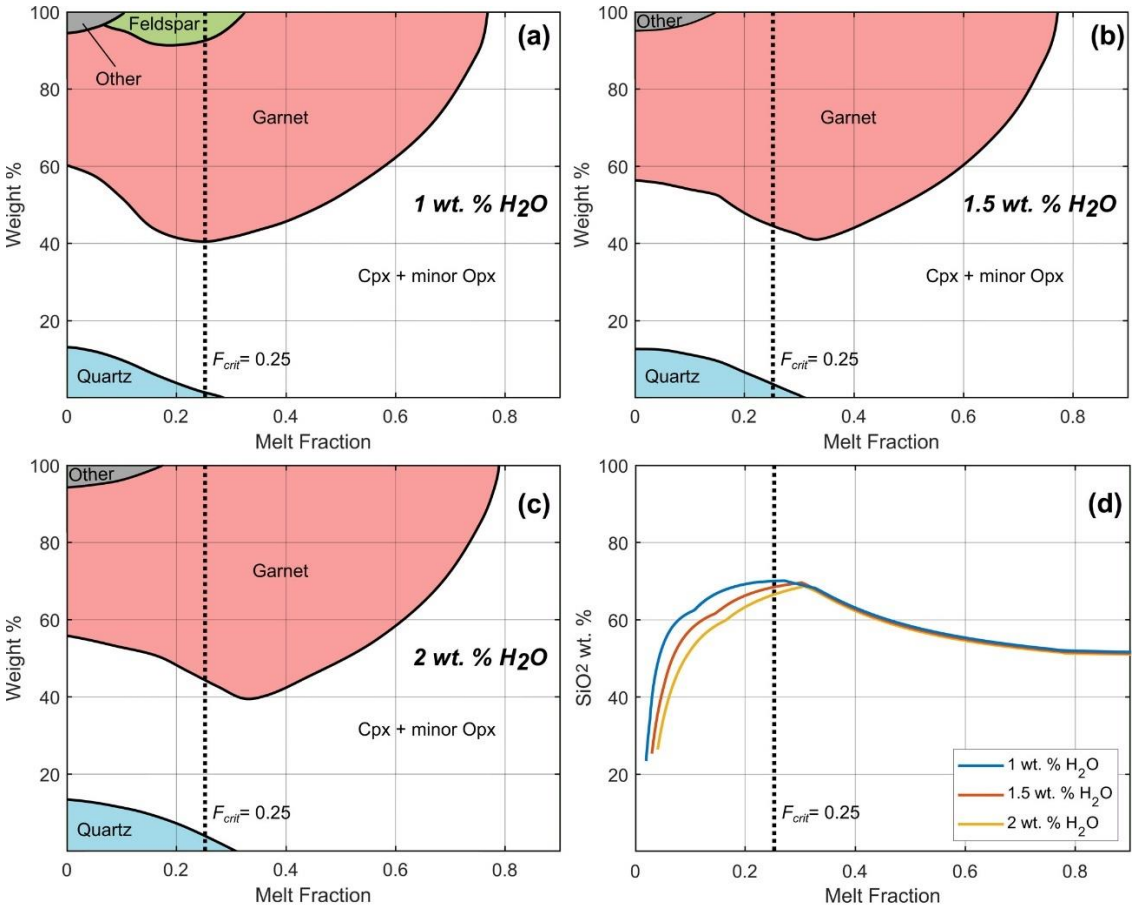

Figure 2.4. MELTS partial melting results of global average lower crust composition (Rudnick & Gao, 2003) containing 1, 1.5, and 2 wt. % H_2O. (**A**, **B**, and **C**) Phase diagram of residual mineral weight percent as a function of melt fraction. (**D**) Silica content in melt vs. melt fraction. F_{crit} is the critical melt fraction (F_{crit} = 0.25 means 25% partial melting).

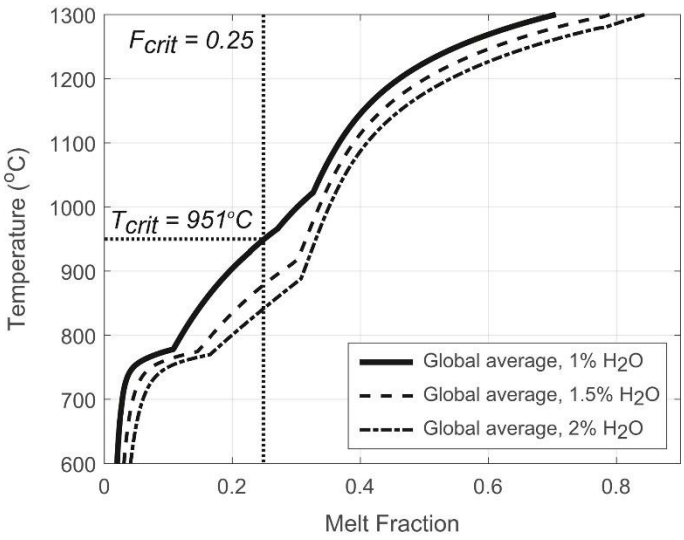

Figure 2.5. Temperature vs. melt fraction diagram for the global average lower crust composition (Rudnick & Gao, 2003) constrained by MELTS. Different water content in weight percent is presented. T_{crit} is the temperature corresponding to F_{crit} = 0.25.

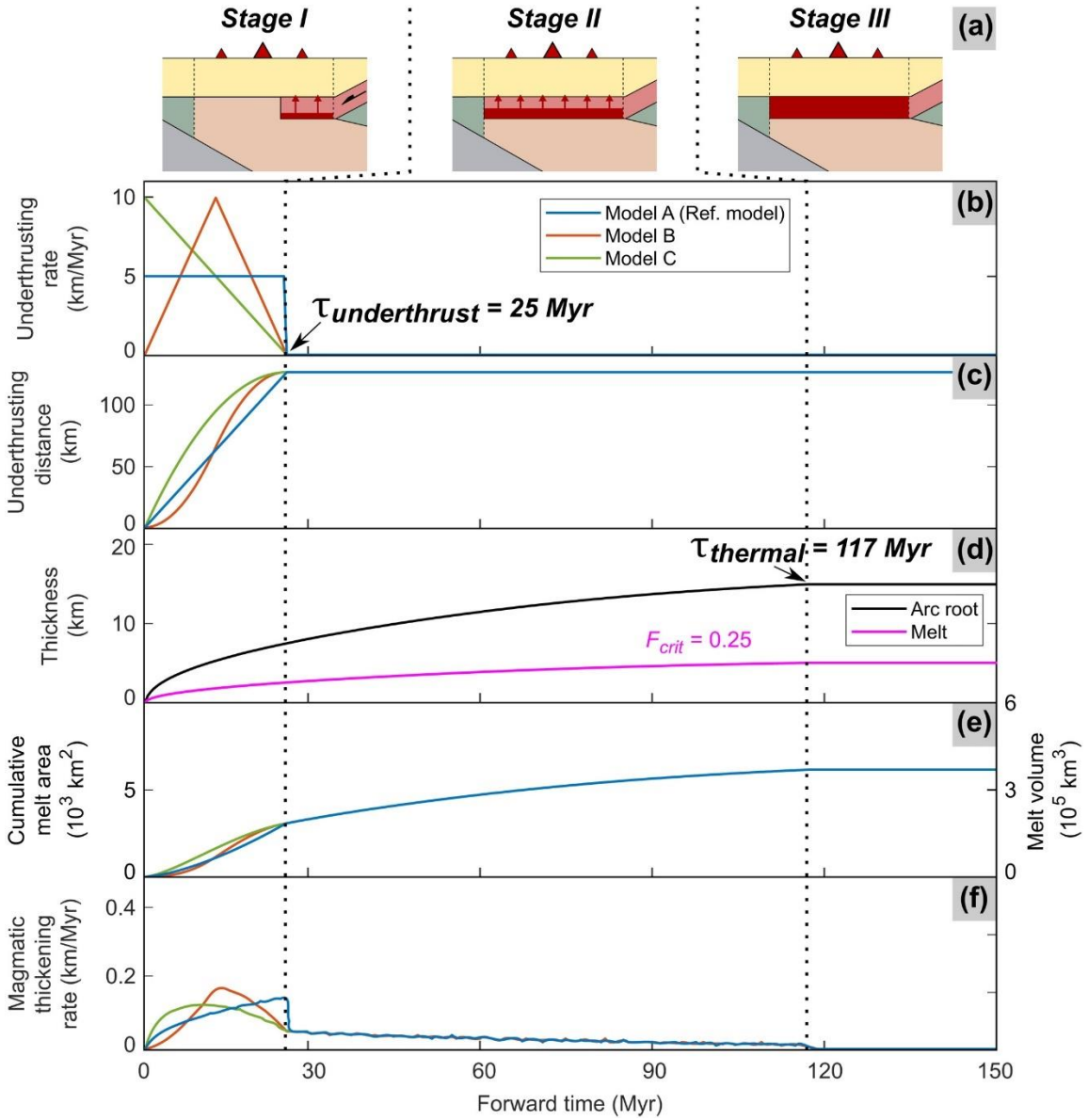

Figure 2.6. Numerical simulation results of case 1 with 1 wt. % water showing the temporal evolution of 3 models with different underthrusting rates. **(A)** The model results are categorized into 3 stages based on underthrusting of the lower crust. The red part of the underthrusted crust refers to the area undergoing partial melting and melt extraction. **(B)** Time dependent underthrusting rate. **(C)** Total underthrusting distance. **(D)** Thickness of arc root generated via partial melting and cumulative melt thicknesses for F_{crit} = 0.25. **(E)** Cumulative 2-D melt area and 3-D melt volume for arc width w = 125 km and arc length l = 600 km. **(F)** Magmatic thickening rate or volumetric flux.

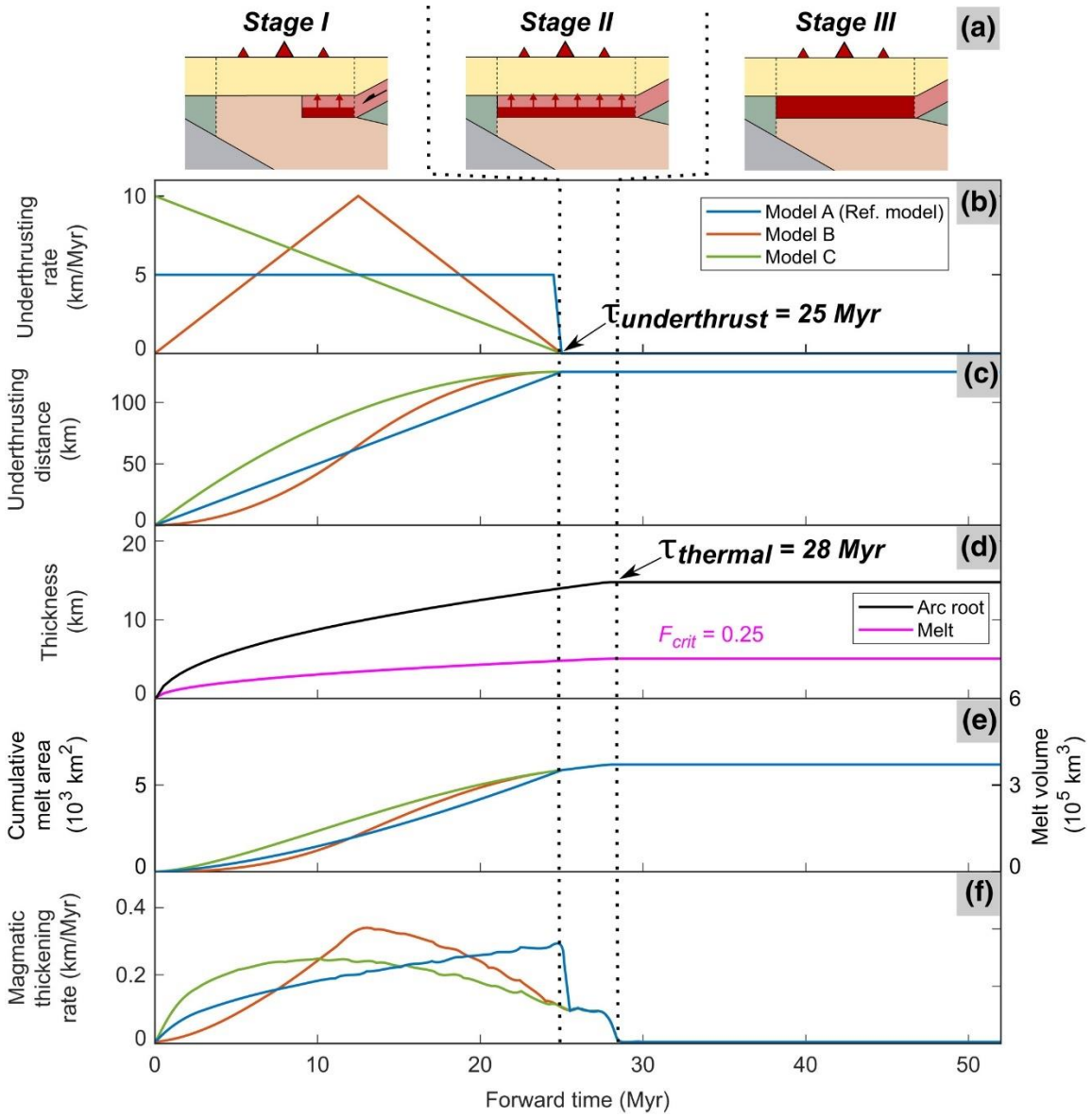

Figure 2.7. Numerical simulation results of case 2 with 2 wt. % water showing the temporal evolution of 3 models with different underthrusting rates. Except for the increased water content, all other parameters are unchanged to illustrate the effect of water on melt generation. **(A)** The model results are categorized into 3 stages. The red part of the underthrusted crust refers to the area undergoing partial melting and melt extraction (see text for detailed explanation). **(B)** Time dependent underthrusting rate. **(C)** Total underthrusting distance. **(D)** Thickness of arc root generated via partial melting and cumulative melt thicknesses for F_{crit} = 0.25. **(E)** Cumulative 2-D melt area and 3-D melt volume for arc width w = 125 km and arc length l = 600 km. **(F)** Magmatic thickening rate or volumetric flux.

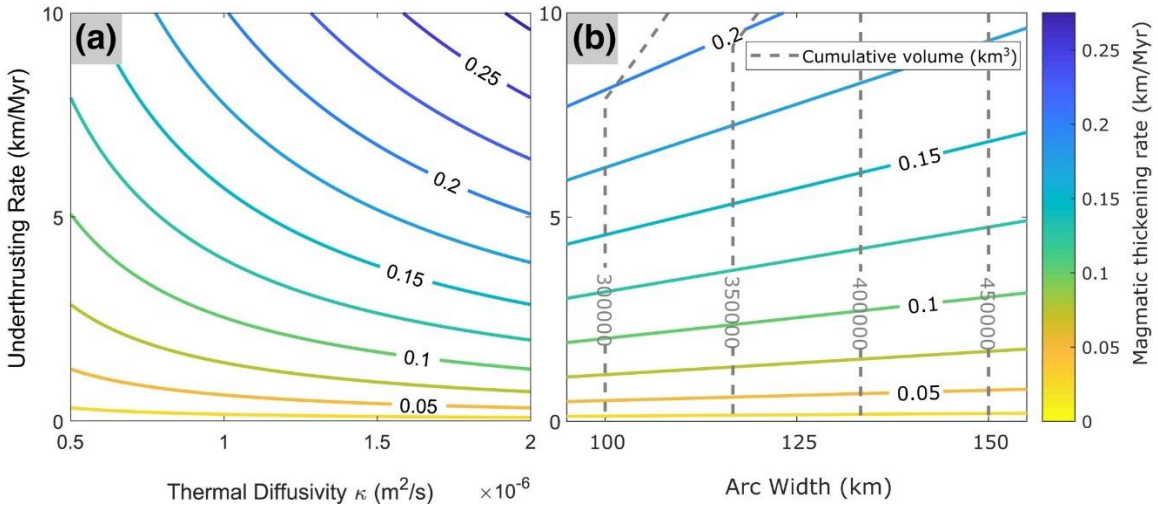

Figure 2.8. Steady-state results showing dependency of magmatic thickening rate (colored contours) with various input parameters. **(A)** Magmatic thickening rate as a function of underthrusting rates and thermal diffusivity with fixed arc width w = 125 km. F_{crit} = 0.25 is used. **(B)** Magmatic thickening rate as a function of arc width and underthrusting rate. Constant thermal diffusivity $\kappa = 10^{-6}$ m^2/s and F_{crit} = 0.25 is used. Cumulative melt volume for a given arc width is shown in dashed gray lines for arc length l = 600 km. Kinks in the dashed gray line of melt volume appear when the underthrust rate is high and arc width is small which results in incomplete partial melting when the underthrusting stops ($\tau_{thermal} > \tau_{underthrust}$).

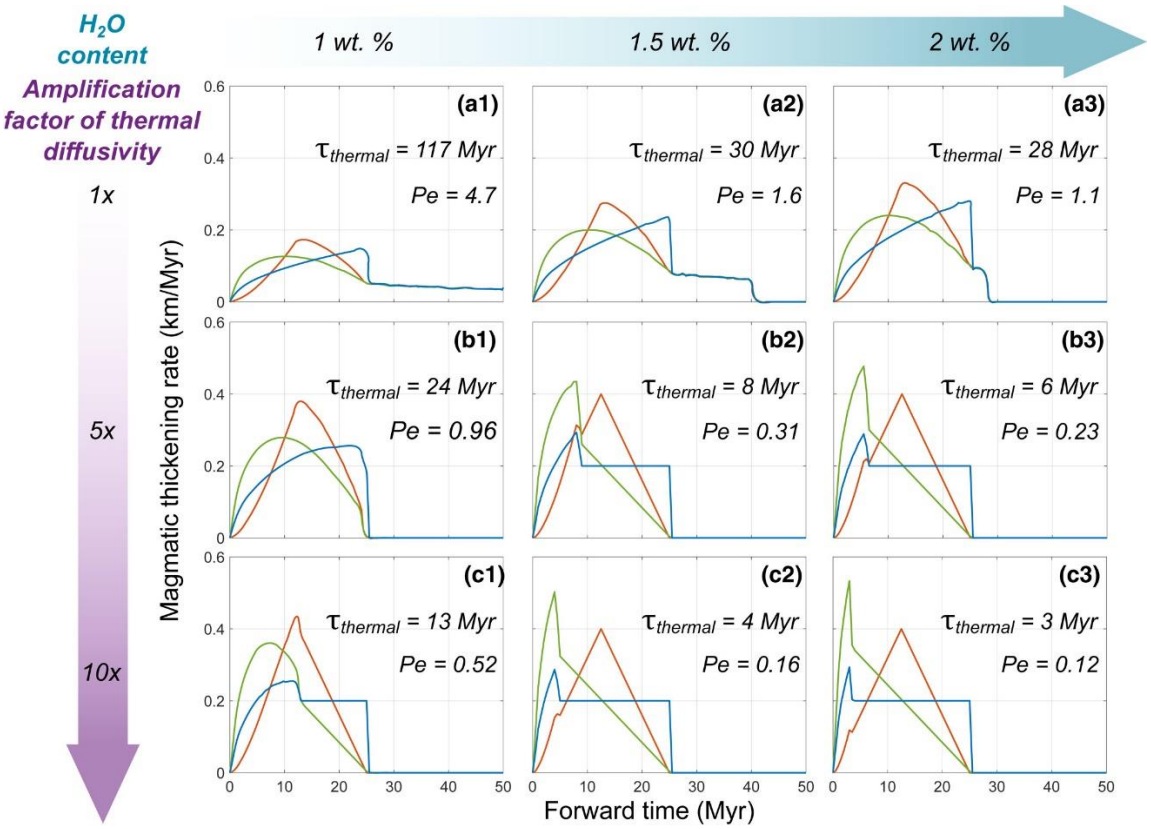

Figure 2.9. Simulation results of magmatic thickening rate (km/Myr) as a function of time. Multiple combinations of water content (horizontal row) and amplification factor of thermal diffusivity (vertical column) are presented. Colored lines represent the three underthrusting rate models: Blue line (Reference Model) is the constant underthrusting rate of 5 km/Myr. Red and green lines represent cases having time-dependent underthrusting rate. Red line is a linearly increasing and decreasing rate which steadily increases to 10 km/Myr during the first half of underthrusting, then decreases to 0 during the second half. Green line is a linear decreasing rate from 10 km/Myr at the start to 0 at the end. All 3 rate models have a underthrusting duration ($\tau_{underthrust}$) of 25 Myr. $\tau_{thermal}$ varies in different models, and Pe is the Péclet number defined as the ratio between $\tau_{thermal}$ and $\tau_{underthrust}$.

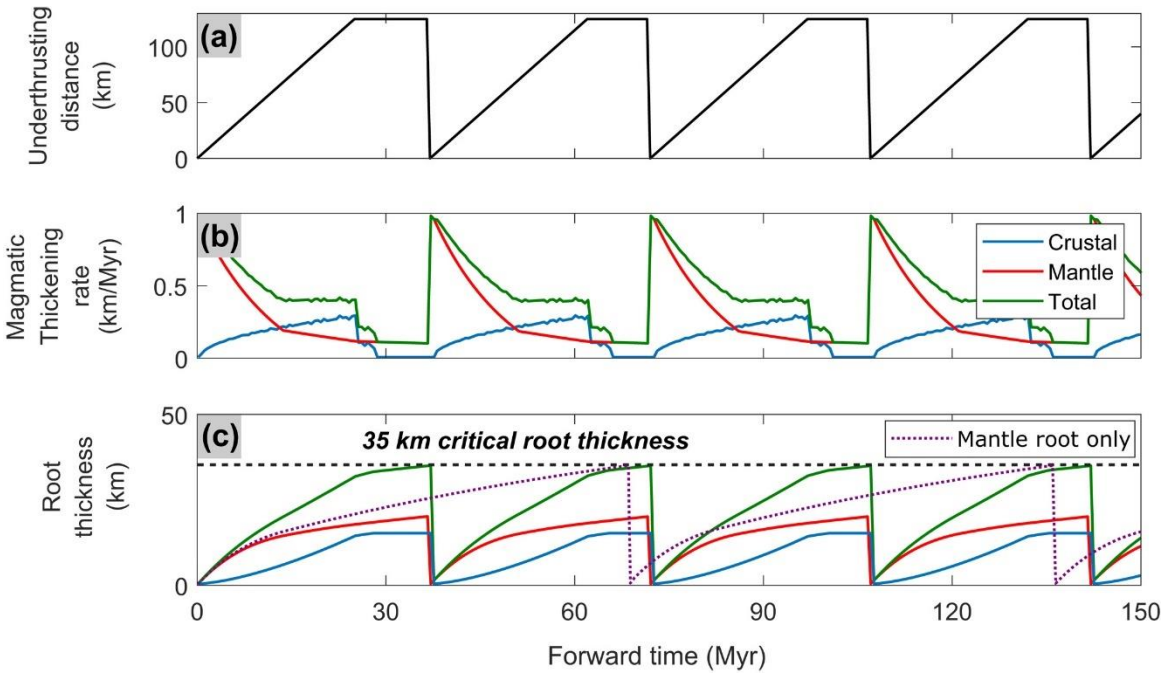

Figure 2.10. Modeling results of cyclic underthrusting and root foundering. **(A)** Lateral distance of the underthrusting lower crust. **(B)** Magmatic thickening rate sourced from the underthrusted crust (blue), mantle (red), and total (green). **(C)** Arc roots contributed by different processes. The horizontal black dashed line is an assigned critical thickness (35 km) for arc root to founder (e.g., Lee et al., 2015a). Purple line is mantle arc root only without the contribution of crustal arc root. Note the time interval of root foundering shortens when the crustal arc root is involved.

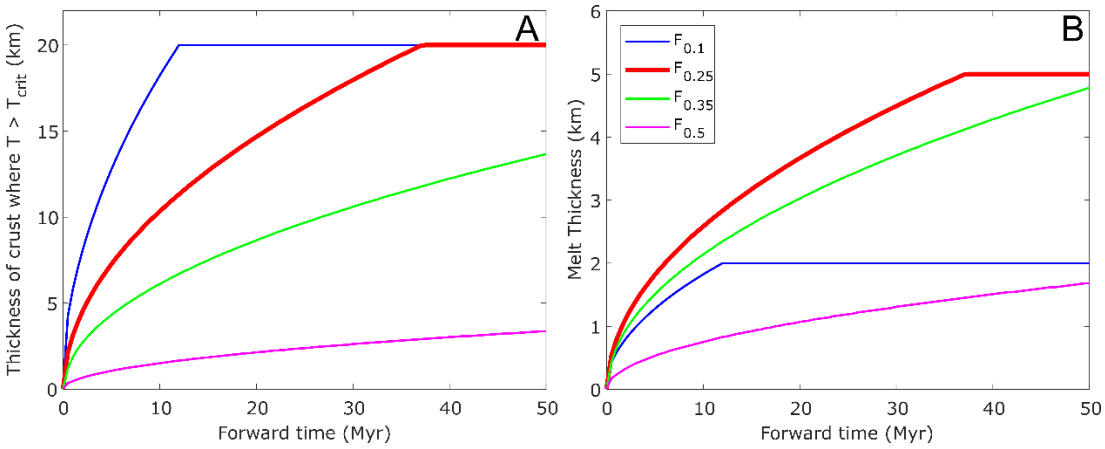

Figure 2.S1. Effects of critical melt fraction (F_{crit}) on melt generation (**A**) Growth of four thermal boundary thicknesses corresponding to F_{crit} = 0.1, F_{crit} = 0.25, F_{crit} = 0.35 and F_{crit} = 0.5. Temperatures corresponding to the selected melt fractions are calculated based on MELTS with a global average lower crust composition (Rudnick and Gao, 2003). (**B**) Cumulative melt thicknesses through time.

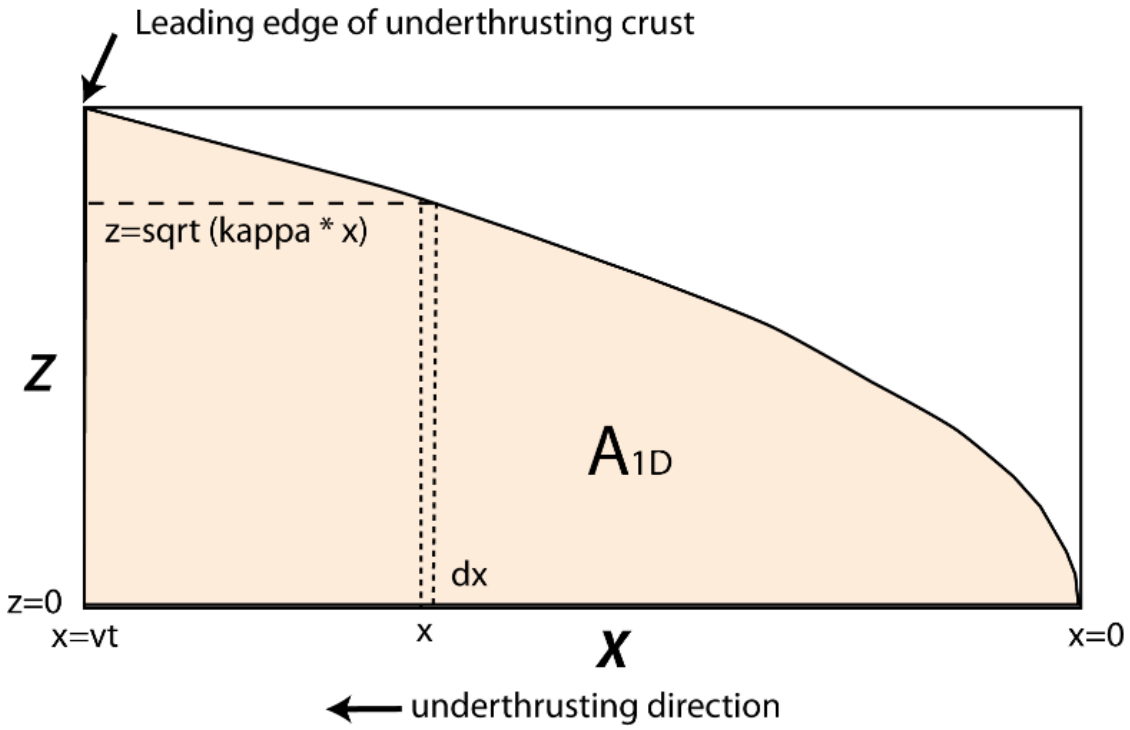

Figure 2.S2. Illustration of melt area with only vertical heat diffusion. Kappa is the thermal diffusivity.

CHAPTER 3: Crustal tilting and differential exhumation of Gangdese Batholith in southern Tibet revealed by bedrock pressures

Wenrong Cao[1], Jiaming Yang[1], Andrew V. Zuza[2], Wei-Qiang Ji[3], Xu-Xuan Ma[4], Xu Chu[5], Quentin P. Burgess[1]

[1]Department of Geological Sciences and Engineering, University of Nevada, Reno, MS-172, 1664 N. Virginia St., Reno, NV 89557, United States of America.

[2]Nevada Bureau of Mines and Geology, University of Nevada, Reno, MS-178, 1664 N. Virginia St., Reno, NV 89557, United States of America

[3]State Key Laboratory of Lithospheric Evolution, Institute of Geology and Geophysics, Chinese Academy of Sciences, P.O. Box 9825, Beijing 100029, China

[4]Key Laboratory of Deep-Earth Dynamics of Ministry of Natural Resources, Institute of Geology, Chinese Academy of Geological Sciences, Beijing 100037, China

[5]Department of Earth Sciences, University of Toronto, 22 Russell Street, Toronto, Ontario, M5S3B1, Canada

This chapter has already been published and is included as part of this dissertation **with permission from Earth and Planetary Science Letters, 543 (2020) 116347, doi.org/10.1016/j.epsl.2020.116347,**

ABSTRACT

The exhumation history of the Gangdese Batholith, southern Tibet, bears on how magmatism and tectonism interact with surface processes in a long-lived magmatic orogen. In this study, we applied Al-in-hornblende barometry across the eastern Gangdese Batholith to obtain pluton emplacement pressures. Our results, together with existing bedrock pressure data, reveal the regional paleo-depth pattern across the Gangdese Batholith. The western part of the batholith near Lhasa exposes plutons emplaced at 1-2 kbar whereas the eastern part, near Nyingchi, exposes crust recording pressures typically of 6-12 kbar. We coupled pressure data with new and published U-Pb zircon ages to constrain the exhumation history of the Gangdese Batholith. The results show that since 100 Ma, the upper crust experienced limited exhumation except a pronounced Oligocene-Miocene pulse. In contrast, the middle-lower crust experienced a complex exhumation and burial history, reflecting major tectonic events including the development of continental arc and continent-continent collision. Since ca. 10 Ma, the eastern Nyingchi domain experienced fast exhumation (total exhumation > 40 km), which was related to the exhumation of the Eastern Himalayan Syntaxis. The Lhasa domain experienced comparatively limited exhumation (total exhumation < 10 km). Such dramatic differential exhumation along the E-W direction requires that the Gangdese Batholith was tilted to present-day exposure levels. Our study shows that during the evolution of a magmatic orogen, the upper and middle-lower crust can behave differently, and the exhumation history reflects integrated tectonic, magmatic, and surface processes. The surface erosion rate estimates can be used to calculate CO_2 consumption and

evaluate the roles of magmatic orogens in the long-term carbon cycle. Given its great exposures of plutonic and metamorphic rocks across a relatively continuous crustal section, the Gangdese Batholith has great potential to serve as a natural laboratory to understand the structures and evolution of the continental crust.

INTRODUCTION

Tilted orogenic crustal sections are valuable geological windows to understand the vertical gradients of the composition and structures of the orogens (e.g., Ducea et al., 2015). Fundamental to establishing the framework in the vertical dimension is to quantitatively establish the bedrock pressure patterns (paleo-depths). The present-day bedrock pressure patterns also reflect the exhumation, burial, and tilting histories of the crust in response to tectonic and magmatic events (Stüwe and Barr, 1998), as well as the surface processes which alter the geomorphology of metamorphism (Willett, 1999). The Gangdese Batholith in the southern Tibet is the magmatic product that developed in response to the northward subduction of the Neo-Tethyan plate beneath the Eurasian plate, and the subsequent India-Eurasia collision (e.g., Yin and Harrison, 2000; Kapp et al., 2007; Zhu et al., 2015; Zuza et al., 2018). Although significant research has focused on the composition and temporal history of the batholith (e.g., Ji et al., 2014; Zhu et al., 2015), the regional bedrock pressure pattern is poorly constrained compared to other well-studied magmatic crustal sections such as the Sierra Nevada Arc in California (Chapman et al., 2012) and the Kohistan Arc in Pakistan (Jagoutz, 2014). Furthermore, existing exhumation/cooling data from the Gangdese Batholith is confined mostly to the Oligocene-Miocene-to-present timeframe (e.g., Harrison et al., 2000; Tremblay et al.,

2015). Little is known about the exhumation of the Gangdese Batholith from the Cretaceous to Paleocene and how rocks of different depths exhume over a ~100 Myr timescale. Finally, there is a recent focus on the role of magmatic orogens as CO_2 sources due to magmatic and metamorphic degassing (e.g., Lee et al., 2012), but the role of the magmatic orogens as CO_2 sinks due to silicate weathering (Jiang and Lee, 2019) is less well established. One of the reasons hampering the CO_2 consumption calculation is that the estimation of the flux of silicate weathering requires a robust understanding of surface erosion rates over geologic timescales, which are poorly resolved for many magmatic orogens including the Gangdese. To address the above challenges, we integrated newly obtained pluton emplacement pressure data with published bedrock pressures to reveal the regional paleo-depth pattern across the Gangdese Batholith and constructed an exhumation history of the Gangdese Batholith that extends back to the Late Cretaceous.

GANGDESE BATHOLITH

The ~1500-km-long Gangdese Batholith in southern Tibet is the central segment of the granitoid belts of "Trans-Himalayan Batholith" along the southern margin of the Eurasian plate (**Figure. 3.1**). Mesozoic-early Cenozoic subduction of the Neo-Tethyan plate accommodated the convergence between the Indian and Eurasian plates until their collision at ca. 60-55 Ma (e.g., Yin and Harrison, 2000; DeCelles et al., 2014). This collision is marked by the Indus-Yarlung suture zone (IYSZ), and intrusions related to the subduction and collision are distributed across the batholith largely to the north of the suture (Zhu et al., 2015). Magmatism of the Gangdese Batholith spans from Middle-Late Triassic to late Miocene, and U/Pb zircon ages display temporal peaks (High-Flux

Events, HFE, or flare-ups) around 90-100 Ma, 50-60 Ma, and 10-20 Ma (Chapman and Kapp, 2017; Ji et al., 2014; Zhu et al., 2015). The 90-100 Ma peak is associated with continental arc magmatism, and the 50-60 Ma peak is attributed to the breakoff of the subducted Neo-Tethyan plate after the initial collision (e.g., Zhu et al., 2015) or arc root foundering (Kapp et al., 2007). The 10-20 Ma peak may represent delamination of the Asian mantle and crustal extension (e.g., Chung, 2009).

GEOLOGY OF THE STUDY AREA

The study area is a ~400-km-long, ~40-km-wide E-W corridor from west of Lhasa (90°E) to east of Nyingchi (95°E) (**Figure. 3.2**). Existing U-Pb zircon ages from the study are show peaks at ca. 90 Ma, 50 Ma, and 15 Ma mimicking the age pattern of the entire Gangdese Batholith **(Figure. 3.3A**).

The stratigraphy of the study area includes the following units, in order from oldest to youngest respectively: (1) reworked mid-Proterozoic and Cambrian crystalline basement, separated with Paleozoic-Triassic marine clastic rocks and limestone by fault contacts (Yin et al., 1988); (2) Triassic-Jurassic volcanics, Upper Jurassic-Lower Cretaceous fluvial, and marginal marine sandstone, shale, and flysch, mid-Cretaceous shallow marine limestone, and Upper Cretaceous fluvial red beds (e.g., Yin, 1988); (3) Paleocene-Eocene volcanics of the Linzizong Formation, made up of ~3500 m of volcanic strata of andesitic lava, dacitic to rhyolitic tuffs that have been dated between 69-50 Ma (He et al., 2007; Zhu et al., 2015); and (4) locally exposed Miocene sandstone

and conglomerate related to the development of regional thrust faults (Yin et al., 1994) and extensional basins (DeCelles et al. 2011).

The exposure level of crustal rocks deepens from west to east as evidenced by an increase in metamorphic grade (**Figure. 3.4A**). Supracrustal rocks, including the Linzizong volcanics, upper Mesozoic sedimentary strata, and porphyritic plutons, are exposed around Lhasa (90.5-92°E) (**Figure 3.5A**, **B**). These volcanic-sedimentary rocks are weakly to non-metamorphosed. Greenschist facies slatey-phyllitic foliation are commonly found in the Mesozoic strata. In contrast, rocks of middle-lower crustal levels are exposed in the east near Nyingchi (93.5-95°E). These rocks include plutons containing magmatic epidote that record intense magmatic-ductile deformation, and migmatitic gneiss (**Figure 3.5C**, **D**). To the east of Nyingchi, and to the south of the Indus-Yarlung suture zone, the Eastern Himalayan Syntaxis (EHS) represents an exhumed highly-strained lower crust of typical pressures of 5-14 kbar (e.g., Ding et al., 2001; Booth et al., 2009).

Most previous research of the exhumation history of Gangdese Batholith in southern Tibet tracked the Oligocene-Miocene cooling history via medium to low-temperature thermochronology, including multi-diffusion domain (MDD) modeling of K-feldspar, biotite and hornblende $^{40}Ar/^{39}Ar$ ages, and (U-Th)/He and fission track dating of apatite and zircon (e.g., Harrison et al., 2000; Dai et al, 2013; Tremblay et al., 2015) (**Figure 3.3B**). Three cooling events have been interpreted to reflect the initial continental collision (e.g., Dai et al., 2013) and conductive cooling of Gangdese plutons around 55 Ma, activation of Gangdese Thrust and Great Counter Thrust during 28-15 Ma (e.g., Harrison et al., 2000; Laskowski et al., 2018), and exhumation of the Eastern Himalayan

Syntaxis and normal faulting since ca. 10 Ma (e.g., Ding et al., 2001; Zeitler et al., 2014; Kapp et al., 2005). Little is known about any earlier Cretaceous to Eocene exhumation. The amount of the exhumation constrained by medium to low-T thermochronology is also typically limited to <10 km due to the lower closure temperatures of the thermochronometers (< 200-400 ℃) and is subjected to the uncertainty of varying geothermal gradients (e.g., Reiners and Brandon, 2006).

Another useful regional marker of exhumation is the Oligocene-Middle Miocene copper-porphyry deposits that are scattered along the southern margin of the Lhasa terrane from 88ºE to 93ºE (Yang et al., 2016) (**Figure 3.2**, **Figure 3.4A**). Copper-porphyry deposits are known to form at a shallow depths (1-5 km with average 2km) (Yanites and Kesler, 2015) and therefore their exposure at the surface requires limited exhumation <5 km. The preservation of the Linzizong Formation also suggests that the overall limited exhumation of the upper crust to the west of 93°E since 69-50 Ma (**Figure 3.2**, **Figure 3.4A**).

APPROACH

To obtain estimates of the paleo-depth of the Gangdese Batholith, we collected granitoid samples for Al-in-hornblende barometry along the highway from Lhasa to Nyingchi, immediately north of the Indus-Yarlung suture (**Figure 3.2**, **Table 3.1**). We used the Tibetan Magmatism Database (Chapman and Kapp, 2017) as a guide. Samples for U-Pb zircon geochronology were also collected from plutons of unknown age. The elevation difference among the samples is less than 2 km (minimum 2930 m, maximum

4520 m). We also compiled existing bedrock pressures from the literature (**Figure 3.2**, **Figure 3.4B**). Metamorphic pressures were obtained from mineral assemblages and metamorphic barometers. Ages associated with the metamorphic pressures were constrained from metamorphic monazite and overgrowth rim of zircon. Existing pluton emplacement pressures have also been compiled into the database. The compiled bedrock pressure data can be found in the Supplementary Materials.

Exhumation or burial of a block of crust can be obtained by calculating the pressure difference between adjacent bedrocks of different ages. Exhumation/burial rate is calculated by dividing the pressure difference by the difference of ages associated with the pressures (**Figure 3.6A**). This approach assumes that the relative position of the existing plutons or metamorphic host rocks remains unchanged although they could move vertically together during a younger exhumation or burial event. We will further justify this approach using Gangdese geology in Section 7.3.1. Ideally, these pressure-age data should be from one locality. Due to the spatial distribution of available pressure-age data, the pressure-age data was binned into five 50-100 km-sized orogen-parallel sectors: from west to east, Lhasa, Zedong, Jiacha, Wolong, and Nyingchi (**Figure 3.2**). We argue that at the 10^3 km orogen-parallel scale, regional exhumation patterns should be approximately consistent for a region of 10^1-10^2 km. In other words, within a sector of 50-100 km size, the crust exhumes similarly. Examples of consistent exhumation patterns across regions of 10^1-10^2 km size include the Eastern Himalayan Syntaxis (Zeitler et al., 2014) and the southern Sierra Nevada (Chapman et al., 2012). Compared to the medium to low-temperature thermochronology, using bedrock pressures to track exhumation has the following advantages: (1) emplacement pressure is difficult to be reset; (2) U-Pb

zircon age associated with the emplacement pressure is unambiguous; (3) pressure can be directly translated to depth, and no assumption of geothermal gradient is needed; and (4) the broad range of crystallization ages of Gangdese plutons allows for tracking the exhumation back to Late Cretaceous.

ANALYTICAL METHODS

Al-in-hornblende barometry

The Al-in-hornblende (Al-in-Hbl) barometry has been widely used to constrain the emplacement pressure of calc-alkaline, felsic-intermediate plutons typical for arcs (e.g., Hammerstrom and Zen, 1986; Ague and Brandon, 1992; Jagoutz, 2014). The requisite mineral assemblage is needed to ensure the barometry work properly (e.g., Anderson and Smith, 1995). The mineral assemblage we used here is quartz+ plagioclase+ K-feldspar+ biotite+ hornblende+ magnetite+ titanite or ilmenite+ melt (assume originally present) corresponding to a system consisting of SiO_2-Al_2O_3-TiO_2-Fe_2O_3-FeO-MgO-CaO-Na_2O-K_2O. Using this mineral assemblage, we filtered out samples that did not meet the criterion. Petrographric descriptions and photomicrographs from each sample are presented in the Supplementary Materials.

We used two different calibrations to calculate the emplacement pressure: (1) the classic temperature-corrected calibration using plagioclase thermometry (Anderson and Smith, 1995; Holland and Blundy, 1994), and (2) a recent calibration that is better for low-P samples (Mutch et al., 2016). Independent constraints for pluton emplacement pressures include the appearance of magmatic epidote in plutons of medium-high

emplacement pressures (Zen and Hammarstrom, 1984, Table 1) and the regional increase of metamorphic grade in the host rocks (**Figure 3.4**).

Electron probe microanalysis (EPMA) was carried out at the Department of Earth, Environmental and Planetary Sciences at Rice University. To obtain the temperature of the solidus using the plagioclase thermometer (Holland and Blundy, 1994), we targeted five pairs of coexisting hornblende and plagioclase in each sample. At each pair, major element compositions of plagioclase and hornblende were made at 10 adjacent points (5 on hornblende, 5 on plagioclase). Inclusions, cracks, and retrograde rims were avoided. Hornblende and plagioclase formulas were then calculated based on 23 oxygens and 5 cations, respectively. Pressure and temperature were solved together using the Excel spreadsheet prepared by J. L. Anderson. Technical details of the EPMA analysis and pressure calculation spreadsheet are presented in the Supplementary Materials.

U/Pb zircon geochronology

Samples of plutons were processed for zircon separates following standard techniques involving crushing, magnetic separation, and heavy liquids. U-Pb geochronology of zircons was conducted by laser ablation inductively coupled plasma mass spectrometry (LA-ICP-MS) at the Arizona LaserChron Center. Cathodoluminescene (CL) images were used as a guide to avoid inclusions and cracks. Data reduction was performed with an in-house routine. We used TuffZirc algorithm in ISOPLOT to calculate the ages of plutonic samples. TuffZirc algorithm yields a more reliable igneous age by excluding ages of older xenocrysts or cores via a statically robust method rather than subjective decision

(Ludwig and Mundil, 2002). Technical details of the LA-ICP-MS analysis are presented in the Supplementary Materials.

RESULTS

Results of Al-in-hornblende barometry

Table 3.1 summarizes the 18 new pluton-emplacement pressures from the Al-in-Hbl barometry and solidus-temperatures derived from the plagioclase thermometry. Pressures show a variation from ~1 kbar to 8 kbar among samples and solidus temperatures show a range of 629-797 ℃. When applying Anderson and Smith (1995)'s barometry, we found that in 12 out 18 samples, the hornblende compositions have either $Fe^{3+}/(Fe^{2+}+Fe^{3+})$ <0.2 or $Fe^{\#}$<0.4 that are not fully in the recommended ranges. For those samples, we present the pressures in parentheses. These pressures are still considered to be valid since the samples pass the $Fe^{\#}$<0.65 and T<800 ℃ filters suggested by Putirka (2016). Pressures from Mutch et al. (2016)'s barometry were calculated for all samples. Mutch et al. (2016)'s calibration is not sensitive to temperature as long as the solidus is close to 725±75 ℃ (Mutch et al., 2016). The calibration uncertainty of Anderson and Smith (1995)'s barometry is ±0.6 kbar and the relative uncertainty of Mutch et al. (2016)'s barometry is 16%. Since these uncertainties obtained via barometry calibration cannot be used for natural samples, we assumed a standard error of 1 kbar to all samples instead. Within the uncertainties, pressures from Anderson and Smith (1995)'s and Mutch et al. (2016)'s calibrations overlap each other validating the results (**Figure 3.S1**). The final pressure of each sample is calculated using the mean value of the two

calibrations. The depth of pluton emplacement is calculated using a characteristic crustal density of 2800 kg/m^3. Full EPMA analytical data tables are presented in the Supplementary Materials.

Results of geochronology

Newly obtained U-Pb zircon ages from seven granitoid samples are reported in **Table 3.1.** Sample 7-6-1 is dated to 50.5±0.7 Ma (weighted mean age, 95% confidence, same for the rest samples) based on a coherent age group of 29 zircons. Sample XCT55 is dated to 177.5±1.1 Ma based on 29 zircons. Sample XCT56 is dated to 196.1±1.2 Ma based on 17 zircons. Sample XCT58 is dated to 46.4±0.4 Ma based on 19 zircons. Sample 10-8 is dated to 91.2 ±0.5 Ma based on 30 zircons. Sample 11-10 is dated to 63.8 ±0.5 Ma based on 27 zircons. Sample 12-14 is dated to 45.4 ±0.4 Ma based on 32 zircons. Full ICPMS analytical data tables and TuffZirc age plots are presented in the Supplementary Materials.

DISCUSSION

Tilted crustal section of Gangdese Batholith

Figure 3.4B and **3.4C** shows the bedrock pressure data across the Gangdese Batholith from 90ºE to 96ºE. Near Lhasa (90.5ºE to 92ºE, Lhasa and Zedong sectors), the pressures have a relatively narrow range of 1 to 3 kbar. These pressures are consistent with the non-metamorphosed or greenschist-facies supracrustal rocks found in that area (**Figure 3.4A**). To the east, pressure gradually increases from ~3 kbar to ~11 kbar between 92.5ºE to 93.5ºE (Jiacha and Wolong sectors). Pressures at the Nyingchi sector

(~ 94.5ºE), where granulite-facies rocks are exposed (Zhang et al., 2010), are typically >10 kbar with the highest pressure reaching 12.3 kbar. Further east of the Nyingchi (94.5ºE to 96ºE), pressures gradually shallow to 2.8 kbar except a metamorphic rock of 10.8 kbar exists at 95.2 ºE (Booth et al., 2009). At some places, juxtaposition of rocks of different paleo-depths and ages suggest significant vertical motion has occurred (see Section 7.3.2 for detailed discussion).

Longitudinal variations of pressure estimate and metamorphic grade show that the Gangdese bedrock pressure overall increases from west (~90 ºE) to east (~94.5 ºE). We interpret that the Gangdese Batholith was broadly tilted westward across from the Lhasa to Nyingchi domains. To the east of Nyingchi, the crust was tilted eastward around the EHS.

The establishment of the paleo-depth of the Gangdese Batholith allows us to further address two topics. First, we can couple depth and age data to track the exhumation/burial paths. This addresses the juxtaposition of rocks of different paleo-depths. Second, we can constrain the differential exhumation that occurred along the orogen-parallel direction, which eventually results in the first-order longitude-pressure pattern observed at the surface today.

Kinematic model for exhumation during thickening and erosion

Here we present a one-dimensional kinematic model linking exhumation and burial processes in an orogen subject to simultaneous crustal thickening and surface erosion. This model provides insights to explain the first-order exhumation/burial pattern for the

Gangdese Batholith discussed in Section 7.3. **Figure 3.6B** illustrates the kinematics of a crustal column undergoing thickening or surface erosion (*z*-axis is positive downward, origin at surface). If we assume the thickening strain rate $\dot{\varepsilon_z}$ is homogenous across depth, the exhumation or burial of a parcel of rock at time t depends on the competition between thickening-induced burial ($\dot{\varepsilon_z} \cdot z$) and surface erosion ($E$) (Eq. 1) (Stüwe and Barr, 1998).

$$v_e(t) = \frac{dz}{dt} = \dot{\varepsilon_z} \cdot z(t) - E \quad (1)$$

where v_e is the exhumation rate (v_e<0) or burial rate (v_e>0) such that if v_e=0 the rock remains at the same depth ("neutral depth", **Figure 3.6B**), E is the surface erosion rate, and $z(t)$ is the depth of the parcel of the rock relative to the surface at time t. In order to obtain the exhumation/burial paths through time, we integrated the above equation assuming the surface erosion rate is a constant:

$$z(t) = \left(z_0 - \frac{E}{\dot{\varepsilon_z}}\right) \cdot e^{\dot{\varepsilon_z} t} + \frac{E}{\dot{\varepsilon_z}} \quad (2)$$

where z_0 is the initial depth of the rock at time t_0= 0. We understand that surface erosion rate can vary through time controlled by topography and climate parameters. The thickening strain rate could also be time- and depth-dependent in an orogen. The model is kept simple so as to show the relative roles of surface erosion and thickening-induced burial. **Figure 3.7** shows the exhumation/burial paths of parcels of rocks at 10, 20, and 40 km initial depths under different combinations of surface erosion rate and thickening strain rate. When *E*=0, all rocks experience burial; faster thickening strain rate results in faster burial (**Figure 3.7 A1-A3**). Increased erosion rates can result in slower burial, or exhumation (e.g., **Figure 3.7 B1**, **C1**, **D1**). We note that for some combinations of the $\dot{\varepsilon_z}$

and E, the exhumation path for rock at z_0=10 km remains effectively flat, suggesting the thickening-induced burial at 10 km depth is balanced by the surface erosion, resulting in minimal exhumation (**Figure 3.7 B1**, **C2**, **D3**, highlighted by gray boxes). We obtain the following insights from this model:

(1) The upper, middle, and lower crust exhume differently under same surface erosion and tectonic thickening conditions. This is because the thickening-induced burial rate ($\dot{\varepsilon_z} \cdot z$) increases toward depth.

(2) Rock can remain at a constant depth (neutral depth) if the thickening-induced burial balances erosion.

(3) A tradeoff exists between erosion rate and thickening strain rate if we only know the exhumation/burial path at a given depth. A unique combination of erosion rate and thickening strain rate can be constrained if we know exhumation/burial rates of rocks at two different depths.

Exhumation history of Gangdese Batholith based on bedrock pressures

Justification of using bedrock pressures based on Gangdese geology

To track the exhumation history, we binned the bedrock pressures from the Lhasa-Nyingchi transect into five 50-100 km-sized sectors. From west to east, they are Lhasa sector, Zedong sector, Jiacha sector, Wolong sector, and West Nyingchi sector (**Figure 3.2**). Bedrock pressures to the east of Nyingchi are not binned because their pressure-associated ages are not well constrained. As previously mentioned, the assumption of using bedrock pressures to track exhumation is that no younger event

affects the existing relative position between plutons or metamorphic host rocks. We further justify this assumption based on the geology in the study area. First, within each sector, younger shear zones of various dip directions and kinematics are required to juxtapose plutons or metamorphic host rocks of different depths and ages. In reality, only a few north-dipping, south-vergent orogen-parallel thrust faults have been recognized in the Lhasa-Nyingchi section of the Gangdese Batholith (Gangdese thrust, e.g., Yin et al., 1994). Near Zedong, where the 30-20 Ma Gangdese thrust has been mapped (Yin et al., 1994), our pressure data are all located in the upper plate of the thrust faults except one (1.8 kbar, 62 Ma) is located at the lower plate of an inferred fault trace. Even if we exclude this datapoint, the overall exhumation history is unaffected. Second, our pressure data are distributed parallel to the orogen with little room to develop complex orogen-parallel faults in between.

Two young (~8-10 Ma) north-south trending normal faults are near or within the study area: the Nyainqentanglha and Cuona-Woka (Cona-Oiga) faults (**Figure 3.2**). The ~8 Ma Nyainqentanglha fault located to the NW of Lhasa is a SE-dipping normal fault with a vertical throw of 12-15 km (Kapp et al., 2005). All of our pressure data are >70 km southeast of this fault, and more importantly, they are all located on its hanging wall side. Thus, we argue any tectonic exhumation related to the Nyainqentanglha fault does not affect the existing pressure pattern in the study area. The ~10 Ma Cuona-Woka faults located at ~92.3 ºE form a ~10-km-wide rift zone with two bounding normal faults dipping at ~60º (Wu et al., 2008). The vertical throw of the Cuona-Woka faults is poorly documented. Since our data are all outside the rift zone, the Cuona-Woka rift is unlikely to affect the regional pressure pattern in the study area.

The exhumation/burial paths of Gangdese crust

The exhumation/burial paths of the five sectors are shown in **Figure 3C**. Since different longitudinal sectors represent rocks of different paleo-depths, these paths reveal contrasting exhumation/burial histories for rocks of different crustal levels before the tilting occurred. The two west sectors (Lhasa and Zedong), representing the upper crust, show relatively flat paths suggesting the exhumation of the two sectors is limited (~10 km) since Late Cretaceous. In contrast, the two eastern sectors (Wolong and Nyingchi), representing the middle-lower crust, show a complex pattern with multiple burial and exhumation trajectories. Only three samples were collected from the Jiacha sector; therefore its exhumation path is not clear based on the available data. Two pressures associated with Early Jurassic age (177.5 Ma and 196.1 Ma) are not discussed here since we focus on the Gangdese history since 100 Ma. To facilitate discussion, we divide the exhumation history into 4 stages based on the pattern of the exhumation paths and regional geological history.

Stage 1 (100-70 Ma) represents the Late Cretaceous phase of the Gangdese continental arc (**Figure 3.3E**). Samples from the Lhasa sector remain isobaric at 2 kbar (~7-8 km depth) during this stage. In contrast, the Wolong sector shows progressive burial from 20 km to 40 km from ca. 95 Ma to 72 Ma. The average burial rate is about 1 km/Myr (**Figure 3.3C**). Our available data cannot recover its temporal pattern of the deeper Nyingchi sector during this stage, but it probably experienced burial similar to the Wolong sector given the spatial proximity.

The different exhumation-burial paths for the upper and middle crust resemble the simulated exhumation/burial paths shown in **Figure 8A** in which a thickening strain rate of 1.6×10^{-15} s^{-1} and a surface erosion rate of 0.35 km/Myr are applied. Several lines of evidence from other orogens support the proposed strain rate and erosion rate. For example, the thickening strain rate of the Mesozoic Sierra Nevada continental arc is estimated from 10^{-15} s^{-1} to 10^{-16} s^{-1} (Cao et al., 2015). An erosion rate of 0.35 km/Myr is also reasonable for many magmatic orogens, such as the Cretaceous Peninsular Range Batholith, which is constrained to 0.2-1 km/Myr (Jiang and Lee, 2017). Mass balance-isostasy modeling for the Cretaceous central Sierra Nevada suggests a 0.2-0.5 km/Myr surface erosion rate (Cao & Paterson, 2016).

In Late Cretaceous (100-70 Ma), the Gangdese crust experienced thickening as predicted by the simple kinematic model (**Figure 3.8A**, **Figure 3.9A**). The Gangdese arc experienced a magmatic flare-up at 100-90 Ma (Chapman and Kapp, 2017) (**Figure 3.3A**) and a major phase of Late Cretaceous (100-70 Ma) north-south shortening (**Figure 3.3E**) (Kapp et al., 2007). Accordingly, magmatic inflation and contractional deformation probably contributed to the inferred thickening. Similar combined tectonic-magmatic thickening has been proposed for North and South American Cordillera (e.g., Allmendinger et al., 1997; Cao et al., 2015), as well as the Gangdese arc (Zhu et al., 2017; DePaolo et al., 2019). However, the relative contributions of magmatic versus tectonic thickening are unknown.

Stage 2 (70-50 Ma) represents a transition phase from continental arc to continental collision that occurred around 55-60 Ma (e.g., DeCelles et al., 2014, **Figure**

3.3E). For the upper crust, the exhumation paths of the Lhasa and Zedong Sectors remains relatively flat (**Figure 3.3C**).

A second magmatic flare-up peaked at ca. 55 Ma, and evidence for major tectonic deformation in the study area is lacking during this period except a brief shortening event in the retro-arc (Kapp et al., 2007, **Figure 3.3E**). For the upper crust, the relative flat exhumation path may suggest that the surface erosion was still more or less balanced by the magmatic thickening and the deposition of the Linzizong volcanics.

Although the number of data points for Stage 2 are insufficient to make meaningful interpretations for middle-lower crust, several dynamic processes may compete with one another during this transition period and complicate the behavior of the middle-lower crust. Proposed processes include arc-root founding at 69-50 Ma (Kapp et al., 2007), slab breakoff and subsequent upwelling of the asthenospheric mantle at 53 Ma (Zhu et al., 2015), or Gangdese lithosphere delamination at 68-60 Ma (Ji et al., 2014). More data is needed to constrain the behavior of the middle-lower crust.

Stage 3 (50-30 Ma) represents the early phase of continental collision. The upper crust exhumation path of the Zedong sector slightly goes up from 10 km to ~3 km corresponding to an average exhumation rate of 0.35 km/Myr. For the middle-lower crust, the Nyingchi sector experienced burial from 30 km to ~45 km, corresponding to an average burial rate of 0.75 km/Myr (**Figure 3.3C**). Referring to our kinematic model, we find that when the thickening strain rate is 1.4×10^{-15} s^{-1}, and surface erosion rate is 0.65 km/Myr, the simulated exhumation/burial paths for 10 km and 30 km deep rocks mimic the exhumation/burial paths in Stage 3 (**Figure 3.8B**).

Crustal thickening during this stage was mainly caused by magmatic inflation during the later stage of the second flare-up (50-60 Ma) and possibly some syn-collisional shortening starting at ~42 Ma evidenced by the accelerated cooling in the retro-arc Linzhou area (He et al., 2007) (**Figure 3.3E**; **Figure 3.9B**). Using La/Yb ratios from the Gangdese plutons to track the crustal thickness, Zhu et al. (2017) shows that the crust thickened between 50 and 30 Ma (**Figure 3.3D**). DePaolo et al. (2019) also suggested major crustal thickening (>30 km thickening) took place between 45 and 32 Ma to the north of the suture near Lhasa based on Nd isotopes and La/Yb data.

The middle-lower crust has thus experienced two burial processes, one in Late Cretaceous related to the continental arc, and the other one in Eocene related to the collision (**Figure 3.3C**). Such burial processes have been recognized by two-stage granulite facies metamorphism by Zhang et al. (2010) in the high-grade terrane near Nyingchi. The collision-related burial is also shown by the P-T-t path of the high-grade rocks from Nyingchi area (Tian et al., 2020).

Stage 4 (30-0 Ma) represents a phase of continued collisional plate convergence and crustal tilting due to differential exhumation along the Lhasa-Nyingchi section (**Figure 3.3C**, **Figure 3.9C**). Although bedrock pressure data is not available during this stage, compiled low-temperature thermochronological data in Lhasa-Zedong area reveal a major cooling event from 25 to 10 Ma (**Figure 3.3B**). Since the closure temperature of the zircon fission track system is ~250 ℃ (e.g., Reiners and Brandon, 2006), the amount of exhumation constrained by the low-temperature thermochronological data is about 6-8 km assuming a 40-30 ℃/km geothermal gradient. This corresponds to an average exhumation of about 0.4-0.5 km/Myr during 25-10 Ma. If the cooling was more

temporally concentrated within 16-12 Ma (Tremblay et al., 2015), the exhumation rate could have been greater at 1.5-2 km/Myr. After 10 Ma, surface erosion in the Lhasa and Zedong Sectors was minimal, <1 km (<0.1 km/Myr) (Tremblay et al., 2015). This interpretation is further supported by the preservation of 20-10 Ma copper porphyry deposits in Lhasa-Zedong area (**Figure 3.3C**).

In contrast, the Nyingchi sector had to have exhumed from at least 45 km depth to the surface during this stage, which corresponds to an average exhumation rate of 1.5 km/Myr. The exact exhumation paths of the Nyingchi sectors are unknown. Given the spatial proximity of the Nyingchi sector to the Eastern Himalayan Syntaxis, we speculate that the Nyingchi sector exhumed together with the Eastern Himalayan Syntaxis since ca. 10 Ma (Ding et al., 2001) with an exhumation rates of ~5-10 km/Myr since ca.10-5 Ma (e.g., Booth et al., 2009; Zeitler et al., 2014) (**Figure 3.3C**).

During Stage 4, north-south contractional deformation resumed in the southern Lhasa terrane represented by the 27-23 Ma Gangdese Thrust and Late Oligocene-Early Miocene Great Counter Thrust (Yin and Harrison, 2000; Laskowski et al., 2018, **Figure 3.3E)**. This phase of contraction resulted in ~20% shortening strain of the Linzizong volcanics during 30-10 Ma (Pan and Kidd., 1999). The activation of the Gangdese Thrust and Great Counter Thrust could be responsible for the coeval major cooling events (Laskowski et al., 2018). The shortening-related crustal thickening resulted in isostatic elevation increase near the Lhasa-Zedong area, but the elevation increase does not induce a fast erosion probably because the mountain building in the Himalaya region shifted the erosional front southwards after 10 Ma (Tremblay et al., 2015). In contrast to the minimal

exhumation in the Lhasa and Zedong sectors, the fast exhumation of the Nyingchi sector is probably related to the fast and focused erosion-driven exhumation of the

Eastern Himalayan Syntaxis (e.g. Zeitler et al., 2014). We suggest that crustal tilting from Lhasa-Nyingchi section occurred during this stage due to the dramatic exhumation difference between the Lhasa and Nyingchi areas (**Figure 3.9C**).

Comparison to La/Yb proxy for crustal thickness

Whole-rock Sr/Y and $(La/Yb)_n$ have been recently used as proxies for crustal thickness (e.g., Profeta et al., 2015). Zhu et al. (2017) used whole-rock $(La/Yb)_n$ from Gangdese plutons to track crustal thickness in the southern margin of the Lhasa terrane. To compare their results to the bedrock pressures in the study area, we filtered Zhu et al. (2017) data using the spatial range of the study area (90-95°E, 29-30°N) (**Figure 3.3D**).

For Stage 1, most of the $(La/Yb)_n$ data cannot be used to track crustal thickness since the plutons are likely originated from the oceanic slab melts (Zhu et al., 2017). Thus, the comparison between the $(La/Yb)_n$ -derived crustal thickness and the burial paths from the bedrock pressures cannot be made.

For Stage 2, the crustal thickness derived from $(La/Yb)_n$ shows a scattered distribution while the bedrock pressure data are too limited to make robust interpretations.

For Stage 3, the $(La/Yb)_n$-derived crustal thickness increased from 30-50 km to ~80 km, consistent with the burial path of the Niyingchi sector. If we assume the crustal thickness was 40 km at 50 Ma, with the proposed thickening strain rate (1.4×10^{-15} s^{-1})

and surface erosion rate (0.65 km/Myr), the crustal thickness could achieve ~80 km by 30 Ma (**Figure 3.8B**).

For Stage 4, the $(La/Yb)_n$-derived crustal thickness shows a similar value to the present-day thickness (~70 km). The bedrock pressure does not cover this stage. Since the EHS has been exhumed for > 30-40 km since ~10 Ma (Zeitler et al., 2014), it may require a lower crustal flow to compensate the exhumation/thinning of the EHS crust and its vicinity (e.g., Zeitler et al., 2014).

In summary, we argue that the bedrock pressure is supplementary to the $(La/Yb)_n$-derived crustal thickness, and they can be used together to test tectonic models. Two datasets are consistent with each other during the early phase of continental collision (50-30 Ma). For other stages, due to the incompleteness of datasets, either $(La/Yb)_n$ or bedrock pressure, the comparison cannot be fully made. More studies are needed to fill the gaps.

OUTSTANDING QUESTIONS

Bedrock pressure samples were mostly obtained along the Indus-Yarlung suture in this study, and an E-W bedrock pressure gradient is revealed. What is the regional pattern of bedrock pressures outside the study area, especially further towards the west and in the suture-perpendicular direction? Is the batholith also tilted in the N-S direction due to the Oligocene-Miocene structures that are localized in the southern part of the batholith (e.g., the Great Counter Thrust and Gangdese Thrust)? Do other segments of the Gangdese Batholith also show the same two phases of burial related to the continental arc and

continental collision? More bedrock pressures are needed to answer these questions. Eventually, with enough data, once can produce a bedrock pressure map of high spatial resolution similar to the one for the Sierra Nevada Batholith (e.g., Chapman et al., 2012). Such regional pressure patterns can be further coupled with the geochronology, geochemistry, isotopes, and magmatic fabrics to investigate depth-dependent processes associated with the arc magmatism and continental collision (e.g., Jagoutz, 2014).

The tilting mechanisms of the Batholith are not discussed in this study. Several possible end-members could be (1) rigid-body-like titling across a large (~400 km) area, (2) tilting accommodated by multiple orogen-perpendicular shear zones, and (3) along-strike crustal flow related to the exhumation of the EHS. Are there unmapped orogen-perpendicular shear zones in the study area permitting east-side-up kinematics? How does the mechanical coupling between the fast-exhuming EHS and the Gangdese crust affect the degree of the tilting? Field studies should be combined with 2D and 3D geodynamic modeling to answer these questions.

Finally, what is the CO_2 consumption related to the erosion and the silicate weathering of the Gangdese Batholith, especially during the continental arc stage and during the last ~10 Myr when the batholith was tilted? For example, one could estimate the amount of crustal materials eroded from the Gangdese Batholith since 10 Ma by integrating the area above the bedrock pressures (**Figure 3.4B**). Such estimates can provide a basis to investigate the roles of magmatic orogens in the long-term carbon budget by evaluating the CO_2 outgassing versus the CO_2 consumption through erosion-chemical weathering processes (Jiang and Lee, 2019).

CONCLUSION

Longitudinal bedrock pressure pattern has been revealed in the Gangdese Batholith from Lhasa to Nyingchi. Bedrock pressure increase from 1-2 kbar near Lhasa to 6-12 kbar near Nyingchi. Upper and middle-lower crust rocks experienced differential exhumation or burial processes since Late Cretaceous. Dramatic differential exhumation along the E-W direction occurred since ca. 10 Ma, which tilted the crust to the present-day exposure levels. The exhumation-burial history of the Gangdese Batholith reflects integrated tectonic, magmatic, and surface processes.

ACKNOWLEDGEMENTS

This study is supported by the National Science Foundation of China (41888101), the second Tibetan Plateau Scientific Expedition and Research Program (STEP) Grant (2019QZKK0802), National Science Foundation (NSF) grants (EAR-1830139; EAR-1914501), and Chinese Academy of Sciences State Key Laboratory of Lithospheric Evolution grant (SKL-Z201706). NSF grant EAR-1649254 is acknowledged for the support of the Arizona LaserChron Center. We thank Gelu Costin at Rice EPMA lab for helping with the analysis, UNR undergraduate student Anthony Florez for map digitalization using QGIS, and Hao Zhang, Ming Tang for field assistance. John McCormack is thanked for the help with mineral identification. We appreciate conversations and feedback at the NSF-supported (EAR-1912713) Himalayan-Karakoram-Tibet 2019 meeting in Bozeman, MT. We thank Paul Kapp, Andrew K. Laskowski, Keith Putirka, and an anonymous reviewer for their critical comments which

helped to improve the quality of the manuscript. Editor An Yin is thanked for handling the manuscript.

APPENDIX 3.1: Technical details of LA-ICP-MS analysis

Zircon separates from samples are incorporated into a 1" epoxy mount together with fragments or loose grains of Sri Lanka, FC-1, and R33 zircon crystals that are used as primary standards. The mounts are sanded down to a depth of ~20 microns, polished, imaged, and cleaned prior to isotopic analysis. U-Pb geochronology of zircons is conducted by laser ablation inductively coupled plasma mass spectrometry (LA-ICPMS) at the Arizona LaserChron Center (Gehrels et al., 2006, 2008; Gehrels and Pecha, 2014). The analyses involve ablation of zircon with a Photon Machines Analyte G2 excimer laser equipped with HelEx ablation cell using a spot diameter of 20 microns. The ablated material is carried in helium into the plasma source of an Element2 HR ICPMS, which sequences rapidly through U, Th, and Pb isotopes. Signal intensities are measured with an SEM that operates in pulse counting mode for signals less than 50K cps, in both pulse-counting and analog mode for signals between 50K and 5M cps, and in analog mode above 5M cps. The calibration between pulse-counting and analog signals is determined line-by-line for signals between 50K and 5M cps, and is applied to >5M cps signals. Four intensities are determined and averaged for each isotope, with dwell times of 0.0052 sec for 202, 0.0075 sec for 204, 0.0202 sec for 206, 0.0284 sec for 207, 0.0026 sec for 208, 0.0026 sec for 232, and 0.0104 sec for 238. With the laser set an energy density of ~5 J/cm^2, a repetition rate of 8 hz, and an ablation time of 10 seconds, ablation pits are ~12 microns in depth. Sensitivity with these settings is approximately ~5,000 cps/ppm. Each analysis consists of 5 sec on peaks with the laser off (for backgrounds), 10 sec with the laser firing (for peak intensities), and a 20 second delay to purge the previous sample and

save files. More information can be found at Arizona LaserChron Center's website: https://sites.google.com/a/laserchron.org/laserchron.

We applied the following filters before we calculate the crystallization ages: (1) Individual analyses with U/Th>10 are excluded since they are likely affected by metamorphic processes (e.g., Yakymchuk et al., 2018); (2) Since all dated samples are younger than 400 Ma, analysis whose concordance (ratio of $^{206}Pb/^{238}U$ and $^{207}Pb/^{235}U$ ages) is smaller than 85% or its reverse concordance (ratio of $^{206}Pb/^{238}U$ and $^{207}Pb/^{235}U$ ages minus 1) is larger than 10% is excluded.

APPENDIX 3.2: Technical details of EPMA analysis

Samples are prepared as polished, epoxy mounted thin sections with a ~20 nm carbon coating. Electron probe microanalysis (EPMA) was carried out with a JEOL JXA8530F Hyperprobe at the Department of Earth, Environmental and Planetary Sciences at Rice University, using 5 crystal wavelength-dispersive spectrometers. The field-emission gun was set at a 15 kV accelerating voltage, with a beam current of 20 nA. For hornblende analyses, the electron beam size was focused to a 300 nm spot while plagioclase analyses utilized a larger, 20 μm spot size to minimize potential alkali migration during analysis. 10 major element compositions (Na, Si, K, Ca, Fe, Ti, Al, Mg, Cr, Mn) of plagioclase and hornblende were collected. Counting times were 10 s on peak and 5 s on lower and upper bounds. Natural and synthetic mineral standards were used for measuring the characteristic X-rays and ZAF matrix correction procedure was applied for quantification.

REFERENCES

Ague, J.J. and Brandon, M.T., 1992. Tilt and northward offset of Cordilleran batholiths resolved using igneous barometry. Nature Publishing Group 360, 146–149. doi:10.1038/360146a0

Allmendinger, R.W., Jordan, T.E., Kay, S.M. and Isacks, B.L., 1997. The evolution of the Altiplano-Puna plateau of the Central Andes. Annual review of earth and planetary sciences, 25(1), pp.139-174.

Anderson, J.L. and Smith, D.R., 1995. The effects of temperature and fO_2 on the Al-in-hornblende barometer. American Mineralogist, 80(5-6), pp.549-559.

Booth, A.L., Chamberlain, C.P., Kidd, W.S.F., Zeitler, P.K., 2009. Constraints on the metamorphic evolution of the eastern Himalayan syntaxis from geochronologic and petrologic studies of Namche Barwa. Geological Society of America Bulletin 121, 385–407. doi:10.1130/B26041.1

Cao, W., Paterson, S., Memeti, V., Mundil, R., Anderson, J.L., Schmidt, K., 2015. Tracking paleodeformation fields in the Mesozoic central Sierra Nevada arc: Implications for intra-arc cyclic deformation and arc tempos. Lithosphere 7, 296–320. doi:10.1130/L389.1

Cao, W., Paterson, S., 2016. A mass balance and isostasy model: Exploring the interplay between magmatism, deformation, and surface erosion in continental arcs using central Sierra Nevada as a case study. Geochem.-Geophys.-Geosyst. 1–19. doi:10.1002/2015GC006229

Chapman, A.D., Saleeby, J.B., Wood, D.J., Piasecki, A., Kidder, S., Ducea, M.N. and Farley, K.A., 2012. Late Cretaceous gravitational collapse of the southern Sierra Nevada batholith, California. Geosphere, 8(2), pp.314-341.

Chapman, J.B. and Kapp, P., 2017. Tibetan magmatism database. Geochemistry, Geophysics, Geosystems, 18(11), pp.4229-4234.

Chung, S.-L., Chu, M.-F., Ji, J., O'Reilly, S.Y., Pearson, N.J., Liu, D., Lee, T.-Y., Lo, C.-H., 2009. The nature and timing of crustal thickening in Southern Tibet: Geochemical and zircon Hf isotopic constraints from postcollisional adakites. Tectonophysics 477, 36–48. doi:10.1016/j.tecto.2009.08.008

Dai, J., Wang, C., Hourigan, J., Li, Z., Zhuang, G., 2013. Exhumation History of the Gangdese Batholith, Southern Tibetan Plateau: Evidence from Apatite and Zircon (U-Th)/He Thermochronology. The Journal of Geology 121, 155–172. doi:10.1086/669250

DeCelles, P.G., Kapp, P., Gehrels, G.E. and Ding, L., 2014. Paleocene-Eocene foreland basin evolution in the Himalaya of southern Tibet and Nepal: Implications for the age of initial India-Asia collision. Tectonics, 33(5), pp.824-849.

DeCelles, P.G., Kapp, P., Quade, J., Gehrels, G.E., 2011. Oligocene-Miocene Kailas basin, southwestern Tibet: Record of postcollisional upper-plate extension in the

Indus-Yarlung suture zone. Geological Society of America Bulletin 123, 1337–1362. doi:10.1130/B30258.1

DePaolo, D.J., Harrison, T.M., Wielicki, M., Zhao, Z., Zhu, D.-C., Zhang, H., Mo, X., 2019. Geochemical evidence for thin syn-collision crust and major crustal thickening between 45 and 32 Ma at the southern margin of Tibet. Gondwana Research 1–57. doi:10.1016/j.gr.2019.03.011

Ding, L., Zhong, D., Yin, A., Kapp, P. and Harrison, T.M., 2001. Cenozoic structural and metamorphic evolution of the eastern Himalayan syntaxis (Namche Barwa). Earth and Planetary Science Letters, 192(3), pp.423-438.

Ducea, M.N., Saleeby, J.B., Bergantz, G., 2015. The Architecture, Chemistry, and Evolution of Continental Magmatic Arcs. Annu. Rev. Earth Planet. Sci. 43, 299–331. doi:10.1146/annurev-earth-060614-105049

Hammarstrom, J.M. and Zen, E.A., 1986. Aluminum in hornblende: an empirical igneous geobarometer. American mineralogist, 71(11-12), pp.1297-1313.

Harrison, T.M., Yin, A., Grove, M., Lovera, O.M., Ryerson, F.J., Zhou, X., 2000. The Zedong Window: A record of superposed Tertiary convergence in southeastern Tibet. Journal of Geophysical Research: Solid Earth 105, 19211–19230. doi:10.1029/2000JB900078

He, S., Kapp, P., DeCelles, P.G., Gehrels, G.E. and Heizler, M., 2007. Cretaceous–Tertiary geology of the Gangdese Arc in the Linzhou area, southern Tibet. Tectonophysics, 433(1-4), 15-37.

Holland, T., Blundy, J., 1994. Non-ideal interactions in calcic amphiboles and their bearing on amphibole-plagioclase thermometry. Contrib Mineral Petrol 116, 433–447. doi:10.1007/BF00310910

Jagoutz, O., 2014. Arc crustal differentiation mechanisms. Earth and Planetary Science Letters 396, 267–277. doi:10.1016/j.epsl.2014.03.060

Ji, W.-Q., Wu, F.-Y., Chung, S.-L., Liu, C.-Z., 2014. The Gangdese magmatic constraints on a latest Cretaceous lithospheric delamination of the Lhasa terrane, southern Tibet. Lithos 210-211, 1–13. doi:10.1016/j.lithos.2014.10.001

Jiang, H. and Lee, C.-T.A., 2017. Coupled magmatism–erosion in continental arcs: Reconstructing the history of the Cretaceous Peninsular Ranges batholith, southern California through detrital hornblende barometry in forearc sediments. Earth and Planetary Science Letters 472, 69–81. doi:10.1016/j.epsl.2017.05.009

Jiang, H. and Lee, C.-T. A., 2019, On the role of chemical weathering of continental arcs in long-term climate regulation: a case study of the Peninsular Ranges batholith, California (USA), Earth and Planetary Science Letters, in press.

Kapp, P., DeCelles, P.G., Leier, A.L., Fabijanic, J.M., He, S., Pullen, A., Gehrels, G.E. and Ding, L., 2007. The Gangdese retroarc thrust belt revealed. GSA today, 17(7), p.4.

Kapp, J. L. D., Harrison, T. M., Kapp, P., Grove, M., Lovera, O. M., and Lin, D.. 2005. Nyainqentanglha Shan: A window into the tectonic, thermal, and geochemical evolution of the Lhasa block, southern Tibet, J. Geophys. Res., 110, B08413, doi:10.1029/2004JB003330.

Laskowski, A.K., Kapp, P., Cai, F., 2018. Gangdese culmination model: Oligocene–Miocene duplexing along the India-Asia suture zone, Lazi region, southern Tibet. Geological Society of America Bulletin 130, 1355–1376. doi:10.1130/B31834.1

Lee, C.T.A., Shen, B., Slotnick, B.S., Liao, K., Dickens, G.R., Yokoyama, Y., Lenardic, A., Dasgupta, R., Jellinek, M., Lackey, J.S. and Schneider, T., 2013. Continental arc–island arc fluctuations, growth of crustal carbonates, and long-term climate change. Geosphere, 9(1), pp.21-36.

Ludwig, K.L. and Mundil, R., 2002. Extracting reliable U-Pb ages and errors from complex populations of zircons from Phanerozoic tuffs: Journal of Conference Abstracts. In 12th Goldschmidt Conference, A-463.

Mutch, E.J.F., Blundy, J.D., Tattitch, B.C., Cooper, F.J. and Brooker, R.A., 2016. An experimental study of amphibole stability in low-pressure granitic magmas and a revised Al-in-hornblende geobarometer. Contributions to Mineralogy and Petrology, 171(10), p.85.

Pan, Y. and Kidd, W.S.F., 1999. Shortening in the southern Lhasa block during India-Asia collision. Abstract of 14th Himalaya-Karakoram-Tibet Workshop. Kloster Ettal, Germany.

Putirka, K., 2016. Amphibole thermometers and barometers for igneous systems and some implications for eruption mechanisms of felsic magmas at arc volcanoes. American Mineralogist 101, 841–858. doi:10.2138/am-2016-5506

Profeta, L., Ducea, M.N., Chapman, J.B., Paterson, S.R., Gonzales, S.M.H., Kirsch, M., Petrescu, L., DeCelles, P.G., 2015. Quantifying crustal thickness over time in magmatic arcs. Sci. Rep. 5, 413–12. doi:10.1038/srep17786

Reiners, P.W. and Brandon, M.T., 2006. Using thermochronology to understand orogenic erosion. Annu. Rev. Earth Planet. Sci., 34, pp.419-466.

Stüwe, K., Barr, T.D., 1998. On uplift and exhumation during convergence. Tectonics 17, 80–88. doi:10.1029/97TC02557

Tian, Z., Brown, M., Zhang, Z., Piccoli, P.M. and Dong, X., 2020. Contrasting CW and CCW tectono-metamorphic belts in the eastern Himalayan syntaxis: quantification of P–T–t paths and tectonic interpretation. Gondwana Research, 79, pp.1-26.

Tremblay, M.M., Fox, M., Schmidt, J.L., Tripathy-Lang, A., Wielicki, M.M., Harrison, T.M., Zeitler, P.K., Shuster, D.L., 2015. Erosion in southern Tibet shut down at ∼10 Ma due to enhanced rock uplift within the Himalaya. Proceedings of the National Academy of Sciences 112, 12030–12035. doi:10.1073/pnas.1515652112

Willett, S.D., 1999. Orogeny and orography: The effects of erosion on the structure of mountain belts. Journal of Geophysical Research: Solid Earth, 104(B12), pp.28957-28981.

Wu, Z.-H., Zhang, Y.-S., Hu, D.-G., Zhao, X.-T., Ye, P.-S., The Quaternary normal faulting of the Cona-Oiga rift. 2008. Seismology and Geology, v.30, p. 144-160. In Chinese with English abstract.

Yanites, B.J. and Kesler, S.E., 2015. A climate signal in exhumation patterns revealed by porphyry copper deposits. Nature Geoscience, 8(6), pp.462-465.

Yang, Z.M., Goldfarb, R. and Chang, Z.S., 2016. Generation of postcollisional porphyry copper deposits in southern Tibet triggered by subduction of the Indian continental plate. Society of Economic Geologists Special Publication, 19, pp.279-300.

Yin, A. and Harrison, T.M., 2000. Geologic evolution of the Himalayan-Tibetan orogen. Annual review of earth and planetary sciences, 28(1), pp.211-280.

Yin, A., Harrison, T.M., Ryerson, F.J., Wenji, C., Kidd, W.S.F., Copeland, P., 1994. Tertiary structural evolution of the Gangdese Thrust System, southeastern Tibet. Journal of Geophysical Research: Solid Earth 99, 18175–18201. doi:10.1029/94JB00504

Yin, J., Xu, J., Liu, C., and Li, H., 1988. The Tibetan plateau: regional stratigraphic context and previous work. Philosophical Transactions of the Royal Society of London. Series A, Mathematical and Physical Sciences, 327(1594), pp.5-52.

Zhang, Z.M., Zhao, G.C., Santosh, M., Wang, J.L., Dong, X. and Liou, J.G., 2010. Two stages of granulite facies metamorphism in the eastern Himalayan syntaxis, south Tibet: petrology, zircon geochronology and implications for the subduction of Neo-Tethys and the Indian continent beneath Asia. Journal of Metamorphic Geology, 28(7), pp.719-733.

Zeitler, P.K., Meltzer, A.S., Brown, L., Kidd, W.S., Lim, C. and Enkelmann, E., 2014. Tectonics and topographic evolution of Namche Barwa and the easternmost Lhasa block, Tibet. Toward an Improved Understanding of Uplift Mechanisms and the Elevation History of the Tibetan Plateau: Geological Society of America Special Paper, 507, pp.23-58.

Zhu, D.-C., Wang, Q., Cawood, P.A., Zhao, Z.-D., Mo, X.-X., 2017. Raising the Gangdese Mountains in southern Tibet. Journal of Geophysical Research: Solid Earth 122, 214–223. doi:10.1002/2016JB013508

Zhu, D.-C., Wang, Q., Zhao, Z.-D., Chung, S.-L., Cawood, P.A., Niu, Y., Liu, S.A., Wu, F.-Y. and Mo, X.-X., 2015. Magmatic record of India-Asia collision. Scientific Reports, 5, p.14289.

Zen, E.A. and Hammarstrom, J.M., 1984. Magmatic epidote and its petrologic significance. Geology, 12(9), pp.515-518.

Zuza, A.V., Wu, C., Wang, Z., Levy, D.A., Li, B., Xiong, X. and Chen, X., 2018. Underthrusting and duplexing beneath the northern Tibetan Plateau and the evolution of the Himalayan-Tibetan orogen. Lithosphere, 11(2), pp.209-231.

TABLES

Table 3.1: Locations, ages, emplacement pressures, and solidus temperatures of barometry samples.

Sample	Lat.	Long.	Elev. (m)	Lithology	Sector	Age (Ma)	P (kbar) A&S[1]	P (kbar) Mutch[2]	P (kbar) Mean	±[3]	Temp (°C)[4]	Age reference[5]
7-6-1*	29.45952	94.42608	2930	Monzodiorite	Nyingchi	50.5 ±0.7	8.1	7.8	8.0	1.0	726	This study
7-13*	29.1855	93.96752	2980	Granodiorite	Wolong	87.2 ±1.1	(6.8)	6.5	6.7	1.0	736	Ji et al. (2014)
7-14	29.17734	93.93331	2997	Granodiorite	Wolong	88.7 ±1.5	(5.5)	6.8	6.2	1.0	797	Ma et al. (2013)
XCT55	29.1360	93.8409	3340	Granite	Wolong	177.5 ±1.1	3.0	2.5	2.7	1.0	655	This study
ML04-1*	29.12564	93.8370	2960	Monzodiorite	Wolong	86.5 ±2.4	7.5	6.5	7.0	1.0	704	Ji et al. (2014)
09FW34*	29.14	93.1283	3100	Tonalite	Wolong	94.9 ±1.7	6.0	5.0	5.5	1.0	699	Ji et al. (2014)
09FW41	29.4193	92.7381	4520	Granite	Jiacha	56.1 ±1.1	6.0	4.5	5.2	1.0	661	Ji et al. (2012)
09FW50*	29.2388	92.6973	3780	Granodiorite	Jiacha	50.2 ±1.9	(3.7)	2.9	3.3	1.0	665	Ji et al. (2012)
XCT56	29.1708	92.6687	3420	Granite	Jiacha	196.1 ±1.2	(4.5)	3.5	4.0	1.0	669	This study
XCT58	29.2301	92.3008	3590	Granite	Zedong	46.4 ±0.4	(1.8)	1.9	1.9	1.0	667	This study
8-4	29.28817	92.09571	3561	Monzodiorite	Zedong	45.4 ±0.7	3.1	2.7	2.9	1.0	695	Ji et al. (2012)
8-6	29.26903	91.9114	3553	Monzodiorite	Zedong	29.6 ±0.4	(0.4)	1.2	0.8	1.0	629	Zhang et al.. (2014)
8-10	29.26566	91.81249	3558	Granodiorite	Zedong	62	(1.4)	2.1	1.8	1.0	745	Jiang et al. (2014)
10-7-1	29.30214	91.40829	3558	Monzodiorite	Lhasa	91.1	(1.7)	1.8	1.7	1.0	633	Jiang et al. (2014)
10-8	29.31496	91.28507	3578	Monzodiorite	Lhasa	91.2 ±0.5	(2.4)	2.3	2.4	1.0	702	This study
11-10	29.4094	91.16078	3770	Granodiorite	Lhasa	63.8 ±0.5	(2.0)	2.1	2.1	1.0	712	This study
12-14	29.37394	91.01984	3756	Qtz Monzodiorite	Lhasa	45.4 ±0.4	(2.1)	2.0	2.1	1.0	683	This study
14-7	29.33386	90.86615	3580	Granodiorite	Lhasa	47.1 ±1.0	(1.3)	1.2	1.3	1.0	662	Ji et al. (2009)

[1.] Pressure results based on Anderson and Smith (1995)'s calibration with temperature effect corrected. Pressures in paracenteses are the results having hornblende compositions of $Fe^{\#}<0.4$ or $Fe^{3+}/(Fe^{3+}+Fe^{2+})$ <0.2. These pressure are still considered to be valid since they pass the $Fe^{\#}$ <0.65 and T<800 ℃ filters (Putirka., 2016).

[2.] Pressure results based on Mutch et al.(2016) 's calibration.

[3.] A standard error of 1 kbar is assumed.

[4.] Solidus temperature obtained from plagioclase thermometer (Holland and Blundy, 1994).

[5.] Information from Tibetan Magmatism Database (Chapman and Kapp, 2017). Original citations are presented in the Supplementary Materials.

* mark in the sample column suggests sample containing magmatic epidote

FIGURES

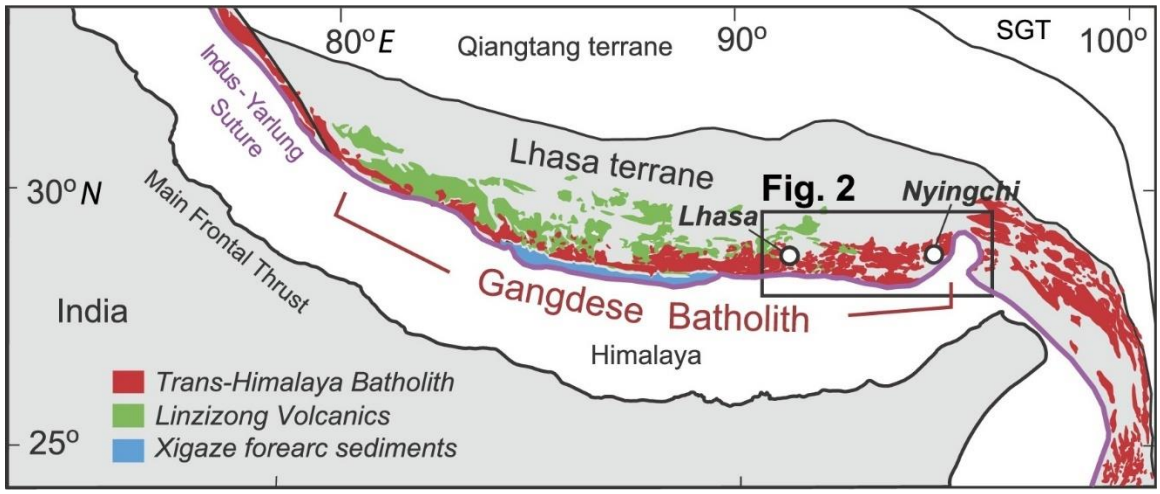

Figure 3.1. Simplified geologic map of southern Tibetan plateau showing major tectonic regimes. The Gangdese Batholith is the central section of the Tans-Himalaya Batholith developed along the southern edge of the Lhasa terrane. SGT: Songpan-Ganze terrane.

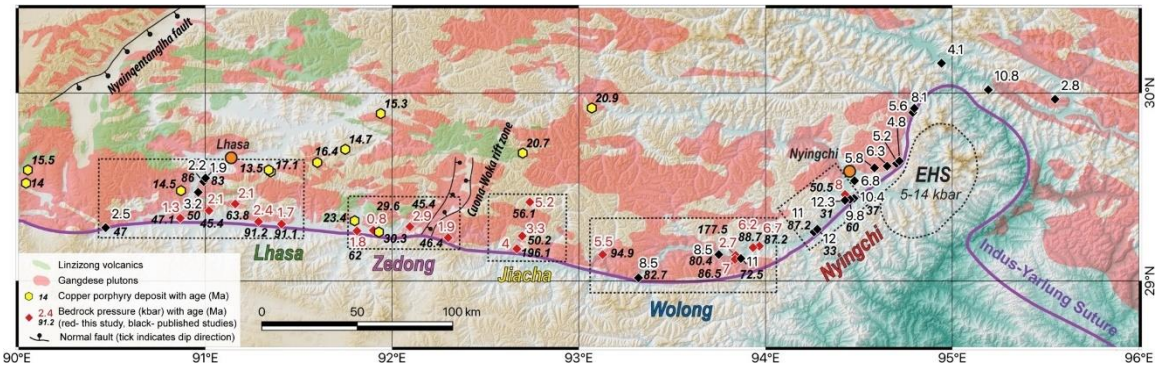

Figure 3.2. Map of Lhasa-Nyingchi area. Gangdese Batholith and Linzizong volcanics are highlighted using red and green colors. Bedrock pressure data and copper porphyry deposits are shown with associated ages. Bedrock pressure data in the study area are binned into five sectors (Lhasa, Zedong, Jiacha, Wolong, Nyingchi) shown as boxes with dashed outlines. EHS: Eastern Himalayan Syntaxis.

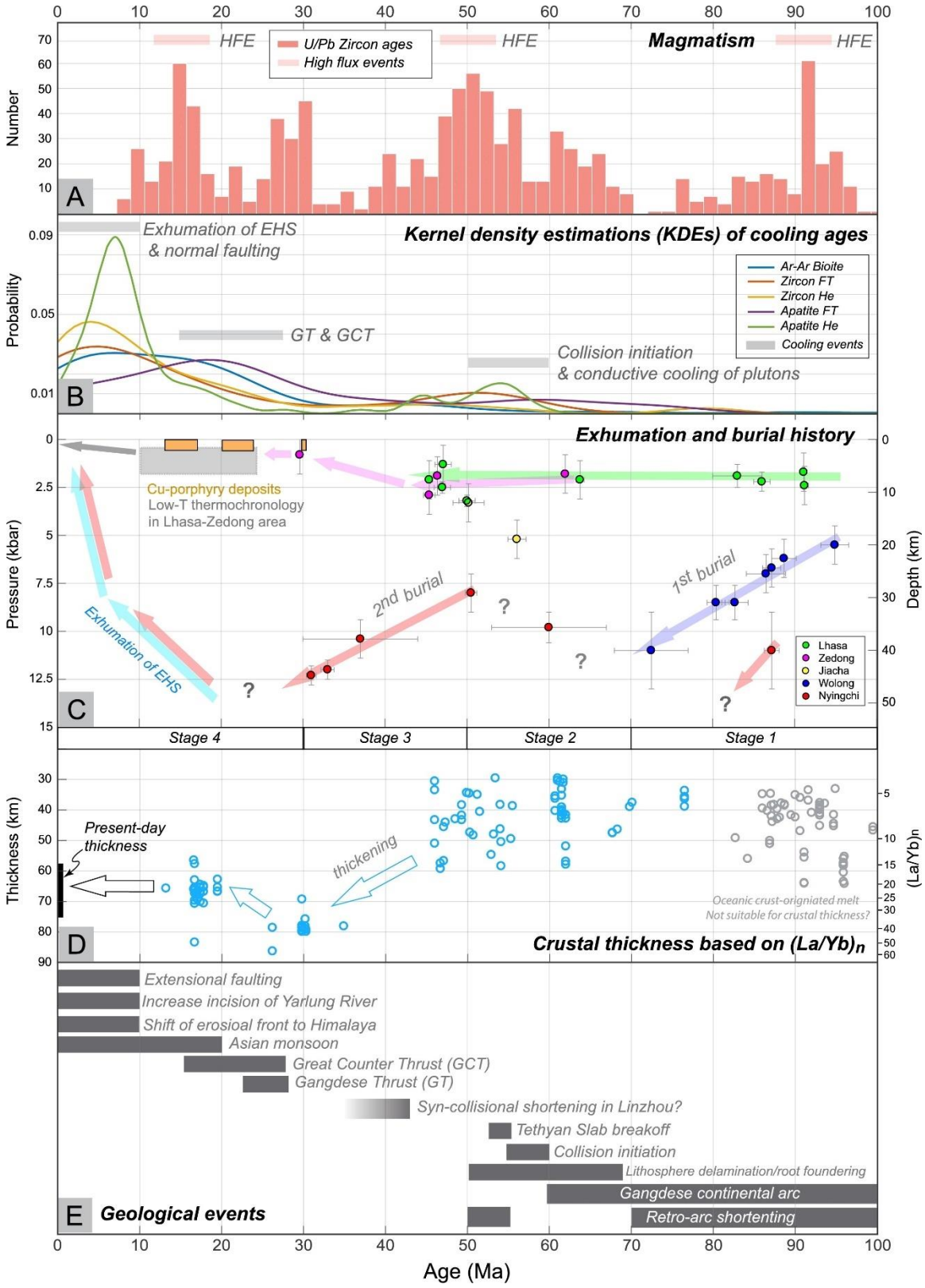
Magmatism
HFE
U/Pb Zircon ages
High flux events
Number
A
Kernel density estimations (KDEs) of cooling ages
Exhumation of EHS
& normal faulting
GT & GCT
Collision initiation
& conductive cooling of plutons
Ar-Ar Bioite
Zircon FT
Zircon He
Apatite FT
Apatite He
Cooling events
Probability
B
Exhumation and burial history
Cu-porphyry deposits
Low-T thermochronology
in Lhasa-Zedong area
2nd burial
1st burial
Exhumation of EHS
Lhasa
Zedong
Jiacha
Wolong
Nyingchi
Pressure (kbar)
Depth (km)
C
Stage 4
Stage 3
Stage 2
Stage 1
Present-day
thickness
thickening
Oceanic crust-originated melt
Not suitable for crustal thickness?
Crustal thickness based on (La/Yb)n
Thickness (km)
(La/Yb)n
D
Extensional faulting
Increase incision of Yarlung River
Shift of erosioal front to Himalaya
Asian monsoon
Great Counter Thrust (GCT)
Gangdese Thrust (GT)
Syn-collisional shortening in Linzhou?
Tethyan Slab breakoff
Collision initiation
Lithosphere delamination/root foundering
Gangdese continental arc
Retro-arc shortenting
Geological events
E
Age (Ma)

Figure 3.3. Multiple panels showing different aspects of the evolution of the Gangdese Batholith. (A) Histogram of U-Pb zircon ages of igneous rocks from the study area. Horizontal bars show the regional High-Flux Event (HFE, or magmatic flare-ups) at 93 Ma, 50 Ma, and 15 Ma. Age data are from Chapman and Kapp (2017)'s Tibetan Magmatism Database. (B) Kernel density estimations (KDEs) of cooling ages including Ar/Ar Biotite ages, zircon and apatite fission-track, (U-Th)He ages. The compiled dataset can be found in the Supplementary Materials. Grey bars show major cooling events suggested by the overlapping of the KDEs. The KDEs are generated using MATLAB fitdist function with the default bandwidth. (C) Exhumation/burial paths constructed based on bedrock pressure data. Colors of the paths correspond to five sectors. (D) Crustal thickness estimates in study area based on whole-rock $(La/Yb)_n$ ratio (Zhu et al., 2017). Present-day crustal thickness is based on CRUST 1.0 model. (E) Regional geological events affected the Gangdese Batholith. GT: Gangdese Thrust. GCT: Great Counter Thrust. EHS: Eastern Himalayan Syntaxis.

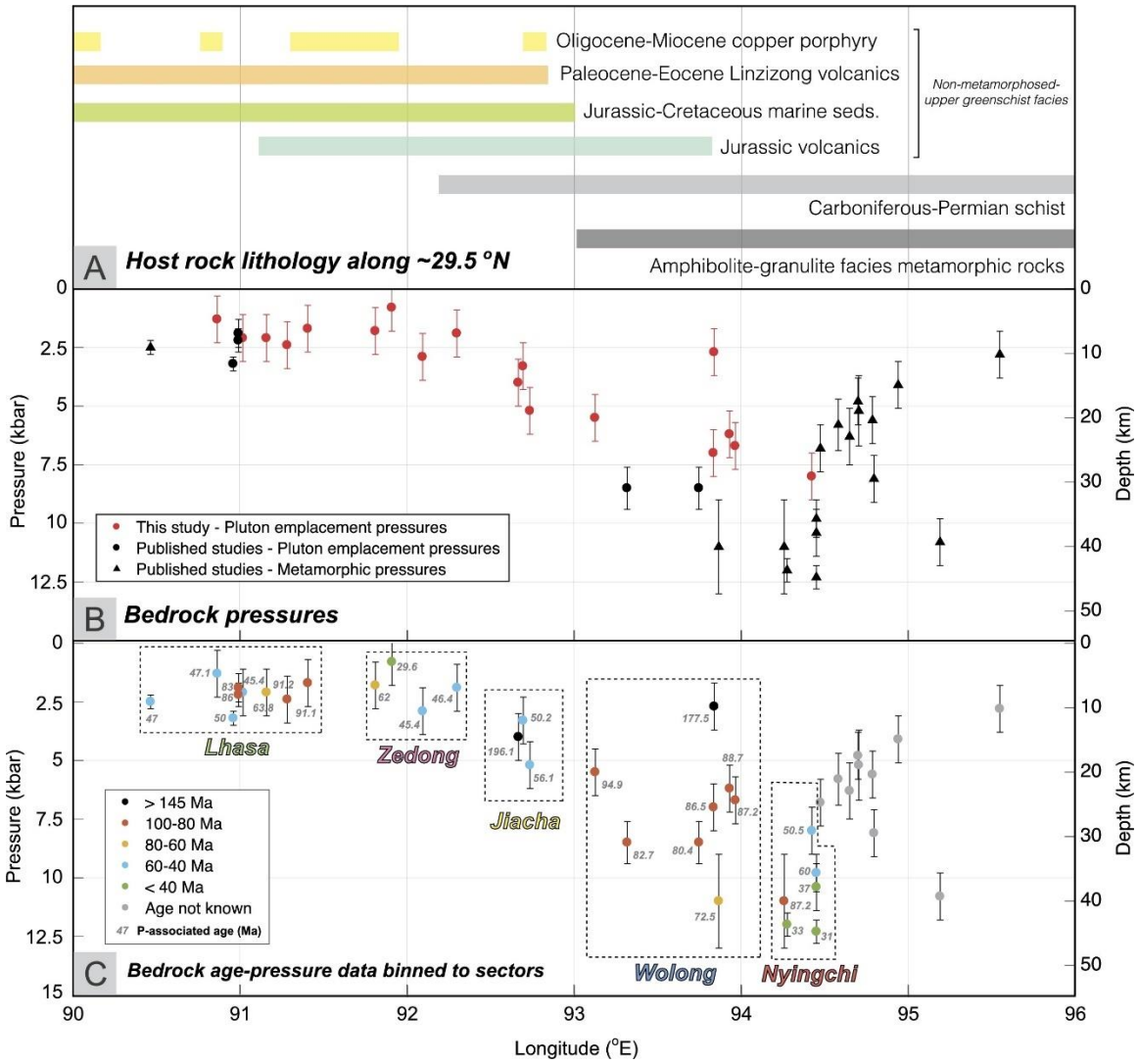

Figure 3.4. Host rock lithology and bedrock pressure data.(A) Host rock lithology along 29.5 °N latitude. (B) Bedrock pressures to the north of the Indus-Yarlung Suture. Error bar presents the standard deviation. Grey symbols show pressure data without associated ages. (C) Bedrock pressures with pressure-associated ages. 1 kbar =3.64 km conversion is used based on the density of crustal rock of 2800 kg/m^3 and gravitational acceleration of 9.8 m/s^2.

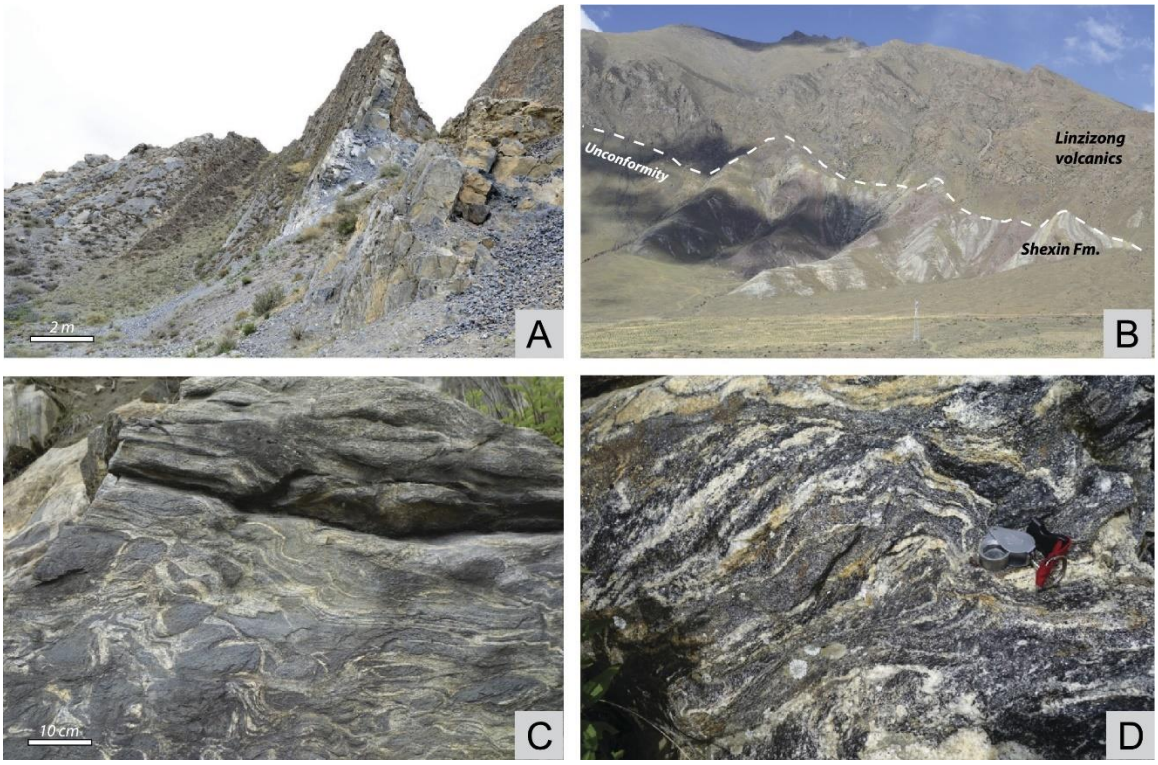

Figure 3.5. Field photos showing different lithology in the Gangdese Batholith. (A) Carbonates of Lower Cretaceous Chumulong Formation near Lhasa. Note the beds have been tilted but rocks are not metamorphosed. (B) Angular unconformity between underlying folded Upper Cretaceous Shexing Formation (clastic sedments) and overlying massive Eocene Linzizong volcanics. Photo taken near Maxiang (40 km to NW of Lhasa). (C) Middle-lower crust magma mingling and complex deformation near Nyingchi. (D) Migmatitic gneiss near Nyingchi .

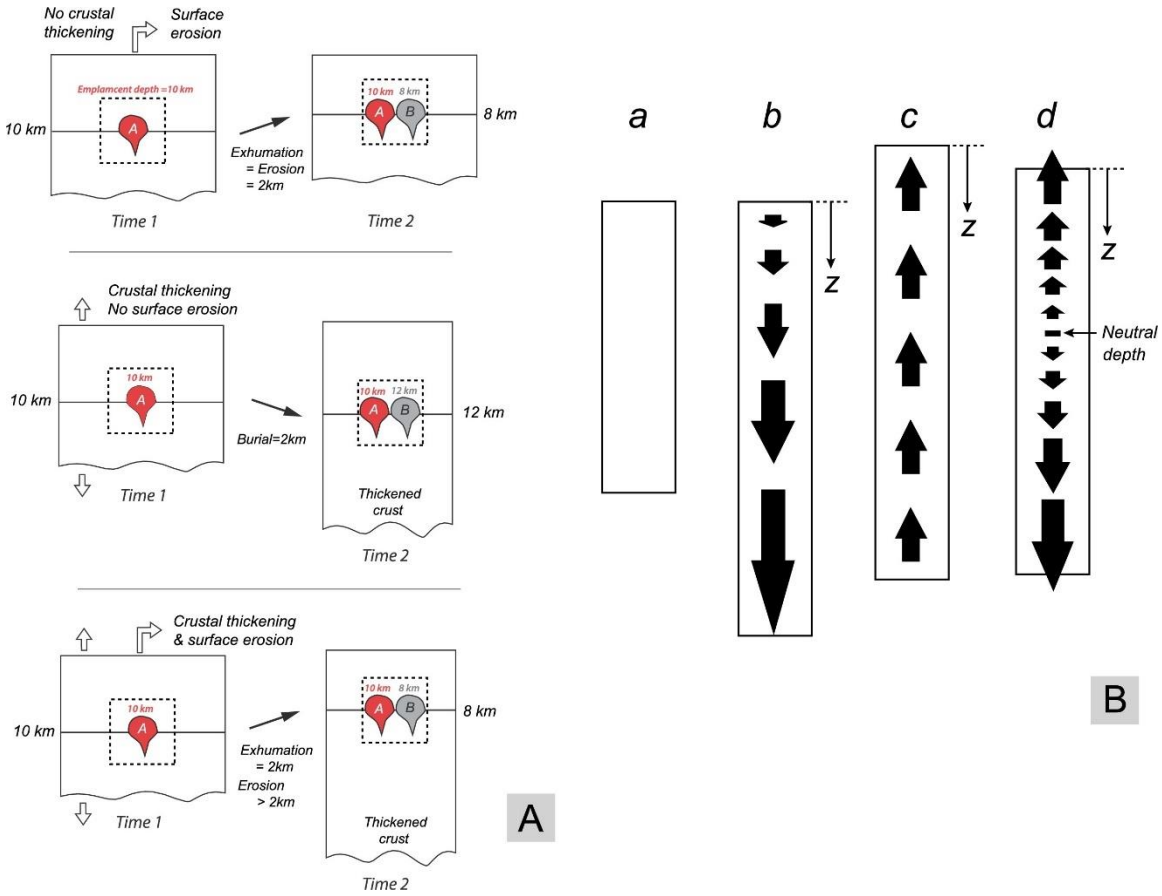

Figure 3.6. Schematic illustrating the vertical transport of materials within the crust. (A) Exhumation or burial processes of block of crust (dashed box) tracked by emplacement pressures (labeled on top of plutons) of two adjacent plutons. Top panel: only surface erosion, no crustal thickening. Emplacement depth difference equals exhumation and surface erosion. Middle panel: only crustal thickening, no surface erosion. Emplacement depth difference equals thickening-induced burial. Bottom panel: simultaneous crustal thickening and surface erosion. Emplacement depth difference equals exhumation but does not equal to erosion based on Eq. 1. (B) Kinematics of material transport within the crust. Arrows indicate the direction (arrowhead) and relative magnitude (arrow length) of the vertical motion of the parcels of the rocks with respect to the surface. (a) Crust prior to deformation. (b) Homogenous thickening in crust. (c) Crust is subject to surface erosion. (d) Crust is subject to simultaneous crustal thickening and surface erosion. Neutral depth is the depth where the thickening-induced burial is balanced with surface erosion. z is the depth direction pointing downwards. Origin of z -axis is at the surface. Modified from Stüwe and Barr (1998).

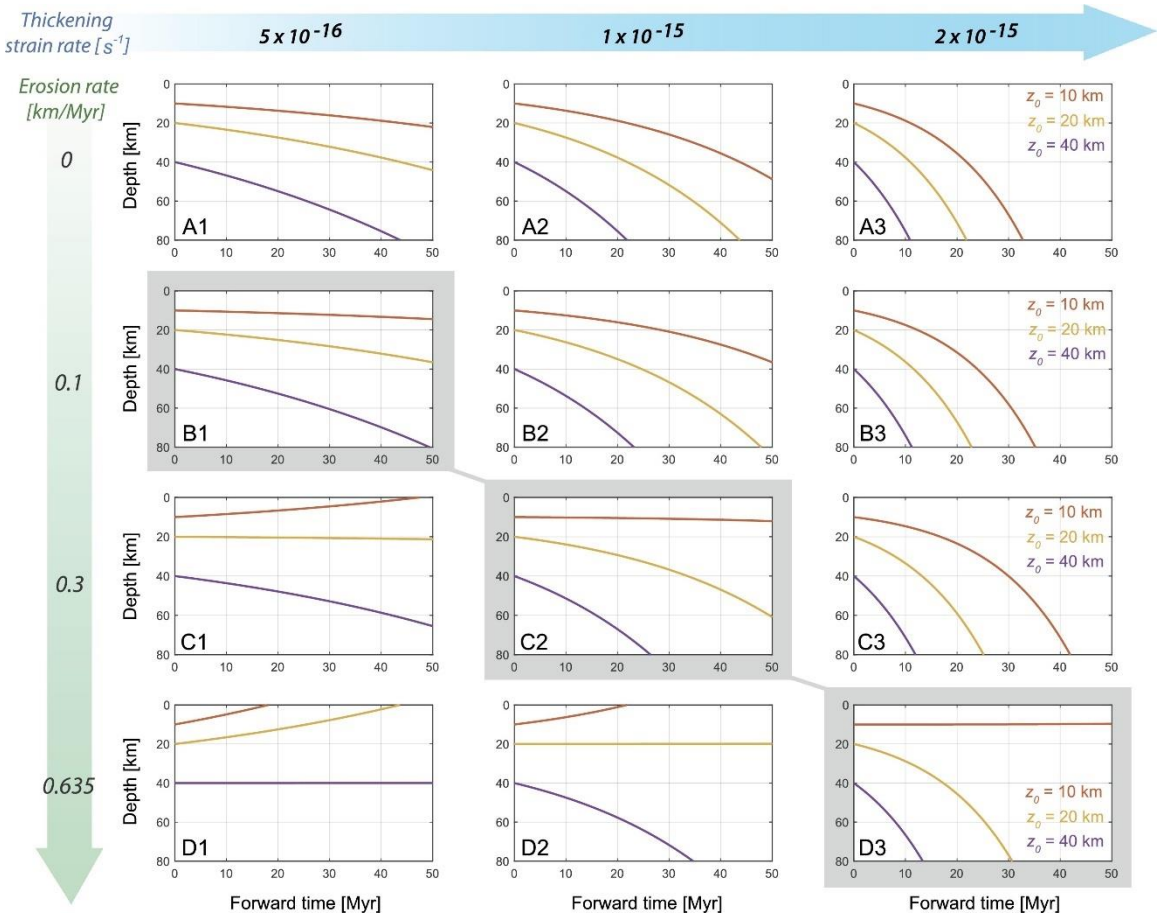

Figure 3.7. Simulated exhumation-burial paths of rocks with different initial depths. Surface erosion rate and thickening strain rate are varied. Three boxes are highlighted with gray color showing more or less flat exhumation paths for rocks at an initial depth of 10 km.

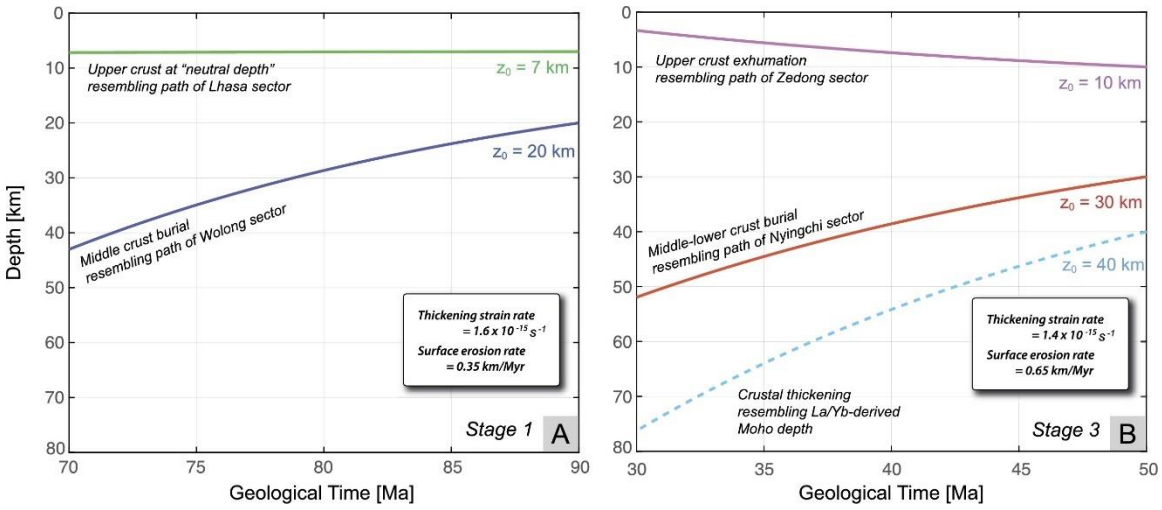

Figure 3.8. Simulated exhumation-burial paths fitted to bedrock data.(A) Simulated exhumation-burial paths for parcels of rocks at 7 km and 20 km under a thickening strain rate of 1.6×10^{-15} s^{-1} and a surface erosion rate of 0.35 km/Myr. These simulated paths resemble the exhumation-burial paths constrained by the bedrock pressures in the Lhasa and Wolong sectors during Stage 1. (B) Simulated exhumation-burial paths for parcels of rocks at 10 km and 30 km and Moho depth at 40 km under a thickening strain rate of 1.4×10^{-15} s^{-1} and a surface erosion rate of 0.65 km/Myr. These simulated paths resemble the exhumation-burial paths constrained by the bedrock pressures in the Zedong and Niyingchi sectors and the $(La/Yb)_n$-derived crustal thickness during Stage 3. Crustal thickness of 40 km is assume at 50 Ma.

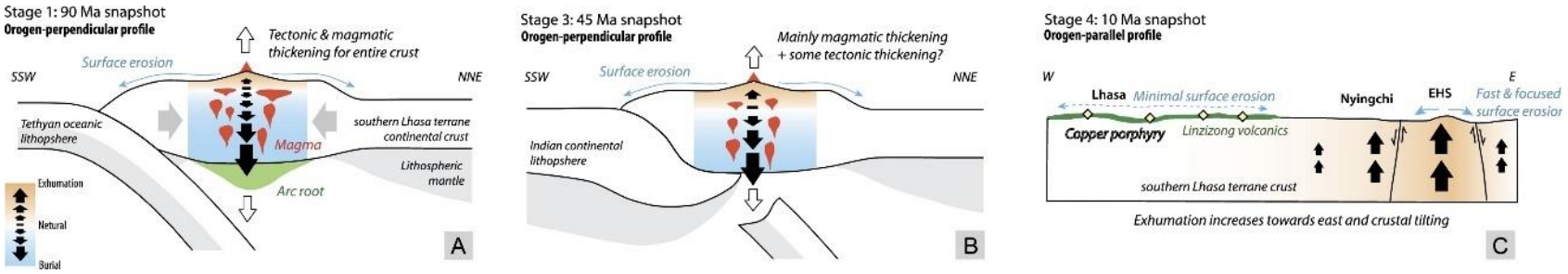
Stage 1: 90 Ma snapshot
Orogen-perpendicular profile
Tectonic & magmatic thickening for entire crust
Surface erosion
SSW
NNE
Tethyan oceanic lithopshere
southern Lhasa terrane continental crust
Magma
Lithospheric mantle
Arc root
Exhumation
Netural
Burial
A
Stage 3: 45 Ma snapshot
Orogen-perpendicular profile
Mainly magmatic thickening + some tectonic thickening?
Surface erosion
SSW
NNE
Indian continental lithopshere
B
Stage 4: 10 Ma snapshot
Orogen-parallel profile
W
E
Lhasa
Minimal surface erosion
Nyingchi
EHS
Fast & focused surface erosion
Copper porphyry
Linzizong volcanics
southern Lhasa terrane crust
Exhumation increases towards east and crustal tilting
C

Figure 3.9. Cartoon of snapshots showing the tectonic evolution of the Gangdese Batholith highlighting the exhumation and burial processes in different depths of the crust. The color bar with arrowheads indicates the motion of rocks relative to the surface (exhumation, neutral or burial). (A) During Stage 1 at 90 Ma, the entire crust was thickened by magmatic inflation and tectonic thickening. Arc root is generated. (B) During Stage 3 at 45 Ma, the crust was mainly thickened by magmatic inflation and some tectonic thickening. (C) During Stage 4 at 10 Ma, the eastern part of the section experienced fast exhumation related to the focused surface erosion at the EHS. The western part of the section has minimal surface erosion and exhumation. Such differential exhumation causes the tilting of the crustal section. Note, (A), (B), are shown for orogen-perpendicular profile, and (C) is shown for orogen-parallel profile. EHS: Eastern Himalayan Syntaxis.

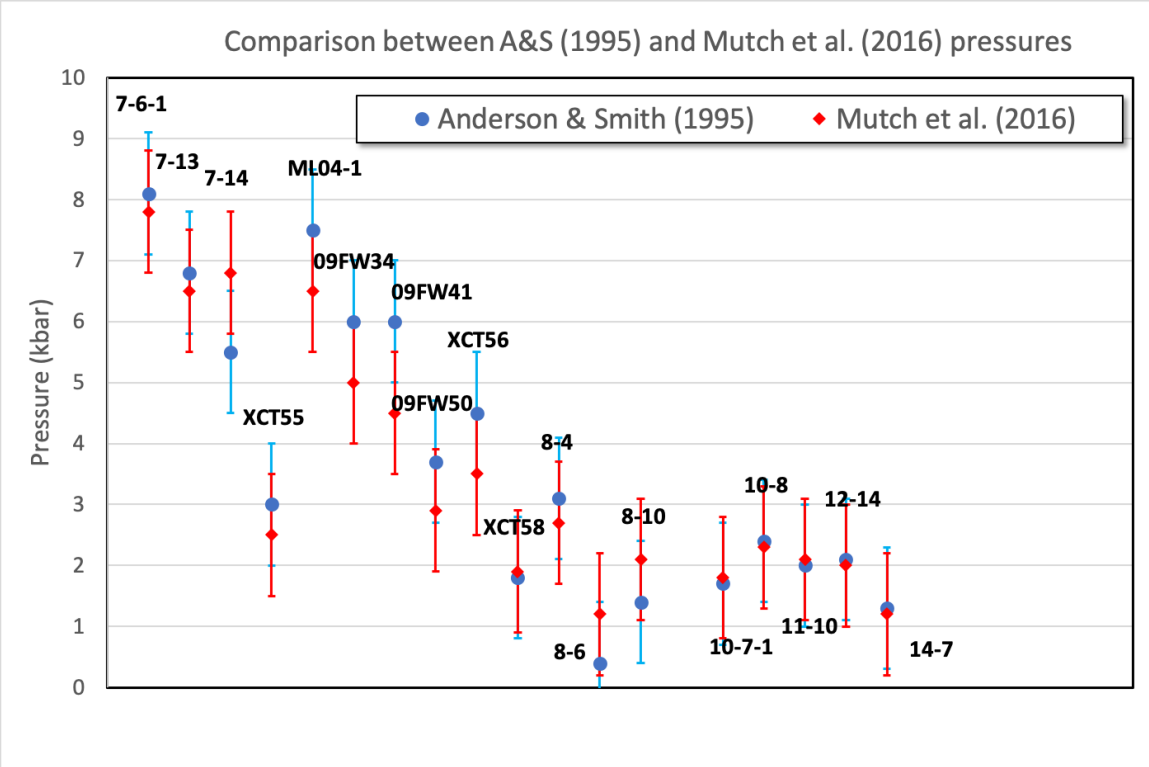

Figure 3.S1. Comparison between pressures calculated based on Anderson and Smith (1995) and Mutch et al. (2016). This figure presents the pressure results with uncertainties from Anderson and Smith (1995)'s and Mutch et al. (2016)'s calibrations. The numerical results are presented in Table 1 of the manuscript. Here, sample numbers are labeled on top of the results. Pressures derived from either method overlap within the uncertainties ($\pm$1 kbar), thus validating the results.

CHAPTER 4: Magmatic fabrics of the Gangdese Batholith as an indicator of upper plate deformation and implications for plate convergence between India and Asia since Late Cretaceous

ABSTRACT

Magmatic fabrics in plutons are foliations and lineations defined by the shape preferred orientations of primary igneous minerals that formed before the magma crystallized completely. Their orientations may represent incremental strain at the pluton emplacement level and can be used to deduce the directions of regional principal stress and constrain crustal deformation and kinematics in response to orogenic processes. We conducted a field study in the eastern Gangdese Batholith in southern Tibet and report magmatic foliation (n = 287) and lineation (n = 54) measurements from 45 dated plutons in the Lhasa to Nyingchi transect along the Yarlung River. Overall, both foliation dip and lineation plunge are moderate to steep and fabric orientations are consistent within each individual pluton. We explore how magmatic foliation strike directions vary with the timing of pluton emplacement to constrain deformation in the upper plate during plate convergence (subduction and collision). Results show that magmatic fabrics orientations are variable thru time and are grouped into: (1) 100-60 Ma plutons with dominantly orogen-parallel foliations and sub-vertical lineations, corresponding to orogen-perpendicular contraction and crustal thickening. (2) 60-40 Ma plutons with orogen-perpendicular fabrics and sub-horizontal lineations, associated with crustal thinning and a change in the crustal stress regime from ~N-S contraction to ~E-W contraction. (3) <30 Ma plutons with foliations of variable strikes and sub-vertical lineations indicative of crustal thickening while the direction of principal stress is unclear. In contrast, foliation in (meta-)volcanic-sedimentary country rocks in the region show consistent orogen-parallel orientations indicative of finite strain dominated by orogen-perpendicular shortening. Kink folds in country rocks suggest orogen-parallel shortening overprinted by

the orogen-parallel foliation. The kinematics of the kinks in the country rocks are consistent with the change in the foliation trend observed in the magmatic fabrics. We interpret pre-collision Late Cretaceous fabrics to record approximate orogen-perpendicular subduction of the Neo-Tethyan oceanic plate beneath the Asian continent during the growth of the Gangdese arc. The post-collision fabrics reflect the enigmatic nature of the India-Asia collision, as well as the complexity of various post-collisional processes. This study shows that magmatic fabrics can be a useful tool to reveal upper plate deformation during subduction and collision.

INTRODUCTION

To understand the structure and evolution of orogenic belts in time and how they are related to plate tectonics, we need to investigate the rock record associated with tectonic deformation and magmatism to reveal its P-T-t-D (pressure-temperature-time-deformation) history (e.g., van Kranendonk, 1996; Willner et al., 2000; Labrousse et al., 2004; Flowers et al., 2006; Beltrando et al., 2010; Hacker et al., 2010; Fossen, 2016). One of the challenges of revealing the deformation history in a multi-phased orogen is the lack of constraints on time-dependent incremental strain. Rock fabrics and regional structures we observe today represent the finite strain that may be associated with multiple deformational events (e.g., McKenzie & Jackson 1983; England & Houseman, 1986; Martelat et al., 2000; Jolivet, 2001; Cao et al., 2015). The conventional way of determining the timing of incremental strain relies on detailed regional structural analysis using cross-cutting relationships or dating of syn-deformation minerals (e.g., Lee et al., 2000; Leloup et al., 2001; Agard et al., 2006; Tunik et al., 2010). Magmatic fabrics in

plutons, coupled with their crystallization age, can be a potential tool to track the incremental strain and the associated regional principal stress (σ_1) (e.g., Saint Blanquat & Tikoff, 1997; Paterson et al., 1998, Archanjo et al., 1999; Callahan & Markley, 2003; Vernon et al., 2008; Zak et al., 2008, de Saint Blanquat et la., 2011; Cao et al., 2015; Paterson et al., 2019).

Magmatic fabrics are formed when the pluton is at a hypersolidus state during the transition from a melt-bearing crystal mush to solid rock (Paterson et al., 1989, 1998; Vernon, 2000; Paterson et al., 2019); therefore, they can track local or regional incremental strain representing the snapshot of principal stress σ_1 at the time of crystallization (e.g., Saint Blanquat & Tikoff, 1997; Archanjo et al., 1999; Paterson et al., 1998; Vernon et al., 2008; Zak et al., 2008). The alignment of magmatic minerals can help us understand the processes affecting magma chambers during pluton emplacement and crystallization (e.g., Balk, 1937; Bouchez, 1997; Callahan & Markley, 2003; Zak et al., 2008; Payacán et al., 2014; Paterson et al., 2019; Ardill et al., 2020). There are three end-member mechanisms for the formation of magmatic fabrics (**Figure 1**), two of which are due to internal magma chamber dynamics and one is the result of external regional tectonic strain (Paterson et al., 1998, Barros et al., 2001). Magmatic fabrics related to flow dynamics inside the magma chamber typically exhibit margin-parallel “onion-skin” patterns or complex variable orientations at the outcrop scale, contrary to fabrics associated with regional tectonic strain that display consistent orientation across kilometers (**Figure 1.** Paterson et al., 1998; Zak et al., 2008).

For a magma chamber with 10 km radius, the duration of its hypersolidus state is ~3 Myr constrained by conductive cooling. Therefore, the time from magmatic fabric formation to complete crystallization is arguably short, in the range of 0.1-1 Myr. The crystallization ages obtained from U-Pb zircon geochronology can be used to represent the approximate formation age of the magmatic fabrics since the timescale of pluton crystallization is typically on the order of 10^5 yr (Petford et al., 2000; Paterson et al., 2011). Thus magmatic fabrics can be used as a proxy for regional incremental strain or snapshot of the maximum principal stress (σ_1) orientation that is perpendicular to the direction of σ_1 (Callahan & Markley, 2003; Zak et al., 2008; Cao et al., 2015). The development of magmatic lineation and foliation can also indicate the general shape of the incremental strain ellipsoid: constrictional or flattening shape that is associated with the L- or S-tectonite, respectively. Further, when paired with the depth at which the pluton was emplaced, the potential differences in incremental strain and stress regimes along the crustal column can be examined.

The Gangdese Batholith developed as the result of the northward subduction of the Neo-Tethyan paleoocean plate beneath Eurasia, and the subsequent India-Eurasia collision (e.g., Yin & Harrison, 2000; Kapp et al., 2007; Ji et al., 2009; 2014; Zhu et al., 2015). Gangdese plutons are well-exposed in southern Tibet with numerous crystallization ages spanning from Cretaceous to Neogene (e.g., Ji et al., 2009; Chapman & Kapp, 2017; Ma et al., 2022). We conduct a field study using in-situ magmatic fabric measurements recorded along an E-W, orogen-parallel transect to address the following: How does incremental strain change with the timing of India-Eurasia collision? Specifically, geological evidence suggests very limited upper plate deformation from 50-

30 Ma immediately following collision (Kapp et al., 2007), what can the magmatic fabrics tell us about the crustal strain history pre, syn, and post-collision? Finally, we will use the strain history derived from magmatic fabrics to evaluate proposed end-member models of India-Asia collision and paleogeography.

GEOLOGY OF THE STUDY AREA

The Tibetan plateau is the world's largest and highest active plateau, and it is supported by thick continental crust up to ~60-80 km thick (Molnar, 1988, 1993; England & Houseman 1988; Murphy et al., 1997; Owens & Zandt, 1997; Wang et al., 2007; Zhu et al., 2017). The plateau is the result of the continent-continent collision between India and Eurasia that began ~55 Ma (e.g., Molnar & Tapponnier, 1975; Murphy et al., 1997; Yin & Harrison, 2000; Leech et al., 2005; Guillot et al., 2008; Royden et al., 2008; Najman et al., 2010; Hu et al., 2016; An et al., 2021). The Indus-Yarlung suture separates the Tethyan Himalaya and Indian lithosphere in the south from the Asian continent in the north (e.g., Dewey et al., 1988; Yin & Harrison, 2000; Royden et al., 2008; Pan et al., 2012). Immediately south of the suture lies the Tethyan Himalaya rocks, which are mainly Cambrian to Eocene sedimentary and low-grade marine metasedimentary units that were in the Tethyan ocean and passive margin of northern India prior to India-Asia collision (e.g., Dewey et al., 1988; Yin & Harrison, 2000; Royden et al., 2008). Farther to the south, the High and Lesser Himalayas are separated by the South Tibetan Detachment Zone and the Main Central Thrust (e.g., Dewey et al., 1988; Yin & Harrison, 2000; Searle et al., 2008). North of the Indus-Yarlung suture and located in the southernmost part of the Asian continent is the Lhasa terrane, which consists of an Archean

microcontinent in the middle and younger accreted terranes on its north and south flanks (Zhu et al., 2015). The Lhasa terrane collided with the Qiangtang terrane to the north and was accreted to southern Asia during Late Jurassic to Early Cretaceous time (e.g., Chang & Zheng, 1973; Yin & Harrison, 2000; Zhu et al., 2016). Since the Mesozoic, the Lhasa terrane has been subjected to multiple phases of magmatism and deformation related to the subduction and collision along its northern and southern margins (e.g., Kapp & DeCelles, 2019). This resulted in extensive Jurassic to Paleogene igneous rocks including the voluminous Gangdese Batholith and the Paleocene-Eocene volcanic Linzizong Formation (e.g., Chung et al., 2005).

The Gangdese Batholith consists of the plutons generated during the ocean-continent subduction (the Gangdese Arc) as well as the syn- and post-collision igneous rocks (e.g., Zhang et al., 2014; Zhu et al., 2019). Plutons in the Gangdese Batholith are mostly diorite, granodiorite, granite, and monzogranite that intrude into the Lhasa terrane host rock (e.g., Ji et al., 2009). The plutonic rocks formed between the late Triassic and the Eocene, with major magmatism at ~100 – 90 Ma and ~60 – 50 Ma (e.g., Chapman & Kapp, 2017). The earlier flare-up event has been attributed to opening of a slab window following ridge subduction (Meng et al., 2014), while the later magmatic pulse is the result of the end stages of subduction and slab-mantle processes during collision (Zhu et al., 2011). Host rocks of the Lhasa terrane include the following sequences (from oldest to youngest): (1) crystalline basement, overlain by Ordovician, Carboniferous, and Triassic shallow marine clastic rocks (e.g., Yin et al., 1988). (2) Mesozoic sedimentary and carbonate rocks which include Jurassic-Lower Cretaceous fluvial and marginal marine sandstone, shale, and flysch; mid Cretaceous shallow marine limestone; and upper

Cretaceous fluvial red beds of the Takena Formation (e.g., Zhang et al., 2004). (3) Paleocene-Eocene volcanics of the Linzizong Formation, mostly andesites and ignimbrites, that have been dated between 65 - 41 Ma (Lee et al., 2009).

Since the Cretaceous, the deformation history of the Lhasa terrane includes three major phases: (1) subduction-related upper plate shortening prior to the onset of India-Asia collision. In the Lhasa area, the upper Cretaceous Takena formation is strongly deformed and steeply tilted (e.g., Tapponnier et al., 1981; He et al., 2007). Pan (1993) estimates ~40% shortening prior to Linzizong volcanism. An active thrust belt near Lhasa in the Gangdese retro-arc was active between 105 – 53 Ma, accommodating ~55% of N-S shortening (Kapp et al., 2007). (2) Syn-collisional shortening and Miocene thrust faulting events. The Indus-Yalung suture zone in southern Tibet is bounded by the older Gangdese thrust (GT) to the north (Harrison et al., 1992) and the younger Great Counter thrust (GCT) to the south (Heim & Gansser, 1939). These thrust systems developed between ~30-10 Ma (e.g., Yin et al., 1999), coeval with regional magmatism. They are interpreted as a late-stage response to India's collision with Asia (e.g., Gansser 1964). Growth of the Gangdese thrust system may have caused denudation of the Gangdese Batholith mainly along the suture (Yin et al., 1994; Laskowski et al., 2018). (3) Post-10 Ma normal faulting. Despite ongoing convergence between India and Asia, the Tibetan plateau is currently undergoing E-W extension, accommodated by N-S trending rifts (e.g., Molnar & Tapponnier, 1978). In the Nyainquentanghla region, timing for the onset of E-W extension has been estimated to be ~8 Ma (Harrison et al., 1995). The largest N-S trending rift, Yadong-Gulu rift cuts the South Tibetan Detachment System, which places an upper bound of ~12 Ma for its initiation (Edwards & Harrison 1997).

It is important to note that the upper Cretaceous Takena Formation is strongly deformed and steeply tilted, but is unconformably overlain by the sub-horizontal, gently folded Linzizong volcanic sequence with the oldest date of ~69 Ma (e.g., Leier et al., 2007), suggesting major upper crustal shortening within the Lhasa terrane occurred prior to the onset of Asia-India collision. Furthermore, compared to the overlying Cretaceous volcano-sedimentary strata, the exposed Cretaceous granitoids show little deformation (Kapp et al., 2005). One possible explanation is that the upper crustal shortening was accommodated in the lower-middle crust by rigid-body underthrusting of the Lhasa terrane beneath the northern Qiangtang terrane during the Cretaceous (Kapp et al., 2003). Finally, the eastern Gangdese Batholith was recently recognized as a tilted crustal section. In Chapter 3, we applied Al-in-hornblende barometry to Gangdese plutons in an orogen-parallel transect from Lhasa (~90°E) to Nyingchi (~95°E) and found bedrock pressures increase from 1-2 kbar in the west near Lhasa to 6-12 kbar in the east near Nyingchi (Cao et al., 2020). However, the mechanisms responsible for tilting the Gangdese Batholith are not well-understood.

METHODS

Magmatic fabric measurements were taken from the eastern portion of the Gangdese Batholith in 2018. We targeted granitoids exposed from Lhasa to Nyingchi (90 - 95°E), immediately north of the Indus-Yarlung suture (**Figure 2**). Most of these plutons have been cataloged with known U-Pb zircon ages in the Tibetan Magmatism Database (Chapman & Kapp, 2017) facilitating our attempt to couple magmatic fabrics with pluton ages. In-situ orientation measurements of foliations and lineations defined by the

alignment of euhedral-subhedral magmatic plagioclase, biotite, and amphibole were recorded using a combination of the digital mapping software FieldMove and traditional Brunton compass. Up to 30 measurements were made for each pluton exposure, which are typically single outcrops spanning tens to a hundred meters. Where available, fabric measurements were recorded from multiple outcrops associated with the same pluton. This helped in determining whether the magmatic fabrics are the result of internal chamber dynamics (varying orientations) or snapshots of regional stress regimes (similar orientations) as well as ensuring statistical robustness. Fabric orientations were taken from massive, in-place granitoids, with the assumption that they have not experienced significant rotation relative to the Indus-Yarlung suture. It has been proposed that the eastern Gangdese Batholith underwent a westward tilting of ~30 km over a linear distance of ~400 km (Cao et al., 2020). While this process does affect the orientation of the fabrics, the resulting westward rotation of ~4° is negligible. In addition to magmatic fabrics, we also recorded fabric and bedding orientations of the host rocks. Due to logistic reasons involving dam construction on the Nyang River and active landslides along the river valley, data collection between 92 - 94°E was limited.

To ensure the fabrics are magmatic in nature without modification of subsolidus deformation, we examined the thin sections under an optical microscope. To be magmatic, the fabrics must meet the following criteria (e.g., Paterson et al., 1989; 1998): First, the sample should contain mostly primary igneous minerals, and the magmatic fabrics are indicative of the shape-preferred orientations of plagioclase, K-feldspar, hornblende, biotite, muscovite. Second, for minerals to be associated with magmatic flow, the mineral grains (including quartz) should be euhedral to subhedral, with no

evidence of subsolidus strain. Fabrics associated with subsolidus deformation will show alterations, recovery textures, microstructures related to diffusion or pressure solution, recrystallized grains, and/or relict porphyroclasts with subgrains or fractures.

Fabric data were first imported into MATLAB, and the following post-processing routines were applied. The strike of the Indus-Yarlung suture undergoes an apparent northward bend (rotated counterclockwise 45° from E-W trend) east of 94°E which is likely to be associated with the formation of the eastern Himalayan syntaxis since ~10 Ma (e.g., Cao et al., 2020). Since plutons are older than 10 Ma, we rotated fabrics collected from plutons near Nyingchi (east of 94°E) clockwise for 40°. In order to show the relationship between fabric orientation relative to the Indus-Yarlung suture, we converted measurements of foliation strike and lineation trend from azimuth (0-360°) to the equivalent 1st quadrant (0-90°) representations. Therefore, 0° means it's perpendicular to the suture, while fabrics parallel to the suture would show orientations of 90°.

Stereonet11 software was used for visualization of fabric data in stereonet projections, as well as calculations of foliation poles, averaging, and contour fitting using the cylindrical best fit method (Allmendinger et al., 2011). Histogram plot, box plot, and Kernel density estimation plot were produced using a Python script. GPlates (Müller et al., 2018) was used for plate kinematic information presented in the discussion.

RESULTS

Magmatic fabrics on outcrops and thin sections

Figure 3 shows magmatic fabrics on outcrops of Gangdese plutons. The foliations are generally moderate to strong, and are defined by the linear alignment of plagioclase, hornblende, and biotite visible on fresh surfaces of granodiorite. Most plutons exhibit a dominant, single set of foliations, with varying strikes and dipping steeply (> 45°). Magmatic lineations defined by plagioclase, hornblende and biotite are relatively weaker compared to foliation. When present, lineations plunge sub-vertically with varying trend. Some plutons contain abundant mafic enclaves on the scale of centimeters, with their long axes parallel to the trace of magmatic foliation (**Figure 3C**).

A representative of magmatic fabrics in thin sections is shown in **Figure 4**. The microphotograph is taken in plain light and consists largely of plagioclase, hornblende, biotite, quartz, and K-feldspar. There is a prominent linear pattern involving the shape-preferred orientations of elongated euhedral hornblende (green). Throughout this sample and in all other plutons where magmatic fabric measurements were taken, we observe single crystals of mostly euhedral mineral grains with little to no evidence of intracrystalline strain. We do not identify any alterations, recovery textures, microstructures related to diffusion or pressure solution, recrystallized grains, nor relict porphyroclasts with subgrains or fractures. Thus, the microstructures and the associated foliations are indeed magmatic fabrics formed by magmatic flow during suspension, not grain-supported solid-state deformation.

Orientations of magmatic fabrics in space and time

We report in-situ magmatic foliation (n = 287) and lineation (n = 54) measurements from 45 plutons of known ages in **Figure 5**. The locations of individual plutons and their foliation measurements are shown in **Figure 2**. When all foliation and measurements are shown in **Figure 5A**, their strikes show significant variance (0-360°), with mostly moderate to steep dips (>45°). Magmatic lineations are typically associated with steep plunge (>45°) with a few having shallow plunge (**Figure 5C**). **Figure 5B** shows a histogram of all foliation measurements based on their equivalent 1st quadrant (0-90°) orientation relative to the orogen. There is significant scattering in the data shown in **Figure 5A**&**B** probably because fabrics can vary both with time and space.

We make a stereonet plot (**Figure 5D**) to show the means of great circles (best fit circle) representing different time groups (Pre-80 Ma, 80 – 60 Ma, 60 – 40 Ma, Post-40 Ma). In general, fabrics formed before 60 Ma are orientated orogen-parallel (E-W), contrasting the orogen-perpendicular (N-S) orientations for fabrics formed after 60 Ma. To better visualize how magmatic foliations change with time, we make a boxplot with a bin size of 5 Myr and color-coded the bins based on their longitudinal positions (**Figure 12B**). The same time progressive trend of orogen-parallel fabrics pre-60 Ma, transitioning to orogen-perpendicular fabrics post-60 Ma is confirmed. The exception to this trend are plutons emplaced near 90°E longitude, where both ~80 and ~50 Ma groups from this region show orogen-parallel fabrics with their equivalent 1st quadrant orientations of ~30°. Similarly, we show a time-progressive boxplot of magmatic lineation in **Figure 15D** and found that pre-60 Ma lineations are generally steep, with sub-vertical plunge of

~70°. 60 - 50 Ma lineations show a shallowing trend in their plunge angles, from ~80° to ~40°. Another shift back to sub-vertical plunge (~70°) is observed ~30 Ma.

To visualize how fabrics change with longitude, we present a series of ridgeline plots showing the density distribution of magmatic foliation orientations based on their longitude groups (**Figure 6**). The results show 93-95°E plutons record mostly orogen-parallel fabrics, contrasting the orogen-perpendicular fabrics found in plutons of 90-93°E.

Orientations of host rock fabrics

Ductile deformation in the host rocks varies from weak to strong, reflected by phyllitic layering to gneissic banding (**Figure 7**). Here we use the term foliation which includes both low- and high-grade fabrics such as cleavage, schistosity, and gneissosity. Depending on the protolith, foliation is defined by the alignment of micas, hornblende, quartz, deformed relic clasts in lower grade metamorphic rocks as well as compositional bands in gneiss. Where exposures allow, both foliation (n = 167) and bedding (n = 201) orientations were recorded (**Figure 8**). In most cases, the orientation of foliation and bedding are the same (**Figure 7C, 8**). The host rock fabrics are dominated by orogen-parallel (E-W) strike that dip moderately to the north. In **Figure 9** we show the locations where the host rock fabrics were taken. While some variance exists in the foliation strike directions, we confirm the majority of the fabrics are orogen-parallel, without any spatial trend.

DISCUSSION

Comparison between host rock and magmatic fabrics

Host rock fabrics are the expression of finite strain, a record of cumulative deformation from its deposition to the present. Host rocks of the study area consist of Mesozoic volcanic-sedimentary rocks of various metamorphic grades. The clear E-W orogen-parallel trend of host rock fabrics indicates that the dominant regional principal stress (σ_1) has been N-S since the Mesozoic. These host rock fabrics are bedding-parallel. Both foliation and bedding are consistently east-west striking and dipping moderately to the north (**Figure 8**). We interpret these structures to represent the Mesozoic to early Cenozoic subduction of the Neo-Tethyan plate beneath the Eurasian plate (e.g., Yin & Harrison, 2000).

In contrast to the consistent fabric orientation of the host rocks, magmatic fabrics of the Lhasa-Nyingchi region are variable (**Figure 5**). However, as shown in **Figure 6**, a longitudinal trend is identified that changes from primarily orogen-perpendicular (N-S) fabrics to the west to orogen-parallel (E-W) fabrics to the east. Since our fabric data coverage is concentrated in the Lhasa region (90°E - 92°E), we isolated both host rock and magmatic fabrics data from the area (**Figure 10**). While some scattering exists for the magmatic fabrics shown in (**Figure 10B**), the concentration of magmatic foliation poles indicates that the dominant foliation direction is north-south or orogen-perpendicular, different from the east-west orogen-parallel fabrics of the host rock. Since magmatic fabrics record regional incremental strain at the time of solidification, the scattering of magmatic fabric orientations implies transient shifts to the direction of regional principal

stress (σ_1), and the weak trend of orogen-perpendicular (N-S) orientation of the magmatic fabrics signifies the dominant direction of regional principal stress (σ_1) is orogen-parallel (E-W) during pluton emplacement.

We interpret the difference between the orientation of magmatic fabrics in the Lhasa region (orogen-perpendicular) and those of the host rock (orogen-parallel) to signify changes in regional principal stress (σ_1) orientations during the transition from subduction to collision. The cumulative finite strain recorded by the host rock reveals an orogen-perpendicular (N-S) contraction likely related to Mesozoic northward subduction of the Neo-Tethys beneath Eurasia. Subsequent magmatism during the Cenozoic is associated with N-S magmatic fabrics corresponding to regional principal stress direction that is oriented orogen-parallel. While host rock fabric orientations differ from the magmatic fabrics, we found kink bands in the host rock outcrops with their kink planes at a high angle to the E-W direction (**Figure 11**), which we interpret to result from the same orogen-parallel contraction that formed the N-S magmatic fabrics.

Correlation between magmatic fabrics and plate kinematics

The magmatic fabrics of the Gangdese batholith record how the upper plate strain is accommodated during the transition from ocean-continent subduction to continent-continent collision. The assumption of using magmatic fabrics to address tectonics is that the magmatic fabrics reflect the regional incremental strain rather than magma-chamber dynamics (see discussion on limitations). In **Figure 12** we compare the temporal history of magmatic foliation orientations with the kinematics of the subducting Indian plate derived from GPlates (Müller et al., 2018). The kinematics plot (**Figure 12A**) is

constructed using the model predicted motions of Indian plate relative to the stable Asian interior (Tarim plate). The convergence rate and angle curves show the same pattern as suggested by other studies (e.g., Copley et al., 2010).

Throughout the Late Cretaceous to Early Paleocene (90-60 Ma), convergence between India and Asia was near perpendicular (**Figure 12A**). The "head-on" convergence is associated with the subduction of the Neo-Tethyan ocean. The plate convergence rate increases from ~40 km/Myr to a peak value of ~160 km/Myr directly before collision. Magmatic foliations are generally subparallel to the orogen for plutons that crystallized during this time, except for fabrics from plutons collected ~90°E longitude; these are more orogen-perpendicular. Such dominant orogen-parallel magmatic fabrics have also been observed in the Late Cretaceous Sierra Nevada Batholith (e.g., Cao et al., 2015), and suggest the direction of principle stress σ_1 is orogen-perpendicular, associated with contractional plate boundary forcing.

From 60 to 30 Ma, the convergence rate drops back down to Late Cretaceous values (~50 km/Myr). Magmatic foliations show a significant change in orientation from orogen-parallel to orogen-perpendicular (**Figure 12B**). Such changes in magmatic fabric orientations have been interpreted to reflect changes in plate motion, resulting in a switch from arc-perpendicular contraction to dextral transpressive for the Mesozoic central Sierra Nevada arc, marking the initiation of oblique convergence between the Farallon and North American plates (Cao et al., 2015). However, for the Gangdese arc, the change in magmatic fabric orientation ~60 Ma is not justified by changes to India-Asia convergence angles. As shown in **Figure 12A**, the convergence angle between India and Asia remains perpendicular. Therefore, while the magmatic fabrics pre 60 Ma are the

result of perpendicular subduction of the Neo-Tethyan oceanic plate, the change in magmatic fabric orientations at ~60 Ma does not show a strong correlation to plate kinematics. Given the initial India-Asia collision age of ~60 Ma (e.g., Guillot et al., 2008; Hu et al., 2016; An et al., 2021), the nature of the transition from subduction to collision may have altered the crustal stress regime significantly. Further, the absence of tectonic deformation in the geologic record during the period between collision initiation (60 - 55 Ma) and activation of Gangdese Thrust (~30 Ma) is demonstrated by the preservation of the Eocene Linzizong Formation (e.g., Lee et al., 2009) in the Lhasa region, a sub-horizontal volcaniclastic strata that is gently folded (**Figure 13**). In **Figure 12B** we show magmatic fabrics formed between 60-30 Ma exhibit orogen-perpendicular fabrics, a shift from orogen-parallel fabrics formed in the Late Cretaceous. Thus, Eocene orogen-perpendicular fabrics in the upper crust are consistent with the argument that southern Tibet underwent minimal N-S contractional strain related to the India-Asia collision (e.g., Murphy et al., 1997).

Post-30 Ma, the convergence rate remains steady around ~50 km/Myr (**Figure 12A**). Magmatic foliation data for this period are limited to the eastern Lhasa region but shows considerable scattering with both orogen-perpendicular and orogen-parallel fabrics (**Figure 12B**). This variability may be due to a change in the Indian plate convergence angle, which shifts from near perpendicular (~90°) to an oblique angle of ~45° at around 20-15 Ma (**Figure 12A**).

Correlation between magmatic fabrics and crustal thickness

In addition to providing a record of regional principal stress orientations, magmatic fabrics can be used to interpret vertical crustal flow within the orogen (e.g., Benn et al., 2001). Field observations from convergent orogens during crustal thickening show constrictional strain corresponding to steep, sub-vertical lineations (e.g., Fossen & Tikoff, 1998; Poli & Oliver 2001; Cao et al., 2016). In contrast, fabrics associated with crustal thinning and extension are associated with sub-horizontal orientations (Klepeis et al., 2009). In **Figure 14D** we show the magmatic fabric lineation plunge angle since the late Cretaceous and identify 3 distinct stages: Pre-collision (100 - 60 Ma), magmatic lineations are sub-vertical. Syn-collision (60 - 50 Ma), fabrics orientations switch from sub-vertical to sub-horizontal, corresponding to the change of from crustal contraction to extension. Post-collision (50 - 30 Ma), fabric orientations switch back to sub-vertical.

The crustal construction-extension history derived from magmatic lineation and foliation orientations supports the exhumation/burial paths constrained using bedrock pressures (Cao et al., 2020) and is consistent with Tang et al. (2021) crustal thickness estimates using Eu anomalies in zircon. Pre-collision 100 - 60 Ma magmatic foliations are orogen-parallel, lineations are sub-vertical, with Al-in-hornblende barometry showing burial and thickening. We interpret this period to represent crustal thickening during normal subduction and continental arc magmatism. Syn-collision 60 - 50 Ma magmatic foliations and lineations both undergo a marked transition (orogen-parallel to orogen-perpendicular foliations, sub-vertical to sub-horizontal lineations), coeval with bedrock exhumation and crustal thinning. These changes may reflect the change of stress regime from contractional to extensional, associated with crustal thinning during the transition

from subduction to collision. Post-collision 50 - 30 Ma foliations are variable, and lineations switch back to sub-vertical. Bedrock pressure data indicate burial during this time and the crust is thought to thicken. This phase of crustal thickening may be related to the activation of regional thrust systems as well as horizontal underthrusting of the Indian lithosphere. While the multiple datasets outlined above and presented in **Figure 15** does show remarkable consistency, some temporal mismatch does exist which can be attributed to the coarse resolution of the available magmatic fabrics data.

Meanwhile, our crustal thickness history disagrees with the findings of Sundell et al. (2021), which predict crustal thinning between 90 - 70 Ma. The pre-collisional crustal thinning is used to argue for the late Cretaceous rifting of the Xigaze backarc, and the resulting Xigaze island arc that collided with India ~60 Ma (**Figure 14B**). Therefore, the orientations of both magmatic foliation and lineation favor the continental or microcontinent collision model involving the existence of the Greater India Basin north of the Indian lithosphere (**Figure 14C**).

Correlation between magmatic fabrics and convergence models

There is much controversy surrounding India's paleogeography and history of the India-Asia collision. The conundrum revolves around the observation that oceanic subduction spanning the entire plate margin ceased after the initial collision ~60 Ma (e.g., Ding et al., 2005), rendering the system continental (Replumaz et al., 2010; Searle et al., 2019). Shortening, extrusion, and horizontal underthrusting only sum up to a small portion of the total convergence, while most of the convergence between India and Asia since the collision is unaccounted for (e.g., van Hinsbergen et al., 2019).

There are three end-member models explaining the convergence between India and Asia since 60 Ma (van Hinsbergen, 2022). The conventional continental subduction model (Model C) predicts a large portion of the Indian continental lithosphere was subducted deeply into the mantle (**Figure 14A**, e.g., Ingalls et al., 2016). Alternative models invoke the existence of oceanic lithosphere to the north of Tibetan Himalaya (Model A) and initial collision with rifted Xigaze intraoceanic arc (**Figure 14B**, Tapponnier et al., 1981; Aitchison et al., 2007; Jagoutz et al., 2015; Kapp et al., 2019; Martin et al., 2020); or to the south (**Figure 14C**, van Hinsbertgen et al., 2012; 2019), as demonstrated by the proposed Greater India Basin and the collision with the Tibetan Himalaya microcontinent (Model M). In the latter 2 models, the proposed oceanic lithosphere is subducted after the initial collision.

For magmatic fabrics of the Gangdese batholith to switch from orogen-parallel to orogen-perpendicular orientations, an interruption to Late Cretaceous Neo-Tethyan oceanic subduction is needed at the southern Lhasa plate margin. Of the 3 end-member models described above, the continental subduction scenario (**Figure 14A**) suggests a change from oceanic to continental subduction, but this change in subduction material should cause enhanced friction and continue to produce orogen-parallel fabrics. In the case of the oceanic lithosphere to the north of the collision zone (**Figure 14B**), the Xigaze terrane rifts southward away from Asia during late Cretaceous and collides with India at ~60 Ma, and subduction along the southern Lhasa margin is thought to be continuous from late Cretaceous until ~45 Ma (Kapp et al., 2019). Therefore little change takes place at ~60 Ma along the southern Lhasa plate boundary to warrant the change in fabric orientations. For the last case (**Figure 14C**), the initial ~60 Ma collision involves the

Tibetan Himalaya microcontinent north of the Indian lithosphere separated by an oceanic lithosphere called the greater India basin (van Hinsbergen et al., 2012). In this scenario subduction at the southern Lhasa margin ceased after initial collision with Tibetan Himalaya and jumped southward. The termination of subduction and subsequent accretion of Tethyan Himalaya is a major reconfiguration of plate dynamics and may have altered the regional crustal stress regime during the transition from oceanic subduction to terrain accretion. Therefore, the microcontinent model which predicts the ~60 Ma collision of Tibetan Himalaya with Asia and the existence of the Greater India Basin north of the Indian lithosphere may be compatible with the observed switch from orogen-parallel to orogen-perpendicular fabrics.

Post 30 Ma, magmatic foliation orientations become more variable with both orogen-perpendicular and orogen-parallel fabrics present (**Figure 12B**). Seismological imaging reveals that the Tibetan lithosphere contains horizontally underthrusted crust and mantle lithosphere of Indian plate affinity (Nabelek et al., 2009; Replumaz et al., 2010; Agius & Lebedev, 2013; van Hinsbergen et al, 2019). The onset of underthrusting of the Indian lithosphere is thought to take place around 28 Ma at the syntaxis, and ~15 Ma at the longitude of Bhutan (van Hinsbergen et al., 2019; Qayyum et al., 2022). The underthrusting event may have altered the regional stress regime and affected the orientations of the magmatic fabrics. In summary, magmatic foliations of the Gangdese batholith record regional principal stress direction that is orogen-perpendicular pre-60 Ma, reflecting normal subduction of the Neo-Tethyan ocean. Since the initial collision ~60 Ma, the dynamics of the southern Lhasa plate boundary become quite complex, with possible terrain accretion, backarc rifting, slab roll back, crustal extrusion, and

underthrusting complicating the preserved magmatic fabrics signal. The change of convergence style from typical ocean-continent subduction to complex continent-continent convergence obscures the correlation between magmatic fabrics and plate kinematics. Therefore, post initial collision the upper Lhasa block may not be influenced by the N-S compressive stress associated with plate convergence as strongly as pre-collision, which may result in changes to the style and locus of tectonic deformation.

Assumptions and limitations

The main assumption in this study is the use of magmatic fabrics as a proxy for regional tectonics. We assume the magmatic fabrics are the result of regional incremental strain and snapshots of the maximum principal stress (σ_1) at the time of pluton emplacement. However, some fabrics maybe related to processes within the magma chamber. While efforts were made during data collection to avoid fabrics due to internal chamber dynamics, detailed mapping of individual plutons and better data coverage are needed to minimize this uncertainty. The fabrics measurements were taken in-situ, from massive outcrops of granitoids, with the assumption that they have not experienced significant rotation during the exhumation. Based on the geology of the study area, only a few thrust faults have been recognized (Gangdese thrust, e.g., Yin et al., 1994) and our fabric data are all located in the upper plate.

While fabrics data were correlated to time, we did not consider how emplacement depth can affect fabric orientations. Of the 45 plutons where magmatic fabrics measurements were taken, 11 plutons have their emplacement depths determined (Cao et al., 2020). In **Figure 16** we couple fabric data with depth and plot the magmatic foliation

strike orientations. 8 plutons were emplaced at 10 km or less (**Figure 16A**), while 3 were emplaced between 20 - 30 km (**Figure 16B**). The results show shallow plutons record mostly orogen-perpendicular fabrics, whereas the orogen-parallel fabrics are found in deeper plutons, consistent with host rock fabric orientations. For plutons with unknown emplacement depths, we can an approximate their emplacement depths based on the westward tilting trend of the eastern Gangdese crust (Cao et al., 2020). Surprisingly, the westernmost fabrics near the 90°E longitude interpreted to represent the shallow upper crust did not experience any orientation changes since the Late Cretaceous, while fabrics associated with the deeper crust to the east underwent a shift from orogen-parallel to orogen-perpendicular orientations pre- and syn-collision (**Figure 12B**). This discrepancy in principal stress orientations between the upper and mid crust may suggest that tectonic deformation and magmatism in different crustal levels are decoupled (e.g., Klepeis et al., 2004; Tornos et al., 2005; Wang et al., 2011). Furthermore, certain tradeoffs may exist between depth and temporal effects on fabric orientations, which warrant future studies. Studies comparing fabrics from other magmatic orogens are needed. However, there are no systematic research done on other major batholiths documenting how magmatic fabrics change with depth.

CONCLUSION

Magmatic fabrics of the eastern Gangdese Batholith are interpreted to represent incremental stain at the time of pluton emplacement and used them to deduce the directions of regional principal stress $\sigma 1$ as well as the expected response in crustal deformation. Through a field study in southern Tibet, we report magmatic foliation (n =

287) and lineation (n = 54) measurements from 45 dated plutons in the Lhasa to Nyingchi transect. While the host rock fabrics show consistent orogen-parallel orientations indicative of orogen-perpendicular finite strain since the Mesozoic associated with N-S contraction resulting from India-Asia convergence, magmatic fabrics orientations are variable thru time and are grouped into: (1) 100 - 60 Ma plutons with dominantly orogen-parallel foliations and sub-vertical lineations, (2) 60 - 30 Ma plutons with orogen-perpendicular fabrics and sub-horizontal lineations, and (3) <30 Ma plutons with variable foliations and sub-vertical lineations. We interpret pre-collision late Cretaceous fabrics to record normal convergence of the Neo-Tethyan subduction and thickening of the Gangdese crust, while syn-collision 60 - 30 Ma fabrics represent a change in crustal stress regime from contraction to extension, leading to crustal thinning. Post-collision <30 Ma fabrics signal another switch back to crustal thickening without a clear, dominant stress regime, perhaps due to the array of post-collisional processes such as horizontal underthrusting of India lithosphere and changes in plate convergence angle. Our fabrics data is compatible with the Greater India Basin hypothesis (van Hinsbergen et al., 2012, 2019), and highlights the geodynamic complexities during and after India-Asia continental collision.

REFERENCES

Agard, P., Monié, P., Gerber, W., Omrani, J., Molinaro, M., Meyer, B., Labrousse, L., Vrielynck, B., Jolivet, L. and Yamato, P., 2006. Transient, synobduction exhumation of Zagros blueschists inferred from P-T, deformation, time, and kinematic constraints: Implications for Neotethyan wedge dynamics. Journal of Geophysical Research: Solid Earth, 111(B11).

Agius, M.R. and Lebedev, S., 2013. Tibetan and Indian lithospheres in the upper mantle beneath Tibet: Evidence from broadband surface-wave dispersion. Geochemistry, Geophysics, Geosystems, 14(10), pp.4260-4281.

Aitchison, J.C., Ali, J.R. and Davis, A.M., 2007. When and where did India and Asia collide?. Journal of Geophysical Research: Solid Earth, 112(B5).

Allmendinger, R.W., Cardozo, N. and Fisher, D.M., 2011. Structural geology algorithms: Vectors and tensors. Cambridge University Press.

An, W., Hu, X., Garzanti, E., Wang, J.G. and Liu, Q., 2021. New precise dating of the India-Asia collision in the Tibetan Himalaya at 61 Ma. Geophysical Research Letters, 48(3), p.e2020GL090641.

Archanjo, C.J., da Silva, E.R. and Caby, R., 1999. Magnetic fabric and pluton emplacement in a transpressive shear zone system: the Itaporanga porphyritic granitic pluton (northeast Brazil). Tectonophysics, 312(2-4), pp.331-345.

Ardill, K.E., Paterson, S.R., Stanback, J., Alasino, P.H., King, J.J. and Crosbie, S.E., 2020. Schlieren-bound magmatic structures record crystal flow-sorting in dynamic upper-crustal magma-mush chambers. Frontiers in Earth Science, p.190.

Balk, R., 1937. The structural behavior of igneous rocks. Geol. Soc. Amer. Mem., (5), p.177p.

Barros, C.E.M., Barbey, P. and Boullier, A.M., 2001. Role of magma pressure, tectonic stress and crystallization progress in the emplacement of syntectonic granites. The A-type Estrela Granite Complex (Carajás Mineral Province, Brazil). Tectonophysics, 343(1-2), pp.93-109.

Beltrando, M., Compagnoni, R. and Lombardo, B., 2010. (Ultra-) High-pressure metamorphism and orogenesis: an Alpine perspective. Gondwana Research, 18(1), pp.147-166.

Bouchez, J.L., 1997. Granite is never isotropic: an introduction to AMS studies of granitic rocks. In Granite: from segregation of melt to emplacement fabrics (pp. 95-112). Springer, Dordrecht.

Callahan, C.N. and Markley, M.J., 2003. A record of crustal-scale stress; igneous foliation and lineation in the Mount Waldo Pluton, Waldo County, Maine. Journal of Structural Geology, 25(4), pp.541-555.

Cao, W., Paterson, S., Memeti, V., Mundil, R., Anderson, J.L. and Schmidt, K., 2015. Tracking paleodeformation fields in the Mesozoic central Sierra Nevada arc: Implications for intra-arc cyclic deformation and arc tempos. Lithosphere, 7(3), pp.296-320.

Cao, W., Paterson, S., Saleeby, J. and Zalunardo, S., 2016. Bulk arc strain, crustal thickening, magma emplacement, and mass balances in the Mesozoic Sierra Nevada arc. Journal of Structural Geology, 84, pp.14-30.

Cao, W., Yang, J., Zuza, A.V., Ji, W.Q., Ma, X.X., Chu, X. and Burgess, Q.P., 2020. Crustal tilting and differential exhumation of Gangdese Batholith in southern Tibet revealed by bedrock pressures. Earth and Planetary Science Letters, 543, p.116347.

Chang, C.F., and Zheng, S.L., 1973. Tectonic features of the Mount Jolmu Lungma region in southern Tibet, China (in Chinese), Sci. Geol. Sin., 1(1–12).

Chapman, J.B. and Kapp, P., 2017. Tibetan magmatism database. Geochemistry, Geophysics, Geosystems, 18(11), pp.4229-4234.

Chung, S.L., Liu, D., Ji, J., Chu, M.F., Lee, H.Y., Wen, D.J., Lo, C.H., Lee, T.Y., Qian, Q. and Zhang, Q., 2003. Adakites from continental collision zones: melting of thickened lower crust beneath southern Tibet. Geology, 31(11), pp.1021-1024.

Chung, S.L., Chu, M.F., Zhang, Y., Xie, Y., Lo, C.H., Lee, T.Y., Lan, C.Y., Li, X., Zhang, Q. and Wang, Y., 2005. Tibetan tectonic evolution inferred from spatial and temporal variations in post-collisional magmatism. Earth-Science Reviews, 68(3-4), pp.173-196.

Copley, A., Avouac, J.P. and Royer, J.Y., 2010. India-Asia collision and the Cenozoic slowdown of the Indian plate: Implications for the forces driving plate motions. Journal of Geophysical Research: Solid Earth, 115(B3).

de Saint Blanquat, M., Horsman, E., Habert, G., Morgan, S., Vanderhaeghe, O., Law, R. and Tikoff, B., 2011. Multiscale magmatic cyclicity, duration of pluton construction, and the paradoxical relationship between tectonism and plutonism in continental arcs. Tectonophysics, 500(1-4), pp.20-33.

Dewey, J.F., Shackleton, R.M., Chengfa, C. and Yiyin, S., 1988. The tectonic evolution of the Tibetan Plateau. Philosophical Transactions of the Royal Society of London. Series A, Mathematical and Physical Sciences, 327(1594), pp.379-413.

Ding, L., Kapp, P. and Wan, X., 2005. Paleocene–Eocene record of ophiolite obduction and initial India-Asia collision, south central Tibet. Tectonics, 24(3).

Dürr, S.B., 1996. Provenance of Xigaze fore-arc basin clastic rocks (Cretaceous, south Tibet). Geological Society of America Bulletin, 108(6), pp.669-684.

Edwards, M.A. and Harrison, T.M., 1997. When did the roof collapse? Late Miocene north-south extension in the high Himalaya revealed by Th-Pb monazite dating of the Khula Kangri granite. Geology, 25(6), pp.543-546.

England, P. and Houseman, G., 1986. Finite strain calculations of continental deformation: 2. Comparison with the India-Asia collision zone. Journal of Geophysical Research: Solid Earth, 91(B3), pp.3664-3676.

Flowers, R.M., Mahan, K.H., Bowring, S.A., Williams, M.L., Pringle, M.S. and Hodges, K.V., 2006. Multistage exhumation and juxtaposition of lower continental crust in the western Canadian Shield: Linking high-resolution U-Pb and 40Ar/39Ar thermochronometry with pressure-temperature-deformation paths. Tectonics, 25(4).

Fossen, H., 2016. Structural geology. Cambridge university press.

Gansser, A., 1964. Geology of the Himalayas.

Guillot, S., Mahéo, G., de Sigoyer, J., Hattori, K.H. and Pecher, A., 2008. Tethyan and Indian subduction viewed from the Himalayan high-to ultrahigh-pressure metamorphic rocks. Tectonophysics, 451(1-4), pp.225-241.

Hacker, B.R., Andersen, T.B., Johnston, S., Kylander-Clark, A.R., Peterman, E.M., Walsh, E.O. and Young, D., 2010. High-temperature deformation during continental-margin subduction & exhumation: The ultrahigh-pressure Western Gneiss Region of Norway. Tectonophysics, 480(1-4), pp.149-171.

Harrison, T.M., Copeland, P., Kidd, W.S.F. and Yin, A.N., 1992. Raising tibet. Science, 255(5052), pp.1663-1670.

Harrison, T.M., Copeland, P., Kidd, W.S.F. and Lovera, O.M., 1995. Activation of the Nyainqentanghla shear zone: Implications for uplift of the southern Tibetan Plateau. Tectonics, 14(3), pp.658-676.

He, S., Kapp, P., DeCelles, P.G., Gehrels, G.E. and Heizler, M., 2007. Cretaceous–Tertiary geology of the Gangdese Arc in the Linzhou area, southern Tibet. Tectonophysics, 433(1-4), pp.15-37.

Heim A, Gansser A. 1939. Central Himalaya Geological Observations of Swiss Expedition, pp. 1–246. Zurich: Gebruder Fretz

Hou, Z.Q., Ma, H.W. and Khin Zaw, Z., Z., Pan, G.-T., Tang, R.-L., 2003. The Himalayan Yulong porphyry copper belt: product of large-scale strike slip faulting in Eastern Tibet. Economic Geology, 98, pp.125-145.

Hu, X., Garzanti, E., Wang, J., Huang, W., An, W. and Webb, A., 2016. The timing of India-Asia collision onset–Facts, theories, controversies. Earth-Science Reviews, 160, pp.264-299.

Ingalls, M., Rowley, D.B., Currie, B. and Colman, A.S., 2016. Large-scale subduction of continental crust implied by India–Asia mass-balance calculation. Nature Geoscience, 9(11), pp.848-853.

Jagoutz, O., Royden, L., Holt, A.F. and Becker, T.W., 2015. Anomalously fast convergence of India and Eurasia caused by double subduction. Nature Geoscience, 8(6), pp.475-478.

Ji, W.Q., Wu, F.Y., Chung, S.L., Li, J.X., Liu, C.Z., 2009. Zircon U–Pb geochronology and Hf isotopic constraints on petrogenesis of the Gangdese batholith, southern Tibet. Chem. Geol. 262 (3–4), 229–245.

Ji, W.-Q., Wu, F.-Y., Chung, S.-L., Liu, C.-Z., 2014. The Gangdese magmatic constraints on a latest Cretaceous lithospheric delamination of the Lhasa terrane, southern Tibet. Lithos 210–211, 1–13. https://doi.org/10.1016/j.lithos.2014.10.001.

Jolivet, L., 2001. A comparison of geodetic and finite strain pattern in the Aegean, geodynamic implications. Earth and Planetary science letters, 187(1-2), pp.95-104.

Kapp, P., Yin, A., Manning, C.E., Harrison, T.M., Taylor, M.H. and Ding, L., 2003. Tectonic evolution of the early Mesozoic blueschist-bearing Qiangtang metamorphic belt, central Tibet. Tectonics, 22(4).

Kapp, P., Yin, A., Harrison, T.M. and Ding, L., 2005. Cretaceous-Tertiary shortening, basin development, and volcanism in central Tibet. Geological Society of America Bulletin, 117(7-8), pp.865-878.

Kapp, P. and DeCelles, P.G., 2019. Mesozoic–Cenozoic geological evolution of the Himalayan-Tibetan orogen and working tectonic hypotheses. American Journal of Science, 319(3), pp.159-254.

Kapp, P., DeCelles, P.G., Leier, A.L., Fabijanic, J.M., He, S., Pullen, A., Gehrels, G.E. and Ding, L., 2007. The Gangdese retroarc thrust belt revealed. GSA today, 17(7), p.4.

Klepeis, K.A., King, D.S., Miller, R.B. and Snoke, A.W., 2009. Evolution of the middle and lower crust during the transition from contraction to extension in Fiordland, New Zealand. Geological Society of America Bulletin, 456, pp.243-265.

Laskowski, A.K., Kapp, P. and Cai, F., 2018. Gangdese culmination model: Oligocene–Miocene duplexing along the India-Asia suture zone, Lazi region, southern Tibet. GSA Bulletin, 130(7-8), pp.1355-1376.

Lee, J., Hacker, B.R., Dinklage, W.S., Wang, Y., Gans, P., Calvert, A., Wan, J., Chen, W., Blythe, A.E. and McClelland, W., 2000. Evolution of the Kangmar Dome, southern Tibet: Structural, petrologic, and thermochronologic constraints. Tectonics, 19(5), pp.872-895.

Lee, H.Y., Chung, S.L., Lo, C.H., Ji, J., Lee, T.Y., Qian, Q. and Zhang, Q., 2009. Eocene Neotethyan slab breakoff in southern Tibet inferred from the Linzizong volcanic record. Tectonophysics, 477(1-2), pp.20-35.Molnar, P., 1988. A review of geophysical constraints on the deep structure of the Tibetan Plateau, the Himalaya and the Karakoram, and their tectonic implications. Phil. Trans. R. Soc. Lond. A, 326(1589), pp.33-88.

Leech, M.L., Singh, S., Jain, A.K., Klemperer, S.L. and Manickavasagam, R.M., 2005. The onset of India–Asia continental collision: early, steep subduction required by the

timing of UHP metamorphism in the western Himalaya. Earth and Planetary Science Letters, 234(1-2), pp.83-97.

Leier, A.L., Kapp, P., Gehrels, G.E. and DeCelles, P.G., 2007. Detrital zircon geochronology of Carboniferous–Cretaceous strata in the Lhasa terrane, Southern Tibet. Basin Research, 19(3), pp.361-378.

Leloup, P.H., Arnaud, N., Lacassin, R., Kienast, J.R., Harrison, T.M., Trong, T.P., Replumaz, A. and Tapponnier, P., 2001. New constraints on the structure, thermochronology, and timing of the Ailao Shan-Red River shear zone, SE Asia. Journal of Geophysical Research: Solid Earth, 106(B4), pp.6683-6732.

Liu, M., Zhu, D.C., Zhao, Z.D., Mo, X.X., Guan, Q., Zhang, L.L., Yu, F. and Liu, M.H., 2010. Magma mixing of late Early Jurassic age from Nyainrong, northern Tibet and its tectonic significance. Acta Petrologica Sinica, 26(10), pp.3117-3130.

Ma, X., Attia, S., Cawood, T., Cao, W., Xu, Z. and Li, H., 2022. Arc tempos of the Gangdese batholith, southern Tibet. Journal of Geodynamics, 149, p.101897.

Martelat, J.E., Lardeaux, J.M., Nicollet, C. and Rakotondrazafy, R., 2000. Strain pattern and late Precambrian deformation history in southern Madagascar. Precambrian research, 102(1-2), pp.1-20.

Martin, C.R., Jagoutz, O., Upadhyay, R., Royden, L.H., Eddy, M.P., Bailey, E., Nichols, C.I. and Weiss, B.P., 2020. Paleocene latitude of the Kohistan–Ladakh arc indicates multistage India–Eurasia collision. Proceedings of the National Academy of Sciences, 117(47), pp.29487-29494.

McKenzie, D. and Jackson, J., 1983. The relationship between strain rates, crustal thickening, palaeomagnetism, finite strain and fault movements within a deforming zone. Earth and Planetary Science Letters, 65(1), pp.182-202.

Meng, F.Y., Zhao, Z., Zhu, D.C., Mo, X., Guan, Q., Huang, Y., Dong, G., Zhou, S., DePaolo, D.J., Harrison, T.M. and Zhang, Z., 2014. Late Cretaceous magmatism in Mamba area, central Lhasa subterrane: products of back-arc extension of Neo-Tethyan Ocean?. Gondwana Research, 26(2), pp.505-520.

Metcalfe, I., 2011. Tectonic framework and Phanerozoic evolution of Sundaland. Gondwana Research, 19(1), pp.3-21.

Mo, X.X., Zhao, Z.D., Deng, J.F., Dong, G.C., Zhou, S., Guo, T.Y., Zhang, S.Q. and Wang, L.L., 2003. Response of volcanism to the India-Asia collision. Earth Science Frontiers, 10(3), pp.135-148.

Molnar, P., 1988. A review of geophysical constraints on the deep structure of the Tibetan Plateau, the Himalaya and the Karakoram, and their tectonic implications. Phil. Trans. R. Soc. Lond. A, 326(1589), pp.33-88.

Molnar, P. and Tapponnier, P., 1975. Cenozoic tectonics of Asia: effects of a continental collision. Science, 189(4201), pp.419-426.

Molnar, P. and Tapponnier, P., 1978. Active tectonics of Tibet. Journal of Geophysical Research: Solid Earth, 83(B11), pp.5361-5375.

Müller, R.D., Cannon, J., Qin, X., Watson, R.J., Gurnis, M., Williams, S., Pfaffelmoser, T., Seton, M., Russell, S.H. and Zahirovic, S., 2018. GPlates: building a virtual Earth through deep time. Geochemistry, Geophysics, Geosystems, 19(7), pp.2243-2261.

Murphy, M.A., Yin, A., Harrison, T.M., Durr, S.B., Ryerson, F.J. and Kidd, W.S.F., 1997. Did the Indo-Asian collision alone create the Tibetan plateau?. Geology, 25(8), pp.719-722.

Nábělek, J., Hetényi, G., Vergne, J., Sapkota, S., Kafle, B., Jiang, M., Su, H., Chen, J., Huang, B.S. and Team, T.H.C., 2009. Underplating in the Himalaya-Tibet collision zone revealed by the Hi-CLIMB experiment. Science, 325(5946), pp.1371-1374.

Najman, Y., Appel, E., Boudagher-Fadel, M., Bown, P., Carter, A., Garzanti, E., Godin, L., Han, J., Liebke, U., Oliver, G. and Parrish, R., 2010. Timing of India-Asia collision: Geological, biostratigraphic, and palaeomagnetic constraints. Journal of Geophysical Research: Solid Earth, 115(B12).

Pan, Y., Copeland, P., Roden, M.K., Kidd, W.S.F. and Harrison, T.M., 1993. Thermal and unroofing history of the Lhasa area, southern Tibet—Evidence from apatite fission track thermochronology. Nuclear Tracks and Radiation Measurements, 21(4), pp.543-554.

Pan, Y. and Kidd, W.S.F., 1999. Shortening in the southern Lhasa block during India-Asia collision. European Journal of Mineralogy, 9, pp.1073-1083.

Pan, G., Wang, L., Li, R., Yuan, S., Ji, W., Yin, F., Zhang, W. and Wang, B., 2012. Tectonic evolution of the Qinghai-Tibet plateau. Journal of Asian Earth Sciences, 53, pp.3-14.

Paterson, S.R., Fowler, T.K., Schmidt, K.L., Yoshinobu, A.S., 1998. Interpreting magmatic fabric patterns in plutons. Lithos 44, 53–82. doi:10.1016/S0024-4937(98)00022-X

Paterson S.R. Okaya D. Memeti V. Economos R. Miller R.B., 2011, Magma addition and flux calculations of incrementally constructed magma chambers in continental margin arcs: Combined field, geochronologic, and thermal modeling studies: Geosphere , v. 7, p. 1439–1468, doi:10.1130/GES00696.1.

Paterson, S. R., Vernon, R. H. & Tobisch, O. T. 1989. A review of criteria for identification of magmatic and tectonic foliations in granitoids. Journal of Structural Geology 11 , 349–63.

Payacán, I., Gutiérrez, F., Gelman, S.E., Bachmann, O. and Parada, M.Á., 2014. Comparing magnetic and magmatic fabrics to constrain the magma flow record in La Gloria pluton, central Chile. Journal of Structural Geology, 69, pp.32-46.

Paterson, S.R., Ardill, K., Vernon, R. and Žák, J., 2019. A review of mesoscopic magmatic structures and their potential for evaluating the hypersolidus evolution of intrusive complexes. Journal of Structural Geology, 125, pp.134-147.

Petford, N., Cruden, A.R., McCaffrey, K.J.W. and Vigneresse, J.L., 2000. Granite magma formation, transport and emplacement in the Earth's crust. Nature, 408(6813), p.669.

Qayyum, A., Lom, N., Advokaat, E.L., Spakman, W., Van Der Meer, D.G. and Van Hinsbergen, D.J.J., 2022. Subduction and slab detachment under moving trenches during ongoing India-Asia convergence.

Replumaz, A., Negredo, A.M., Villasenor, A. and Guillot, S., 2010. Indian continental subduction and slab break-off during Tertiary collision. Terra Nova, 22(4), pp.290-296.

Roeder, D., Roberts, D.G. and Bally, A.W., 2013. Convergent margins and orogenic belts. Regional Geology and Tectonics: Principles of Geologic Analysis A, 1, pp.114-177.

Searle, M.P., 2019. Timing of subduction initiation, arc formation, ophiolite obduction and India–Asia collision in the Himalaya. Geological Society, London, Special Publications, 483(1), pp.19-37.

Sundell, K.E., Laskowski, A.K., Kapp, P.A., Ducea, M.N. and Chapman, J.B., 2021. Jurassic to Neogene quantitative crustal thickness estimates in southern Tibet. GSA Today, 31(6), pp.4-10.

Tang, M., Ji, W.Q., Chu, X., Wu, A. and Chen, C., 2021. Reconstructing crustal thickness evolution from europium anomalies in detrital zircons. Geology, 49(1), pp.76-80.

Tapponnier, P., Mattauer, M., Proust, F. and Cassaigneau, C., 1981. Mesozoic ophiolites, sutures, and arge-scale tectonic movements in Afghanistan. Earth and Planetary Science Letters, 52(2), pp.355-371.

Tunik, M., Folguera, A., Naipauer, M., Pimentel, M. and Ramos, V.A., 2010. Early uplift and orogenic deformation in the Neuquén Basin: constraints on the Andean uplift from U–Pb and Hf isotopic data of detrital zircons. Tectonophysics, 489(1-4), pp.258-273.

van Hinsbergen, D.J., Lippert, P.C., Dupont-Nivet, G., McQuarrie, N., Doubrovine, P.V., Spakman, W. and Torsvik, T.H., 2012. Greater India Basin hypothesis and a two-stage Cenozoic collision between India and Asia. Proceedings of the National Academy of Sciences, 109(20), pp.7659-7664.

van Hinsbergen, D.J., Lippert, P.C., Li, S., Huang, W., Advokaat, E.L. and Spakman, W., 2019. Reconstructing Greater India: Paleogeographic, kinematic, and geodynamic perspectives. Tectonophysics, 760, pp.69-94.

van Hinsbergen, D.J., 2022. Indian Plate paleogeography, subduction, and horizontal underthrusting below Tibet: paradoxes, controvercies, and opportunities.

van Kranendonk, M.J., 1996. Tectonic evolution of the Paleoproterozoic Torngat Orogen: Evidence from pressure-temperature-time-deformation paths in the North River map area, Labrador. Tectonics, 15(4), pp.843-869.

Vernon R.H., 2000, Review of microstructural evidence of magmatic and solid-state flow: Visual Geosciences , v. 5, p. 1–23, doi:10.1007/s10069-000-0002-3.

Willner, A.P., Krohe, A. and Maresch, W.V., 2000. Interrelated PTtd paths in the Variscan Erzgebirge dome (Saxony, Germany): Constraints on the rapid exhumation of high-pressure rocks from the root zone of a collisional orogen. International Geology Review, 42(1), pp.64-85.

Yin, A., Harrison, T.M., Ryerson, F.J., Wenji, C., Kidd, W.S.F. and Copeland, P., 1994. Tertiary structural evolution of the Gangdese thrust system, southeastern Tibet. Journal of Geophysical Research: Solid Earth, 99(B9), pp.18175-18201.

Yin, A., Harrison, T.M., Murphy, M.A., Grove, M., Nie, S., Ryerson, F.J., Xiao Feng, W. and Zeng Le, C., 1999. Tertiary deformation history of southeastern and southwestern Tibet during the Indo-Asian collision. Geological Society of America Bulletin, 111(11), pp.1644-1664.

Yin, A. and Harrison, T.M., 2000. Geologic evolution of the Himalayan-Tibetan orogen. Annual Review of Earth and Planetary Sciences, 28(1), pp.211-280.

Zak, J., Verner, K. and Tycova, P., 2008. Multiple magmatic fabrics in plutons: an overlooked tool for exploring interactions between magmatic processes and regional deformation?. Geological Magazine, 145(4), pp.537-551.

Zhang, P.Z., Shen, Z., Wang, M., Gan, W., Bürgmann, R., Molnar, P., Wang, Q., Niu, Z., Sun, J., Wu, J. and Hanrong, S., 2004. Continuous deformation of the Tibetan Plateau from global positioning system data. Geology, 32(9), pp.809-812.

Zhang, Z.M., Dong, X., Santosh, M. and Zhao, G.C., 2014. Metamorphism and tectonic evolution of the Lhasa terrane, Central Tibet. Gondwana Research, 25(1), pp.170-189.

Zhu, D.C., Zhao, Z.D., Niu, Y., Mo, X.X., Chung, S.L., Hou, Z.Q., Wang, L.Q. and Wu, F.Y., 2011. The Lhasa Terrane: Record of a microcontinent and its histories of drift and growth. Earth and Planetary Science Letters, 301(1-2), pp.241-255.

Zhu, D.C., Zhao, Z.D., Niu, Y., Dilek, Y., Hou, Z.Q. and Mo, X.X., 2013. The origin and pre-Cenozoic evolution of the Tibetan Plateau. Gondwana Research, 23(4), pp.1429-1454.

Zhu, D.-C., Wang, Q., Zhao, Z.-D., Chung, S.-L., Cawood, P.A., Niu, Y., Liu, S.A., Wu, F.-Y., Mo, X.-X., 2015. Magmatic record of India-Asia collision. Sci. Rep. 5, 14289.

Zhu, D.C., Li, S.M., Cawood, P.A., Wang, Q., Zhao, Z.D., Liu, S.A. and Wang, L.Q., 2016. Assembly of the Lhasa and Qiangtang terranes in central Tibet by divergent double subduction. Lithos, 245, pp.7-17.

FIGURES

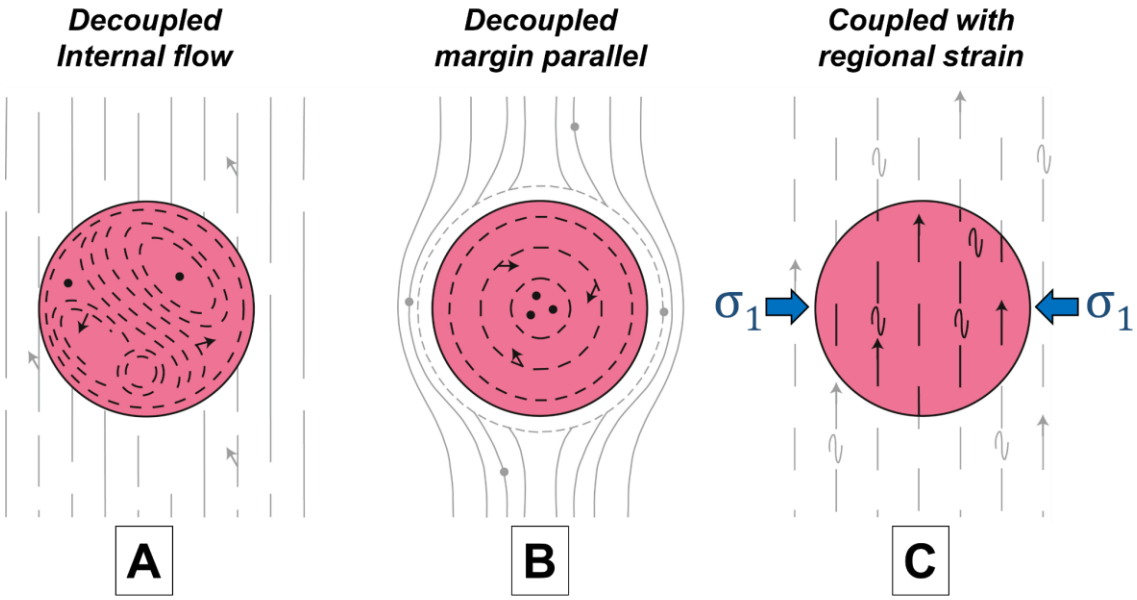

Figure 4.1. Cartoon showing the coupling of magmatic fabrics in plutons (pink) with regional host rock strain. (**A**) Decoupled system showing complex internal flow. (**B**) Decoupled margin-parallel pattern associated with magma chamber dynamics. (**C**) Coupled magmatic foliation and regional deformation. Note the orientation of the regional principal stress (σ_1) is orthogonal to the resulting fabrics. Modified from Paterson et al. (2019).

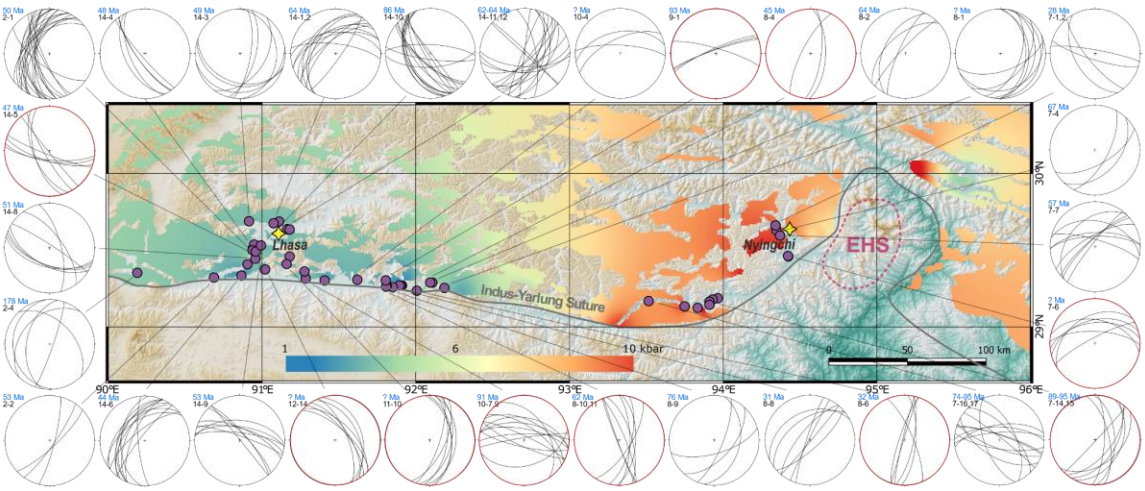

Figure 4.2. Topographic map of the Lhasa-Nyingchi study area showing locations of in-situ magmatic fabric measurements (purple dots). Colored shading represents pluton emplacement pressures using IDW interpolation. This area is an example of a tilted crustal section, exposing deeper (~10 kbar) rocks to the east (Cao et al., 2020). Red highlight is used to indicate emplacement pressure is known for the pluton.

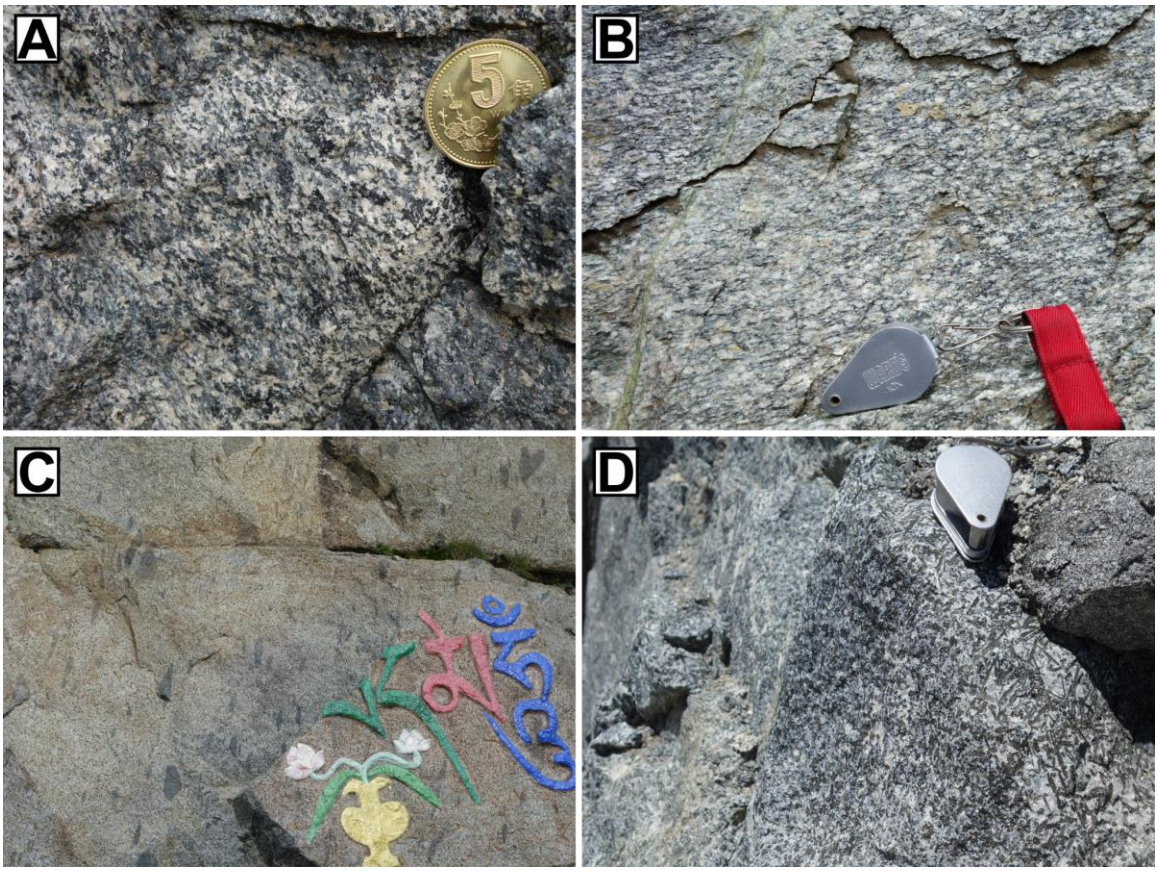

Figure 4.3. Field photos showing magmatic fabrics on outcrops from four different Gangdese plutons. The shape-preferred orientation of plagioclase, hornblende, and biotite mineral grains are linearly aligned, forming magmatic foliations with various orientations. Vertically (**A**) and horizontally (**B**) oriented foliations. (**C**) Mafic enclaves are present in some plutons, their long axes paralleling the direction of magmatic foliation. (**D**) Euhedral lath-shaped hornblende crystals.

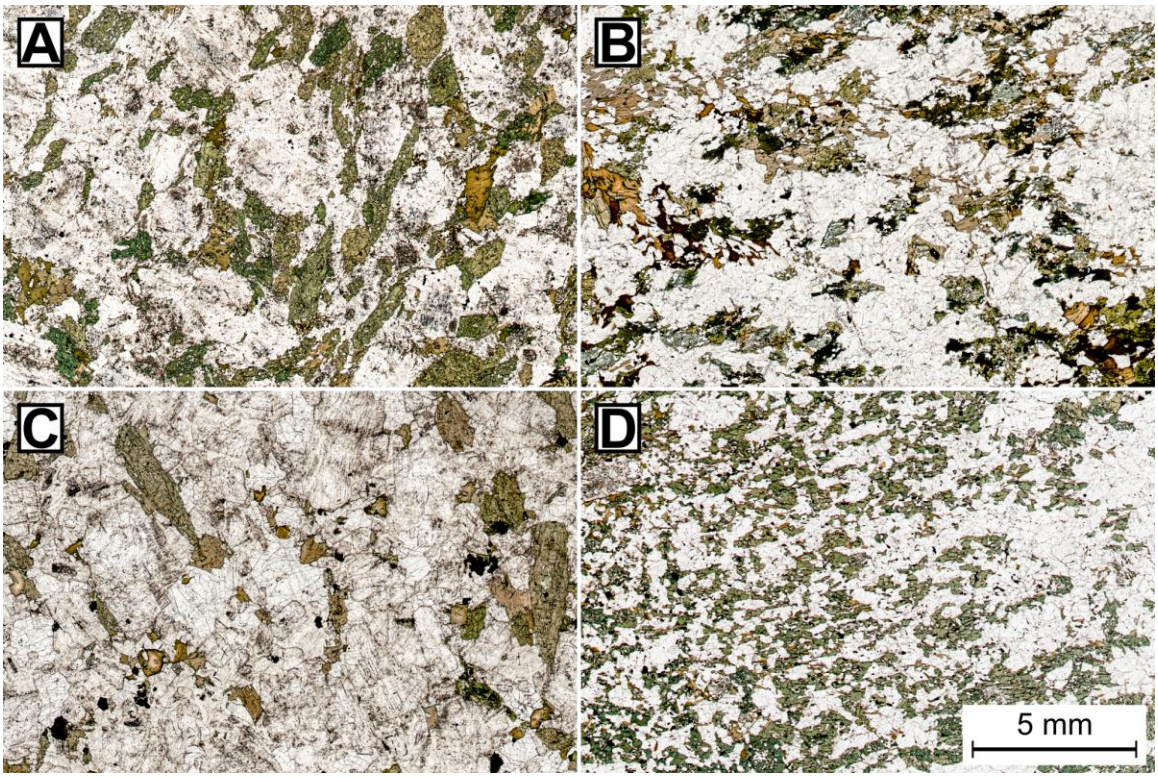

Figure 4.4. Microphotographs of representative thin sections in plain light, showing the shape-preferred alignment of elongated euhedral hornblende (green). Plutons emplaced in the shallow upper crust include sample XCT58 (**A**), with a crystallization age of 46.4 Ma and 1.9 kbar emplacement depth; sample 11-10 (**C**), located near Lhasa with 44.5 Ma crystallization age and 2.1 kbar emplacement depth. Examples of plutons emplaced in the mid-lower crust include sample 7-14 (**B**), with a crystallization age of 88.7 Ma, and an emplacement depth of 6.8 kbar; sample ML04 (**D**), located near Nyingchi with a crystallization age of 86.5 Ma and an emplacement depth of 7.5 kbar. Sample age and depth data are taken from Cao et al. (2020).

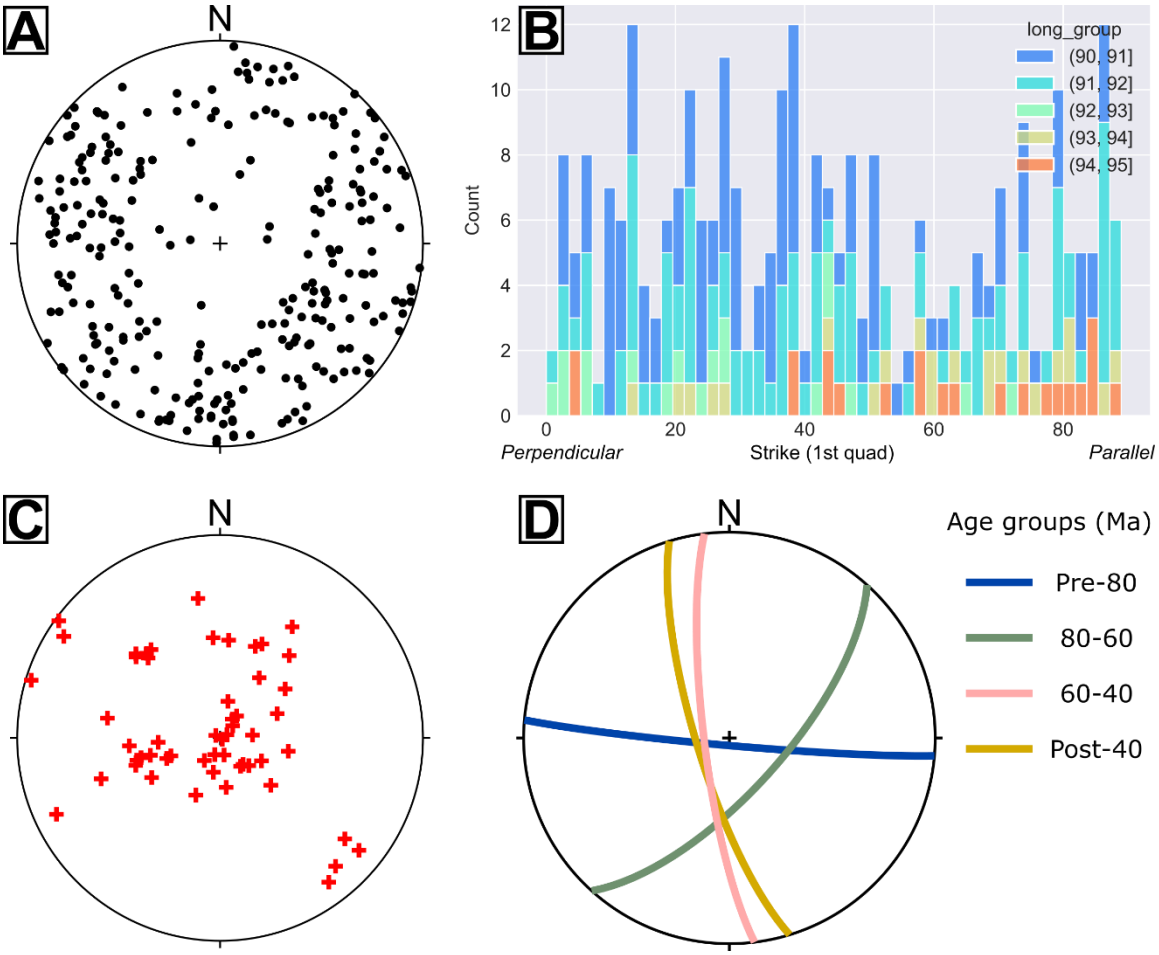

Figure 4.5. Plots of magmatic fabric data. (**A)** All measurements of magmatic foliations (n = 287) with their poles projected in the lower hemisphere stereonet. The majority of the foliations dip steeply. (**B**) Histogram of all magmatic foliation strike measurements converted to their equivalent 1st quadrant orientations. (**C**) All magmatic lineations (n = 54). (**D**) Temporal averages of magmatic foliation measurements showing the orogen-parallel (E-W) fabric orientations pre-60 Ma (blue and green lines) contrasting the orogen-perpendicular (N-S) fabrics post-60 Ma (pink and yellow lines).

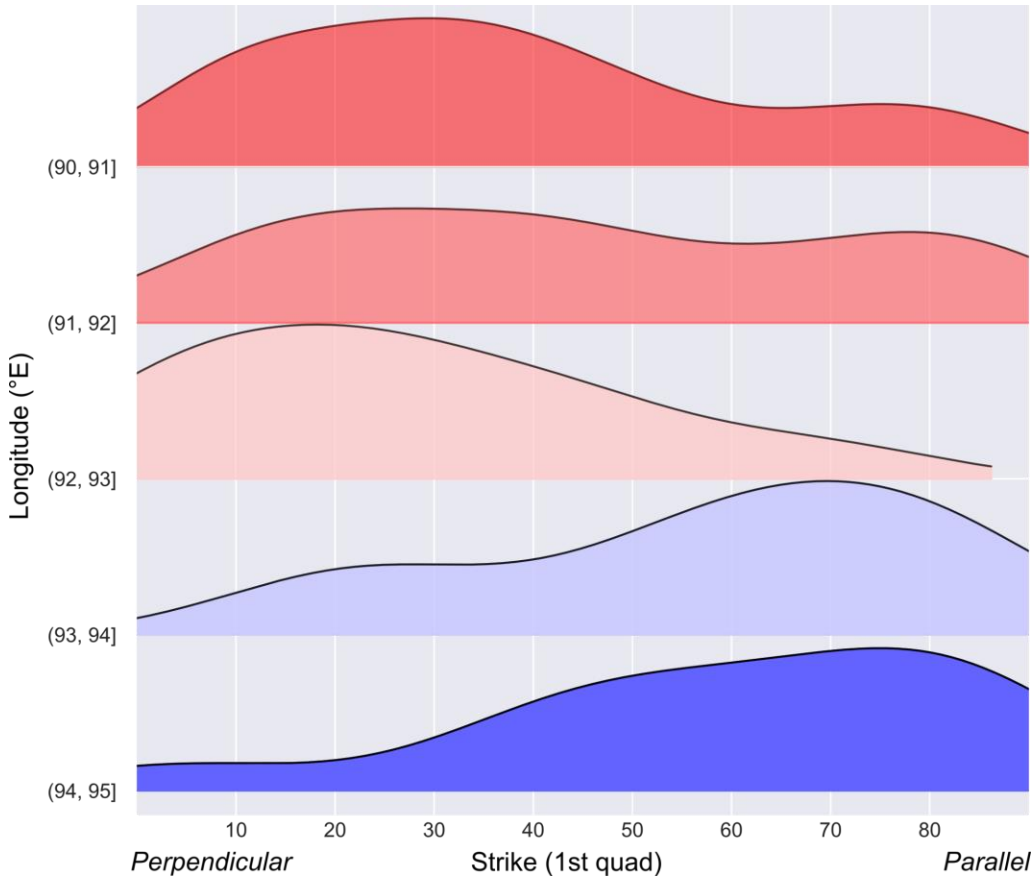

Figure 4.6. Magmatic foliation strike measurements binned based on longitude (westernmost at the top, progressively more east downward). The strike measurements are converted to their equivalent 1st quadrant orientations. Note a shift from primarily orogen-perpendicular fabrics in the west to orogen-parallel fabrics in the east.

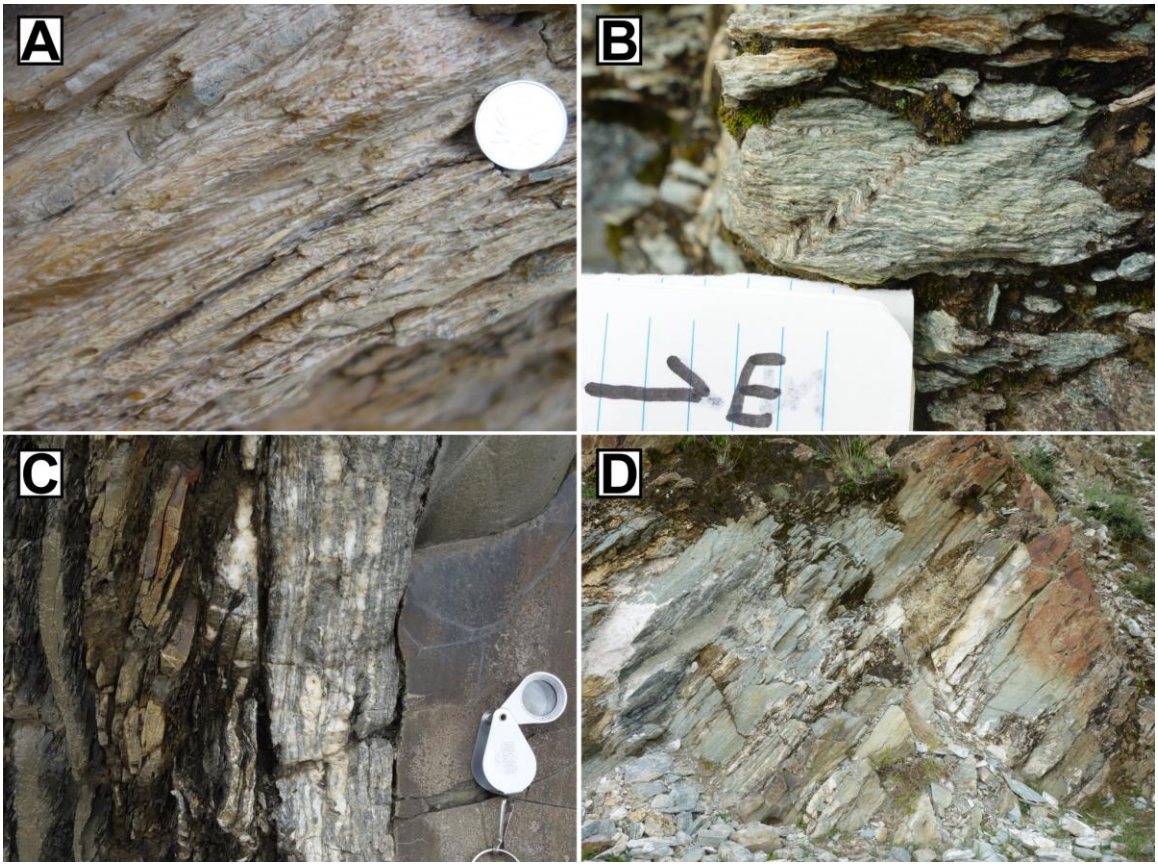

Figure 4.7. Field photos of Gangdese host rocks showing: (**A**) wavy phyllitic foliation, (**B**) kink bends, (**C**) gneiss in between 2 layers of shale, where cleavage parallels bedding, and (**D**) package of steeply dipping beds.

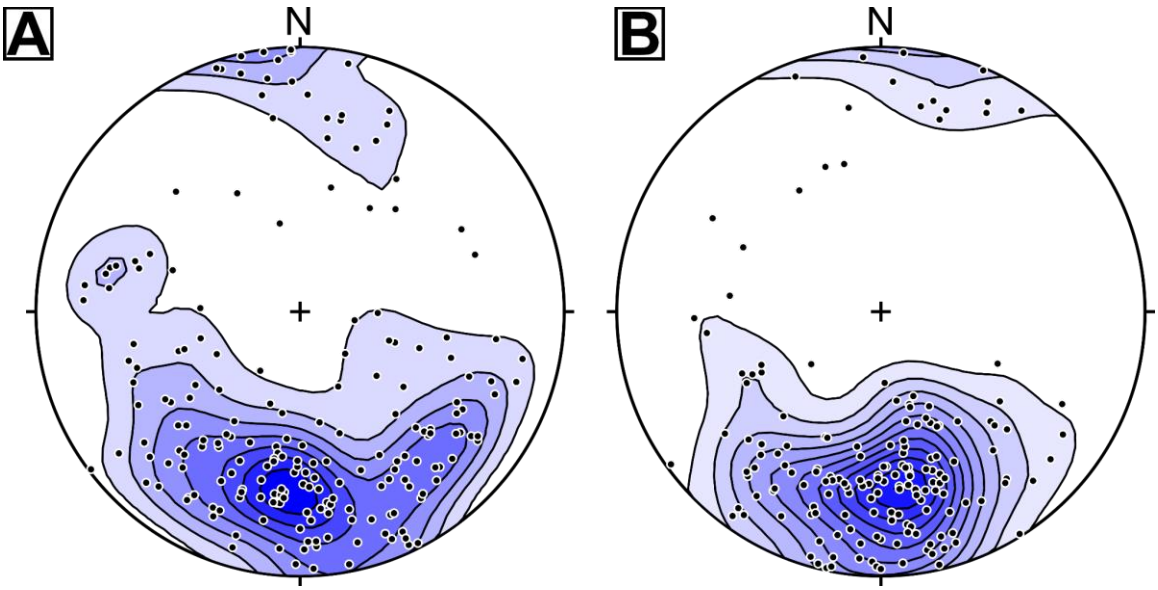

Figure 4.8. Stereonet plot of host rock bedding (**A**) and cleavage (**B**) orientations showing their poles. Each black dot represents a single measurement. Contours were fitted to show the concentration of data.

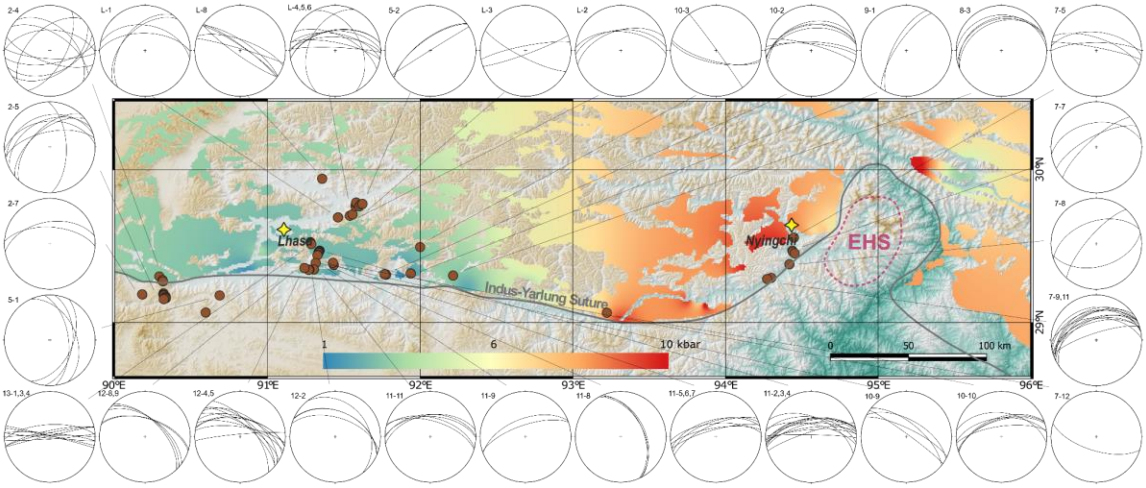

Figure 4.9. Topographic map of the Lhasa-Nyingchi study area showing locations of in-situ host rock fabric measurements (brown dots). Colored shading represents pluton emplacement pressures using IDW interpolation. Host rock fabrics were measured in-situ and foliation strike directions are plotted using equal-area stereonet projection.

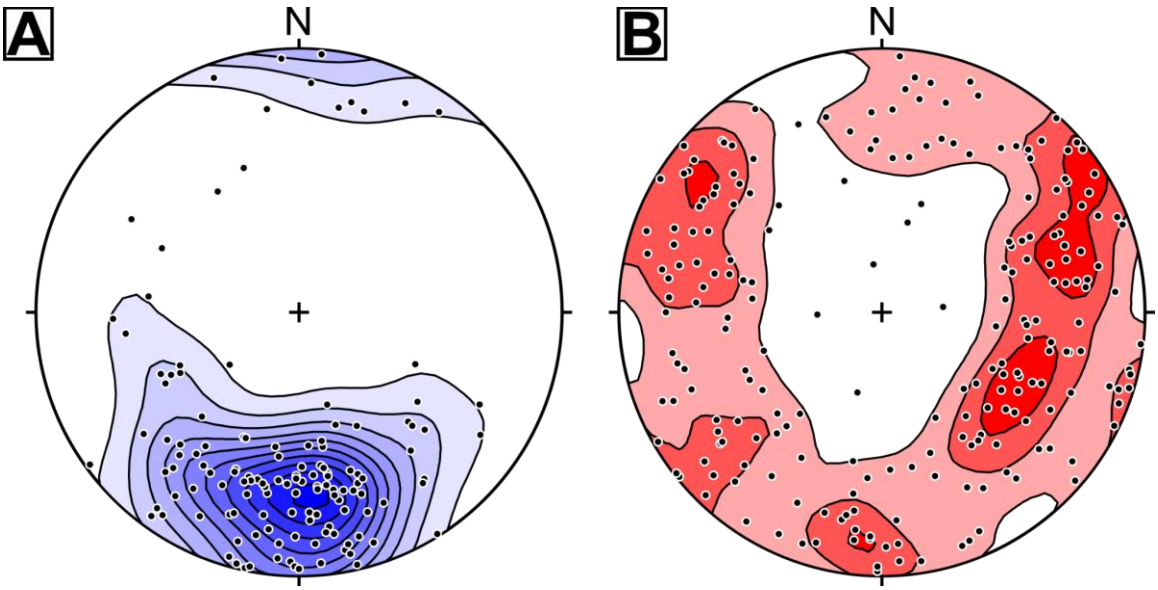

Figure 4.10. Stereonet plot of (**A**) host rock cleavage and (**B**) magmatic foliation orientations of the Lhasa region (90°E - 92°E) showing their respective poles. Each black dot represents a single measurement. Contours were fitted to show the concentration of data.

Figure 4.11. Outcrop photo of weakly deformed phyllite showing kink folds with their kink planes at a high angle to the E-W direction, resulting from E-W contraction.

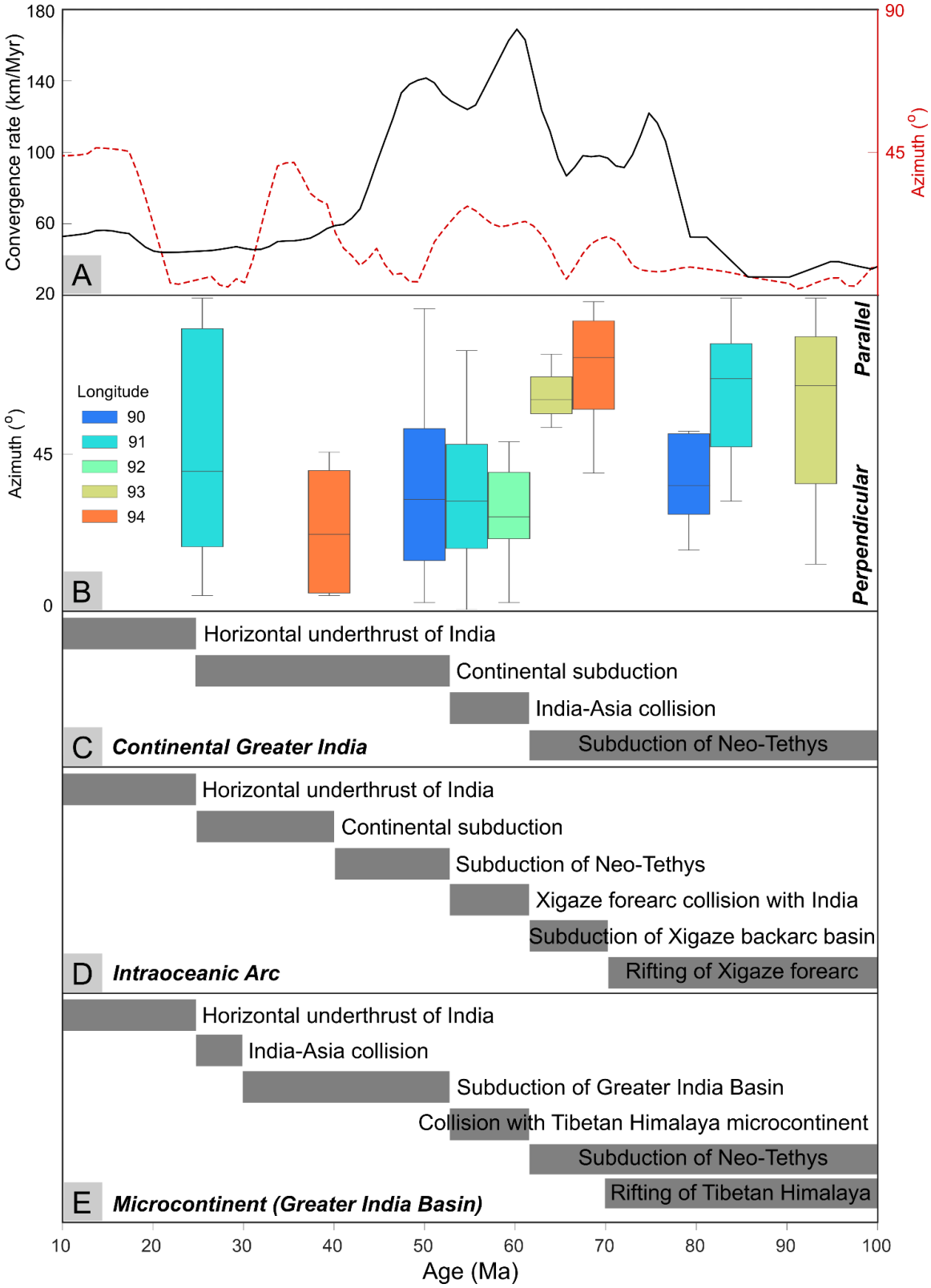

Figure 4.12. Comparison of plate kinematics history between India and Asia. (**A**) and magmatic foliation orientations relative to the orogen color-coded by longitude (**B**).

Panels **C**, **D**, and **E**, summarizes the major geological events associated with the three end-member models for India-Asia collision. Plate kinematics (Indian plate motion relative to Tarim basin (black line) and Indian plate velocity azimuth (red dashed line) are calculated using GPlates (Müller et al., 2018).

Figure 4.13. Field photo taken near Lhasa showing folded Upper Cretaceous Shexin Formation (lower light gray) unconformably below weakly deformed Eocene Linzizong volcanics (upper dark unit). The deformation of the Linzizong Formation is thought to take place 30-10 Ma (Pan & Kidd, 1999).

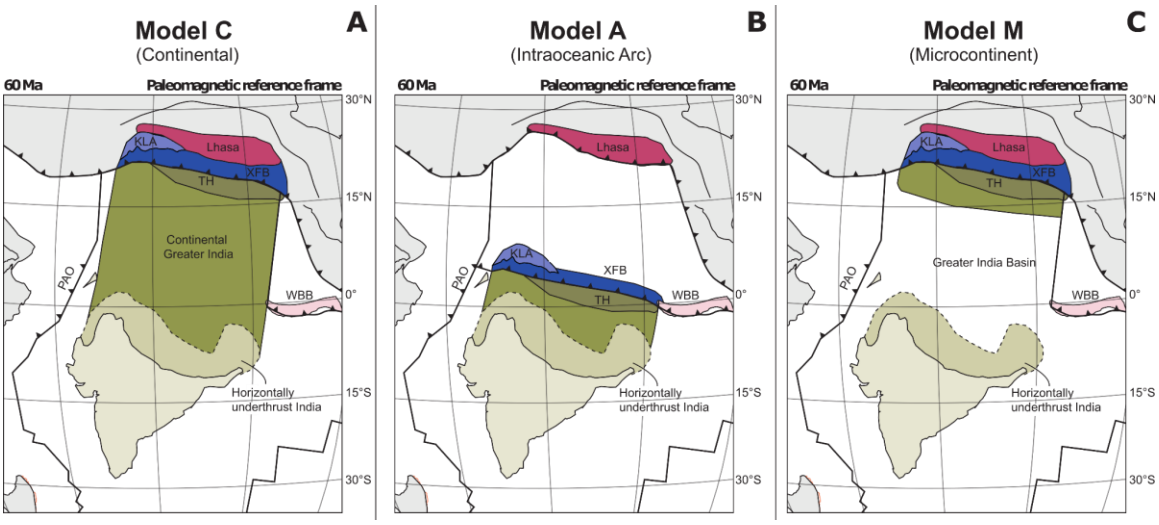

Figure 4.14. Paleogeographic maps for three end models at the time of initial India-Asia collision ~60 Ma. (**A**) Fully continental Greater India and subduction of the crustal lithosphere. (**B**) Intraoceanic arc collides with India around the equator due to rifting of the Xigaze backarc. Subsequent collision of India with Asia occurs at ~40 Ma (e.g. Kapp et al., 2019). (**C**) Initial collision with the Tibetan Himalaya microcontinent and the existence of the Greater India Basin north of the Indian lithosphere. Modified from van Hinsbergen (2022).

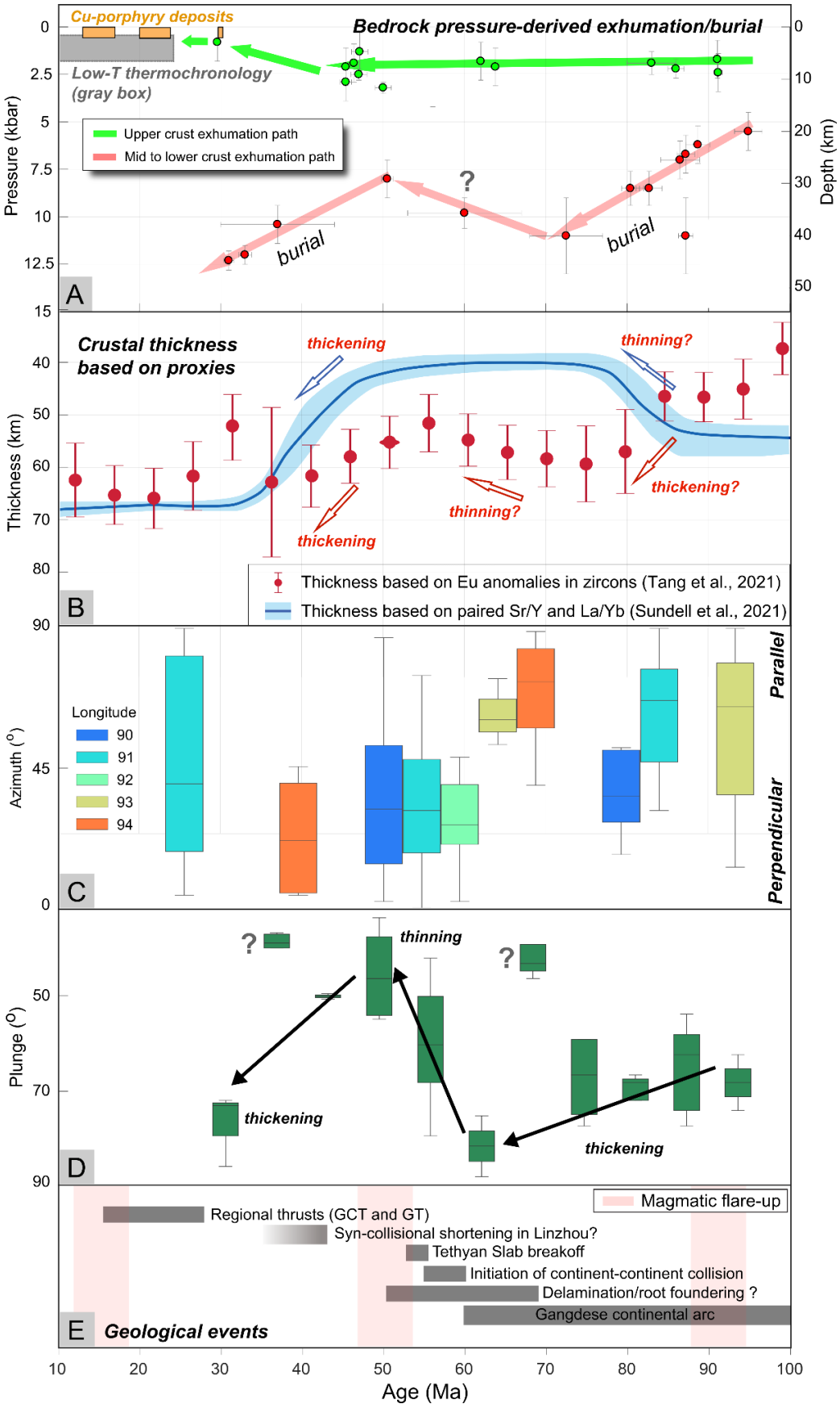
Cu-porphyry deposits
Bedrock pressure-derived exhumation/burial
Low-T thermochronology (gray box)
Upper crust exhumation path
Mid to lower crust exhumation path
Pressure (kbar)
Depth (km)
burial
burial
?
A
Crustal thickness based on proxies
thickening
thinning?
thickening?
thinning?
thickening
Thickness (km)
Thickness based on Eu anomalies in zircons (Tang et al., 2021)
Thickness based on paired Sr/Y and La/Yb (Sundell et al., 2021)
B
Longitude
90
91
92
93
94
Azimuth (°)
Parallel
Perpendicular
C
?
thinning
?
thickening
thickening
Plunge (°)
D
Magmatic flare-up
Regional thrusts (GCT and GT)
Syn-collisional shortening in Linzhou?
Tethyan Slab breakoff
Initiation of continent-continent collision
Delamination/root foundering ?
Gangdese continental arc
E Geological events
Age (Ma)

Figure 4.15. Evolution of the Gangdese crust inferred from various proxies. (**A**) Upper and mid to lower crust exhumation history derived from bedrock pressures (modified from Cao et al., 2020). (**B**) Crustal thickness estimates from zircon Eu anomalies (Tang et al., 2021) and whole rock La/Yb-Sr/Y ratios (Sundell et al., 2021). (**C**) Temporal history of magmatic foliation strike orientations relative to the orogen color-coded by longitude. (**D**) Temporal history of magmatic lineation plunge angles. Sub-vertical lineations are associated with crustal thickening, while sub-horizontal plunges indicate crustal thinning. (**E**) Summary of geological events of the Gangdese crust.

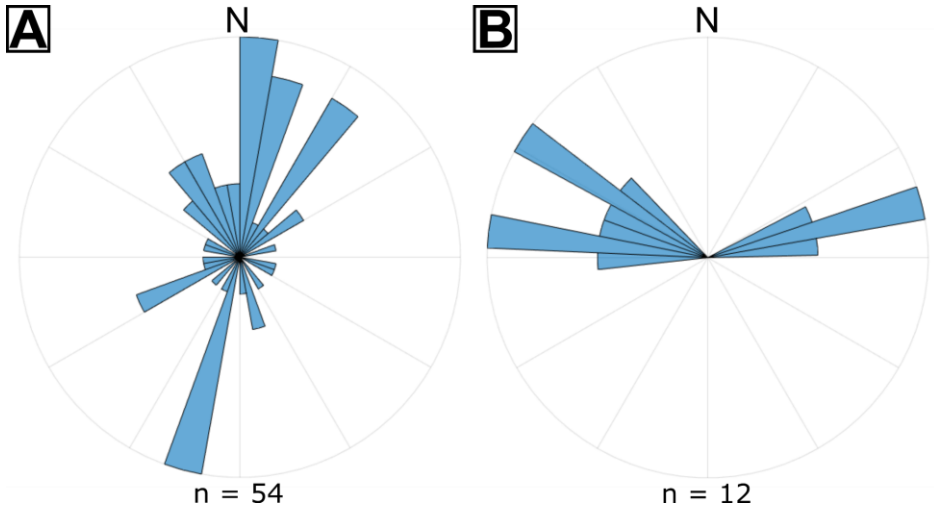

Figure 4.16. Magmatic foliation strike orientations grouped by pluton emplacement depth. (**A**) Fabrics of shallow plutons emplaced in the upper 10 km. (**B**) Fabrics of deeper plutons emplaced between 20 - 30 km. The shallow plutons record mostly orogen-perpendicular fabrics, contrasting the orogen-parallel fabrics found in deeper plutons.

CHAPTER 5: Numerical and scaling models of erosion-driven isostatic flow and diapirism in continental crust: implications for the evolution of the eastern Himalayan syntaxis, southern Tibet

Jiaming Yang[1], Wenrong Cao[1], Xiaoping Yuan[2], Jianfeng Yang[3]

[1] Department of Geological Sciences and Engineering, University of Nevada, Reno, MS-172, 1664 N. Virginia St., Reno, NV 89557, United States of America

[2] Hubei Key Laboratory of Critical Zone Evolution, School of Earth Sciences, China University of Geosciences, Wuhan, China

[3] State Key Laboratory of Lithospheric Evolution, Institute of Geology and Geophysics, Chinese Academy of Sciences, Beijing, China

ABSTRACT

The eastern Himalayan syntaxis (EHS) is one of the fastest exhuming regions on Earth since ~10 Ma. While multiple models such as crustal buckling, syntaxis expansion, adjustment of river incision, and tectonic aneurysm have been proposed to explain the evolution of the EHS, the mechanism of its fast exhumation is still under debate. Previous studies have mostly focused on using thermochronology to investigate the exhumation history of the EHS. Here we perform numerical simulations to quantify the effects of erosion-driven exhumation on the lithosphere using a 2-D thermo-mechanical finite difference code implemented with visco-elasto-plastic rheology and particle-in-cell approach. Results show that constant, focused surface erosion (5 km/Myr) is able to exhume lower crust of >40 km on the timescale of ~10 Myr, produce high topography, and generate partial melt. Erosion-driven advection elevates the local geothermal gradient and reduces crustal viscosity, promoting tectonic deformation. Exhumation is sustained by isostatic flow resulting from lithostatic pressure difference and amplified by the occurrence of crustal diapirism, associated with the presence of hot and buoyant molten rocks in the weakened advection channel. Such diapiric upwellings trigger a rapid acceleration in rock uplift rates to values greater than the driving erosional forcing and causes surface uplift, resulting in a central bulge that exceeds the surrounding elevation. Our erosion-driven exhumation model demonstrates the intricate coupling between surface erosion and rock uplift, as well as the active role of surface erosion in driving tectonic evolution. To establish a long-lasting positive feedback between surface erosion and rock uplift through our erosion-driven model is possible, but both high surface erosion rate (>10 km/Myr) and topographic diffusivity (10^{-4} m^2/s) are necessary.

INTRODUCTION

Studies from multiple orogenic systems (e.g., Himalaya, Taiwan, European Alps) reveal the important role of surface erosion in driving deep crustal processes (e.g., Gilchrist et al., 1994; Willett, 1999; Zeitler, 2001; Beaumount et al., 2001; Dadson et al., 2003; Bishop, 2007; Braun et al., 2014; Olive et al., 2014; Steer et al., 2014). Surface erosion may alter the lithospheric stress state, elevate the regional geothermal gradient, and in turn affect the rheology of the lithosphere (e.g., Davis et al., 1983; Dahlen et al., 1984; Liu et al., 2020; Molnar & England, 1990; Braun et al., 2014; Cao et al., 2020). The linkage between surface erosion and solid earth processes are best manifested in areas where erosion is spatially focused and the erosion rate is high (e.g., Zeitler et al., 2001, 2014). One of the best places to investigate the interaction between surface and solid earth processes is the eastern Himalayan syntaxis (EHS), also known as the Namche Barwa massif in southern Tibet (**Figure 1**) (e.g., Wadia, 1931; Gansser, 1980). The EHS is located at the eastern terminus of the Himalayan orogen belt where the Indian crust is tectonically juxtaposed against the Asian crust (e.g., Burg et al., 1998; Zhang et al., 2004). The EHS is characterized by extreme topographic relief (Korup et al., 2010; Larsen & Montgomery, 2012), intense deformation (e.g., Burg & Podladchikov, 1999; Ding et al., 2001; Zhang et al., 2004), high-grade metamorphism and partial melting (e.g. Booth et al., 2009; Zeitler et al., 2014; Tu et al., 2016), and a focused “bullseye” pattern of rapid exhumation (>5 km/Myr) since the Miocene (e.g. Burg et al., 1988; Burg et al. 1997; Ding et al., 2001; Gong et al., 2015; Lang et al., 2016; King et al., 2016; Bracciali et al., 2016; Wang et al., 2016; Yang et al., 2017; Govin et al., 2020). Recent studies show the exhumation rate of the EHS has not been uniform since ~10 Ma (Gong et al.,

2015; Govin et al., 2020). Gong et al., (2015) suggested an acceleration in rock exhumation rates since 7 Ma based on biotite $^{40}Ar/^{39}Ar$ thermochronology. Further, rapid acceleration in exhumation rates has been evidenced by low-T thermochronology (Govin et al., 2020) as well as the discovery of buried Yarlung Tsangpo River canyon, signifying a pulse of rapid uplift ~2 Ma (Wang et al., 2014).

The formation mechanism of the EHS and the cause of its fast exhumation is under debate. End-member models explaining the formation and the exhumation of the EHS include (**Figure 2**): (1) lithospheric-scale buckling due to India-Asia convergence (e.g. Burg et al., 1998), (2) subduction basal indentation (Bendick & Ehlers, 2014), (3) lower crustal flow (Whipp et al., 2014), (4) enhanced exhumation caused by the captures of the rivers to the north of the EHS (e.g., King et al., 2016; Yang et al., 2021) , (5) river incision in response to tectonic uplift (Lang et al., 2016), and (6) "tectonic aneurysm"(e.g. Zeitler et al., 2001; Koon et al., 2002, 2013; Zeitler et al., 2014).

Among these models, the "tectonic aneurysm" model proposes a positive feedback between erosion and rock uplift. This positive feedback relies on the coupling between erosion-driven rock uplift and exhumation, enhanced surface erosion, and thermal weakening of the crust due to temperature-dependent rheology (e.g., Zeitler et al., 2001; Koon et al., 2002; 2013). Once the feedback is established, high rates of rock uplift, exhumation, and associated surface erosion can be sustained for millions of years. As such, a steady-state topography can be maintained in the EHS region which potentially halts the migration of knickpoints into the interior of the plateau (Zeitler et al., 2001). This model has been numerically tested by Koon et al. (2002) and Koon et al. (2013).

However, existing numerical models investigating the mechanism of "tectonic aneurysm" implements surface erosion as a passive process and removes all material above a prescribed elevation in the deforming orogen (e.g., Koon et al., 2002). Different from these models, we use numerical and analytical models to directly test how surface erosion acting as the driving force, can influence solid earth processes. In our models, surface erosion actively "excavates" the topmost crust in a restricted region, simulating erosion caused by the Yarlung River. The questions we address in this study are: (1) How does the upper and lower crust respond to focused surface erosion both kinematically and thermomechanically? (2) Can constant surface erosion alone trigger and sustain rapid exhumation over ~10 Myr? (3) Could such imposed surface erosion further establish a positive feedback between erosion and rock uplift as envisioned in the "tectonic aneurysm" model? In addition, we highlight the isostatic and diapiric flows triggered by fast surface erosion and discuss their implications on the interactions and potential feedback between surface erosion and solid earth processes.

METHODS

To assess the effect of focused surface erosion on the continental crust, we performed numerical simulations using MVEP2 (MVEP2, an updated version of MILAMIN_VEP, e.g., Kaus 2010; Thielmann & Kaus 2012, Baumann & Boris, 2015). MVEP2 is a thermo-mechanical finite element code with marker-in-cell approach which employs the efficient MATLAB based finite element library MILAMIN (Dabrowski et al., 2008). The code is capable of simulating partial melt, phase change, and free surface topography in responding to magmatic-tectonic processes. Material properties such as

viscosity and melt content are recorded by markers, which are used to update the new mesh after each timestep (Thielmann & Kaus, 2012). Visco-elasto-plastic rheology is used in the code (see detailed rheology setup in Thielmann & Kaus, 2012). The governing equations describing the conservation of energy, momentum, and mass for incompressible fluids are listed below:

$$\rho Cp\left(\frac{\partial T}{\partial t}+v_i\frac{\partial T}{\partial x_i}\right)=\frac{\partial}{\partial x_i}\left(k\frac{\partial T}{\partial x_i}\right) \quad (1)$$

$$\frac{\partial P}{\partial x_i}-\frac{\partial \tau_{ij}}{\partial x_j}=\rho g \quad (2)$$

$$\frac{\partial v_i}{\partial x_i}=0 \quad (3)$$

Where ρ is density, Cp is heat capacity, T is temperature, t is time, x_i is spatial coordinate, v_i is velocity, k is thermal conductivity, P is pressure, g is gravity, and τ_{ij} is the deviatoric stress tensor.

We omit radiogenic and shear heating in the conservation of energy equation to focus on the crustal thermal evolution caused by erosion-driven advection for the following reasons. Radiogenic heat production in the thickened Tibetan crust is poorly constrained. The average radioactivity of the Tibetan crust is assumed to be 0.8×10^{-6} W/m^3 (e.g., Wang et al., 2013). Yet, radiogenic heating plays a minor role in altering the thermal structure of a system that is subject to strong thermal advection as our model shows. Viscous shear heating generates local thermal perturbations around shear zones

and can be important in lithospheric scale shear zones where shear stress and strain rates are high and the characteristic thickness of the shear zone is significant (Burg & Gerya, 2005). However for our simulated crustal system, we do not develop such major shear zones in the simulations.

Geometry and boundary conditions

The model consists of a 2-layer crust that is 500 km wide and 70 km thick (**Figure 3**). The 70 km crustal thickness is representative for the modern Tibetan Plateau (e.g., Cheng & Jiang, 2020; Kundu et al., 2022). The upper and lower crusts are each 35 km. In some cases, different rheologies representative of felsic upper and mafic lower crusts were used. We did not include a mantle layer in our simulations in order to focus on crustal processes in response to surface forcing. Since the mantle lithosphere is much stronger than the warm lower crust in an orogenic belt, it behaves as a passive base; therefore, it does not affect crustal scale dynamics on timescales of ~10 Myr (e.g., Rey et al., 2011). The domain grid resolution is 1 km in both the horizontal and vertical direction, with a total of 501 × 71 nodes. Thermal boundary conditions are isothermal for the top and bottom (fixed surface and Moho temperatures, thermal conditions are described in the next section), and zero flux left and right. Mechanical boundary conditions are no stress for the top, free slip for the bottom, and constant strain rate for the sides. A constant background shortening strain rate of 10^{-16} s^{-1} is imposed. This strain rate is of typical order of magnitude for large-scale orogenic belts (e.g., Cao et al., 2015; Zuza et al., 2020), but is several times smaller than the published values for the modern Himalayan-Tibetan orogen (e.g., Zhang et al., 2004; Allmendinger et al., 2007; Zuza et

al., 2020). We omitted testing of higher background shortening strain rates in order to isolate the effects of erosion-induced crustal processes. The physical properties used in the simulations are shown in **Table 1**.

Partial melting and densities for solid and partial molten rocks

During partial melting, melt fraction (*M*) is interpolated linearly between the solidus ($T_{solidus}$) and the liquidus ($T_{liquidus}$) temperatures (Gerya & Yuen, 2003; Burg & Gerya, 2005). $T_{solidus}$ and $T_{liquidus}$ depend on the phase (felsic vs. mafic) and lithostatic pressure (e.g., Gerya, 2019). For the felsic and mafic rocks used in our simulation, we used the $T_{solidus}$ and $T_{liquidus}$ from Gerya (2019). $T_{solidus}$ and $T_{liquidus}$ are shown in Table 2. Densities of solid and partial molten rocks are calculated based on Gerya (2019).

$$M = 0 \ \ at \ \ T \leq T_{solidus} \tag{4}$$

$$M = \frac{(T - T_{solidus})}{(T_{liquidus} - T_{solidus})} \ \ at \ \ T_{solidus} < T \leq T_{liquidus} \tag{5}$$

$$M = 1 \ \ at \ \ T \geq T_{liquidus} \tag{6}$$

$$\rho_m = \rho_{solid}(1 - M + M\frac{\rho_{molten}}{\rho_{solid}}) \tag{7}$$

where ρ_{molten} is the density of molten rock (**Table 1**), and ρ_{solid} is the temperature and pressure dependent density of solid rocks (Gerya, 2019):

$$\rho_{solid} = \rho_0[1 - \alpha(T - T_0)][1 + \beta(\rho - \rho_0)] \quad (8)$$

where ρ_0 is the reference density at T_0 = 293 K, P = 0.1 MPa, α is coefficient of thermal expansion, and β is compressibility coefficient (**Table 1**).

Rheology and rocks and viscosity of partially molten rocks

We use a temperature and strain rate dependent rheology to compute the effective viscosity associated with dislocation creep. Following Gerya (2019), wet quartzite flow law (Ranalli, 1995) and plagioclase An_{75} flow laws (Ranalli, 1995) are coupled with solid felsic and mafic rocks, respectively (**Table 2**). Rocks exposed on the surface of the EHS consists of high-grade paragneiss, amphibolite, schist, marble, felsic and mafic granulite, migmatitic gneiss, and felsic plutons (e.g., Liu & Zhong, 1997, Burg et al., 1998). Recent study also shows that the average crustal Poisson's ratio at the EHS is particularly low (~0.2-0.3), indicating massive quartz-rich, felsic composition in the bulk EHS crust (**Figure 1C**, Kundu et al., 2022). Therefore, our reference model uses wet quartzite flow law and felsic rock phases for both the upper and lower crusts. We also tested a stronger, mafic lower crust in other models.

When rocks undergo partial melting with melt fraction $M > 0.05$, we assign a low constant Newtonian viscosity (10^{18} Pa s) to the partially molten rock. The threshold of the viscosity drop is based on the dramatic decrease in viscosity between the solidus and melt connectivity transition (MCT), where 90% of the rock strength is lost over this small range (Rosenberg & Handy, 2004). It is also noted that 10^{18} Pa s is much larger than the viscosity of magma and partially molten rocks (~10^2 – 10^{14} Pa s) (e.g., Dingwell, 2006;

Petford, 2009). Similar to many numerical codes, MVEP2 can only handle a range of 6-7 orders of magnitude for viscosity to avoid numerical instabilities. As such, 10^{18} Pa s is the lowest threshold of viscosity in MVEP2. As we show in our simulation results, the dynamics of the diaprism depends on the viscosity of the solid host rocks (Cao et al., 2016), which we solved in a systematic manner.

Initial geothermal profile

Numerical simulations suggest temperatures of the upper and middle southern Tibetan crust are controlled by underthrusting of the relatively cold Indian shield as well as shear heating between the two convergent plates (Wang et al., 2013). Both numerical simulation and geophysical observations based on shear-wave (V_s) anomalies show the southern Tibet is characterized by a warm (400-600°C) crust with relatively cold Moho temperatures (e.g., Huang et al., 2010, 2011). Earthquake thermometry of mantle earthquakes indicate the Moho temperature beneath the southern Tibetan crust is about 650°C (Chen et al., 2013).

Based on the above geophysical observations, we tested two different initial geothermal gradients. First a linear gradient of 9.7°C/km from the surface (20°C) to the Moho depth of 70 km (700°C). We use this geotherm for the “cold crust” models. The other is a 2-stage geotherm where the upper 10 km has a geothermal gradient of 40°C/km representing the hot upper crust in a magmatic orogen (Rothstein & Manning, 2003). Below 10 km temperature increases linearly to 700°C at the Moho depth of 70 km, resulting in a 4.7°C/km gradient. This 2-stage geothermal gradient represents an elevated thermal state of the post-collisional orogenic crust heated by magmatism. We use this 2-

stage initial geotherm for the "warm crust" models. The Moho temperature used in our model is lower than the peak temperature determined from lower crust metamorphic assemblages of the EHS (800 - 850°C, Liu & Zhong, 1997; Booth et al., 2009; Guilmette et al., 2011). We chose a modest Moho temperature (700°C) to suppress extensive partial melting (~30% if Moho temperature is 800 °C) in our reference model where a generic felsic continental crust is used.

Surface erosion: focused erosion and topographic diffusion

In geomorphic studies, the stream power law is commonly used to simulate river incision (e.g., Whipple & Tucker, 1999). Yet, the implementation of km to sub-km scale surface erosion process in a 10-100 km geodynamic model is a challenge for numerical modeling (e.g., Olive et al., 2022). Here, we simply simulate the incision of the Yarlung river using prescribed focused surface erosion in the central portion of the crust ("pseudo-valley"). Such focused erosion essentially "excavates" a rectangular region in the pseudo-valley. This is justified based on the broad region of modern fast erosion rates in the EHS area (**Figure 1B**). To avoid vertical walls in the valley, we used the following logistic function to smooth the topographic change near the walls of the valley:

$$dz = \frac{E \cdot dt}{1+e^{\frac{(-x+w)}{s}}} + \frac{E \cdot dt}{1+e^{\frac{(x+w)}{s}}} \quad (9)$$

For each time step (*dt*), we lower the topography or elevation of the central "pseudo-valley" by the amount of *dz* (**Figure 4**). Outside of the valley, the elevation reduction is zero. By implementing the logistic function with smooth valley walls, we can avoid

sharp, vertical shoulders of the erosional area when a simple squared erosional profile is used. The vertical shoulders of the squared erosional profile cause the instability and convergence issue of the numerical code. Our choice of erosional valley half width (w = 25 km) (total width $2w$ = 50 km) is based on the spatial extent of Namche Barwa massif that is undergoing fast erosion (**Figure 1B**) (e.g., Zeitler et al., 2014; King et al., 2016; Yang et al., 2018). In our simulations, we tested three pseudo-valley erosion rates: 2, 5, and 10 km/Myr, representing the slow, moderate, and fast erosion rates that cover the range of thermochronologically determined erosion rate in the past ~10 Myr (e.g., Enkelmann et al., 2011; King et al., 2016; Yang et al., 2018; Grovin et al., 2020). The moderate value of E = 5 km/Myr is used in our reference model.

It is noted that we do not attempt to resolve the km- or sub-km scale incision process in the river channel since the complexities are beyond the capability of our existing numerical code. Instead, our simulated erosional valley profile is aimed to capture the first-order erosion rate that shows a semi-bullseye pattern in the EHS area (an approximate circular shaped region of 20-30 km radius) (King et al., 2016; Bracciali et al., 2018; Yang et al., 2018). **Figure 4** illustrates the topography reduction as a result of the pseudo-valley erosion after 0.1 Myr, with a rate of 5 km/Myr, showing a flat bottom at the center with an elevation reduction of 0.5 km, as well as valley walls connecting the valley bottom to the unperturbed periphery. The crustal material removed by imposed surface erosion acts as a net mass outflow.

In addition to focused surface erosion in the center of the model, we also included the topographic diffusion for the entire surface. Diffusion of topography is parameterized in the model based on the classic diffusion equation in 2D:

$$\frac{\partial z}{\partial t} = D\frac{\partial^2 z}{\partial x^2} \tag{10}$$

where t is time, and D is the topographic diffusivity. Topographic diffusion has been used in other numerical models simulating EHS dynamics (e.g., Burg & Podiadchokov, 1999). At sub-km scale, the topographic diffusion coefficient depends on specific climate and lithological factors and nonlinearly depends on slope gradient (e.g., Fernandes & Dietrich, 1997; Roering et al., 1999). Therefore, the value of topographic diffusion coefficient is associated with a wide range that varies many orders of magnitude. Our numerical model does not simulate hillslope processes and generates topography in the kilometer scale. As such, the effective topographic diffusivity for our 100-km scale model should be a representative mean of the local diffusivities. However, the equivalent value of topographic diffusion coefficient at 100-km scale is unknown. For the EHS region where hillslope is steep, climate is warm and wet, and landslides are frequent, we vary the topographic diffusion coefficient D from 10^{-4} m^2/s to 10^{-6} m^2/s. The lower bound of topographic diffusion coefficient D is the same as $D = 10^{-6}$ m^2/s used in Koons et al. (2002) and Ruh et al. (2022), and higher than the $D = 10^{-7}$ m^2/s used in Burg and Podiadchokov (1999).

At each timestep in our numerical model, pseudo-valley erosion first removes crustal material out of the model using the logistic function (Eq. 9). Within the same

timestep, diffusion of topography is performed. Different from the pseudo-valley erosion, topographic diffusion is a mass conservative process. During topographic diffusion, materials eroded from hilltops fill into basins. Since our model consists of two separate surface processes, total surface erosion is the combined effect of pseudo-valley erosion plus topographic diffusion. To determine the net mass removal from the combined surface processes, we calculate the effective erosion rate accounting for the two separate processes, which is the net mass removal rate in one complete timestep. As we show later in our discussion, this effective erosion rate acts as the driving force of crustal isostatic flow.

RESULTS

We conducted simulations with varying parameters including imposed erosion rate in the pseudo-valley, geothermal gradient, topographic diffusion coefficient, and crustal composition (**Table 3**). The computations were carried out using the Pronghorn cluster located at University of Nevada, Reno. In the following sections we present the results from several representative cases to illustrate the effect of varying parameters.

Reference model: Focused erosion in a felsic, cold crust

Our reference model consists of felsic upper and lower crusts that are coupled with wet quartzite rheology. A moderate erosion rate of 5 km/Myr in the pseudo-valley and a topographic diffusivity of 10^{-5} m^2/s are used. The Moho temperature is fixed at 700°C with an initial linear geothermal gradient. **Figure 5** shows the simulation result

focusing on the central 150-km-wide region. After 1.2 Myr, initial focused surface erosion excavates a central pseudo-valley of ~2 km depth. The topographic relief between the valley bottom and its shoulder is about 3 km. There are very minor convex-shaped perturbations to crustal temperature and effective viscosity. Strain rate starts to increase beneath the pseudo-valley to ~$10^{-14.5}$ 1/s. At the bottom of the lower crust, a ~10-km-thick lateral channel of high strain rate ~10^{-14} 1/s is formed. After 4.4 Myr, the crustal response becomes apparent where both temperature and viscosity of the crustal column exhibits an upward bend of hotter and weaker crust, due to upward advection beneath the pseudo-valley. The upward flow of the crust also causes shallowing of the pseudo-valley. After 8.7 Myr, lower crust with an initial depth of 35 km is exhumed to the surface in the pseudo-valley. The surrounding crust is tilted away from the pseudo-valley. Temperature of the crust becomes more elevated and viscosity is further reduced at the center, directly below the pseudo-valley. In the bottom of the lower crust, partially melted crust starts to concentrate in the middle region. Relief of the valley is further reduced to ~1 km. The final column in **Figure 5** illustrates the effects of a crustal diapir. The diapiric body is initiated from the bottom of the lower crust with melt fractions less than 10%. The diapiric body rises quickly in the warm, low viscosity mid-lower crust at a strain rate of ~10^{-13} 1/s or greater. The temperature plot also shows a rising thermal plume that compresses the geothermal gradient in the top ~10 km crust. Viscosity beneath the pseudo-valley is significantly reduced to 10^{19} to 10^{18} Pa s. A central topographic bulge and flanked valleys are observed in the middle part of the model.

Given the finite size of the simulation (500 km wide), the overall crustal thickness and elevation will decrease with time due to the net mass outflow of the erosional

pseudo-valley. Such decrease in crustal thickness and overall elevation are limited and they can be easily corrected. More importantly, they have little effect on the geodynamics we aim to explore. For example, for the reference model, the net mass outflow can be estimated using the product of imposed erosion rate and width of the pseudo-valley. In 10-Myr, the mass outflow is 5 km/Myr × 50 km × 10 Myr = 2500 km^2. Given the 500 km width of the simulated crust, the overall elevation reduction is 2500 km^2/500km = 5 km over 10 Myr across the entire area, resulting in a surface lowering rate of 0.5 km/Myr. To investigate the changes of the local topography in the center of the model, we plot the topography relative to the far-field elevation (elevation at x = 250 km). A discussion on rock exhumation rate based on the model predicted surface lowering rate and rock uplift rate is discussed in the Model limitations section.

Effects of erosion rate in pseudo-valley

In **Figure 7** we present the results of a simulation run with high erosion rate (E = 10 km/Myr) while keeping all other parameters the same as the reference model. The simulated crust undergoes similar processes: initial pseudo-valley formation, followed by upward advection of crust and elevated geothermal profile, leading to crustal viscosity reduction that eventually give rise to lower crustal diapirism and the central topographic bulge. There are two key differences compared to the reference model: (1) topographic relief of the pseudo-valley at ~1 Myr (~3.5 km) is slightly higher than the one in the reference model (~3 km); (2) the crust responds faster to the increased erosion rate: mass and thermal advection in the mid-lower crust are more vigorous with a higher strain rate, crustal diapir initiates in a shorter period of time (~4 Myr instead of ~9 Myr in the

reference model), and the central topographic bulge within the pseudo-valley develops faster (also ~4 Myr instead of ~9 Myr in the reference model). Compared to the reference model, the time to exhume the lower crust and diapir formation is reduced by about a factor of 2. It is noted that at 7 Myr, the top of the central topographic bulge is flattened due to topographic diffusion.

We also tested a low erosion rate (E = 2 km/Myr) in the pseudo-valley (**Figure 8**). Not only does it take much longer to exhume the lower crust, the resulting perturbations to crustal strain rate, viscosity, and topography are much smaller compared to the reference model. The upward advection of the temperature field is limited (**Figure 9**). Most importantly, the diapiric body does not form and the pseudo-valley remains concave downward without the formation of a central bulge.

Effects of initial crustal thermal profile

In **Figure 10** we present the results of a simulation run with a 2-stage geothermal gradient while keeping all other parameters the same as the reference model. This is a "warm crust" scenario representing an elevated thermal state of the post-collisional orogenic crust heated by magmatism (e.g., Zhu et al., 2015). Such a warm crust reduces the bulk crustal viscosity and generates a slightly thicker partially molten layer at the base of the lower crust. Compared to the reference model, the hotter and weaker crust readily deforms in a larger region and responds faster to the erosion. The formation of the diapir occurs at ~4 Myr at the bottom of the lower crust and its partially molten plume head quickly ascends to the upper crust at ~5 Myr. By 8.7 Myr, convection of the lower crust drags down slivers of the upper crust. The topography shows a smoother pattern: relief

across the pseudo-valley is only about 0.5-1 km and a central bulge starts to grow at 1.6 Myr.

Effects of topographic diffusion

In **Figure 11** we present the results of a simulation run with high topographic diffusivity ($D = 10^{-4}$ m^2/s) while keeping all other parameters the same as the reference model. A major difference, as expected, is that increased topographic diffusion exerts a "smoothing" effect on the topography, reducing the relief across the pseudo-valley (< 1 km). The overall topography is also gentler with less than a few hundred meters of relief across the simulated surface at later stages of the simulation (12.3 and 18.9 Myr). Such a high topographic diffusivity significantly affects the crustal dynamics. We observe a slight delay of the initiation of the diapir compared to the reference model (~12 Myr here instead of ~9 Myr in the reference model) probably because the higher topographic diffusivity is associated with increased deposition that counteracts the effects of focused erosion in the pseudo-valley, reducing the effective erosion rate that drives crustal advection.

When a lower topographic diffusivity ($D = 10^{-6}$ m^2/s) is used, the "smoothing" effect is reduced, resulting in a more jagged topography (**Figure 12**). The pseudo-valley is much deeper with a high relief of ~5 km at 3.4 Myr. A prominent central bulge of ~3 km as well as sharp "shoulders" of the pseudo-valley are seen at 7.6 Myr. Compared to the reference model and the model with higher topographic diffusivity, the widths of the crustal upwelling and the diapir are narrower.

Figure 13 compares the evolving topography resulting from different topographic diffusivity values. It illustrates the rate of topographic diffusivity is inversely correlated with the "smoothness" of the topography. Sharp, short-wavelength topography with high relief (~5 km) are associated with relatively low values of topographic diffusivity (D = 10^{-6} m^2/s), whereas gentle, long-wavelength topography with low relief (~0.5 km) are the result of high topographic diffusivity ($D = 10^{-4}$ m^2/s).

Effects of lower crust rheology

In **Figure 14** we present the results of a simulation run with a mafic lower crust (Gerya, 2019) and plagioclase An_{75} flow law (Ranalli, 1995) while keeping all other parameters the same as the reference model. We observe the presence of a 4 km deep pseudo-valley resulting from focused erosion, twice the depth of the reference model. The viscosity of the mafic lower crust with plagioclase flow law is much higher than the felsic lower crust with wet quartzite flow law. The stronger mafic lower crust is more resistant to deformation, with strain rates 10-100 times smaller than those with a felsic lower crust. The decreased strain rate corresponds to slower rock uplift, such that it takes longer time for the lower crust to exhume to the surface. A weak thermal plume is seen at 16.6 Myr in the temperature plot but the diapir is not obvious in neither strain rate nor viscosity plots. The rising thermal plume also does not cause crustal convection as seen in previous models with a felsic lower crust and wet quartzite rheology. Different from simulations with a felsic lower crust, there is no topographic bulge in the middle of the pseudo-valley.

We also tested a scenario with a "warm" mafic lower crust using the 2-stage geothermal gradient (**Figure 15**). The elevated geotherm causes significant weakening in the middle and lower portion of the felsic upper crust, with an effective viscosity of ~10^{20} Pa s. Deformation is concentrated in the felsic upper crust and a shallow pseudo-valley (~1-1.5 km) is maintained until the stronger mafic lower crust is exposed at the surface at 12.3 Myr. Without the readily deforming upper crust below, the pseudo valley deepens and gradually widens, similar to the mafic lower crust with the cold, linear geotherm. We do not observe the formation of a thermal plume or crustal diapir.

DISCUSSION

Scaling analysis: isostatic flow model with constant erosion rate

In all simulations we have performed, we observed the same first-order dynamics of upward crustal flow directly beneath the pseudo-valley accompanied by lateral flow of the mid-lower crust towards the central area. Below we present a simple Airy isostatic flow model where the lithostatic pressure difference across the pseudo-valley provides a lateral pressure gradient that drives the lower crust to flow into the central region. We use this model to explore the relationships between rock uplift, surface uplift, and surface erosion. Our derivation is similar to the scaling approach related to the post-glacial rebound.

Figure 16 shows the idealized setup of the scaling model. A homogenous crust of constant density (ρ) and viscosity (η) is subject to surface erosion (E) within the pseudo-valley with width (w). The topographic relief across the pseudo-valley, or the valley

depth, is *h*. $h > 0$ when the valley is a topographic low. The lateral size of the crust is infinite in this conceptual setup. Focused surface erosion restricted within the pseudo-valley results in an elevation relief (*h*) between the inside and outside of the valley (**Figure 16**). This elevation relief causes a difference in crustal thickness and focused surface erosion creates a lateral pressure gradient in the crust by preferentially removing the overburden within the pseudo-valley. Consequently, driven by this lateral lithostatic pressure gradient, rocks move from regions of higher pressure to lower pressure by migrating from the surrounding area towards the center (Eq. 16). In turn, material directly beneath the pseudo-valley moves upward to reduce the relief of the pseudo-valley and attempts to restore isostatic equilibrium.

The rock uplift rate (*u*) is the upward velocity of rocks relative to the fixed geoid (here also relative to the constant far-field elevation). Here we assume rock uplift rate (*u*) is spatially homogeneous across the bottom of the pseudo-valley. Surface uplift rate (*v*) is the upward velocity of the surface relative to the geoid. For both *u* and *v*, positive values indicate their velocity vectors are pointing upwards. *E* is the constant surface erosion rate, where a positive value means erosion is occurring. The variables *v*, *u*, and *E* satisfy the following relationship:

$$v = u - E \tag{11}$$

Therefore, if rock uplift rate (*u*) is greater than surface erosion rate (*E*) or $u > E$, then surface uplift rate $v > 0$. If $u = E$, then the surface elevation doesn't change ($v = 0$). When

$E > u$, surface lowering occurs ($v < 0$), and valley depth (h) increases with time ($dh/dt > 0$). We have:

$$\frac{dh}{dt} = E - u = -v \tag{12}$$

We use the ratio of h and the half-width of the pseudo-valley (w) to define the strain relevant to the deformation of the system:

$$\varepsilon = \frac{h}{w} \tag{13}$$

We can obtain an expression for strain rate ($d\varepsilon/dt$) by taking the time derivative of Eq. 13 and combining with Eq. 12:

$$\frac{d\varepsilon}{dt} = \frac{1}{w}\frac{dh}{dt} \tag{14}$$

Assuming the lower crust has a Newtonian viscosity of η, the product of strain rate and viscosity yields the characteristic stress that drives crustal flow. Here the characteristic stress in our simple model is the result of the pressure difference across the pseudo-valley. We balance the viscous stress with the pressure difference:

$$\eta\frac{d\varepsilon}{dt} = \eta\frac{1}{w}\frac{dh}{dt} = -\Delta P \tag{15}$$

The negative sign in front of ΔP means that a positive ΔP will cause reduction of h with time ($dh/dt < 0$), which is the result of isostasy. The ΔP is associated with the valley relief:

$$\Delta P = \rho g h \tag{16}$$

where ρ is crustal density, g is gravity. By combining Eq. 11 and Eq. 14 with Eq. 15 we obtain an expression of rock uplift rate (u):

$$u = E + \frac{\rho g h w}{\eta} \tag{17}$$

now we take the time derivative of rock uplift rate (u):

$$\frac{du}{dt} = \frac{\rho g w}{\eta} \cdot \frac{dh}{dt} \tag{18}$$

replace dh/dt using Eq. (12):

$$\frac{du}{dt} = \frac{\rho g w}{\eta} \cdot (E - u) \tag{19}$$

We can simplify the above equation by combining constants and assigning a few variables:

$$\frac{du}{dt} = -k \cdot u + C \tag{20}$$

where $k = \frac{\rho g w}{\eta}$ and $C = \frac{\rho g w}{\eta} E$. The form of Eq. 20 is a classic ordinary differential equation commonly used in box models where the outward flux of a quantity depends on the size of the reservoir (Slingerland and Kump, 2011). In our simulation, Eq. 20 states that time derivative of rock uplift rate (u) depends on u itself. The steady-state rock uplift rate (u_{ss}) can be obtained by setting $\frac{du}{dt} = 0$:

$$u_{ss} = \frac{C}{k} = E \tag{21}$$

After reaching steady-state, rock uplift rate (u) equals the imposed erosion rate (E) and the surface elevation of the pseudo-valley is stationary. We can calculate the "e-folding time" of the system:

$$t_e = \frac{1}{k} = \frac{\eta}{\rho g w} \tag{22}$$

Here, the "e-folding time" is the time required for u to reach ~63% of the steady-state value (Slingerland and Kump, 2011). To better compare the scaling model and our numerical model, we assign the 3x "e-folding time" which is the amount of time for u to reach ~95% of the steady-state value as the characteristic timescale (τ) for u to reach the steady-state:

$$\tau = 3t_e \tag{23}$$

Figure 17 shows how rock uplift rate and surface lowering rate change with time in response to a constant erosion rate. We used ρ = 2800 kg/m3, g = 9.8 m/s^2, w = 25000 m, E = 5 km/Myr, and we tested $\eta = 10^{22}$ Pa s as well as 10^{21} Pa s for viscosities.

From the above scaling analysis and **Figure 17**, we make several observations: (1) u approaches E to the steady-state value in an exponential fashion. The steady-state rock uplift rate (u_{ss}) only depends on the surface erosion rate (E) and the rock uplift rate (u) cannot ever surpass erosion rate (E); (2) Surface lowering rate decreases as u increases. Once steady-state rock uplift rate is achieved, the surface lowering rate becomes zero and surface elevation does not change thereafter; (3) For a given pseudo-valley width (w), the characteristic timescale of reaching steady-state is directly proportional to the viscosity. Higher viscosity corresponds to a longer characteristic timescale but viscosity does not affect the steady-state rock uplift rate.

Many of the insights gained from the isostatic flow model are reflected in the results of the numerical simulations. For the high erosion rate case (10 km/Myr, **Figure 7**), the apparent rate of rock uplift rate is significantly higher than the reference case, such that the lower crust is exhumed to the surface in approximately half the time compared to the reference case with half the imposed erosion rate (5 km/Myr, **Figure 5**). The amount of time to exhume the lower crust is slightly shorter for the case with 2-stage geothermal gradient (**Figure 10**). This is due to the crust being hotter on average, corresponding to a lower crustal viscosity and reducing the response time of rock uplift. In **Figure 18** we show that the uplift rate of a rock parcel whose initial depth is 20 km at the center of the advection channel quickly approaches the effective erosion rate during its ascent, but

never exceeding it. Note, the effective erosion rate is plotted for simulation results, which is the combined effect of imposed, constant erosion in the pseudo-valley and the topographic diffusion. One of the implications is that the height of the central bulge will never be higher than the shoulders when crustal flow is only driven by the isostasy.

In our simplified isostatic flow model, rock uplift rate is spatially uniform beneath the pseudo-valley. The actual flow of rocks is complex and gradients of rock uplift rate exist in both vertical and horizontal directions. **Figure 18** shows the rock uplift rate in the deeper crust (initial depth at 30 km) lags behind the one in the shallower crust (initial depth at 20 km). This can be explained by the greater proportion of vertical flow in the shallower crust. In other words, the upward flow in the shallower crust reflects the integrated vertical and lateral flows across different depths. The central bulge can also be explained by the changing upward rock uplift rate across the lateral profile of the "flow channel" beneath the pseudo-valley: the central velocity is higher than the ones on the sides resembling the velocity profile of the classic Poiseuille flow.

Advection-induced temperature increase and viscosity reduction

Another important observation from our numerical simulations is that the upward advection of rocks increases the crustal temperature and reduces the effective viscosity. We can use a dimensionless number, the Péclet number, to quantify the effect of this advective heating. The Péclet number is defined as the ratio between the rates of advection and diffusion (e.g., Patankar, 1980; Turcotte & Schubert, 2002; Huysmans & Dassargues, 2005; Cao et al., 2019).

$$Pe = \frac{uH}{\kappa} \sim \frac{EH}{\kappa} \quad (24)$$

Where u is rock uplift rate, H is crustal thickness, and κ is thermal diffusivity. Since the rock uplift rate approaches the surface erosion rate (E) relatively quickly, the steady-state rock uplift rate (U_{ss}) equals surface erosion rate (E). We can replace u with E to characterize the Péclet number (Pe) of the system. For our setup where H = 70 km, κ = 1e-6 m^2/s, Pe = ~1 if E = 0.5 km/Myr. It means that any surface erosion rate greater than 0.5 km/Myr should result in Pe >1. Specifically, for the tested surface erosion rates, when E = 2 km/ Myr, Pe = 4.4; when E = 5 km/Myr, Pe = 11; when E = 10 km/Myr, Pe = 22. Thus, for all tested surface erosion rate, Pe >1 suggesting advective heating is significant via isostatic flow. The effect of heat advection can be seen in **Figure 6** and **Figure 9**, where the initial linear thermal profile becomes elevated with time, becoming more convex upward. The higher erosion rate results in a more convex shape of the thermal profile. One key result of upward heat advection is the viscosity reduction of the bulk crust and associated "thermal weakening" or decrease in viscous strength (e.g., Koons, 1987, Zeitler et al., 2001). The effective viscosity can be fully expressed using power law where R is the ideal gas constant, έ is strain rate, A_D, Ea, and n are flow law constants for crustal rocks (Ranalli 1995):

$$\eta_{eff} = \frac{1}{(A_D)^{1/n}(\acute{\varepsilon})^{(n-1)/n}} exp\left(\frac{E_a}{nRT}\right) \quad (25)$$

We use a constant strain rate of $\dot{\varepsilon} = 10^{-15}s^{-1}$ and felsic rocks with wet quartzite flow law to show how viscosity decreases with increasing temperature. Under the initial condition of the reference model, the average crustal temperature is 400 °C (corresponding to a viscosity of 1.5×10^{21} Pa s) at a depth of 40 km based on the initial linear geotherm in the "cold" crust setup. **Figure 19A** shows the viscosity decrease as the temperature of the bulk crust increases due to heat advection. When the temperature increases to 700 °C viscosity has decreased for about 2 orders of magnitude.

As viscosity decreases, isostatic flow responds to surface erosion more quickly (a smaller characteristic timescale) according to Eq. 22 and 23 while the steady-state rock uplift rate (u_{ss}) remains unchanged. As a result, for a system where Pe >1, the rock uplift rate should increase nonlinearly with time. To demonstrate advection-induced viscosity reduction and how it affects the rock uplift rate with time, in **Figure 20B** we enforce 2 orders of magnitude drop in viscosity from 5×10^{22} Pa s to 5×10^{20} Pa s at time t = 2 Myr. The result is a sharp increase in the rock uplift rate vs. time curve, such that a concave upward shape is formed around 2.5 Myr. This matches the concave upward rock uplift rate curves from the numerical result (**Figure 8**, **14**, and **15**). Such viscosity reduction and associated crustal strength weakening is proposed to play an important role in the EHS system (e.g., Zeilter et al., 2001; 2014), to provide a positive feedback loop between erosion and rock uplift rates. Here we show under constant surface erosion, advection-induced viscosity reduction will indeed accelerate rock uplift rate with time. Yet, the maximum rock uplift rate is still limited by the imposed erosion rate.

Decompression melting, erosion-driven diapir, and combined rock uplift rate

When there is enough melt in the lower crust and the bulk crustal viscosity is reduced due to advective heating, a lower crust diapir will form and it quickly ascends to the upper crust (**Figure 5**, **7**, **10**, **11**, and **12**). The increase of melt content is caused by decompression melting of the lower crust demonstrated by intersection of the geothermal profile with the solidus (**Figure 6**). It is noted that for the reference model, we have a thin layer of < 1% melting at the base of the lower crust under the initial geothermal profile. This thin layer of partial melt is not able to generate a diapir by itself until melt content further is increased and the bulk crustal viscosity is reduced.

The formation of a diapir is related to the Rayleigh-Taylor instability. Certain conditions have to be met in order to start the instability. We can use a dimensionless number, the Rayleigh number (*Ra*) to evaluate the likelihood of diapir formation. For our model setup that is a rectangular box where the only heat source is the fixed bottom temperature boundary (without internal radiogenic heating), the Rayleigh number is defined as (Turcotte & Schubert, 2002):

$$Ra = \frac{\Delta\rho g H^3}{\kappa\eta} \tag{26}$$

Where $\Delta\rho$ is density reduction due to thermal expansion and partial melting, ΔT is temperature difference between the surface and Moho, g is gravitational acceleration, H is thickness of the crust, κ is thermal diffusivity, and η is viscosity. The critical Rayleigh number (Ra_{cr}) marks the onset of convection: if $Ra > Ra_{cr}$, convection occurs. The value of critical Rayleigh number (Ra_{cr}) depends on the geometry of the system and boundary

conditions. For our case, Ra_{cr} is in the range of 657.5 to 1708 (Turcotte & Schubert, 2002).

Since crustal thickness reduces slightly (~5-10%) with time in our model due to net mass outflow, its effect on the value of *Ra* is minimal. The solid rock density reduction due to thermal expansion is also minimal (~$\alpha\rho\Delta T$, in the range of 1%). When partial melting occurs, density reduction ($\Delta\rho$) will increase due to the increase of melt content. Using Eq. 7, we estimate the $\Delta\rho$ will increase 10% associated with 10% partial melting. Therefore, the influences of changes in crustal thickness (*H*) and density reduction ($\Delta\rho$) on *Ra* are minimal. In our simulation, the most important factor in increasing *Ra* is the viscosity reduction. The effective viscosity can drop several orders of magnitude due to advective heating.

Next, we use a constant strain rate of $\dot{\varepsilon} = 10^{-15}s^{-1}$ and felsic rocks with wet quartzite flow law to evaluate how *Ra* increases during advective heating. At the beginning before isostatic flow and decompression melting occurs, the average crustal temperature is 400°C (corresponding to an effective viscosity of 1.5×10^{21} Pa s) at a depth of 40 km based on the initial linear geotherm. The resulting *Ra* is about 200. This value is smaller than the Ra_{cr} to start convection. When crustal temperature increases due to advection, viscosity drops exponentially (**Figure 19A**). We plot *Ra* as a function of the average temperature of the crust within the "advective channel" beneath the pseudo-valley (**Figure 19B**). Once temperature reaches 575°C, *Ra* has increased roughly 10 times to a value of $Ra \approx 2\times10^3$ (**Figure 19B**). At this point *Ra* is greater than Ra_{cr}, hence the occurrence of convection and diapirism. In **Figure 5** we observe the initiation of

diapir at 8.7 Myr. Here the temperature at mid crust levels is ~600 °C, corresponding to a *Ra* of ~3×10^3 ($Ra > Ra_{cr}$). As the simulation progresses, *Ra* further increases due to the fast advective heating associated with the ascent of the diapir. Crustal diapirism does not form for cases with a mafic lower crust. Although the crust does heat up and viscosity is reduced, the mafic crust is too viscous to convect. (**Figure 19B**) as shown in the simulation results (**Figure 14**, **15**). In addition, the high solidus temperature of the mafic lower crust also reduces the degree of partial melting (**Figure 6**).

Our calculation for the value of *Ra* shown above may be still underestimated since we do not take the increase of strain rate into account: the effective viscosity of rocks decreases under higher strain rate conditions. In **Figure 5**, strain rate (έ) is slightly less than $10^{-15}s^{-1}$ initially and increases to $10^{-14}s^{-1}$ at steady-state after 15 Myr. Strain rate (έ) is inversely proportional to viscosity (η) as shown in Eq. 26, and has an exponent of *(n-1)/n*. If we were to use the actual higher strain rate, it would cause a further decrease of the effective viscosity, resulting in a larger *Ra* than what we presented here. However, the strain rate-induced viscosity reduction is minor compared to the effect of increased temperature.

Once convection is established and rocks are able to move upward in the form of a diapir, the ascent rate can be estimated using Stokes velocity (Turcotte & Schubert, 2014):

$$v_{diapir} = \frac{2}{9}\frac{\Delta\rho g r^2}{\eta} \tag{27}$$

For a density difference $\boldsymbol{\Delta\rho}$ = 30 kg/m^3 between the diapir and host rock (~10% partial melting), radius of the diapir column r = 5 km, and host rock viscosity $\eta = 10^{19}$ Pa s, the ascent velocity v_{diapir} is about 5 km/Myr. In many simulations, the diapir is developed within solid host rocks whose viscosity is close to 10^{18} Pa s or the diapir ascends through partially molten rocks with a viscosity of 10^{18} Pa (**Figure 5**, **7**, **10**, **11,** and **12**). In these cases, the v_{diapir} can be as high as ~15-50 km/Myr. It is important to note that v_{diapir} is a buoyancy-driven flow and not the pressure-gradient-driven flow. While the pressure-gradient-driven flow is limited by the topographic relief that is in turn bounded by the surface erosion rate (Eq. 21), v_{diapir} can exceed the surface erosion rate.

We can calculate the total rock uplift rate by taking both isostatic flow and diapir into account. v_{diapir} is the velocity of the diapir relative to the host medium, which itself is moving upward due to isostasy. The total uplift rate of rocks within the diapir is equal to the sum of v_{diapir} and the pressure-driven isostatic flow (u, **Figure 16**):

$$v_{total} = u + v_{diapir} \tag{28}$$

In this case, the combined rock uplift rate could reach 20 or even 50 km/Myr depending on the thermal condition and rock rheology in the model. This is very similar to the simulated rock uplift rate presented in **Figure 21**, where a rock parcel whose initial depth is 60 km that's entrained within the diapir after 10 Myr (blue curve). The rock parcel rises through the diapiric column for roughly 1 Myr, reaching a maximum uplift rate of ~35 km/Myr before arriving at the plume head of the diapir. Thus, diapiric rise augments pressure-driven isostatic flow resulting in rock uplift rates that are much higher

than the effective surface erosion rate (5-6 km/Myr). In cases where the total rock uplift rate exceeds the imposed surface erosion rate a central bulge is formed that is higher than the surrounding surface.

Interactions and possible feedback between surface erosion and solid earth processes

The imposed constant surface erosion in the pseudo-valley play an important role in controlling the steady-state rock uplift rate, the Péclet number, and viscous weakening of the crust due to advective heating. The topographic diffusion tends to smooth out existing topographic relief and modifies the effective erosion rate (**Figure 13**). As expected, a higher topographic diffusivity results in a more flattened topography across the pseudo-valley regardless of diapiric ascent.

The role of topographic diffusion becomes more interesting when the diffusion process starts to amplify surface erosion. The accelerated erosion rate caused by topographic diffusion is more obvious where the central bulge is more developed, and the peak elevation of the bulge is higher than the "shoulders" of the valley (**Figure 22**). A more pronounced central bulge is likely to increase the surface erosion rate due to diffusion where the slopes of the bulge have a greater curvature. These observations provide an insight to investigate the role of the topographic diffusion in the "aneurysm model".

In the conceptual aneurysm model (e.g., Zeitler et al., 2001; 2014; Koons et al., 2013), a positive feedback was proposed between surface erosion and rock uplift. Koons et al. (2002)'s numerical treatment on the aneurysm model demonstrated this positive

feedback mainly relies on the crustal strength reduction due to erosion-driven heat advection in the crust and a tectonic wedge permitting the crustal materials being "pushed" up. In our study, we prescribe constant surface erosion over a pseudo-valley and find that the crust can respond to erosion via isostatic and diapiric flows. It is intriguing to see if we can trigger positive feedback between rock uplift and surface erosion under our model setup. A conceptual way to achieve the positive feedback in our model is through the following steps. Initial focused erosion establishes a rock advection channel. If the rates of rock uplift exceed the imposed erosion rate with the help of diapirism, a pronounced central protruding topography is created. This bulging topography causes the effective erosion rate to increase with an increased component of topographic diffusion rate, which leads to higher rates of rock uplift, completing the positive feedback loop. The establishment of such a positive feedback loop would be evidenced by exponential increases in both effective surface erosion and rock uplift rates.

The results from our reference and all other simulations (e.g., **Figure 21**) do not show the expected behaviors of positive feedback. First, we don't see an exponential increase in the effective erosion rate. On the contrary, we observe a steady increase that eventually levels off reaching steady-state after ~14 Myr. Second, while some of the rock uplift rates do show exponential increase patterns, as discussed previously this is due to the effect of viscosity decrease and entrainment into the diapir during their ascent through the crustal column. The rock uplift rate closely matches the pattern of the flatlining effective erosion rate. In the best cases, the effective erosion rates are larger than the imposed erosion rate by ~30% but both rock uplift and surface erosion rates flatten afterwards.

We were able to produce a more significant exponential increase of erosion and rock uplift rates associated with positive feedback by using a high imposed erosion rate (10 km/Myr) and a large topographic diffusivity (10^{-4} m^2/s). The very high topographic diffusivity effectively smooths out any central bulge that would otherwise form, maintaining the concave shape of the pseudo-valley. Shown in **Figure 23**, both the rock uplift and effective erosion rates show exponential growth to values almost 3 times the initial. The positive feedback established in this case maintains for about <10 Myr and does not continue forever. The effective erosion rate reaches steady-state around 26 km/Myr indicating the growth of the central bulge is limited by topographic diffusion. We suggest that under the simulated conditions for a felsic, wet-quartzite-rheology crust, a high surface erosion rate and a large topographic diffusivity are needed to enable the high effective erosion rate.

We summarize the dynamics of the erosion-driven system based on the values of the Péclet (*Pe*) and Raleigh (*Ra*) numbers (**Figure 24**):

(1) $Pe < 1$: very slow isostatic flow, pronounced valley topography, longer response time, little thermal advection.

(2) $Pe \sim 1$: slightly faster isostatic flow, reduced valley topography, shorter response time, thermal advection become important.

(3) $Pe > 1$ & $Ra < Ra_{cr}$: isostatic flow rate increases with time due to strong advective heating and associated viscosity reduction, smoothed valley topography (but no higher than the surrounding topography), rock uplift rate is still limited by the erosion rate.

(4) Pe >1 & $Ra > Ra_{cr}$: decompression melting starts and diapir forms, significant increase of rock uplift rate which exceeds the surface erosion rate, increased valley elevation exceeding the surrounding topography. Time-limited positive feedback between rock uplift and surface erosion can be established if topographic diffusivity is high.

It is noted that our model setup is different from the one by Koons et al. (2002). Compared to Koons et al. (2002), our model does not generate any thrust or back-thrust fault/shear zones, allowing crustal materials to "pop-up" under contraction. Instead, we focused on the role of surface erosion itself and how the crust responds to imposed surface erosion. Therefore, the interactions between surface erosion and solid earth processes (e.g., rock uplift, advective heating, and possible diapirism) in our model slightly differs from the ones in Koons et al. (2002). While both models (ours and Koons et al.2002) emphasize the key role of crustal strength reduction (mainly due to the reduction of crustal viscosity) resulting from erosion-driven advection, our model attributes high topography to the combined effects of isostatic and diapiric flows.

Model limitations

Our simulation results are meant to be taken with the consideration of the model assumptions and limitations listed below. (1) The modeled crust is homogenous with no preexisting structures. The presence of the Indus-Yarlung suture zone and the associated thrust systems can pose as weak points for deformation to exploit. (2) Surface erosion is modeled as constant river valley incision, with prescribed spatial variance and does not depend on time nor elevation. (3) The linear parameterization of topographic diffusion based on surface slope is associated with large uncertainties. Diffusive transport has been

argued to depend on slope gradient nonlinearly (Roering et al., 1999) and may vary by several orders of magnitude from hillslope to regional scale. (4) The model domain is in 2D, which consists of vertical depth, as well as the orogen-parallel dimension. It does not include the orogen-perpendicular dimension. (5) Melt extraction is not included in the model. Partial melt produced from decompression melting helps to lower viscosity and participates in crustal flow, but it is not extracted.

Rock uplift rates derived from our simulations are calculated relative to the fixed Eulerian grid and can be interpreted as the geological true rock uplift rate relative to a stationary surface reference frame. Most geo-thermochronologic studies report rock exhumation rates, which represent the vertical motion of a rock parcel relative to the topographic surface. Since our models also simulate the morphology of topography, the rock uplift rates obtained from numerical models can be converted to rock exhumation rates by accounting for the change of surface elevation (exhumation = rock uplift – surface uplift; England & Molnar, 1990). Given an imposed erosion rate, we can calculate the steady-state rate of surface elevation change by taking the product of erosion rate and pseudo valley width and divide by the width of the model domain (500 km). For the reference model with an imposed erosion rate of 5 km/Myr over the 50-km-wide pseudo valley, the surface elevation decreases at a rate of 0.5 km/Myr (5 km/Myr × 50 km ÷ 500 km). Therefore, the model predicted steady-state rock exhumation rates are 0.5 km/Myr higher than the rock uplift rates. Such a small difference between the rock uplift and exhumation rates in our model is within the uncertainty of thermochronologically estimated exhumation rates, and we make the argument that the

rock uplift rates presented here can be directly compared to the rock exhumation rates from published studies.

Implication for the evolution of eastern Himalayan syntax

Our numerical model and scaling analysis highlight how surface erosion can drive deep crustal processes and explore the possible feedback between the two. The erosion-driven model reproduces high relief, overall domal structure, and young thermochronologic ages (**Figure 25C**, **D**) associated with rapid exhumation (e.g., Enkelmann et al., 2011; Bracciali et al., 2016; King et al., 2016). Other models used to explain these key features of the EHS including the indentation of the subducting Indian plate (Bendick & Ehlers, 2014) and lithospheric scale buckling (Burg et al., 1998) are tectonic-driven, requiring specific lithospheric geometry, rheology, and thermal state. We chose to minimize the effect of tectonic shortening to better isolate the effects of erosion-induced solid earth processes. In this sense, our model represents an erosion-driven endmember that could complement the tectonic-driven models. While we do not claim to fully solved the long-standing questions regarding the ultimate mechanisms of fast rock exhumation and surface erosion in the EHS, the results of this study have the following implications for EHS evolution.

Our modeling results suggest that fast and focused surface erosion alone is able to induce upward crustal flow, thermally weaken the crust through advective heating, and exhume lower crust within ~10 Myr. The isostatic flow of crustal rocks due to erosion can produce an antiform-like or domal structure in the EHS crust that mimics geological observations (e.g., Burg et al., 1998; Zeiter et al., 2004). Our model also highlights partial

melting of the lower crust resulting from decompression and thermal weakening of the crust can generate diapirs that significantly accelerate the uplift rates of rocks entrained in the diapir. The geodynamic consequence of crustal diapirism is overlooked in previous models.

Compared to the "buckling" model, our erosion-driven model does not need to have significant crustal shortening as a prerequisite (e.g., Burg et al., 1998; Seward & Burg, 2008). In the crustal buckling model, fast rock uplift of the EHS since ~10 Ma represents the short "buckling" period that was accumulated from ~50 Myr of crustal shortening (Burg et al., 1998). Thus, the ~10 Ma evolution of the EHS is largely a result of a 40-Myr-long incubation of plate convergence. In this sense, surface erosion plays a passive role to accommodate the sudden increase of rock uplift rate, and the fast uplift of the EHS is not driven by surface processes. Additionally, the "buckling" model also requires the pre-existence of certain initial temperature anomalies or weakening in the future "buckling" region (Burg & Podladchikov, 1999). While rheological heterogeneities exist along the plate margin, exactly how such heterogeneities are distributed in space is hard to define. Future studies are needed to test the erosion-driven model under higher strain rate conditions since complex patterns may emerge with the interaction between crustal folding and diapirism (e.g., Burg et al., 2004; Kaus, 2005).

Our simulation results could explain the isothermal decompression paths inferred from thermobarometric studies on metamorphic units of the EHS (e.g., Booth et al., 2009, Palin et al., 2015). However, due to model limitations and assumptions stated earlier, the results do not perfectly match what's been observed at the EHS. For example, **Figure**

25A depicts the model predicted P-T-t path of EHS crustal rocks. While the overall isothermal decompression trend is similar to other published studies (e.g., Booth et al., 2009; Palin et al., 2015; Govin et al., 2020), the model predicted temperatures are significantly lower than the rock record.

Additionally, our model also shed light on the proposed onset and late acceleration of EHS exhumation identified by Govin et al. (2020). Their thermochronologic data suggest exhumation rates increased from 1 to 4 km/Myr at ~8 Ma and again to 9 km/Myr at ~2 Ma. Here we offer a plausible scenario where efficient river incision began at ~8 Ma. Continued upward advection caused thermal and strain weakening of the EHS crust, leading to the formation of a crustal diapir as well as the increase of exhumation rates at ~2 Ma. Associated with the diapir is a ~50 km dome-like structure of high topography centered within the erosional valley (**Figure 5**), an analogue for the Quaternary uplift of the Namche Barwa massif that is responsible for the deposition of alluvium sediments above the Yarlung Tsangpo gorge (Wang et al., 2014). The increased regional rock uplift rates associated with or contributed by the diapiric rock ascend could be responsible for the stability of the Yarlung Tsangpo knickpoint (e.g., Zeitler et al., 2001, Wang et al., 2017), as well as the observed northward migration and expansion of EHS exhumation within the past ~1 Myr (King et al., 2016; Yang et al., 2021).

Similar to the tectonic aneurysm model (Zeiter et al., 2001, Koons et al., 2013), our erosion-driven model confirms the coupling between surface erosion and rapid uplift of the EHS. To establish a long-lasting positive feedback between surface erosion and

rock uplift through our erosion-driven model is possible, but both high surface erosion rate (>10 km/Myr) and seemingly too-large topographic diffusivity (10^{-4} m^2/s) are necessary. We envision that with some additional tectonic driving force, the required surface erosion rate and topographic diffusivity could be lowered and a positive feedback may be achievable.

As demonstrated by the isostatic flow model, rock uplift rate closely matches the imposed surface erosion rate. Therefore, when rock uplift is only driven by isostatic flow, the EHS erosion history can be directly inferred from the thermochronological data. However, workers must be careful when applying this method when crustal diapirism is present. We suggest the rock uplift rate may be augmented by the buoyancy-driven diapir. In this case, the rock uplift rate could be an overestimate of the regional surface erosion rate.

CONCLUSION

Numerical modeling results show that surface erosion is able to generate partial melt, produce localized high topography, and exhume lower crustal rocks from >40 km depth to the surface within 10 Myr. Erosion-driven rock exhumation is sustained by isostatic flow and amplified by crustal diapirism. Continued surface erosion localized to an area such as incision of the EHS by the Yarlung-Tsangpo river is able to promote tectonic deformation via thermal advection and strain weakening. The presence of hot, buoyant molten rocks in a weakened crust may trigger the formation of a diaper in the crustal column, leading to rapid rock uplift with rates greater than the driving erosional

forcing. This increase in rock uplift causes surface uplift, resulting in a central bulge that exceeds the surrounding elevation. The bulging topography causes the effective erosion rate to increase with an increased component of topographic diffusion rate, leading to higher rates of rock uplift, completing a positive feedback loop. Our erosion-driven exhumation model demonstrates the intricate coupling between surface erosion and rock uplift, as well as the active role of surface erosion in driving tectonic evolution. To establish a long-lasting positive feedback between surface erosion and rock uplift through our erosion-driven model is possible, but both high surface erosion rate (>10 km/Myr) and topographic diffusivity (10^{-4} m^2/s) are necessary. Although we do not claim to have solved the age-old debate on the driver of EHS exhumation, we highlight that buoyancy-driven diapiric flow is a result of Rayleigh-Taylor instability triggered by fast surface erosion. The erosion-driven diapir can be one of the missing pieces or alternative mechanisms explaining the evolution of the eastern Himalayan syntaxis.

REFERENCES

Allmendinger, R.W., Reilinger, R. and Loveless, J., 2007. Strain and rotation rate from GPS in Tibet, Anatolia, and the Altiplano. Tectonics, 26(3).

Baksi, A.K., 2007. Geological Society of America Special Papers. Geological Society of America Special Papers, 430, pp.285-303.

Braun, J., Simon-Labric, T., Murray, K.E. and Reiners, P.W., 2014. Topographic relief driven by variations in surface rock density. Nature Geoscience, 7(7), pp.534-540.

Baumann, T.S. and Kaus, B.J., 2015. Geodynamic inversion to constrain the non-linear rheology of the lithosphere. Geophysical Journal International, 202(2), pp.1289-1316.

Beaumont, C., Jamieson, R.A., Nguyen, M.H. and Lee, B., 2001. Himalayan tectonics explained by extrusion of a low-viscosity crustal channel coupled to focused surface denudation. Nature, 414(6865), pp.738-742.

Bendick, R. and Ehlers, T.A., 2014. Extreme localized exhumation at syntaxes initiated by subduction geometry. Geophysical Research Letters, 41(16), pp.5861-5867.

Bittner, D. and Schmeling, H., 1995. Numerical modelling of melting processes and induced diapirism in the lower crust. Geophysical Journal International, 123(1), pp.59-70.

Booth, A.L., Chamberlain, C.P., Kidd, W.S. and Zeitler, P.K., 2009. Constraints on the metamorphic evolution of the eastern Himalayan syntaxis from geochronologic and petrologic studies of Namche Barwa. Geological Society of America Bulletin, 121(3-4), pp.385-407.

Bracciali, L., Parrish, R.R., Najman, Y., Smye, A., Carter, A. and Wijbrans, J.R., 2016. Plio-Pleistocene exhumation of the eastern Himalayan syntaxis and its domal 'pop-up'. Earth-Science Reviews, 160, pp.350-385.

Burg, J.P. and Gerya, T.V., 2005. The role of viscous heating in Barrovian metamorphism of collisional orogens: thermomechanical models and application to the Lepontine Dome in the Central Alps. Journal of Metamorphic Geology, 23(2), pp.75-95.

Burg, J.P., Nievergelt, P., Oberli, F., Seward, D., Davy, P., Maurin, J.C., Diao, Z. and Meier, M., 1998. The Namche Barwa syntaxis: evidence for exhumation related to compressional crustal folding. Journal of Asian Earth Sciences, 16(2-3), pp.239-252.

Burg, J.P. and Podladchikov, Y., 1999. Lithospheric scale folding: numerical modelling and application to the Himalayan syntaxes. International Journal of Earth Sciences, 88(2), pp.190-200.

Cao, W., Yang, J., Zuza, A.V., Ji, W.Q., Ma, X.X., Chu, X. and Burgess, Q.P., 2020. Crustal tilting and differential exhumation of Gangdese Batholith in southern Tibet revealed by bedrock pressures. Earth and Planetary Science Letters, 543, p.116347.

Chen, W.-P., Yu, C.-Q., Tseng, T.-L., Yang, Z., Wang, C., Ning, J., Leonard, T., 2013. Moho, seismogenesis, and rheology of the lithosphere. Tectonophysics, Moho: 100

years after Andrija Mohorovicic 609, 491–503. https://doi.org/10.1016/j.tecto.2012.12.019

Chen, W.P. and Jiang, Y., 2020. Undulating Moho beneath a near-uniform surface of central Tibet. Earth and Planetary Science Letters, 543, p.116343.

Dabrowski, M., Krotkiewski, M. & Schmid, D., 2008. Milamin: MATLAB-based finite element method solver for large problems, Geochem. Geophys. Geosyst., 9(4), doi:10.1029/2007GC001719.

Dahlen, F.A., Suppe, J. and Davis, D., 1984. Mechanics of fold-and-thrust belts and accretionary wedges: Cohesive Coulomb theory. Journal of Geophysical Research: Solid Earth, 89(B12), pp.10087-10101.

Davis, D., Suppe, J. and Dahlen, F.A., 1983. Mechanics of fold-and-thrust belts and accretionary wedges. Journal of Geophysical Research: Solid Earth, 88(B2), pp.1153-1172.

Ding, L. and Zhong, D., 1999. Metamorphic characteristics and geotectonic implications of the high-pressure granulites from Namjagbarwa, eastern Tibet. Science in China Series D: Earth Sciences, 42(5), pp.491-505.

Ding, L., Zhong, D., Yin, A., Kapp, P. and Harrison, T.M., 2001. Cenozoic structural and metamorphic evolution of the eastern Himalayan syntaxis (Namche Barwa). Earth and Planetary Science Letters, 192(3), pp.423-438.

Enkelmann, E., Ehlers, T.A., Zeitler, P.K. and Hallet, B., 2011. Denudation of the Namche Barwa antiform, eastern Himalaya. Earth and Planetary Science Letters, 307(3-4), pp.323-333.

Fernandes, N.F. and Dietrich, W.E., 1997. Hillslope evolution by diffusive processes: The timescale for equilibrium adjustments. Water Resources Research, 33(6), pp.1307-1318.

Finnegan, N.J., Hallet, B., Montgomery, D.R., Zeitler, P.K., Stone, J.O., Anders, A.M. and Yuping, L., 2008. Coupling of rock uplift and river incision in the Namche Barwa–Gyala Peri massif, Tibet. Geological Society of America Bulletin, 120(1-2), pp.142-155.

Gerya, T., 2019. Introduction to numerical geodynamic modelling. Cambridge University Press.

Gerya, T.V. and Yuen, D.A., 2003. Characteristics-based marker-in-cell method with conservative finite-differences schemes for modeling geological flows with strongly variable transport properties. Physics of the Earth and Planetary Interiors, 140(4), pp.293-318.

Gong, J., Ji, J., Zhou, J., Tu, J., Sun, D., Zhong, D. and Han, B., 2015. Late Miocene thermal evolution of the eastern Himalayan syntaxis as constrained by biotite 40Ar/39Ar thermochronology. The Journal of Geology, 123(4), pp.369-384.

Govin, G., Najman, Y., Dupont-Nivet, G., Millar, I., Van Der Beek, P., Huyghe, P., O'sullivan, P., Mark, C. and Vögeli, N., 2018. The tectonics and paleo-drainage of the

easternmost Himalaya (Arunachal Pradesh, India) recorded in the Siwalik rocks of the foreland basin. American Journal of Science, 318(7), pp.764-798.

Govin, G., van der Beek, P., Najman, Y., Millar, I., Gemignani, L., Huyghe, P., Dupont-Nivet, G., Bernet, M., Mark, C. and Wijbrans, J., 2020. Early onset and late acceleration of rapid exhumation in the Namche Barwa syntaxis, eastern Himalaya. Geology, 48(12), pp.1139-1143.

Guilmette, C., Indares, A. and Hébert, R., 2011. High-pressure anatectic paragneisses from the Namche Barwa, Eastern Himalayan Syntaxis: textural evidence for partial melting, phase equilibria modeling and tectonic implications. Lithos, 124(1-2), pp.66-81.

Hung, S.-H., Chen, W.-P., Chiao, L.-Y., Tseng, T.-L., 2010. First multi-scale, finite frequency tomography illuminates 3-D anatomy of the Tibetan plateau. Geophysical Research Letters 37. http://dx.doi.org/10.1029/2009GL041875.

Hung, S.-H., Chen, W.-P., Chiao, L.-Y., 2011. A data-adaptive, multi-scale approach of finite-frequency, travel-time tomography with special reference to P- and S- wave data from central Tibet. Journal of Geophysical Research 116, B06307. http://dx.doi.org/10.1029/2010JB008190.

Huysmans, M. and Dassargues, A., 2005. Review of the use of Péclet numbers to determine the relative importance of advection and diffusion in low permeability environments. Hydrogeology Journal, 13(5), pp.895-904.

Kaus, B.J.P., 2005. Modelling approaches to geodynamic processes. ETH.

King, G.E., Herman, F. and Guralnik, B., 2016. Northward migration of the eastern Himalayan syntaxis revealed by OSL thermochronometry. Science, 353(6301), pp.800-804.

Koons, P.O., 1987. Some thermal and mechanical consequences of rapid uplift: an example from the Southern Alps, New Zealand. Earth and planetary science letters, 86(2-4), pp.307-319.

Koons, P.O. , Zeitler, P.K. , and Hallet, B. , 2013, Tectonic aneurysms and mountain building, in Owen, L.A. , ed., Treatise on Geomorphology, Volume 5: Tectonic Geomorphology: London , Academic Press, p. 318–349, https://doi.org/10.1016/B978-0-12-374739-6.00094-4.

Kundu, A., Hazarika, D., Yadav, D.K. and Ghosh, P., 2022. Crustal thickness and Poisson's ratio variations in the Siang Window and adjoining areas of the Eastern Himalayan Syntaxis. Journal of Asian Earth Sciences, p.105225.

Lang, K.A., Huntington, K.W., Burmester, R. and Housen, B., 2016. Rapid exhumation of the eastern Himalayan syntaxis since the late Miocene. Bulletin, 128(9-10), pp.1403-1422.

Liu, Y. and Zhong, D., 1997. Petrology of high-pressure granulites from the eastern Himalayan syntaxis. Journal of Metamorphic Geology, 15(4), pp.451-466.

Liu, Y., Tan, X., Ye, Y., Zhou, C., Lu, R., Murphy, M.A., Xu, X. and Suppe, J., 2020. Role of erosion in creating thrust recesses in a critical-taper wedge: An example from Eastern Tibet. Earth and Planetary Science Letters, 540, p.116270.

Molnar, P., England, P. Late Cenozoic uplift of mountain ranges and global climate change: chicken or egg?. Nature 346, 29–34 (1990). https://doi.org/10.1038/346029a0

Olive, J.A., Behn, M.D. and Malatesta, L.C., 2014. Modes of extensional faulting controlled by surface processes. Geophysical Research Letters, 41(19), pp.6725-6733.

Palin, R.M., Searle, M.P., St-Onge, M.R., Waters, D.J., Roberts, N.M.W., Horstwood, M.S.A., Parrish, R.R. and Weller, O.M., 2015. Two-stage cooling history of pelitic and semi-pelitic mylonite (sensu lato) from the Dongjiu–Milin shear zone, northwest flank of the eastern Himalayan syntaxis. Gondwana Research, 28(2), pp.509-530.

Patankar, S.V., 1980. Numerical heat transfer and fluid flow, Hemisphere Publ. Corp., New York, 58, p.288.

Rayleigh, L., 1916. LIX. On convection currents in a horizontal layer of fluid, when the higher temperature is on the under side. The London, Edinburgh, and Dublin Philosophical Magazine and Journal of Science, 32(192), pp.529-546.

Rey, P.F., Teyssier, C., Kruckenberg, S.C., Whitney, D.L., 2011. Viscous collision in channel explains double domes in metamorphic core complexes. Geology 39, 387–390. https://doi.org/10.1130/G31587.1

Roering, J.J., Kirchner, J.W. and Dietrich, W.E., 1999. Evidence for nonlinear, diffusive sediment transport on hillslopes and implications for landscape morphology. Water Resources Research, 35(3), pp.853-870.

Roering, J.J., Perron, J.T. and Kirchner, J.W., 2007. Functional relationships between denudation and hillslope form and relief. Earth and Planetary Science Letters, 264(1-2), pp.245-258.

Rothstein, D.A. and Manning, C.E., 2003. Geothermal gradients in continental magmatic arcs; constraints from the eastern Peninsular Ranges Batholith, Baja California, Mexico. Geological Society of America Special Papers, 374, pp.337-354.

Seward, D. and Burg, J.P., 2008. Growth of the Namche Barwa Syntaxis and associated evolution of the Tsangpo Gorge: Constraints from structural and thermochronological data. Tectonophysics, 451(1-4), pp.282-289.

Slingerland, R. and Kump, L., 2011. Mathematical Modeling of Earth's Dynamical Systems. In Mathematical Modeling of Earth's Dynamical Systems. Princeton University Press.

Sokoutis, D., Burg, J.P., Bonini, M., Corti, G. and Cloetingh, S., 2005. Lithospheric-scale structures from the perspective of analogue continental collision. Tectonophysics, 406(1-2), pp.1-15.

Thielmann, M. and Kaus, B.J., 2012. Shear heating induced lithospheric-scale localization: Does it result in subduction?. Earth and Planetary Science Letters, 359, pp.1-13.

Tu, J.Y., Ji, J.Q., Gong, J.F., Yan, Q.R. and Han, B.F., 2016. Zircon U–Pb dating constraints on the crustal melting event around 8 Ma in the eastern Himalayan syntaxis. International Geology Review, 58(1), pp.58-70.

Turcotte, D.L. and Schubert, G., 2002. Geodynamics. Cambridge university press.

Wang, C., Chen, W.-P., Wang, L.-P., 2013. Temperature beneath Tibet. Earth and Planetary Science Letters 375, 326–337. https://doi.org/10.1016/j.epsl.2013.05.052

Wang, P., Scherler, D., Liu-Zeng, J., Mey, J., Avouac, J.P., Zhang, Y. and Shi, D., 2014. Tectonic control of Yarlung Tsangpo Gorge revealed by a buried canyon in Southern Tibet. Science, 346(6212), pp.978-981.

Wang, Y., Zhang, H., Zheng, D., von Dassow, W., Zhang, Z., Yu, J. and Pang, J., 2017. How a stationary knickpoint is sustained: New insights into the formation of the deep Yarlung Tsangpo Gorge. Geomorphology, 285, pp.28-43.

Whipp Jr, D.M., Beaumont, C. and Braun, J., 2014. Feeding the "aneurysm": Orogen-parallel mass transport into Nanga Parbat and the western Himalayan syntaxis. Journal of Geophysical Research: Solid Earth, 119(6), pp.5077-5096.

Whipple, K.X. and Tucker, G.E., 1999. Dynamics of the stream-power river incision model: Implications for height limits of mountain ranges, landscape response timescales, and research needs. Journal of Geophysical Research: Solid Earth, 104(B8), pp.17661-17674.

Yang, R., Herman, F., Fellin, M.G. and Maden, C., 2018. Exhumation and topographic evolution of the Namche Barwa Syntaxis, eastern Himalaya. Tectonophysics, 722, pp.43-52.

Yang, R., Herman, F., Liu, T., Biswas, R.H., Fellin, M.G., Tian, Y., Gong, J., Jiao, R., Maden, C. and Chen, H., 2021. Enhanced Quaternary exhumation in the Namche Barwa syntaxis, eastern Himalaya. Geology, 49(8), pp.958-962.

Zeitler, P.K., Meltzer, A.S., Koons, P.O., Craw, D., Hallet, B., Chamberlain, C.P., Kidd, W.S., Park, S.K., Seeber, L., Bishop, M. and Shroder, J., 2001. Erosion, Himalayan geodynamics, and the geomorphology of metamorphism. Gsa Today, 11(1), pp.4-9.

Zeitler, P.K., Meltzer, A.S., Brown, L., Kidd, W.S., Lim, C. and Enkelmann, E., 2014. Tectonics and topographic evolution of Namche Barwa and the easternmost Lhasa block, Tibet. In Toward an improved understanding of uplift mechanisms and the elevation history of the Tibetan Plateau (Vol. 507, pp. 23-58). Geological Society of America Special Papers.

Zhang, J., Ji, J., Zhong, D., Ding, L. and He, S., 2004. Structural pattern of eastern Himalayan syntaxis in Namjagbarwa and its formation process. Science in China Series D: Earth Sciences, 47(2), pp.138-150.

Zhang, P.Z., Shen, Z., Wang, M., Gan, W., Bürgmann, R., Molnar, P., Wang, Q., Niu, Z., Sun, J., Wu, J. and Hanrong, S., 2004. Continuous deformation of the Tibetan Plateau from global positioning system data. Geology, 32(9), pp.809-812.

Zhong, D.L., and Ding, L. 1996. Discovery of high-pressure basic granulite in Namjagbarwa area, Tibet, China. Chinese Science Bulletin, 41, pp. 87-88

Zhu, D.C., Wang, Q., Zhao, Z.D., Chung, S.L., Cawood, P.A., Niu, Y., Liu, S.A., Wu, F.Y. and Mo, X.X., 2015. Magmatic record of India-Asia collision. Scientific reports, 5(1), pp.1-9.

Zuza, A.V., Gavillot, Y., Haproff, P.J. and Wu, C., 2020. Kinematic evolution of a continental collision: Constraining the Himalayan-Tibetan orogen via bulk strain rates. Tectonophysics, 797, p.228642.

TABLES

Table 5.1: Parameters, symbols, values, and units used in the model.

Parameter	Symbol	Value	Unit
Crustal thickness	z	70	km
Crustal width	W	500	km
Moho temperature	T_{moho}	700	°C
Surface temperature	$T_{surface}$	20	°C
Reference density	ρ_0		kg m^{-3}
Melt density	ρ_{molten}		kg m^{-3}
Shortening strain rate	ε	10^{-16}	s^{-1}
Erosional valley half width	w	25	km
Imposed erosion rate	E	variable	km Myr^{-1}
Topographic diffusivity coefficient	D	variable	m^2 s^{-1}
Critical melt fraction	F_{crit}	0.05	
Melt viscosity	η	10^{18}	Pa s
Thermal diffusivity[a]	k	10^{-6}	m^2 s
Thermal expansion coefficient[a]	α	$3*10^{-5}$	K^{-1}
Compressibility coefficient[a]	β	10^{-11}	Pa^{-1}
Shear modulus[a]	G	10^{10}	Pa
Gravitational acceleration	g	9.8	m s^{-2}

[a] Turcotte and Schubert (2002)

Table 5.2: Material properties of the felsic and mafic crusts used in numerical simulations.

Crustal composition	Density[a] (kg m^{-3})	Solidus temperature[a] (K)	Liquidus temperature[a] (K)	Coupled flow law	*Ea* (kJ mol^{-1})	*n*	*AD*	Friction angel (°)
Felsic	2800 (ρ_0) 2500 (ρ_{molten})	$889 + 17900/(P + 54) + 20200/(P + 54)^2$ at $P < 1200$ MPa, $831 + 0.06P$ at $P > 1200$ MPa	$1262 + 0.09P$(MPa)	wet quartzite[b]	154	2.3	3.2×10^{-4}	20
Mafic	2900 (ρ_0) 2600 (ρ_{molten})	$973–70400/(P + 354) + 77800000/(P + 354)^2$ at $P < 1600$ MPa, $935 + 0.0035P + 0.0000062P^2$ at $P > 1600$ MPa	$1423 + 0.105P$(MPa)	plagioclase An_{75}[b]	238	3.2	3.3×10^{-4}	20

[a] Gerya (2019)

[b] Ranalli (1995)

[c] Turcotte and Schubert (2002)

Table 5.3: Simulations and their varied parameters.

Simulation	Upper crust	Lower crust	Erosion rate (km Myr^{-1})	Topographic diffusion (m^2/s)	Geothermal gradient
Reference model	Felsic, wet qtz	Felsic, wet qtz	5	10^{-5}	Linear
High topographic diffusion	Felsic, wet qtz	Felsic, wet qtz	5	10^{-4}	Linear
Low topographic diffusion	Felsic, wet qtz	Felsic, wet qtz	5	10^{-6}	Linear
High erosion	Felsic, wet qtz	Felsic, wet qtz	10	10^{-5}	Linear
High erosion, high topographic diffusion	Felsic, wet qtz	Felsic, wet qtz	10	10^{-4}	Linear
High erosion, low topographic diffusion	Felsic, wet qtz	Felsic, wet qtz	10	10^{-6}	Linear
Low erosion	Felsic, wet qtz	Felsic, wet qtz	2	10^{-5}	Linear
Low erosion, high topographic diffusion	Felsic, wet qtz	Felsic, wet qtz	2	10^{-4}	Linear
Low erosion, low topographic diffusion	Felsic, wet qtz	Felsic, wet qtz	2	10^{-6}	Linear
2-stage geotherm	Felsic, wet qtz	Felsic, wet qtz	5	10^{-5}	2-stage
2-stage geotherm, high erosion	Felsic, wet qtz	Felsic, wet qtz	10	10^{-5}	2-stage
2-stage geotherm, low erosion	Felsic, wet qtz	Felsic, wet qtz	2	10^{-5}	2-stage
Mafic lower crust	Felsic, wet qtz	Mafic, plag	5	10^{-5}	Linear
Mafic lower crust	Felsic, wet qtz	Mafic, plag	5	10^{-5}	2-stage

FIGURES

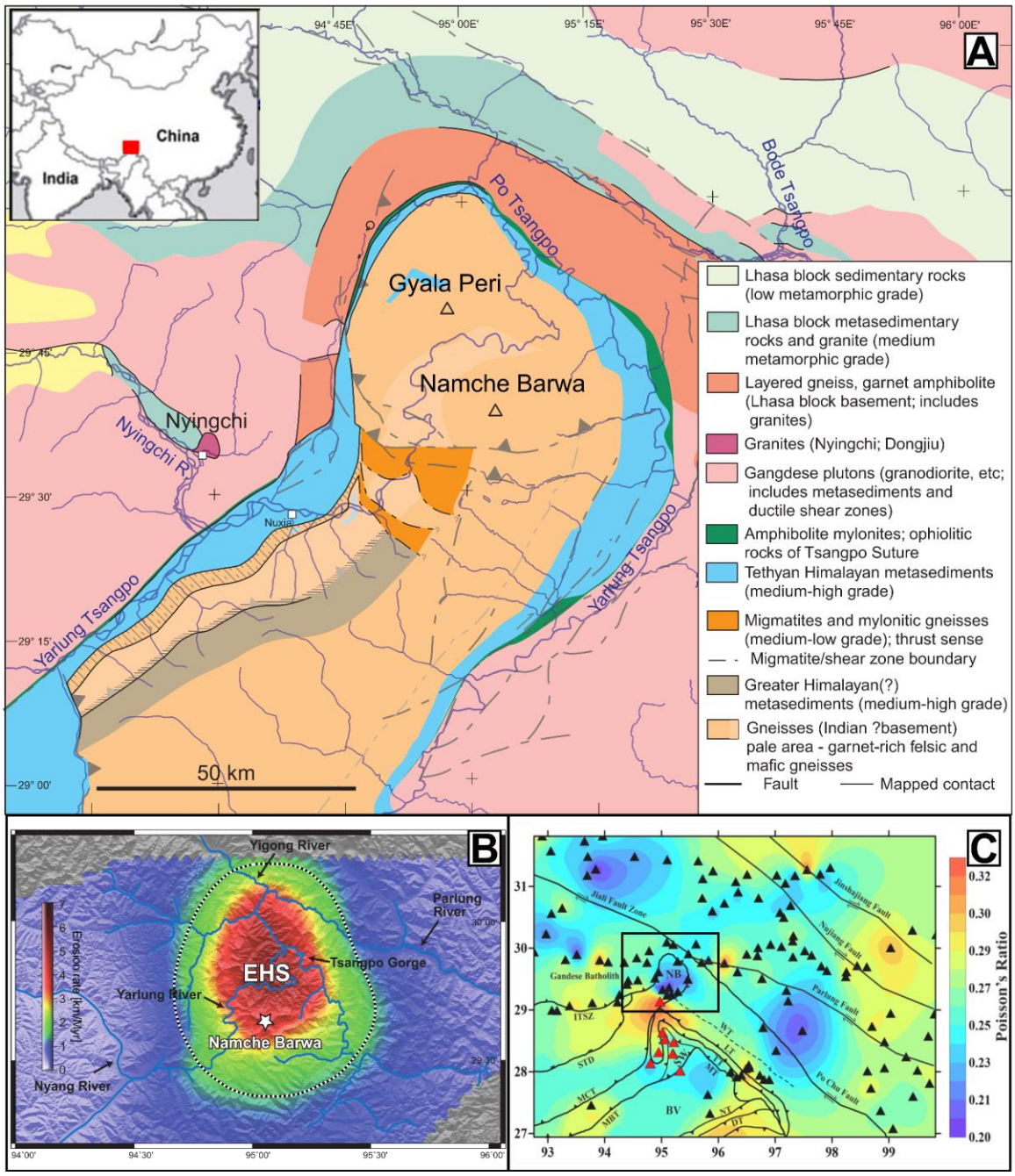

Figure 5.1. Map of the Eastern Himalayan Syntaxis (EHS). (**A**) Geological map showing major lithological units and faults (Booth et al., 2009). (**B**) Digital elevation map of the EHS and surrounding region color coded by erosion rates for the past 2 Myr inferred from thermochronologic data (Modified from King et al., 2016). Note the focused "bullseye" concentric pattern of high erosion rates. (**C**) Map of crustal Poisson's ratio

(Kundu et al., 2022). Black box indicates the area shown in **A.** Notice the low values at the EHS indicating quartz-rich, felsic composition for bulk crust.

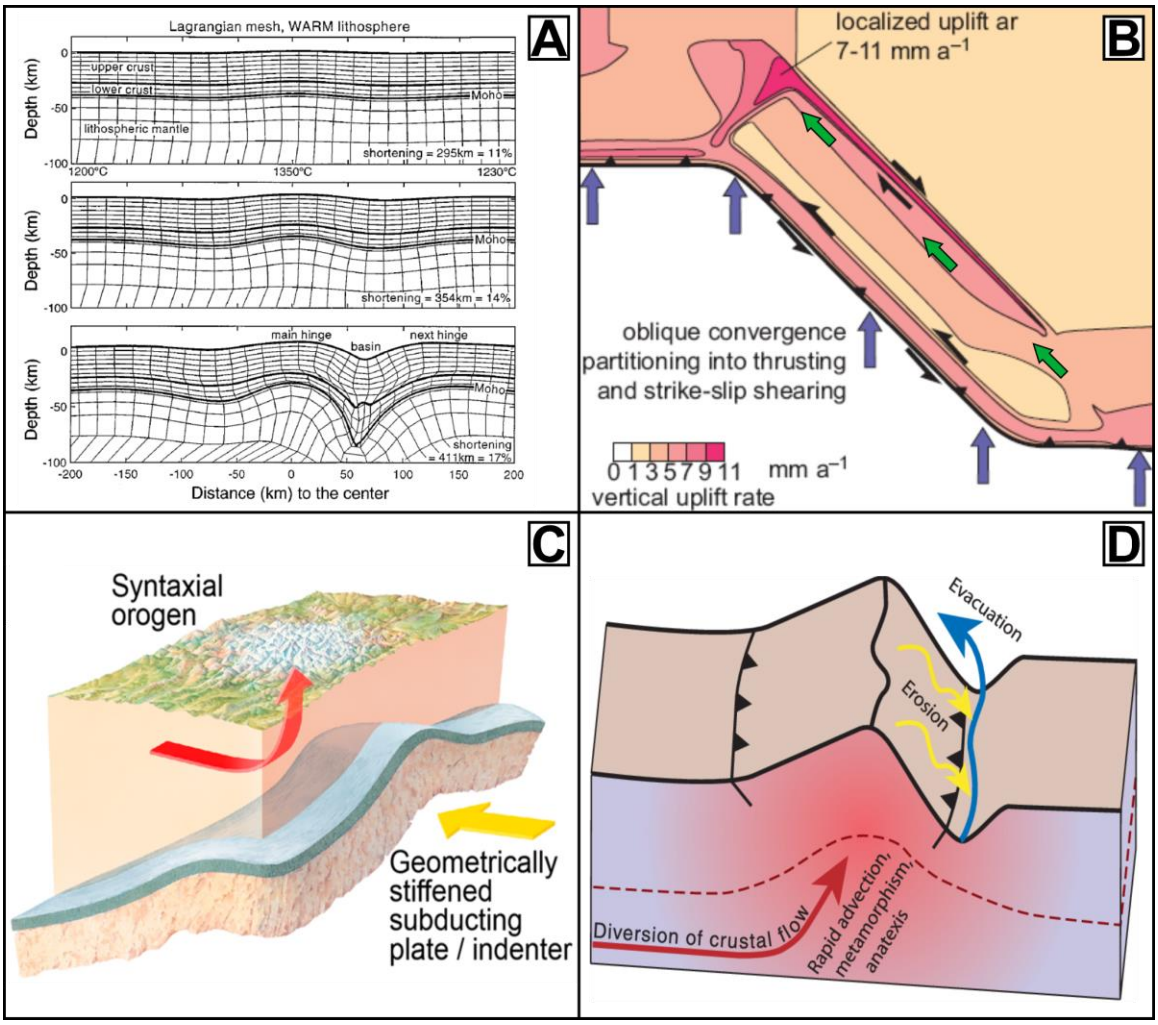

Figure 5.2. A review of end-member models for the EHS.(**A**) Lithospheric buckling as a result of progressive shortening of 10-17% (Burg & Podladchikov, 1999). (**B**) Numerical modelling output showing the channel flow model resulting from partitioned oblique convergence (Whipp et al., 2014). (**C**) Schematic representation of the subduction basal indenter (Bendick & Ehlers, 2014). (**D**) The "tectonic aneurysm" model coupling erosion and sediment removal by rivers to focused exhumation, elevated temperatures, and deformation.

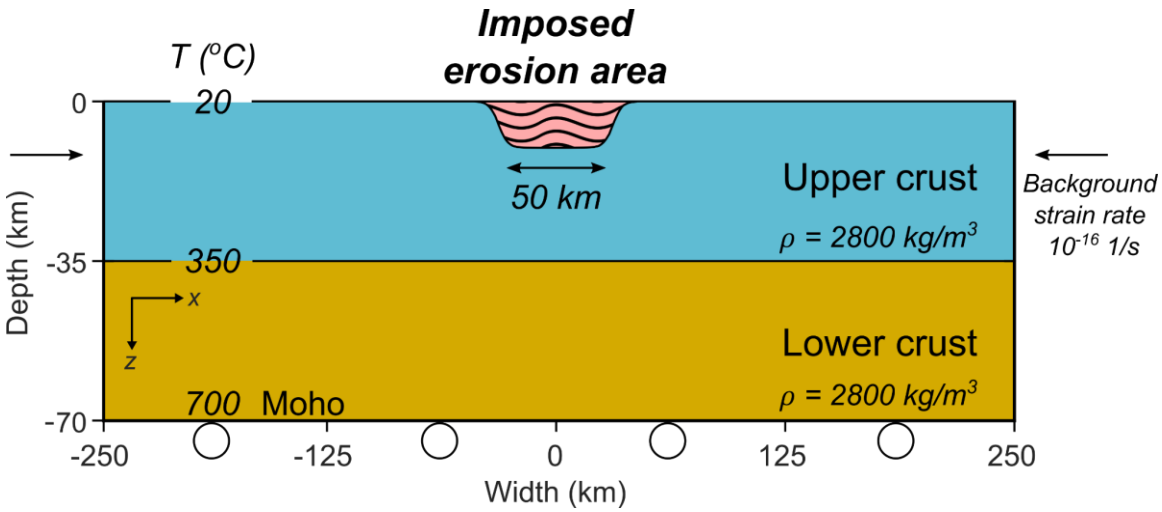

Figure 5.3. Schematic of numerical model setup, showing the initial and boundary conditions.

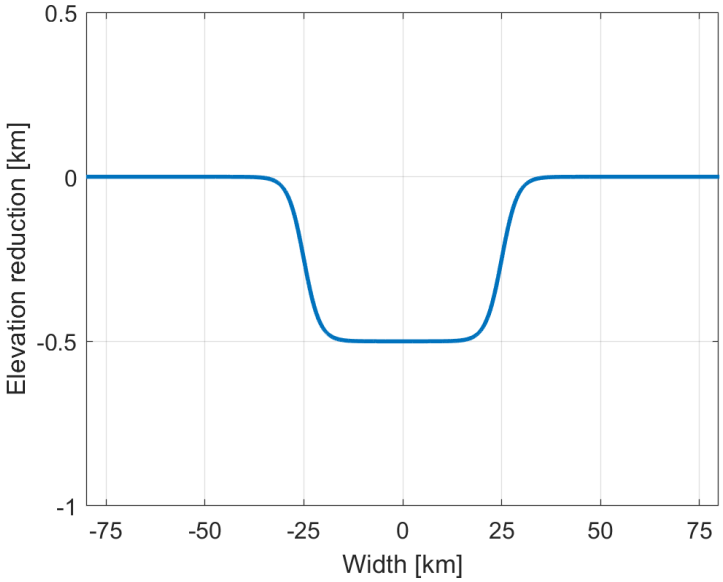

Figure 5.4. Topography defined by the logistic function, after 0.1 Myr of imposed surface erosion (E = 5 km/Myr, w = 25 km, s = 5 km). The logistic function is aimed to mimic the topographic profile resulting from river incision.

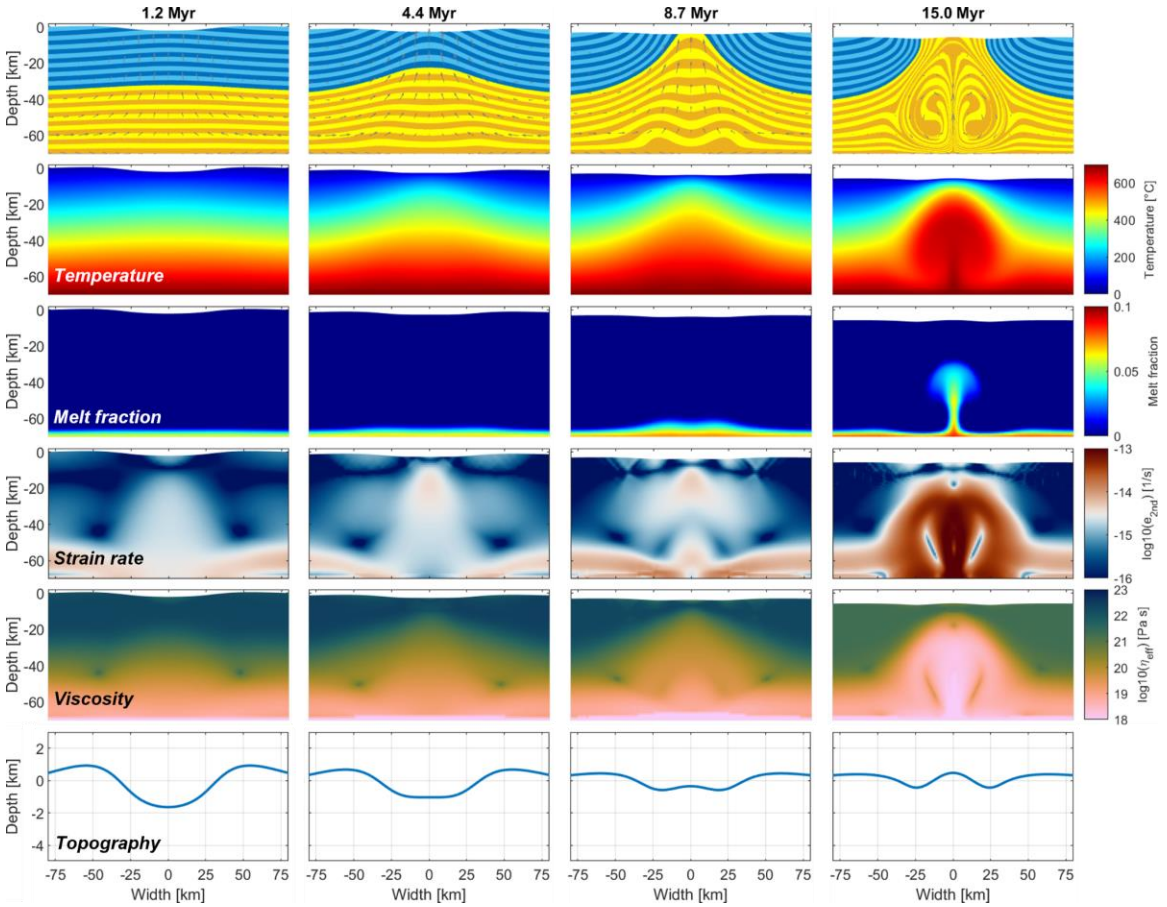

Figure 5.5. Results of reference model with 5 km/Myr imposed erosion rate, 10^{-5} m^2/s topographic diffusion rate, and initial linear geothermal gradient. Time slices of phase, temperature, melt content, strain rate, viscosity, and topography are shown. Topography is plotted relative to the far field elevation, which highlights the changes in local relief due to focused surface erosion.

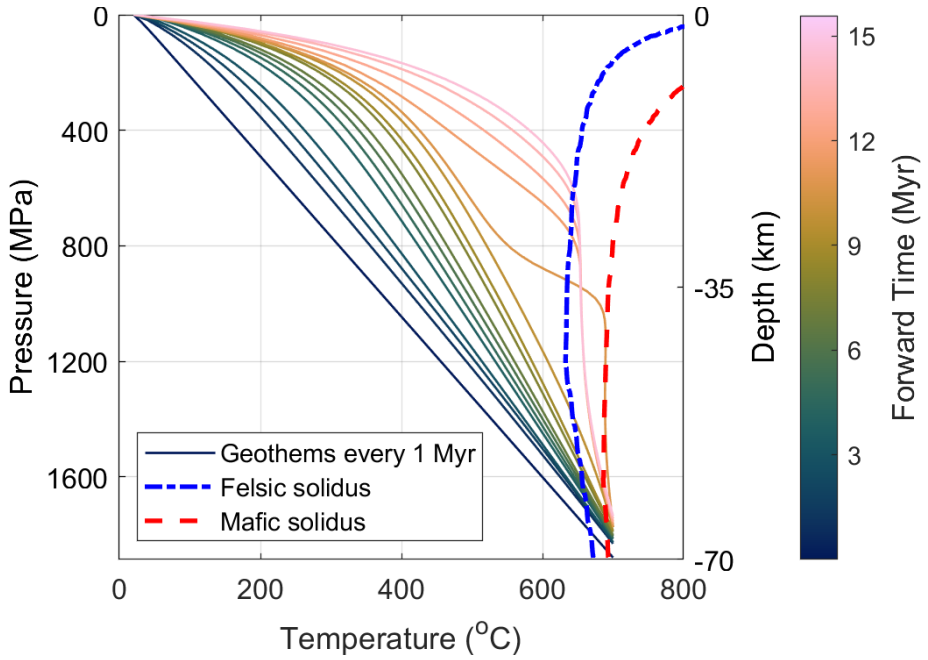

Figure 5.6. Time sequences of geothermal profiles at the center of the simulated crust for the reference model. The initial profile is linear, subsequent geotherms are plotted at every 1 Myr. Solidi for mafic and felsic crustal composition are also shown. Note the thickness of the partial melt layer increases as geotherm becomes elevated.

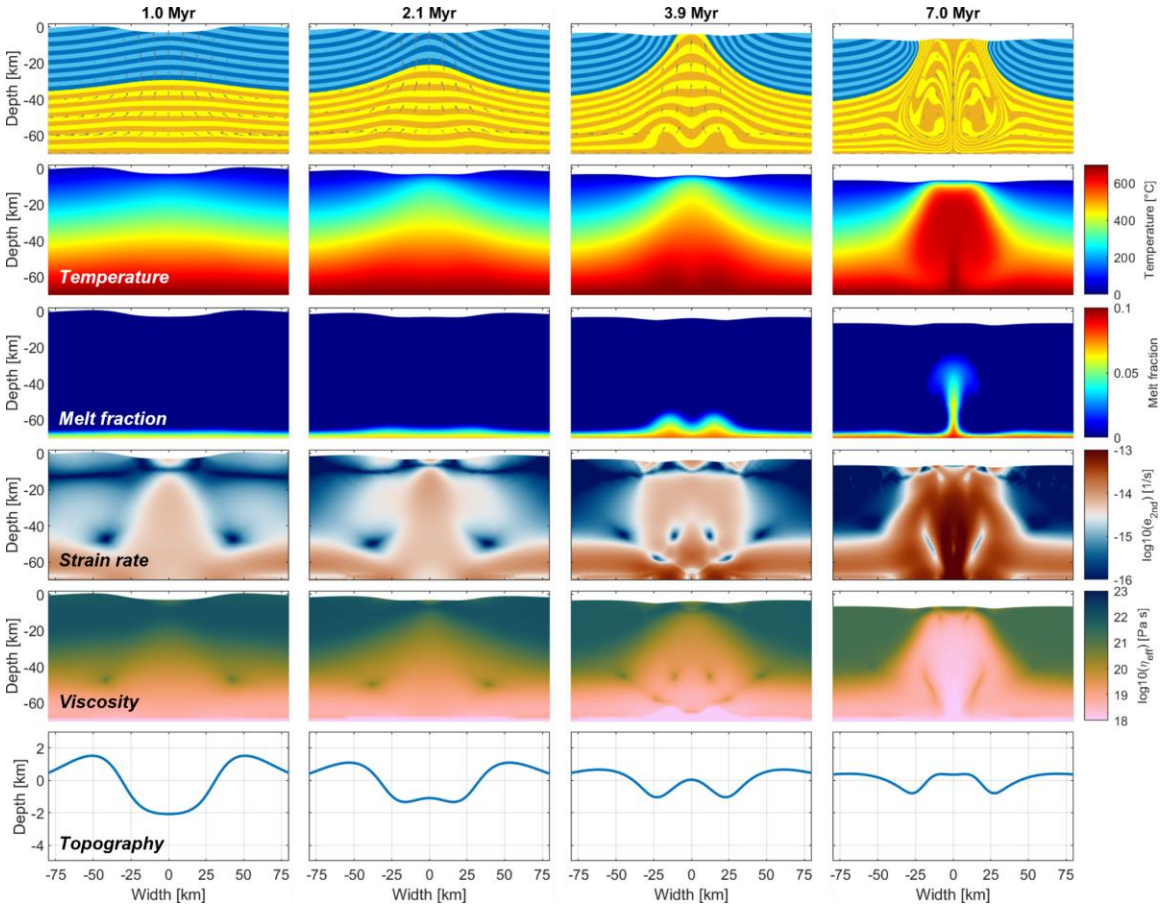

Figure 5.7. Simulation results with high erosion rate (10 km/Myr). The amount of time to exhume the lower crust is much shorter than the reference case with lower erosion rate.

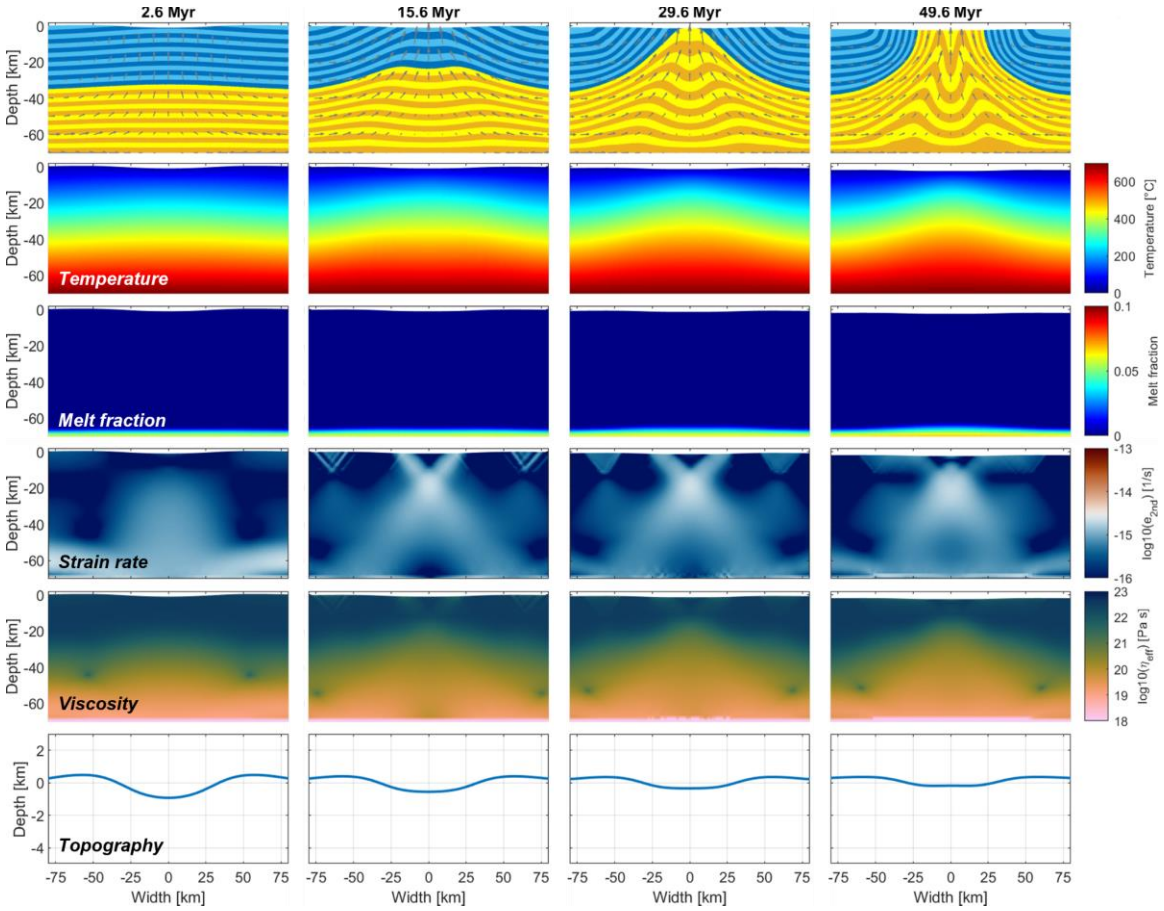

Figure 5.8. Simulation results with low erosion rate (2 km/Myr). The amount of time to exhume the lower crust is much longer than the reference case with higher erosion rate. Note the absence of thermal plume and crustal diapirism.

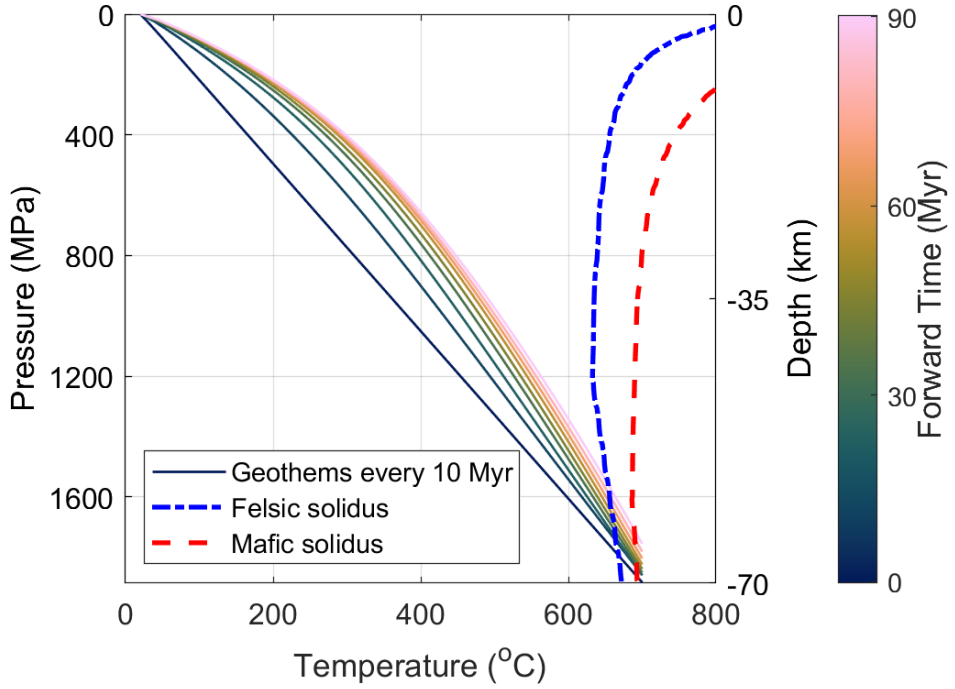

Figure 5.9. Time sequences of geothermal profiles at the center of the simulated crust for the low erosion case (E = 2 km/Myr). The initial profile is linear, subsequent geotherms are plotted at every 10 Myr. Solidi for mafic and felsic crustal composition are also shown.

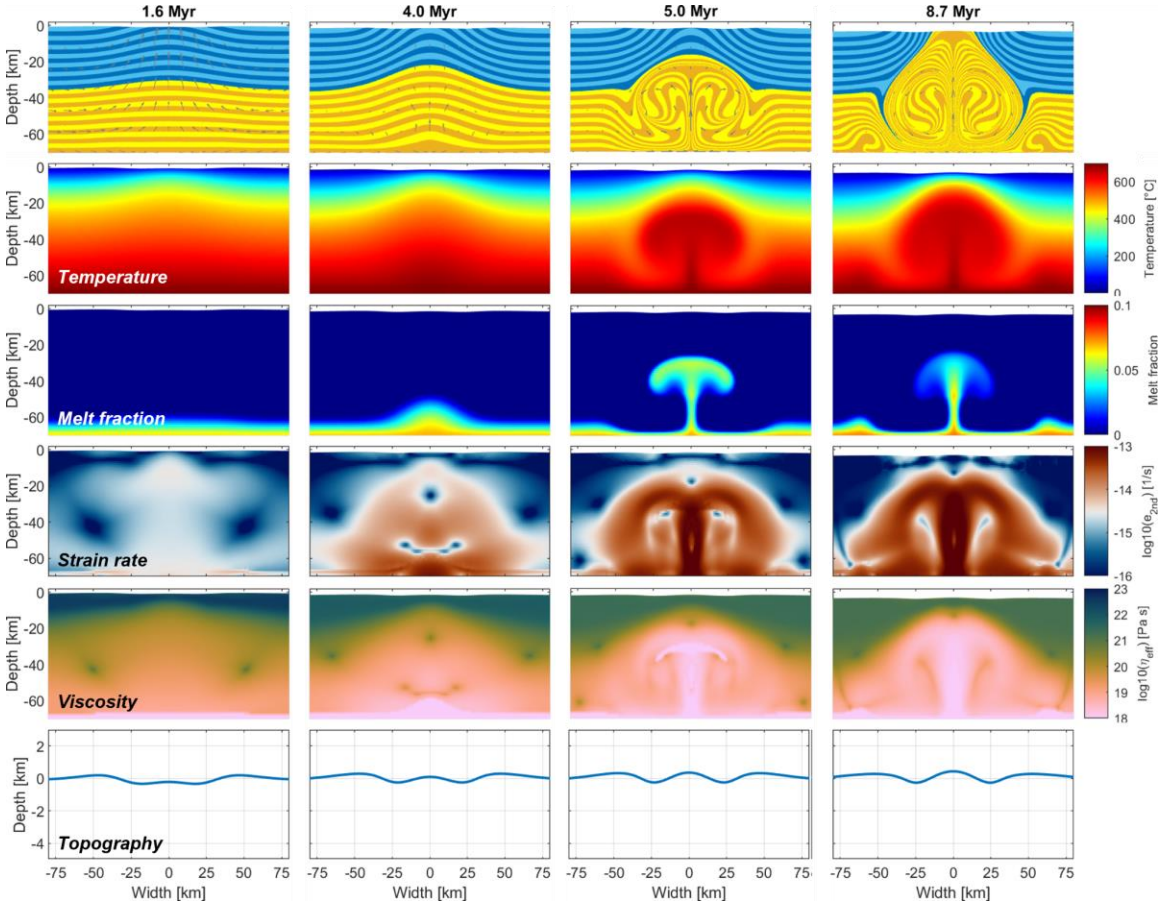

Figure 5.10. Simulation results with 2-stage geothermal gradient (steep 40°C/km in the upper 10 km, below that 4.7°C/km). The lower crust is much more deformed with lower viscosity and higher strain rate. Crustal diapir also forms much earlier compared to the reference case.

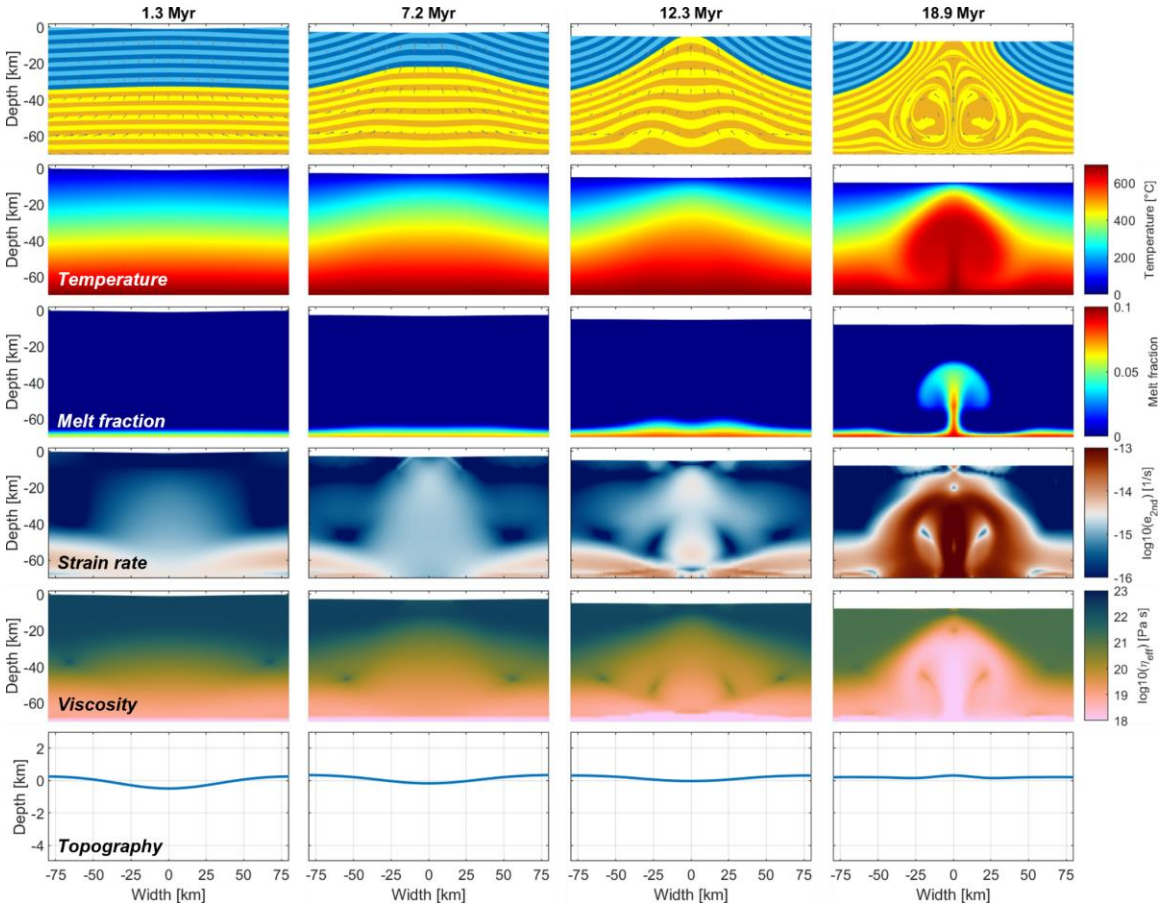

Figure 5.11. Simulation results with high topographic diffusivity (10^{-4} m^2/s). Notice the smoother topography and the broader overall patterns.

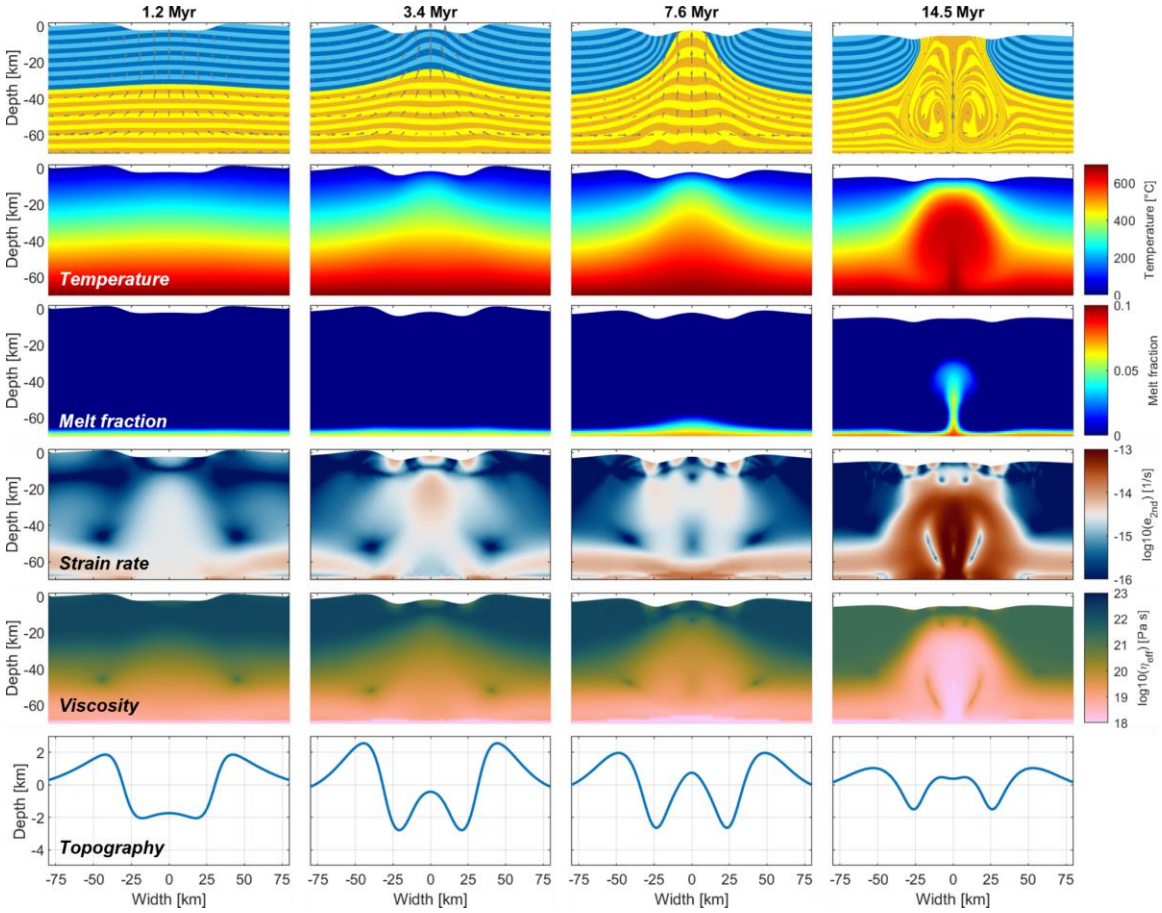

Figure 5.12. Simulation results with low topographic diffusivity (10^{-6} m^2/s). Notice the pronounced topographic relief and the narrow overall patterns.

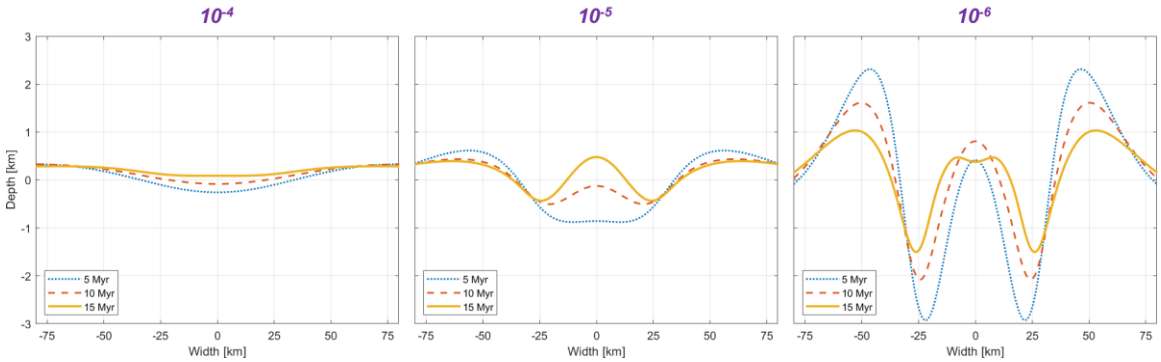

Figure 5.13. Plots of topographic profile at different times (5, 10, and 15 Myr) when different topographic diffusion is used. Topography is calculated relative to far field elevation. The pseudo-valley erosion channel is restricted to the center 50 km.

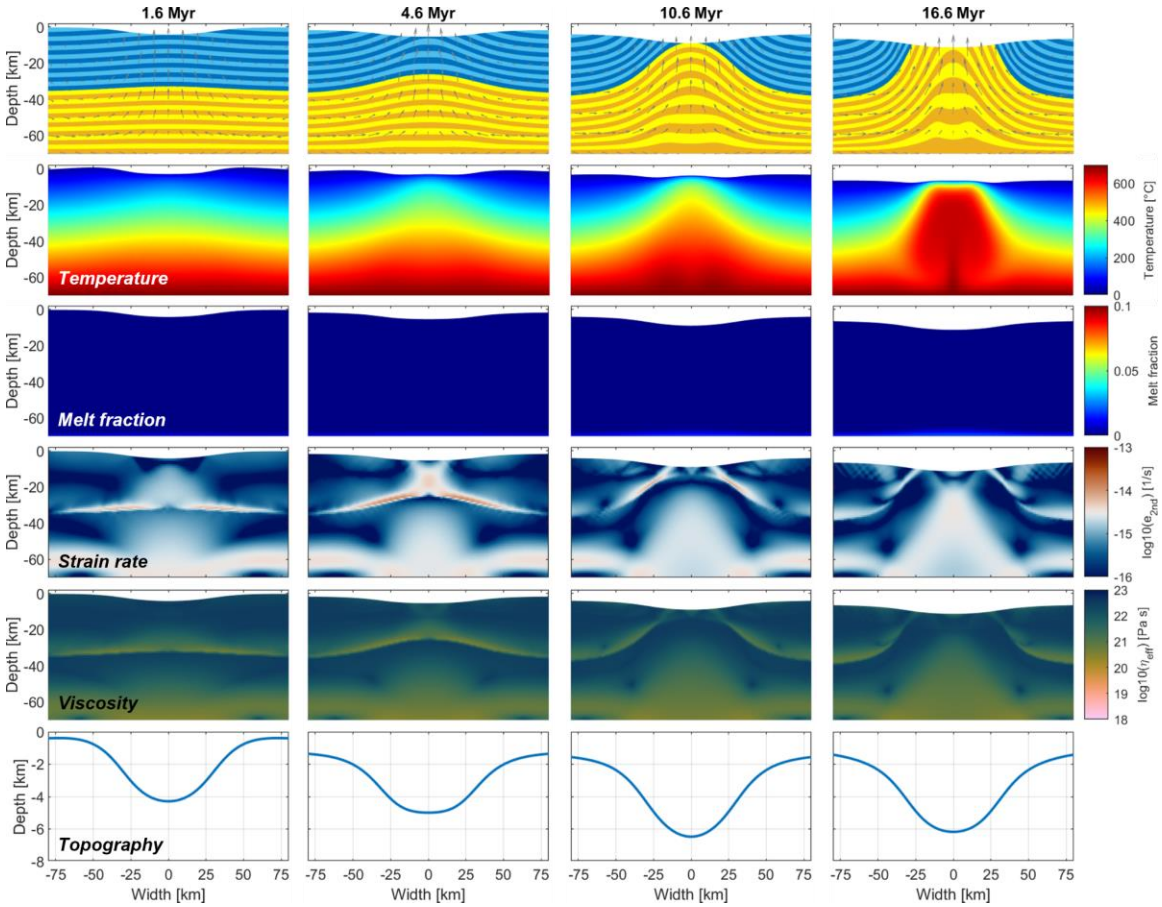

Figure 5.14. Simulation results with mafic lower crust. There is very little melt generation, the viscosity is higher and strain rate is significantly lower. In the absence of diapir, focused erosion produced a deep pseudo-valley.

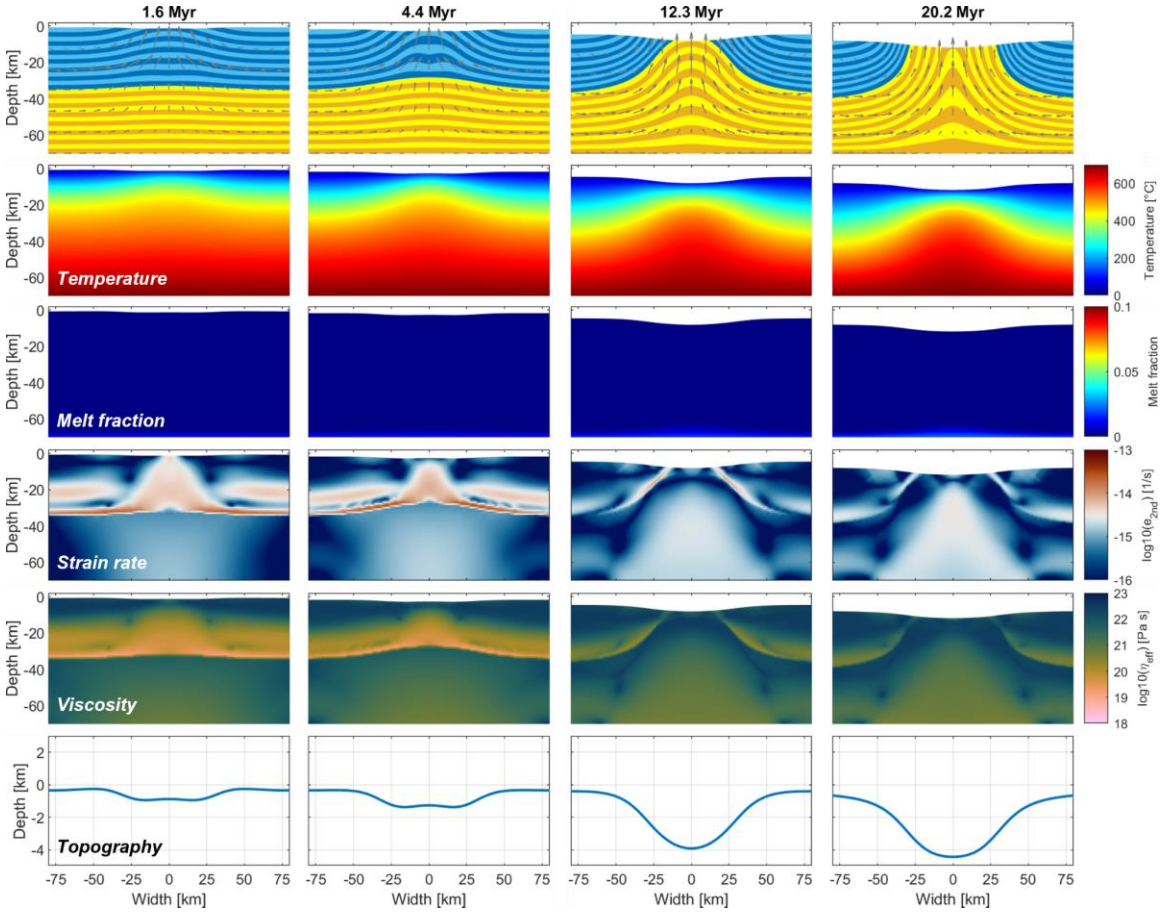

Figure 5.15. Simulation results with mafic lower crust and 2-stage geothermal gradient. The felsic upper crust is significantly weaker and readily deforms. A deep pseudo-valley is produced after the strong mafic lower crust is exhumed to the surface.

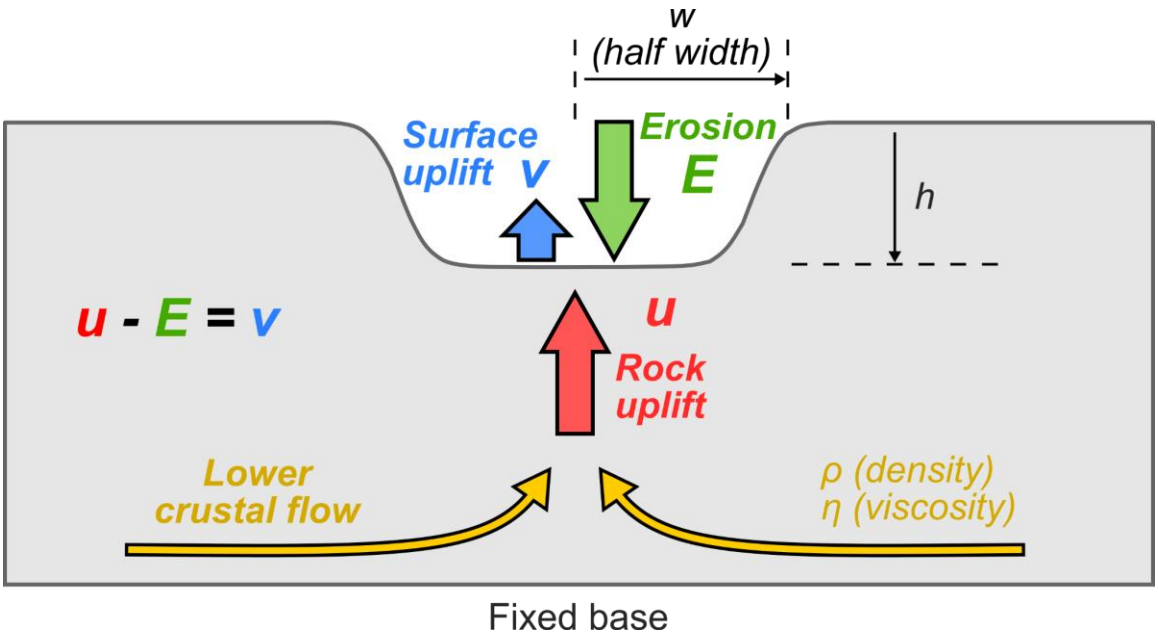

Figure 5.16. Schematic illustration of the isostatic flow model showing the various factors that contribute to the vertical motions within the erosion channel. Constant erosion rate is prescribed, which perturbs the isostatic equilibrium within the crust, causing lateral gradients in lithostatic pressure and driving lateral lower crustal flow. The valley relief is exaggerated for visualization.

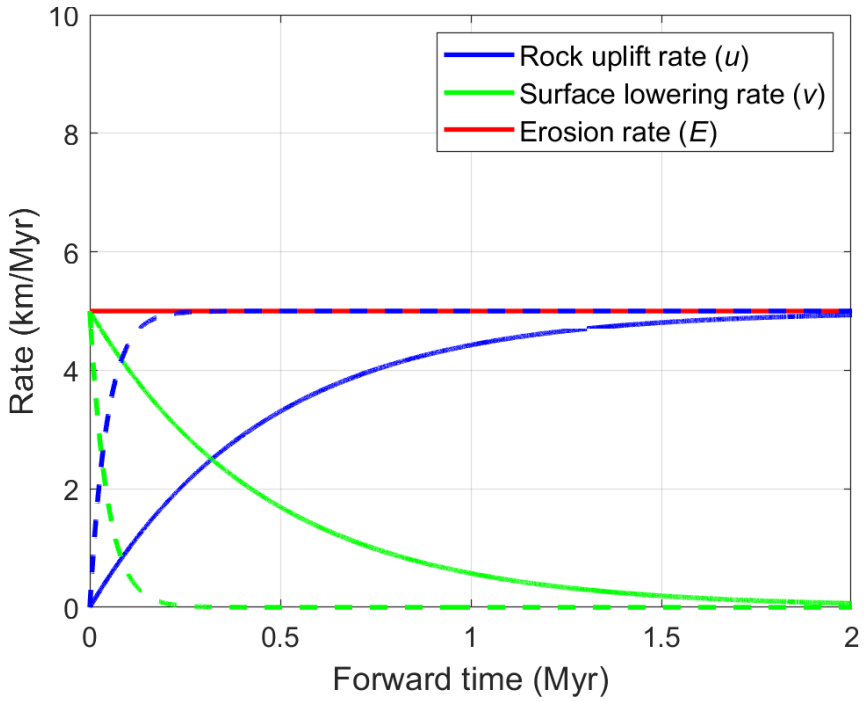

Figure 5.17. Plot of rock uplift rate (u) and surface uplift rate (v) over time. Solid lines correspond to a crustal viscosity of $\eta = 10^{22}$ Pa s and dashed lines correspond to a viscosity of $\eta = 10^{21}$ Pa s. Surface erosion rate (E) is prescribed as a constant 5 km/Myr. Note the rock uplift rate (u) approaches the surface erosion rate (E) after ~2 Myr when $\eta = 10^{22}$ Pa s. The characteristic steady-state timescale for the $\eta = 10^{21}$ Pa s case is much shorter (~0.2 Myr).

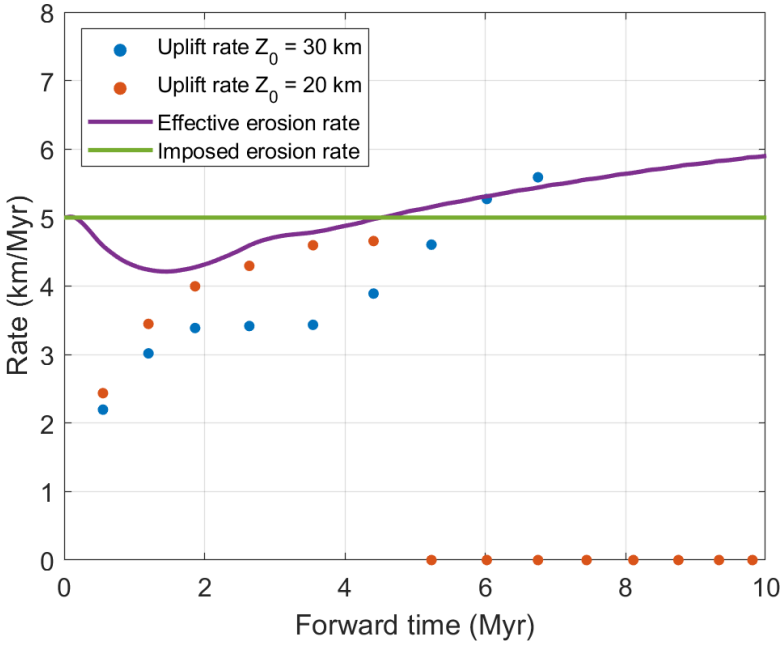

Figure 5.18. Plot of rock uplift rate for rock parcels whose initial depths are 30 and 20 km, located at the center of the pseudo-valley. Rock uplift rates are relative to the numerical grid. Imposed erosion rate and effective erosion rate (imposed erosion + topographic diffusion) are also plotted. Note rocks with shallower initial depth (Z_0 = 20 km) respond to surface erosion faster than deeper rocks.

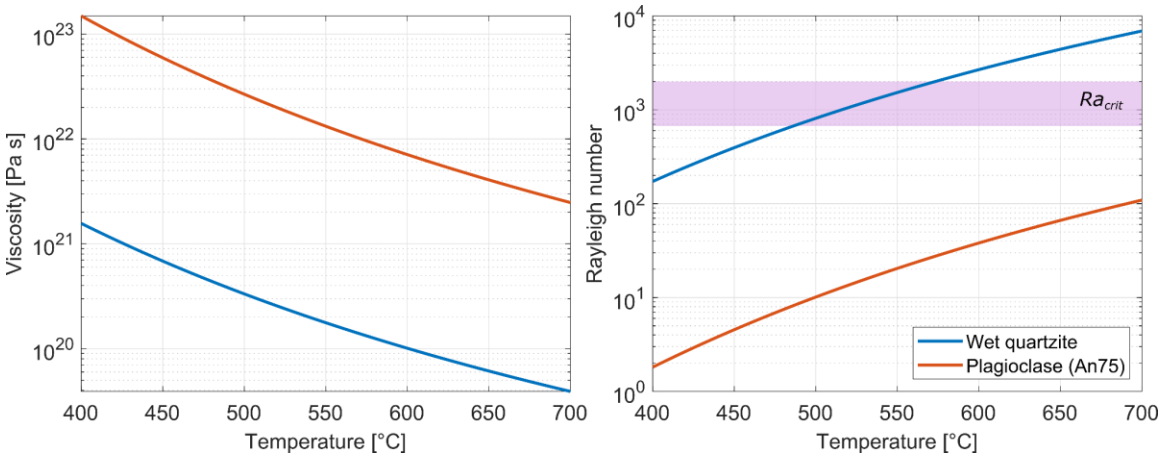

Figure 5.19. Viscosity (A) and Raleigh number (B) as a function of temperature in the advective channel. The range of critical Raleigh number (Ra_{cr}) is highlighted in pink. Scaling of *Ra* is purely based on viscosity changes, which decreases as erosion-induced thermal advection heats up the crust below. Note for a crust of wet quartzite rheology, its *Ra* exceeds the range of critical Raleigh number (Ra_{cr}) as temperature rises above ~575°C, signifying the onset of convection.

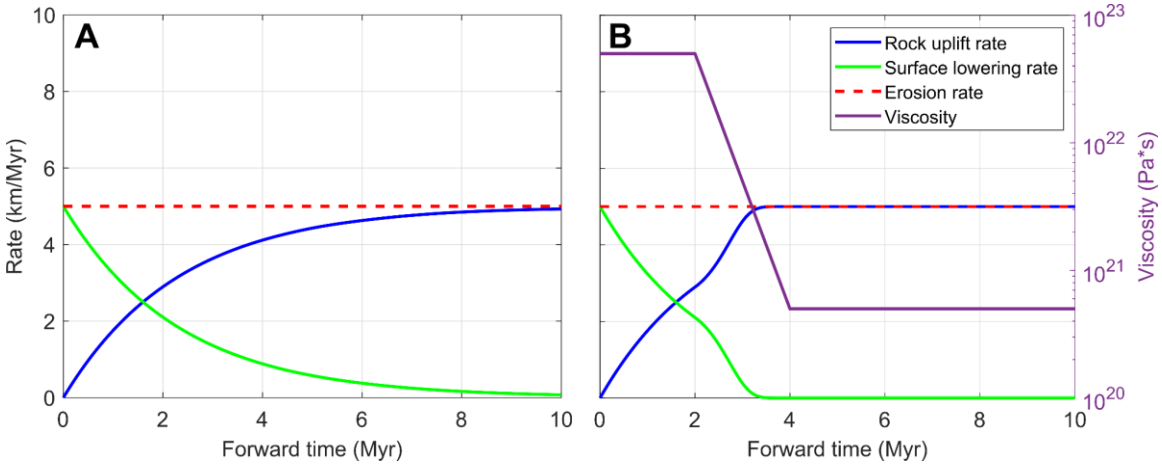

Figure 5.20. Plots showing the effect of changing crustal viscosity on rock uplift and surface lowering rates. **(A)** A high viscosity of 5×10^{22} Pa s is used, lengthening the response time to ~10 Myr. **(B)** Exponential viscosity decreases by 2 orders of magnitude from 5×10^{22} Pa s to 5×10^{20} Pa s between 2 and 4 Myr. Notice the change in the curvature of the rock uplift rate through time and the reduced timescale to reach the steady state (~3 Myr in **B** vs. ~9 Myr in **A**).

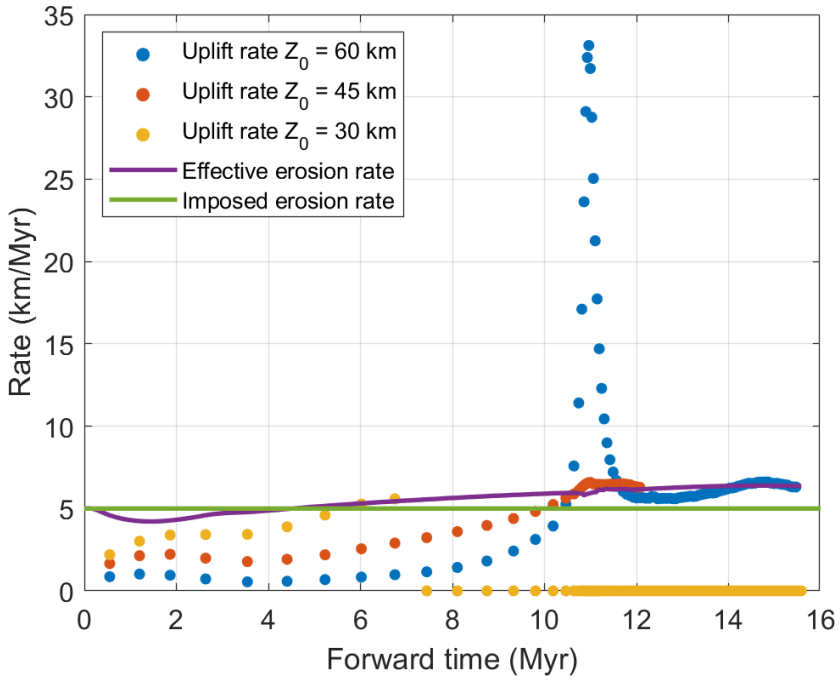

Figure 5.21. Results of the reference model showing rock uplift rates for parcels initially at the horizontal center with 3 different depths (60 km, 45 km, and 30 km). Imposed erosion rate and effective erosion rate (imposed erosion + topographic diffusion) are also plotted. Rocks closer to the surface start uplifting sooner and faster compared to deeper rocks below. Rock with initial depth of 60 km (blue) shows a rapid pulse of uplift rate increase that exceed the imposed erosion rate associated with the entrainment into the diapir column.

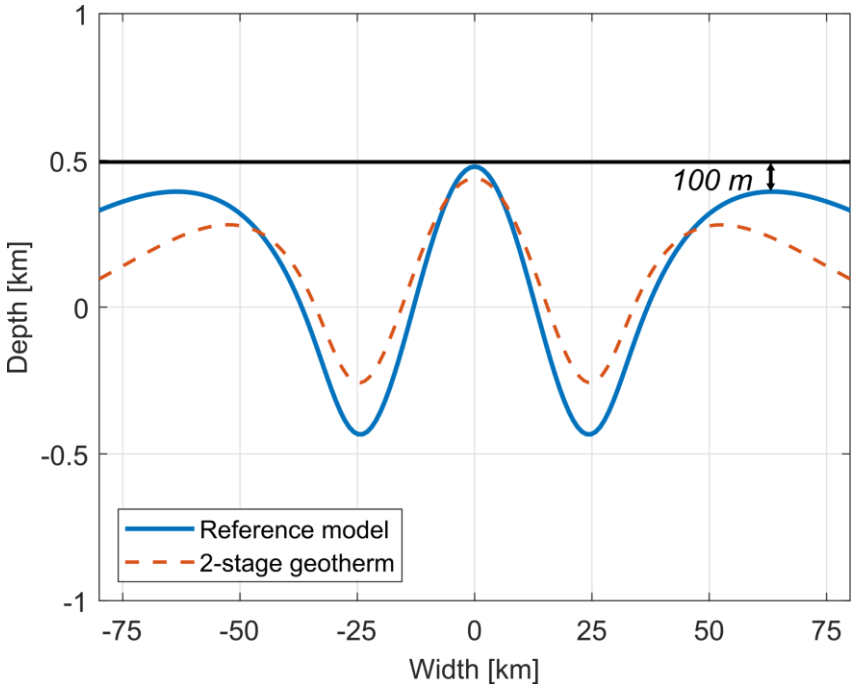

Figure 5.22. Steady-state topographic profile showing the protruding central bulge (100 m higher than the valley shoulders) for the reference model after 15 Myr (blue solid line) as well as the 2-stage geothermal gradient model (160 m higher than the valley shoulders) after 9 Myr (red dashed line). Topography is calculated relative to far field elevation.

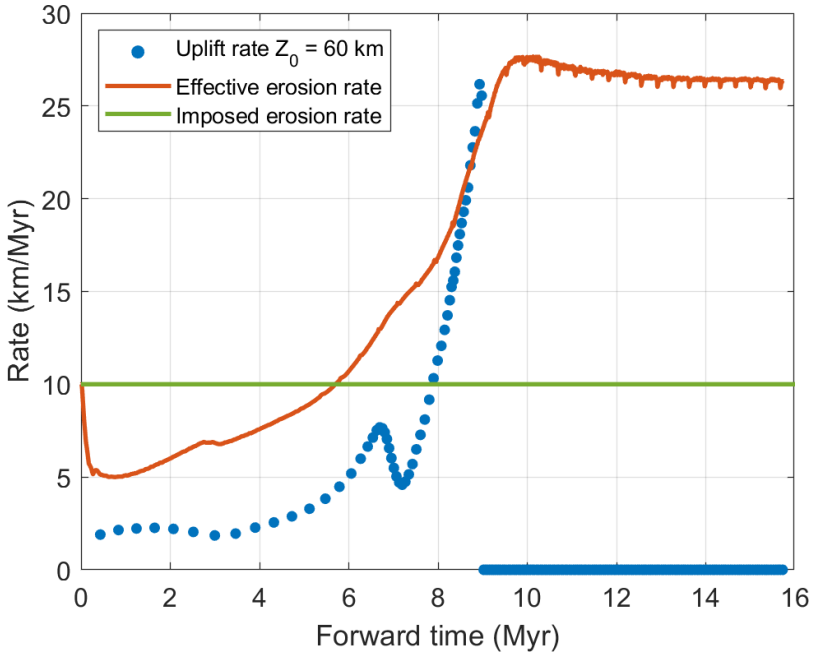

Figure 5.23. Simulation with high imposed erosion rate (10 km/Myr) and topographic diffusion rate (10^{-4} m^2/s) showing rock uplift rate initially at the horizontal center and 60 km depth. Imposed erosion rate and effective erosion rate (imposed erosion + topographic diffusion) are also plotted.

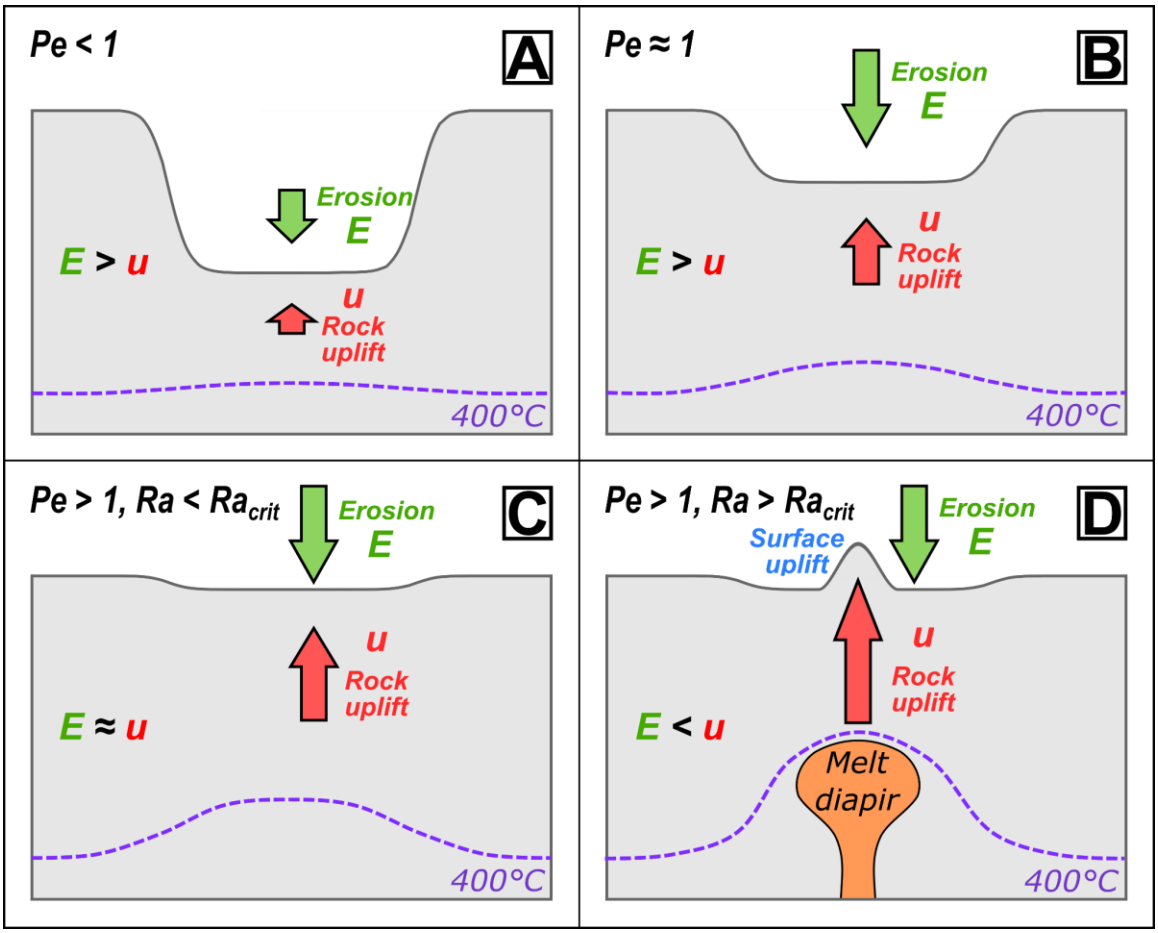

Figure 5.24. Cartoon to illustrate the different scenarios representing the dynamics of the erosion-driven system based on the values of the Péclet (*Pe*) and Raleigh (*Ra*) numbers. Purple dashed line indicates the idealized 400°C isotherm. (**A**) When $Pe < 1$, rock uplift driven by isostatic flow is slow and thermal advection is weak, resulting in pronounced valley topography. (**B**) When $Pe \approx 1$, isostatic flow is faster, valley topography is reduced, and thermal advection becomes important. (**C**) When $Pe > 1$ and $Ra < Ra_{cr}$, isostatic flow further increases due to strong advective heating reducing crustal viscosity, valley topography is minimized and rock uplift rate approaches erosion rate. (**D**) When $Pe > 1$ and $Ra > Ra_{cr}$, crustal convection initiates driving decompression melting and the formation of melt diapir, rock uplift rate increases beyond erosion rate, causing surface uplift with a central bulge that exceeds the surrounding elevation. A transient positive feedback between rock uplift and surface erosion can be established if topographic diffusivity is high.

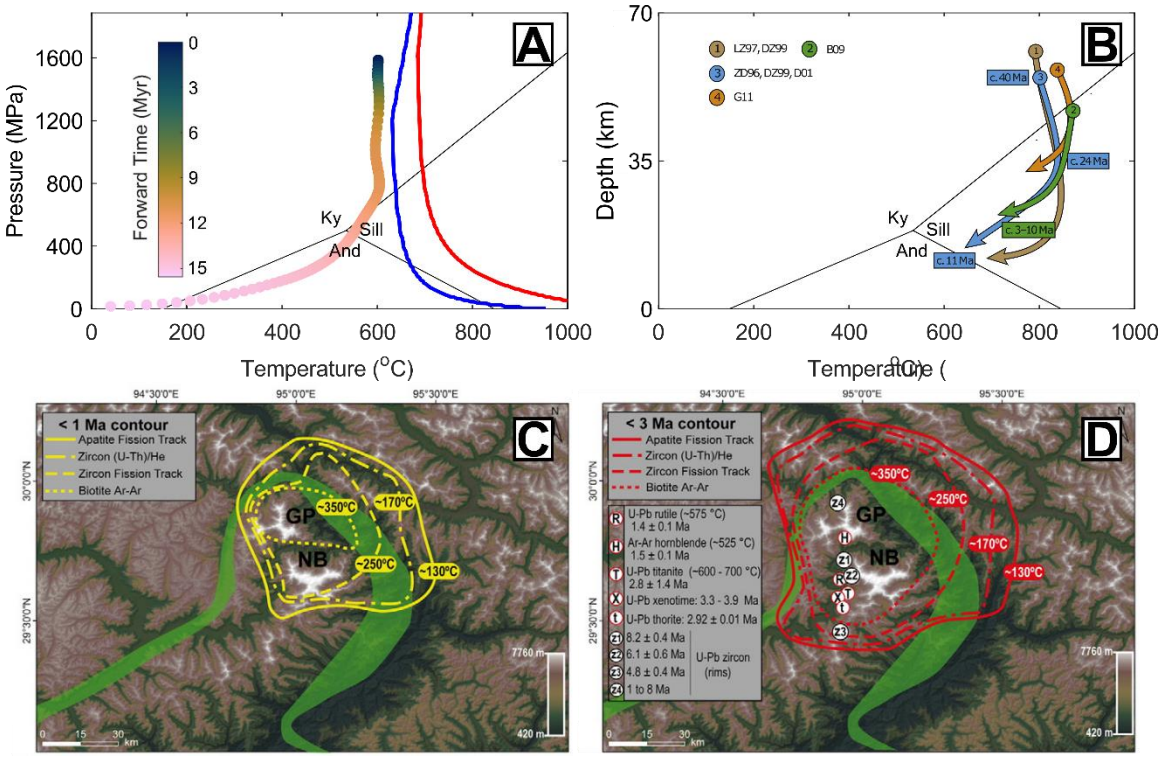

Figure 5.25. Comparison of modeled pressure-temperature-time (P-T-t) path with published thermochronological data. (**A**) Results of the reference model tracking the P-T-t path (colored dots) for the simulated rock parcel with initial depth Z_0 = 60 km located at the horizontal center X_0 = 0 km. Blue and red lines represent felsic and mafic solidus, respectively. (**B**) Synthesis of P-T-t paths from published data using granulite-facies metamorphic units from the EHS (Modified from Palin et al., 2015). Abbreviations for different paths indicate data source: LZ97 = Liu & Zhong (1997), DZ99 = Ding & Zhong (1999), B09 = Booth et al. (2009), ZD96 = Zhong and Ding (1996), D01 = Ding et al. (2001), and G11 =Guilmette et al. (2011). Contour lines showing the spatial distribution of published cooling mineral age data (AFT, (U–Th)/He Zircon, ZFT and Ar–Ar biotite) of bedrock paleo-temperature at < 1 Ma (**C**) and at < 3 Ma (**D**) superimposed on a SRTM (Shuttle Radar Topography Mission) DEM V4 image at 90 m resolution (Modified from Bracciali et al., 2016 and references therein).

CHAPTER 6: Conclusion to the dissertation

MASS AND HEAT TRANSFER PROCESSES IN MAGMATIC OROGENS ALONG THE VERTICAL DIMENSION

This dissertation presented an evaluation of how mass and heat transfer processes affect the evolution of magmatic orogens. At the lower crust and upper mantle level, melt generation may occur through several processes. First, hydrous flux melting facilitated by fluid input derived from dehydration reactions of the subducting slab (e.g., Sisson & Grove, 1993; Kelemen et al., 2003). Second, decompression melting associated with corner flow in the mantle wedge driven by the downgoing motion of the slab (e.g., Sisson & Bronto, 1998, England & Katz, 2010; Bouilhol et al., 2015). Both models predict a correlation between the vigor of arc magmatism and subduction parameters such as convergence velocity and slab age, which is recently challenged by the observations of episodic magmatism in continental arcs and the lack of correlation between subduction kinematics and magmatic episodicity (e.g., Kirsch et al., 2016).

Chapter 2 of this dissertation investigated a third option, heat-induced partial melting of the lower crust (e.g., Petford & Gallagher, 2001). Specifically, transfer of crustal mass into the upper mantle level via horizontal underthrusting of the lower crust (e.g., Ducea, 2001; DeCelles et al., 2009, 2015; De Silva et al., 2015; Kirsch et al., 2016). The results of thermodynamic and kinematic modeling show that partial melting of the underthrusted crust alone does not generate the volume nor thickening rates needed to produce a magmatic flare-up. Based on this conclusion, I suggest mantle melt and/or melt sourced from the lower crust of the overriding plate would account for most of the arc magma. Several recent geochemical studies reveal primitive compositions during arc flare-up events, proposing a mantle source (Schwartz et al., 2017; Ardila et al., 2019;

Attia et al., 2020). It's been proposed that arc root foundering may trigger asthenospheric upwelling, resulting in rapid decompression melting (e.g., Kay & Kay, 1993) of the mantle and causing a magmatic pulse that is above the mantle flux baseline (Lee & Anderson, 2015). Through a numerically simulated cycle of lower crustal underthrusting, arc root buildup, foundering, and renewed underthrusting, I demonstrate that crustal underthrusting contributes to the formation of the arc root via mass addition, resulting in reduced timescales of root foundering. At the same time, the increase in thickness of the arc crust exerts a self-limiting effect on arc magmatism and controls the arc tempo (Chin et al., 2015; Cao et al., 2016). Thus, while underthrusting of lower crust does not directly trigger a magmatic flare-up, it has the potential in limiting arc magma generation and regulating the magmatic tempo via mass contribution to the arc root and subsequent foundering.

Magma generated in the mantle ascends into the tectonically deforming crust, resulting in crustal thickening (e.g., Haschke & Gunther, 2003). Melt flux into the crust also plays a fundamental role in the composition of arc magmas (e.g., Hildreth & Moorbath, 1988), as well as the thermal and rheological evolution of the orogenic crust (e.g., Dufek & Bergantz, 2005, Annen, 2009). Melt rises through the orogenic crust making intrusions and eventually erupts through surface volcanoes (e.g., England & Katz, 2010). In an actively deforming magmatic orogen, a challenge is to quantify both the effects of tectonic thickening from contractional plate forcing and magmatic thickening from magma addition into the crust (Lee et al., 2015; Cao & Paterson, 2016). In addition, surface erosion modulates the crustal thickness by removing the topmost portion of the crust. The combined effect of magmatic and tectonic thickening and

surface erosion show the depth-dependent nature of rock exhumation-burial paths during crustal thickening. In Chapter 3 we revealed a tilted crustal section of the Gangdese Batholith via the determination of bedrock pressures. In doing so, we investigated how crust at different depths responds to magmatism, tectonic deformation, and surface erosion. The results showed the upper, middle, and lower crust exhume differently under the same surface erosion and tectonic thickening conditions. We also identified two major phases of crustal thickening and a potential phase of crustal thinning that can be explained by the plate convergence history as well as the transition from subduction to collision, respectively.

The investigation of Gangdese magmatic fabrics data presented in Chapter 4 further supports the exhumation/burial paths constrained using bedrock pressures and is consistent with Tang et al. (2021) crustal thickness estimates. Contrary to previous studies that show a dependence of fabric orientations on plate motion (e.g., Cao et al., 2015), the magmatic fabrics of the Gangdese Batholith are not correlated with plate convergence velocity. Instead, the changes in fabric orientations may record how strain is accommodated during the transition from ocean-continent subduction to continent-continent collision, thus providing an insight into the controversy surrounding India's paleogeography and history of the India-Asia collision. Of the three end-member models: fully continental greater India (e.g., Ingalls et al., 2016), Xigaze interoceanic arc (e.g., Kapp et al., 2019), and Tibetan Himalaya microcontinent (e.g., van Hinsbertgen et al., 2012); the fabrics data favors the microcontinent model which predicts ~60 Ma collision of Tibetan Himalaya microcontinent with Asia and the existence of the Greater India Basin north of the Indian lithosphere.

Magmatic addition and tectonic contraction drive crustal thickening in orogens, resulting in high topography (e.g., Cawood et al., 2009). The high topography gives rise to ridges and peaks generating greater relief, which then promotes accelerated erosion (e.g., Duff & Duff, 1993). In orogens, erosion not only removes surficial material and thins the crust, but also alters the lithospheric thermal and stress state and in turn affects the style, pattern, and vigor of tectonic deformation as well as the degree of melt generation (magmatism) (e.g., Davis et al., 1983; Dahlen et al., 1984; Liu et al., 2020).

One of the best places to investigate the interactions between surface and solid earth processes is the eastern Himalayan syntaxis (EHS) due to its spatially focused high erosion rates (e.g., Finnegan et al., 2002, 2008). It has been argued that in the EHS region, solid earth tectonics and surface processes work in tandem, resulting in a positive feedback loop (e.g., Beaumont et al., 2001; Zeitler et al., 2001; Whipple, 2009; Koons et al., 2013). In Chapter 5, I explored the role of surface erosion in driving solid earth processes and showed that localized surface erosion is able to drive tectonic deformation via thermal advection and strain weakening. The process of erosion-driven rock exhumation is sustained by isostatic flow and amplified by crustal melt diapirism, leading to rapid rock uplift that may further induce fast surface erosion and establish positive feedback under some extreme conditions, as envisioned by the tectonic aneurysm model (Zeiter et al., 2001, Koons et al., 2013). While I do not claim to have solved the age-old debate on the driver of EHS exhumation, I highlight that the erosion-driven diapiric flow is an overlooked process that can be one of the missing pieces or alternative mechanisms explaining the evolution of the eastern Himalayan syntaxis.

REFERENCES

Annen, C., 2009. From plutons to magma chambers: Thermal constraints on the accumulation of eruptible silicic magma in the upper crust. Earth and Planetary Science Letters, 284(3-4), pp.409-416.

Ardila, A.M.M., Paterson, S.R., Memeti, V., Parada, M.A. and Molina, P.G., 2019. Mantle driven Cretaceous flare-ups in Cordilleran arcs. Lithos, 326, pp.19-27.

Attia, S., Cottle, J.M. and Paterson, S.R., 2020. Erupted zircon record of continental crust formation during mantle driven arc flare-ups. Geology, 48(5), pp.446-451.

Beaumont, C., Jamieson, R.A., Nguyen, M.H. and Lee, B., 2001. Himalayan tectonics explained by extrusion of a low-viscosity crustal channel coupled to focused surface denudation. Nature, 414(6865), pp.738-742.

Bouilhol, P., Magni, V., van Hunen, J. and Kaislaniemi, L., 2015. A numerical approach to melting in warm subduction zones. Earth and Planetary Science Letters, 411, pp.37-44.

Cao, W., Paterson, S., Memeti, V., Mundil, R., Anderson, J.L. and Schmidt, K., 2015. Tracking paleodeformation fields in the Mesozoic central Sierra Nevada arc: Implications for intra-arc cyclic deformation and arc tempos. Lithosphere, 7(3), pp.296-320.

Cao, W. and Paterson, S., 2016. A mass balance and isostasy model: Exploring the interplay between magmatism, deformation and surface erosion in continental arcs using central Sierra Nevada as a case study. Geochemistry, Geophysics, Geosystems, 17(6), pp.2194-2212.

Cao, W., Paterson, S., Saleeby, J. and Zalunardo, S., 2016. Bulk arc strain, crustal thickening, magma emplacement, and mass balances in the Mesozoic Sierra Nevada arc. Journal of Structural Geology, 84, pp.14-30.

Cawood, P.A., Kröner, A., Collins, W.J., Kusky, T.M., Mooney, W.D. and Windley, B.F., 2009. Accretionary orogens through Earth history. Geological Society, London, Special Publications, 318(1), pp.1-36.

Chin, E.J., Lee, C.T.A. and Blichert-Toft, J., 2015. Growth of upper plate lithosphere controls tempo of arc magmatism: Constraints from Al-diffusion kinetics and coupled Lu-Hf and Sm-Nd chronology. Geochemical Perspectives Letters, 1(1), pp.20-32.

Dahlen, F.A., 1984. Noncohesive critical Coulomb wedges: An exact solution. Journal of Geophysical Research: Solid Earth, 89(B12), pp.10125-10133.

Davis, D., Suppe, J. and Dahlen, F.A., 1983. Mechanics of fold-and-thrust belts and accretionary wedges. Journal of Geophysical Research: Solid Earth, 88(B2), pp.1153-1172.

De Silva, S.L., Riggs, N.R. and Barth, A.P., 2015. Quickening the pulse: Fractal tempos in continental arc magmatism. Elements, 11(2), pp.113-118.

DeCelles, P.G., Ducea, M.N., Kapp, P. and Zandt, G., 2009. Cyclicity in Cordilleran orogenic systems, Nat.

DeCelles, P.G. and Graham, S.A., 2015. Cyclical processes in the North American Cordilleran orogenic system. Geology, 43(6), pp.499-502.

Ducea, M., 2001. The California arc: Thick granitic batholiths, eclogitic residues, lithospheric-scale thrusting, and magmatic flare-ups. GSA today, 11(11), pp.4-10.

Dufek, J. and Bergantz, G.W., 2005. Lower crustal magma genesis and preservation: a stochastic framework for the evaluation of basalt–crust interaction. Journal of Petrology, 46(11), pp.2167-2195.

Duff, P.M.D. and Duff, D. eds., 1993. Holmes' principles of physical geology. Taylor & Francis.

England, P.C. and Katz, R.F., 2010. Melting above the anhydrous solidus controls the location of volcanic arcs. Nature, 467(7316), pp.700-703.

Finnegan, N.J., Anders, A.M., Hallet, B., Montgomery, D.R. and Stone, J.O., 2002, December. Defining Spatial Gradients in Fluvial Erosion Across the Eastern Himalayan Syntaxis. In AGU Fall Meeting Abstracts (Vol. 2002, pp. T71A-1164).

Finnegan, N.J., Hallet, B., Montgomery, D.R., Zeitler, P.K., Stone, J.O., Anders, A.M. and Yuping, L., 2008. Coupling of rock uplift and river incision in the Namche Barwa–Gyala Peri massif, Tibet. Geological Society of America Bulletin, 120(1-2), pp.142-155.

Haschke, M. and Gunther, A., 2003. Balancing crustal thickening in arcs by tectonic vs. magmatic means. Geology, 31(11), pp.933-936.

Hildreth, W. and Moorbath, S., 1988. Crustal contributions to arc magmatism in the Andes of central Chile. Contributions to mineralogy and petrology, 98(4), pp.455-489.

Ingalls, M., Rowley, D.B., Currie, B. and Colman, A.S., 2016. Large-scale subduction of continental crust implied by India–Asia mass-balance calculation. Nature Geoscience, 9(11), pp.848-853.

Kapp, P. and DeCelles, P.G., 2019. Mesozoic–Cenozoic geological evolution of the Himalayan-Tibetan orogen and working tectonic hypotheses. American Journal of Science, 319(3), pp.159-254.

Kay, R.W. and Kay, S.M., 1993. Delamination and delamination magmatism. Tectonophysics, 219(1-3), pp.177-189.

Kelemen, P.B., Hanghøj, K. and Greene, A.R., 2003. One view of the geochemistry of subduction-related magmatic arcs, with an emphasis on primitive andesite and lower crust. Treatise on geochemistry, 3, p.659.

Kirsch, M., Paterson, S.R., Wobbe, F., Ardila, A.M.M., Clausen, B.L. and Alasino, P.H., 2016. Temporal histories of Cordilleran continental arcs: Testing models for magmatic episodicity. American Mineralogist, 101(10), pp.2133-2154.

Koons, P.O., Zeitler, P.K. and Hallet, B., 2013. Tectonic aneurysms and mountain building. Treatise on geomorphology, 5, pp.318-349.

Lee, C.T.A. and Anderson, D.L., 2015. Continental crust formation at arcs, the arclogite "delamination" cycle, and one origin for fertile melting anomalies in the mantle. Science Bulletin, 60(13), pp.1141-1156.

Lee, C.T.A., Thurner, S., Paterson, S. and Cao, W., 2015. The rise and fall of continental arcs: Interplays between magmatism, uplift, weathering, and climate. Earth and Planetary Science Letters, 425, pp.105-119.

Liu, Y., Tan, X., Ye, Y., Zhou, C., Lu, R., Murphy, M.A., Xu, X. and Suppe, J., 2020. Role of erosion in creating thrust recesses in a critical-taper wedge: An example from Eastern Tibet. Earth and Planetary Science Letters, 540, p.116270.

Petford, N. and Gallagher, K., 2001. Partial melting of mafic (amphibolitic) lower crust by periodic influx of basaltic magma. Earth and Planetary Science Letters, 193(3-4), pp.483-499.

Schwartz, J.J., Klepeis, K.A., Sadorski, J.F., Stowell, H.H., Tulloch, A.J. and Coble, M.A., 2017. The tempo of continental arc construction in the Mesozoic Median Batholith, Fiordland, New Zealand. Lithosphere, 9(3), pp.343-365.

Sisson, T.W. and Bronto, S., 1998. Evidence for pressure-release melting beneath magmatic arcs from basalt at Galunggung, Indonesia. Nature, 391(6670), pp.883-886.

Sisson, T.W. and Grove, T.L., 1993. Experimental investigations of the role of H2O in calc-alkaline differentiation and subduction zone magmatism. Contributions to mineralogy and petrology, 113(2), pp.143-166.

Tang, M., Ji, W.Q., Chu, X., Wu, A. and Chen, C., 2021. Reconstructing crustal thickness evolution from europium anomalies in detrital zircons. Geology, 49(1), pp.76-80.

Van Hinsbergen, D.J., Lippert, P.C., Dupont-Nivet, G., McQuarrie, N., Doubrovine, P.V., Spakman, W. and Torsvik, T.H., 2012. Greater India Basin hypothesis and a two-stage Cenozoic collision between India and Asia. Proceedings of the National Academy of Sciences, 109(20), pp.7659-7664.

Whipple, K.X., 2009. The influence of climate on the tectonic evolution of mountain belts. Nature geoscience, 2(2), pp.97-104.

Zeitler, P.K., Meltzer, A.S., Koons, P.O., Craw, D., Hallet, B., Chamberlain, C.P., Kidd, W.S., Park, S.K., Seeber, L., Bishop, M. and Shroder, J., 2001. Erosion, Himalayan geodynamics, and the geomorphology of metamorphism. Gsa Today, 11(1), pp.4-9.